

Millimeter-wave spectroscopy of highly nitrogenous molecules of potential astrochemical
interest

By

Brent K. Amberger

A dissertation submitted in partial fulfillment of
the requirements for the degree of

Doctor of Philosophy

(Chemistry)

at the

University of Wisconsin-Madison

2015

Date of final oral examination: 8/24/15

The dissertation is approved by the following members of the Final Oral Committee:

Robert J. McMahon, Professor, Chemistry

R. Claude Woods, Professor, Chemistry

Etienne Garand, Assistant Professor, Chemistry

Timothy H. Bertram, Assistant Professor, Chemistry

Gilbert M. Nathanson, Professor, Chemistry

Dedicated to my family, my friends, and to all those who helped me along the way.

Acknowledgements

A great many people deserve my sincere thanks for helping me to get to this point in my scientific career. Starting in autobiographical order, my parents and the rest of my family have always supported me. They taught me to be inquisitive, to be creative, and to solve problems. They have my thanks and my love for all that they have done.

As an undergraduate I was lucky to meet several advisors who helped steer me onto the chemistry pathway. Professors Helen Leung and Mark Marshall, in particular, showed me the thrill and unadulterated joy that comes with correctly assigning a rotational spectrum. That experience truly opened my eyes, as there is no clearer proof either for, or against, the existence of a God than the ability to predict the frequency of thousands of transitions to experimental accuracy.

I arrived at the University of Wisconsin just in time to join a growing rotational spectroscopy collaboration between Professors Bob McMahon and Claude Woods. The research group led by these two advisors has been an excellent place for me to grow as a scientist over the past six years. Bob has always supported and encouraged me, giving me everything I needed to succeed. He has been a constant patron and advocate for me and my science, whether I felt like I deserved it or not. Claude's contribution to my education has been thousands upon thousands of hours of his time, teaching me almost everything I know about spectroscopy, and attempting to teach me many things I still do not know. Perhaps most importantly, Claude has taught me the mantra 'we'll get it working'. If you watch a pressure gauge long enough, it always reveals its secrets.

My coworkers in graduate school have been outstanding friends and collaborators. My first contact in the group was Dr. Brian Esselman, who has made numerous contributions to this work. Besides providing me with *ab initio* insights and maintaining the instrument code, he has served as a mentor throughout my time here, and will continue to mentor me in my next job as lecturer. In the early years I also spent a lot of time in lab with Mitch Daane, Alex Nolan, and Josh Shutter, all of whom helped get the initial projects off of the ground. I have greatly enjoyed the blossoming of the rotational spectroscopy subgroup in last few years, and I thank Nicholas Walters, Vanessa Orr, Zachary Heim, Hunter Lau, Cara Schwarz, and Maria Zdanovskaia for driving many projects forward and contributing young blood to the group. Though not rotational spectroscopists, I also thank my long-time office mates Steph Knezz and Ben Haenni, just for being there. Around the department, Tracy Drier, Matt Martin, Steve Myers, Jerry Stamn, Ed Vasiukevicius, and Bill Goebel have been invaluable in rebuilding our instrument and keeping it running. I have made many other friends who have helped me on my way in graduate school. You know who you are, and I thank you.

Finally I thank you, the reader. Thank you for taking the time to open this up!

Table of Contents

Dedication	i
Acknowledgments	ii
Table of Contents	iv
Chapter 1: Thesis overview	1
Chapter 2: Synthesis and millimeter-wave spectroscopy of carbonyl diazide	8
Abstract	9
Introduction	9
Synthesis of carbonyl diazide	13
Computational studies	18
IR spectroscopy	19
Millimeter-wave spectroscopy	23
Summary	46
Acknowledgements	46
References	47

Chapter 3: Equipment and preliminary work towards the generation of diazirinone	50
Abstract	51
Introduction	51
Improvements to the spectrometer	52
Pyrolysis apparatus	60
Impurity identification in carbonyl diazide sample	64
Summary	69
References	70
Chapter 4: Precise equilibrium structure determination of hydrazoic acid (HN₃) by millimeter-wave spectroscopy	72
Abstract	73
Introduction	73
Computational methods	77
Synthesis	78
Increase in spectrometer range	80
Analysis of rotational spectra	84
Hyperfine splitting	97
Structure determination	101
Discussion	107
Conclusions	111
Acknowledgments	112
References	112

Chapter 5: Analysis of the lowest eight vibrational states of hydrazoic acid (HN₃) and deuterated hydrazoic acid (DN₃) by millimeter-wave spectroscopy and FTIR data	117
Abstract	118
Introduction	118
Assignment of lines	127
Rotational vibration interaction corrections	129
Combination differences	131
Loomis-Wood plots	134
Linear plots of <i>a</i> -type R-branch transitions	136
Confirming assignments of locally perturbed <i>a</i> -type series	156
Analysis of splitting of <i>a</i> -type lines	169
Analysis of <i>b</i> -type transitions	175
Perturbation analysis	183
Simultaneous fits of the ground, ν_5 , and ν_6 states of DN ₃	188
Simultaneous fits of the ground, ν_5 , and ν_6 states of HN ₃	192
Summary	194
Acknowledgments	195
References	195
Appendix A: Pyridazine equilibrium structure publication	198
Appendix B: Carbonyl diazide synthesis publication	212

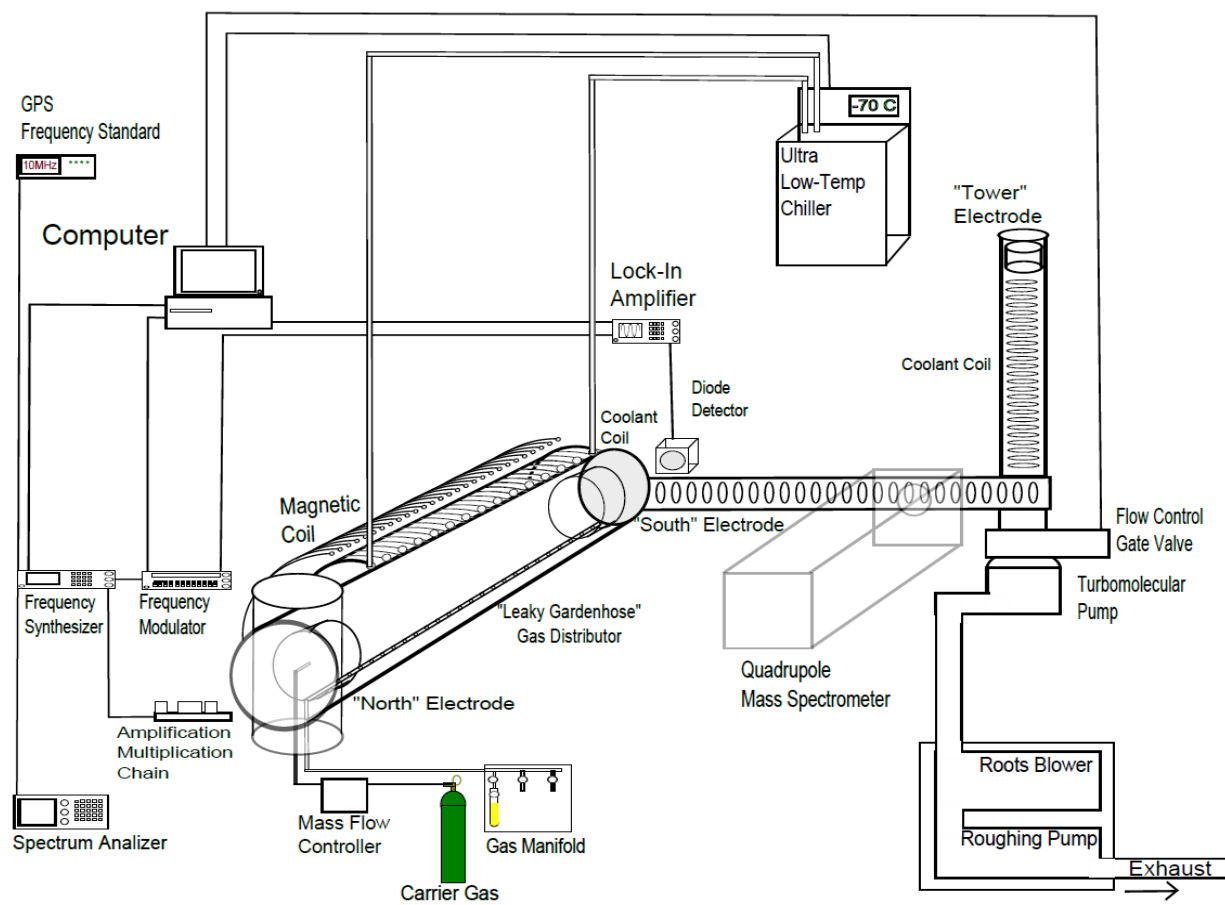
Appendix C: Carbonyl diazide rotational spectroscopy publication

219

Appendix D: Hydrazoic acid equilibrium structure publication

226

Chapter 1: Thesis overview



The focus of this thesis is the pure-rotational spectroscopy of several small, highly nitrogenous molecules. The central player in this work is a millimeter-wave absorption spectrometer. This spectrometer was originally constructed in the early 1980's, but in 2010 the McMahon/ Woods collaborative research group received a generous grant to completely overhaul it. In the first year, the entire instrument was rebuilt, with new signal generation, detection, cooling system, pumps, valves, pressure gauges, mass flow controllers, and a computer control system for all of the above. The modern incarnation of the spectrometer has been collecting publishable data since 2011, since which time we have made numerous further improvements to the instrument. Just as importantly, the group has built a high level of experience and competency, and we are continually advancing our capability to obtain and analyze interesting spectra

The first molecular target for our rebuilt spectrometer was pyridazine. This is a stable, highly polar aromatic molecule, features which made it a straightforward spectroscopic target, but also make it a possible candidate to be the first six-member aromatic ring to be detected in interstellar space by rotational spectroscopy. A collaborator has since tried to find this molecule in space using the Arecibo observatory, but has been unsuccessful thus far. With pyridazine we were able to observe multiple isotopologues, either in natural abundance in our spectra or through synthetic substitution. Computed vibration-rotation interaction corrections (α_i 's) were used to correct the observed rotational constants (B_0 's) for these isotopologues to equilibrium rotational constants (B_e 's), which were then used to obtain a highly precise equilibrium structure. The rotational spectra for several of the vibrationally excited states of pyridazine were observed in our spectra, and we were able to analyze many of them. The details of the spectrometer construction and the inaugural pyridazine project were published in the thesis of Dr. Brian Esselman (PhD.

2012).¹ The subsequent publication for pyridazine² is supplied herein in Appendix A. Joshua Shutter, an undergraduate, was a major contributor to both the reconstruction of the instrument and to the pyridazine project.

In choosing spectroscopic targets, potential astrochemical species are a high priority, because radio astronomers rely on data acquired by rotational spectroscopists to make their assignments. Benzonitrile, phenylisocyanate, triazole, and pyrimidine are all actively being studied in the group. These are all potential space molecules, and they are all polar aromatic molecules with 6π electrons, a category of molecules with is surprisingly lacking in positive astronomical detections.³ This group of molecules are also stable, store bought compounds, and four talented undergraduate students (or recent graduates) have been responsible for studying them. These projects are led by Hunter Lau, Cara Schwarz, Maria Zdanovskaia, and Zachary Heim under the guidance of Claude Woods, Brian Esselman, and myself. Our spectrometer is equipped with the capability for *in situ* electric discharge or pyrolysis, so future projects will involve highly unstable molecules, radicals, and ions. One ongoing target is the acylium cation, which we hope to generate through the electric discharge of ketene or acetone. This is a graduate student level project initiated by Brian Esselman and myself, on which Vanessa Orr has taken the lead.

We have studied several azide-containing molecules. The main topics of this document are carbonyl diazide and hydrazoic acid, but formyl azide is also under investigation (Nicholas Walters is the primary graduate student working on formyl azide). These molecules are not commercially available and are somewhat tricky to synthesize and handle due to their explosive nature and potential for rapid decomposition. They are worthwhile spectroscopic targets in their

own right. Additionally, the synthesis and characterization of these azides was thought to be necessary in order to obtain their decomposition products for study.

Chapter 2 describes our work on the molecule carbonyl diazide ($\text{OC}(\text{N}_3)_2$). Carbonyl diazide is commercially unavailable and tricky to synthesize, because it is extremely explosive and detonates readily. Our interest in this molecule comes from reports of several interesting decomposition products, including diazirinone (c-OCN_2), a possible space molecule. While there is no reason to suspect carbonyl diazide itself of being a likely space molecule, it is a fascinating high energy molecule, with 6 out of 8 atoms (and almost exactly 75% of its mass) being nitrogen. We felt carbonyl diazide was worth studying both in its own right, and as a necessary step in the ultimate acquisition of a diazirinone spectrum. We found several successful methods for synthesizing carbonyl diazide, with the safest, most straightforward, and most effective method being the combination of triphosgene and sodium azide in polyethylene glycol and isolating the gaseous products. We took spectra at room temperature and -60°C , and were able to assign the spectra of two conformers and 4 vibrationally excited states for the molecule. We did not observe any isotopologues. We published a paper on the synthesis of this molecule and analysis of the IR spectrum⁴ which is available in Appendix B, and a paper on the millimeter-wave spectroscopy⁵ which is available in Appendix C. Chapter 2 elaborates on the material found in Appendices B and C.

Chapter 3 describes various upgrades to the spectrometer, and preliminary attempts to generate the molecule diazirinone from carbonyl diazide. These attempts have not yet been successful, but two new apparatus for the pyrolysis of carbonyl diazide have just been fabricated with help from the glass shop and the machine shop. One is a quartz ‘hot finger’ heater which we

have installed in the vacuum chamber of our spectrometer. The temperature can be controlled with a variac, and the expectation is that we can set the heater to a temperature and observe *in situ* pyrolysis in real time using the spectrometer. The second new pyrolysis apparatus is more in line with the literature description of diazirinone generation,⁶ with a heated quartz tube running between a series of steel U-traps for pyrolysis and trap-to-trap distillation. Both of these pyrolysis devices may also be useful in the pyrolysis of diketene to ketene, towards the eventual detection of acylium ion. Chapter 3 also describes an impurity which was found in an aging carbonyl diazide sample. It had a clean spectrum, which we were able to assign, but despite knowing its approximate dimensions and the direction of its dipole we do not know what the molecule is.

Chapter 4 discusses the structural determination for hydrazoic acid. We started looking at hydrazoic acid because it was a common impurity in our carbonyl diazide spectra, but it quickly became apparent that the ability of our spectrometer to detect transitions for ¹⁵N isotopologues could be leveraged towards an excellent equilibrium structure determination, a massive improvement over the best literature structure,⁷ and one of the best structure determinations for any molecule to date. We were able to synthesize HN₃, DN₃, H¹⁵NNN, HNN¹⁵N, D¹⁵NNN, and DNN¹⁵N. From these we were able to see the isotopologues with one additional ¹⁵N at natural abundance, for a total of 14 isotopologues. Considering the reasonable isotopes of hydrogen and nitrogen, only H¹⁵N₃ and D¹⁵N₃ were not observed. Similar to our pyridazine project, we used *ab initio* vibration-rotation corrections to derive mixed experimental/theoretical equilibrium rotational constants for each isotopologue, and used the xrefit module of Stanton's CFOUR program⁸ to obtain an equilibrium geometry from this data. The manuscript on the equilibrium structure of hydrazoic acid has been accepted by the Journal of Chemical Physics, but is not yet in print. The

accepted draft is attached in Appendix D. Chapter 4 contains the same material as is found in Appendix D, but expands upon it.

Chapter 5 examines the vibrationally excited states of HN_3 and DN_3 . For most of our spectroscopic projects the rotational transitions for excited vibrational states are observed, and perturbations between these states are reasonably common. Assigning and fitting the vibrationally excited states of HN_3 serves as a challenge to build our skill at solving this type of problem. At room temperature, four of the six fundamental vibrational modes are observable, as well as two overtone states and a combination state for each of these isotopologues. A massive difference in the A rotational constant between HN_3 and DN_3 results in enough of a difference in the vibrational energies and in the rotational transitions available in our spectrometer range to make the challenges for each isotopologue distinct. There are massive perturbations between many of the states, to the point where only the ground state can be considered independently of the others, and even so the ground state has many highly perturbed lines which must be excluded from the dataset for this to be possible. The ultimate goal is multi-state fits where rotational constants, distortion constants, and perturbation terms for multiple states are fit to a dataset of transitions for multiple states. The first step towards this is the assignment of lines, many of which are highly perturbed. A series of published FTIR papers was extremely helpful in making our initial assignments. In Chapter 5 we present reasonably successful 3-state fits (ground, ν_5 and ν_6) for both HN_3 and DN_3 . The ν_6 state in HN_3 is more strongly coupled to the 5-state polyad at higher energy than is the case for ν_6 in DN_3 , so the 3-state DN_3 fit is better. For the 3-state DN_3 fit we were successful in our inclusion of rovibrational FTIR transitions and pure rotational FIR transitions from the literature in our dataset. Work towards 5-state fits of the higher polyad and, ultimately, 8-state fits is ongoing.

References

1. Esselman, B. J. Computational and Spectroscopic Investigations of Species of Astrochemical Relevance. University of Wisconsin-Madison, Madison, Wisconsin, 2012.
2. Esselman, B. J.; Amberger, B. K.; Shutter, J. D.; Daane, M. A.; Stanton, J. F.; Woods, R. C.; McMahon, R. J., Rotational spectroscopy of pyridazine and its isotopologs from 235-360 GHz: Equilibrium structure and vibrational satellites. *J. Chem. Phys.* **2013**, *139*, 224304 1-13.
3. Müller, H. S. P.; Schlöder, F.; Stutzki, J.; Winnewisser, G., The Cologne Database for Molecular Spectroscopy, CDMS: a useful tool for astronomers and spectroscopists. *J. Mol. Struct.* **2005**, *742* (1-3), 215-227.
4. Nolan, A. M.; Amberger, B. K.; Esselman, B. J.; Thimmakonda, V. S.; Stanton, J. F.; Woods, R. C.; McMahon, R. J., Carbonyl Diazide, OC(N₃)₂: Synthesis, Purification, and IR Spectrum. *Inorg. Chem.* **2012**, *51* (18), 9846-9851.
5. Amberger, B. K.; Esselman, B. J.; Woods, R. C.; McMahon, R. J., Millimeter-wave spectroscopy of carbonyl diazide, OC(N₃)₂. *J. Mol. Spectrosc.* **2014**, *295*, 15-20.
6. Zeng, X.; Beckers, H.; Willner, H.; Stanton, J. F., Elusive Diazirone, N₂CO. *Angew. Chem. Int. Ed.* **2011**, *50* (7), 1720-1723.
7. Winnewisser, B. P., The substitution structure of hydrazoic acid, HN₃. *J. Mol. Spectrosc.* **1980**, *82* (1), 220-223.
8. Stanton, J. F.; Gauss, J.; Harding, M. E.; Szalay, P. G.; with contributions from A.A. Auer, R. J. B., U. Benedikt, C. Berger, D.E. Bernholdt, Y.J. Bomble, L. Cheng, O. Christiansen, M. Heckert, O. Heun, C. Huber, T.-C. Jagau, D. Jonsson, J. Jusélius, K. Klein, W.J. Lauderdale, D.A. Matthews, T. Metzroth, L.A. Mück, D.P. O'Neill, D.R. Price, E. Prochnow, C. Puzzarini, K. Ruud, F. Schiffmann, W. Schwalbach, S. Stopkowitz, A. Tajti, J. Vázquez, F. Wang, J.D. Watts and the integral packages MOLECULE (J. Almlöf and P.R. Taylor), PROPS (P.R. Taylor), ABACUS (T. Helgaker, H.J. Aa. Jensen, P. Jørgensen, and J. Olsen), and ECP routines by A. V. Mitin and C. van Wüllen. For the current version, see <http://www.cfour.de>.

Chapter 2: Synthesis and millimeter-wave spectroscopy of carbonyl diazide

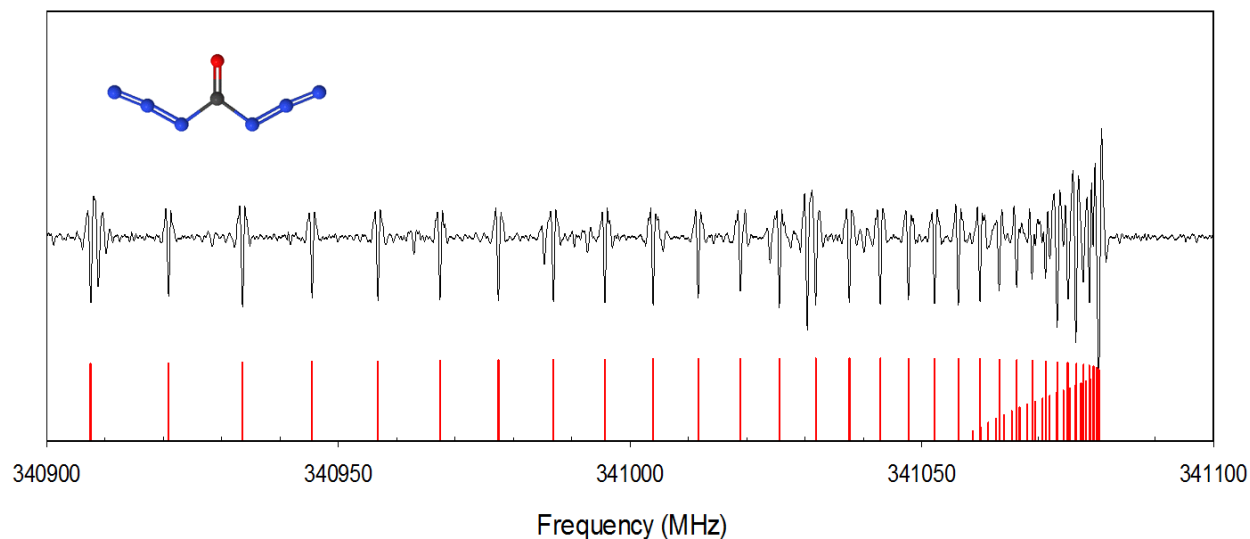
Includes material from previously published works:

Amberger, B. K.; Esselman, B. J.; Woods, R. C.; McMahon, R. J., Millimeter-wave spectroscopy of carbonyl diazide, $\text{OC}(\text{N}_3)_2$. *Journal of Molecular Spectroscopy* **2014**, 295, 15-20.

Nolan, A. M.; Amberger, B. K.; Esselman, B. J.; Thimmakonda, V. S.; Stanton, J. F.; Woods, R. C.; McMahon, R. J., Carbonyl Diazide, $\text{OC}(\text{N}_3)_2$: Synthesis, Purification, and IR Spectrum. *Inorganic Chemistry* **2012**, 51 (18), 9846-9851.

Includes the work of several collaborators:

Brian J. Esselman, Alex M. Nolan, John F. Stanton, R. Claude Woods, Robert J. McMahon



Abstract

Carbonyl diazide ($\text{CO}(\text{N}_3)_2$) was synthesized from triphosgene and azide salts. Over the course of many iterations, a fast, reliable, and safe synthetic method was developed in which sodium azide is combined with triphosgene in a minimal amount of polyethylene glycol (PEG) in a stainless steel vacuum flask. Anharmonic VPT2 calculations including the effects of Fermi resonances successfully reproduce the observed IR spectrum, which includes both the *anti-syn* and *syn-syn* conformations of $(\text{OC}(\text{N}_3)_2)$. The millimeter-wave spectrum of carbonyl diazide was taken at 293 and 213 degrees Celsius. The *anti-syn* and *syn-syn* isomers were both found in the spectrum, and a comparison of their line intensities allowed for an estimation of the energy separation between them. This estimate of 2.4 ± 0.6 kcal/mol is consistent with CCSD(T) level calculations of the potential energy surface. Pure-rotational transitions for four vibrationally excited states of the *syn-syn* isomer were also observed. Rotation-vibration correction terms (α_i 's) calculated at the CCSD(T)/ANO1 level were largely successful in assigning these transitions. Least-squares fitting was successful for all observed lines of the ground state and ν_{12} . The states ν_9 , ν_7 , and $2\nu_{12}$ showed signs of perturbation, but many lines were seemingly unaffected by the perturbation (or only slightly affected) and could be modeled using a single-state least-squares fitting routine.

Introduction

Carbonyl diazide ($\text{CO}(\text{N}_3)_2$) is a high energy compound which has existed in the literature since 1895.¹⁻⁵ Recently, carbonyl diazide has been the subject of multiple theoretical, synthetic, and spectroscopic studies.⁶⁻⁸ This recent attention stems from the work of Zeng *et al.*, which showed that carbonyl diazide can be decomposed to several interesting species on the CON_4 and CON_2 potential energy surfaces.⁹⁻¹¹ As shown in Figure 2.1, gas phase pyrolysis of carbonyl

carbonyl diazide (**1**) has been shown to yield diazirinone (**2**), while irradiation of (**1**) in an inert gas matrix yields both the acylnitrene (**3**) and its Curtius rearrangement product, the isocyanate (**4**). To date, carbonyl diazide appears to be the only synthetically practical precursor for generating the CON₂ isomer diazirinone, a molecule of recent interest.¹⁰⁻¹⁷ Diazirinone can be considered a covalent dimer of the ubiquitous interstellar species N₂ and CO and is structurally analogous to the known space molecule cyclopropenone¹⁸ (a covalent dimer of CO and acetylene). Thus, diazirinone may itself be of astrochemical interest.

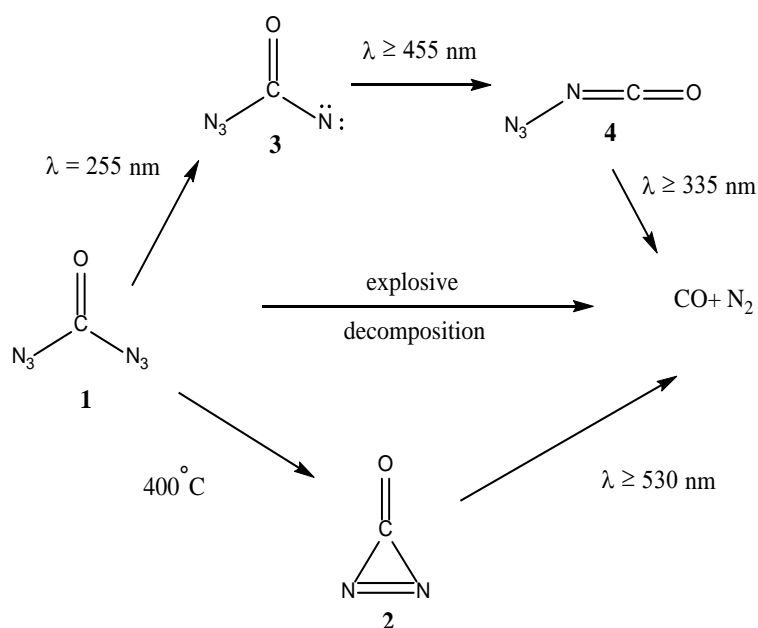


Figure 2.1 Known decomposition pathways of carbonyl diazide.

The reported yield of the pyrolysis of carbonyl diazide to diazirinone very low (~0.5%), so finding a reliable source of carbonyl diazide is critical. Carbonyl diazide was synthesized in the 1920s via the diazotization of carbohydrazide (**5**)²⁻³ (Figure 2.2) but was not studied in pure form due to its explosive nature. In 2007, carbonyl diazide was produced through the incidental hydrolysis of tetraazidomethane (**6**) in undried solvent⁵ and was identified by ¹³C and ¹⁵N NMR

spectroscopy. In 2010, Zeng *et al.* synthesized their feedstock of carbonyl diazide by sealing chlorofluorocarbonyl (ClC(O)F) (**7**) in an ampoule with sodium azide for a period of 4 days.⁶ Their product was isolated using trap to trap distillation and thoroughly characterized by IR spectroscopy (Gas phase and argon matrix), Raman spectroscopy, and X-ray crystallography. We have developed our own synthetic scheme which we deem to be safer and more efficient than those reported in the literature. We have used triphosgene (**8**) and azide in solution phase syntheses to synthesize carbonyl diazide (Figure 2.2).

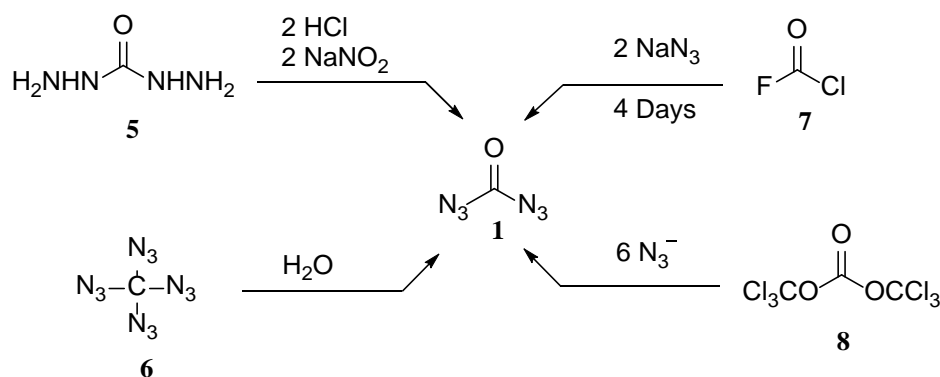


Figure 2.2 Known synthetic routes for generating carbonyl diazide.

Our synthetic approach is fundamentally similar to Zeng *et al.*,⁶ in that our reagents are a carbonyl electrophile and an azide source, but our synthesis offers several advantages. Triphosgene is a ‘synthetic analogue’ of three equivalents of phosgene.¹⁹⁻²⁰ Although we did not carry out a mechanistic study, the mechanism proposed in Figure 2.3 has good precedent in the literature.²¹ Sequential nucleophilic attack of azide on the carbonyl carbon of triphosgene results in the formation of 1 equivalent of $\text{OC(N}_3)_2$ and the liberation of 2 equivalents of trichloromethoxide ion. Trichloromethoxide ion rapidly eliminates chloride ion to generate

phosgene. Phosgene generated *in situ* is more reactive than triphosgene, and subsequent reaction with azide yields additional $\text{OC}(\text{N}_3)_2$.

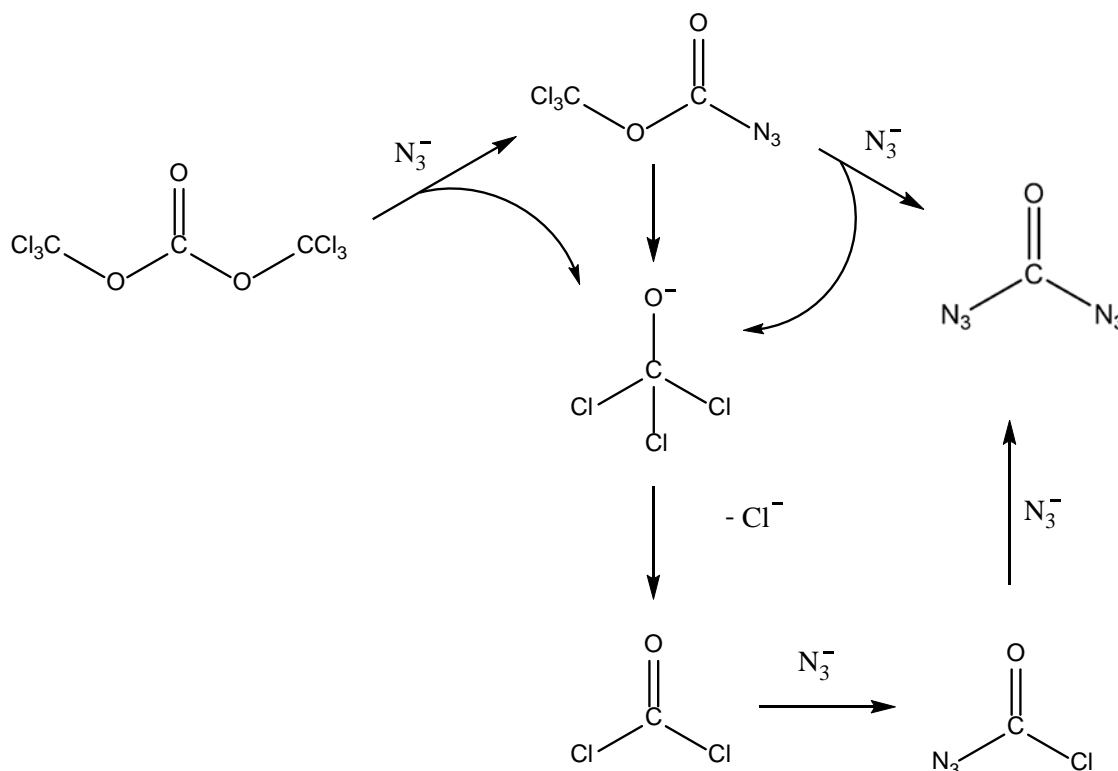


Figure 2.3 A likely mechanism for the nucleophilic addition of 6 equivalents of azide ion to triphosgene to yield 3 equivalents of carbonyl diazide.

Unlike phosgene (or chlorofluorocarbonyl), triphosgene is a crystalline solid and therefore much easier to safely handle. Our solution phase syntheses result in faster reaction times, and both the reactants and products of the reaction are less likely to detonate in solution. Our syntheses were designed to only ever isolate carbonyl diazide in stainless steel vessels, so batches as large as ~0.25 g could be synthesized without fear of an occasional accidental detonation.

Synthesis of Carbonyl Diazide

Carbonyl diazide is shock-sensitive and explosive. Proper safety precautions, which include the use of leather gloves, face shields, and blast shields must be taken when handling this compound. Sodium azide (NaN_3) and its hydrolysis product, hydrazoic acid (HN_3) are toxic. Sodium azide, as well as metal azides that may be formed by reaction of sodium azide, represent explosion hazards.

Many of the manipulations involved in the preparation and purification of carbonyl diazide were performed using a stainless-steel vacuum manifold designed and built with safety in mind. Instead of attempting to condense and weigh the products of our reactions, we measured the gas pressure in this custom manifold and percent yields were estimated using the known manifold volume. The purity of our products was assessed by allowing 1-2 Torr of product to expand into an IR cell. The IR spectra were compared with a gas phase IR spectrum published by Zeng *et al.*,⁶ and later compared with the results of Stanton's VPT2 anharmonic calculation. In later synthetic batches, once the rotational spectrum was understood, sample purity could be verified in the millimeter-wave spectrometer, further streamlining the synthetic procedure and allowing less chances for explosive decomposition.

We successfully synthesized carbonyl diazide using three different methods based around three different solvents: diethyl ether, dimethyl ether, and polyethylene glycol (MW=400). These solvents are, respectively, more volatile than carbonyl diazide, massively more volatile than carbonyl diazide, and massively less volatile than carbonyl diazide. The three methods used substantially different experimental setups. We experimented with these various methods in order to find a preferred synthesis which maximized efficiency, purity, and safety. In all cases, the

reagents we used to generate carbonyl diazide were triphosgene and an azide source, either sodium azide or tetra-n-butylammonium azide (TBAN₃).

Unless noted otherwise, chemicals were acquired from commercial sources and were used without further purification. Tetra-n-butylammonium Azide. (TBAN₃) was prepared using a literature procedure and recrystallized from toluene.²² On occasion, a residual toluene contaminant in TBAN₃ was carried through the subsequent synthetic procedures and could not be removed via distillation from the desired carbonyl diazide. In order to remove the toluene contaminant, a slurry of TBAN₃ (ca. 5 g) in 75 mL of diethyl ether was brought to reflux with stirring. The slurry was then cooled to room temperature; crystals were collected by filtration and washed with cold diethyl ether. Residual diethyl ether solvent was removed from TBAN₃ under high vacuum.

Method A. Tetra-n-butylammonium azide (TBAN₃) (1.64 g, 5.77 mmol) was added to an oven-dried round bottom flask, followed by anhydrous diethyl ether (10 mL) under positive nitrogen pressure. The volume of solvent was not sufficient to completely dissolve the ammonium salt. Triphosgene (194 mg, 0.655 mmol) was added, and the suspension was stirred for 2 h. The solution was then passed through a silica plug to remove the suspended ammonium salts, and diethyl ether (5 mL) was used to wash the silica.

The organic layer was washed with saturated aqueous sodium chloride (10 mL) and dried over magnesium sulfate, and the drying agent removed by gravity filtration. Although a dilute solution of OC(N₃)₂ in diethyl ether seems comparatively safe to handle in glass, a concentrated solution or the isolated material is not. In one instance, a neat sample of OC(N₃)₂ detonated upon insertion of a glass pipet; the round-bottom flask containing the sample was pulverized by the blast. Thereafter, all manipulations following the removal of the magnesium sulfate drying agent were

conducted in a 200-mL stainless-steel flask. The solution of $\text{OC}(\text{N}_3)_2$ in diethyl ether in a stainless-steel flask was frozen at -196°C , and the vessel was evacuated. The sample was allowed to warm to room temperature, and all volatile materials were cryopumped to a second stainless-steel flask at -196°C to ensure that absolutely no nonvolatile or particulate matter contaminated the sample. The second flask was then held at -78°C , a temperature at which Et_2O is volatile but $\text{OC}(\text{N}_3)_2$ is not, and the ether was removed with a diffusion pump in conjunction with a liquid nitrogen trap. To remove all traces of ether from the flask, it was necessary to perform three or four freeze-pump-thaw cycles, wherein the sample flask was isolated from the vacuum, warmed to room temperature, and cooled back to -78°C before pumping was resumed. Carbonyl diazide synthesized and purified in this way typically afforded a yield of ca. 7.1 Torr-liter, (0.38mmol, 19%). A serious drawback to this method is the amount of time required for these freeze-pump-thaw cycles. Fully removing the ether often took a full day, and in the phases where most of the ether had been removed the sample was at risk for explosive decomposition.

Method B. A modified version of the preparation allowed the entire procedure to be carried out on the stainless-steel manifold. The use dimethyl ether (bp -24°C), which is more volatile than diethyl ether (bp 35°C), improves the ease and efficiency of solvent removal from carbonyl diazide, although it also requires that the reaction be performed at low temperature or under pressure. Triphosgene (0.153 g, 0.516 mmol) and sodium azide (0.207 g, 3.184 mmol) were added to a 35-mL stainless-steel flask. The flask was attached to the stainless-steel manifold and evacuated, and gaseous dimethyl ether was condensed into the vessel at -196°C . In the 35-mL flask, 1400 Torr-liter of dimethyl ether was calculated to afford ~ 4 mL as liquid solvent. After stirring for 16 h, the solvent was distilled from the flask at -78°C . The flask was then allowed to

warm to room temperature, and carbonyl diazide (**1**) was cryopumped to a clean stainless-steel flask at $-196\text{ }^{\circ}\text{C}$. Yields as high as 32% were observed. This procedure, however, proved more fickle than the synthesis in diethyl ether. A possible reason for the fickle nature of this method is that the reaction vessel was opaque (steel), and the presence or absence of dimethyl ether in the liquid phase could not be visually confirmed. Additionally, the narrow mouth of the small reaction vessel meant that it could take several minutes to load the extremely hygroscopic TBAN_3 , introducing an unknown quantity of H_2O to the reaction mixture.

Method C

Triphosgene and sodium azide were allowed to react in a very small volume of polyethylene glycol (MW 400). Polyethylene glycol was chosen as a heavy solvent, from which we could vacuum distill our product after the reaction. Polyethylene glycol also acts as a catalyst by sequestering the Na^+ ions of NaN_3 , much like a crown ether, giving higher soluble concentrations of the nucleophilic anion. In a typical reaction, 240 mg (0.82 mmol) triphosgene and 490 mg (7.6 mmol) NaN_3 were placed in a specially constructed brass reaction vessel (inner diameter 1 cm). The reaction vessel was placed in a stainless steel vacuum flask. A volume of 0.3 ml polyethylene glycol was dripped onto the crystalline reagents, and the vacuum flask was quickly attached to a vacuum manifold, evacuated to less than 100 mTorr, and then sealed. The blast-proof reaction vessel is shown in Figure 2.4.

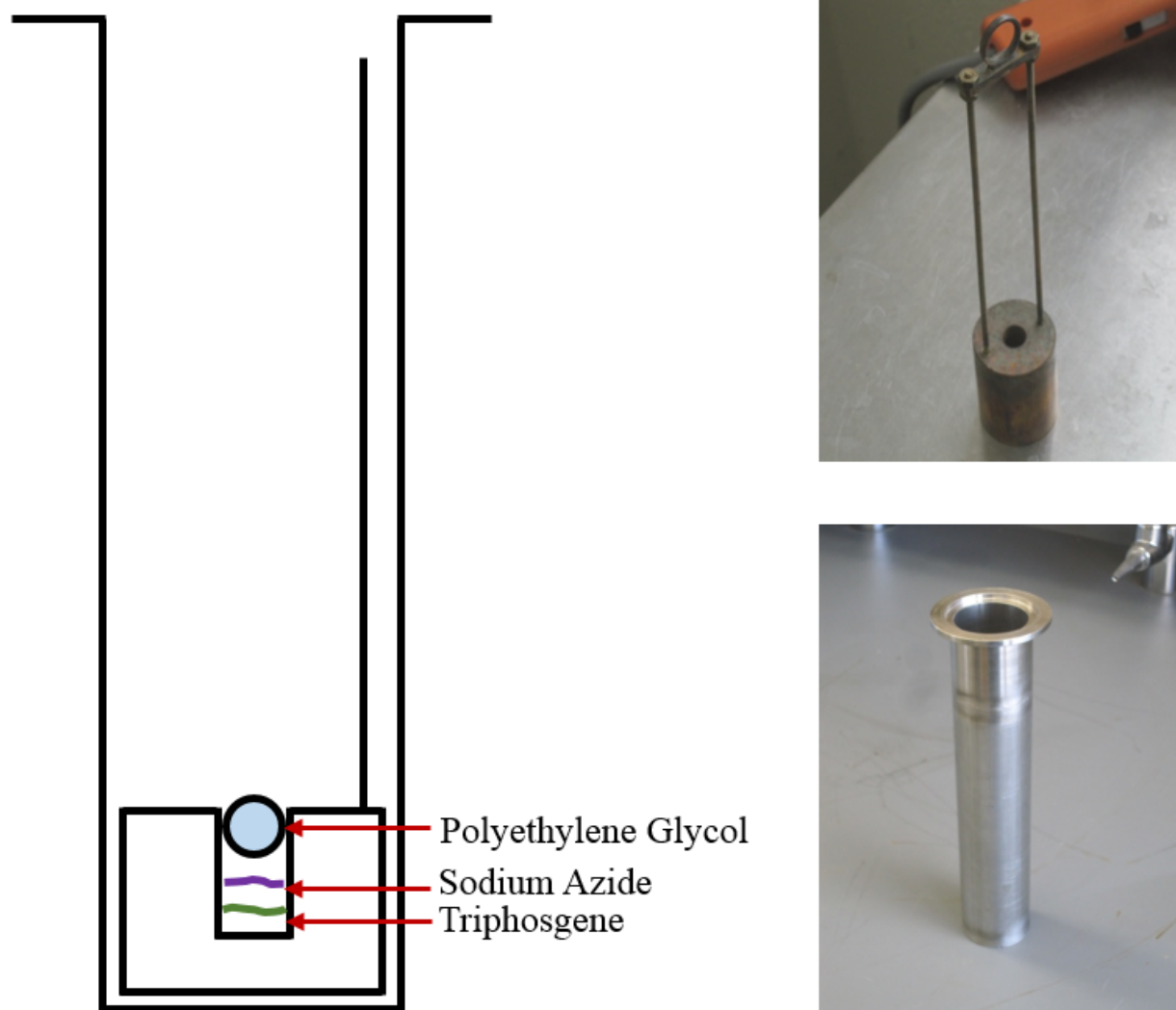


Figure 2.4 Experimental setup for the preferred synthesis of carbonyl diazide from triphosgene and sodium azide in a minimum quantity of polyethylene glycol solvent.

After being sealed for ~16 hours, any condensable gasses which had been generated were transferred to a second stainless steel flask held at liquid nitrogen temperature. In a final purification step, this second flask was cooled to dry ice-acetone temperature, and pumped on with a high vacuum for 5 minutes to remove any impurities more volatile than carbonyl diazide. The resulting product was analyzed for purity by gas phase IR spectroscopy, and the yield was estimated by measuring the pressure of the sample in a large gas manifold of known volume. A

typical yield was 7.0 Torr liters of gas (0.38 mmol, 15%) and thus comparable to our previous method using ether as a solvent. A benefit of this new method of synthesis is that the carbonyl diazide is generated and handled entirely in stainless steel vessels until it is introduced into the spectrometer, enhancing the safety of the procedure. Additionally, purification is rapid and straightforward, which is convenient and lessens the chance of losing the sample to an accidental explosive decomposition. The development of the expedited synthesis was motivated by the need to produce multiple samples for spectroscopic study. Samples much larger than the size just mentioned were not safe to handle, and because of the degradation of the sample in the spectrometer over a period of a few hours, samples of this size were only adequate for 1 or 2 days of experiments.

We found that the reaction time could be shortened to just a few minutes and still yield large amounts of carbonyl diazide. Additionally, the gas evolving from the sample flask could be used for rotational spectroscopy without the additional purification step, albeit hydrazoic acid tended to be a larger impurity in this case.

Computational Studies

The conformational isomers (*anti-anti*, *anti-syn*, and *syn-syn*) were optimized at CCSD(T)/ANO1 and CCSD(T)/cc-pVTZ levels of theory. Molecular geometries were optimized in CFOUR²³ using analytic gradients²⁴⁻²⁵ with the frozen core approximation. The transition states were connected to their minima via IRC calculations. The results are shown in Figure 2.5.

To determine the vibration-rotation interaction constants (α_i 's), the cubic and quartic constants were calculated by numerical differentiation of the analytic second derivatives at displaced points following the approach of Stanton *et al.*²⁶⁻²⁷ Rotational constants, centrifugal

distortion constants, and vibration-rotation interaction constants were calculated with CFOUR using the structure and force field results.

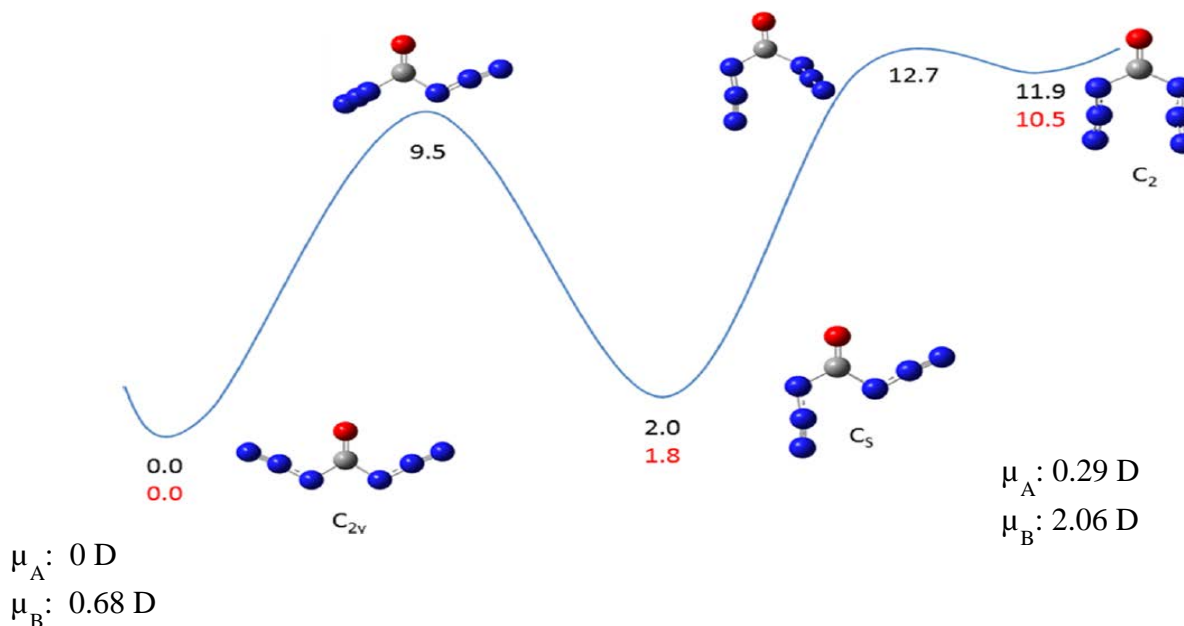


Figure 2.5 *Ab initio* calculations showing the relative energies (in kcal/mol) of the three conformers of carbonyl diazide at CCSD/cc-pVDZ (upper, black) and CCSD(T)/cc-pVTZ (lower, red).

IR Spectroscopy

Infrared spectroscopy was used to confirm that we had synthesized carbonyl diazide. The spectrum for a pure sample is shown in Figure 2.6. To understand this spectrum we performed harmonic calculations (CCSD(T)/ANO0 and CCSD(T)/ANO1). The results of these calculations are shown in Table 2.1 for the *syn-syn* conformation of carbonyl diazide, and in Table 2.2 for the *anti-syn* conformation.

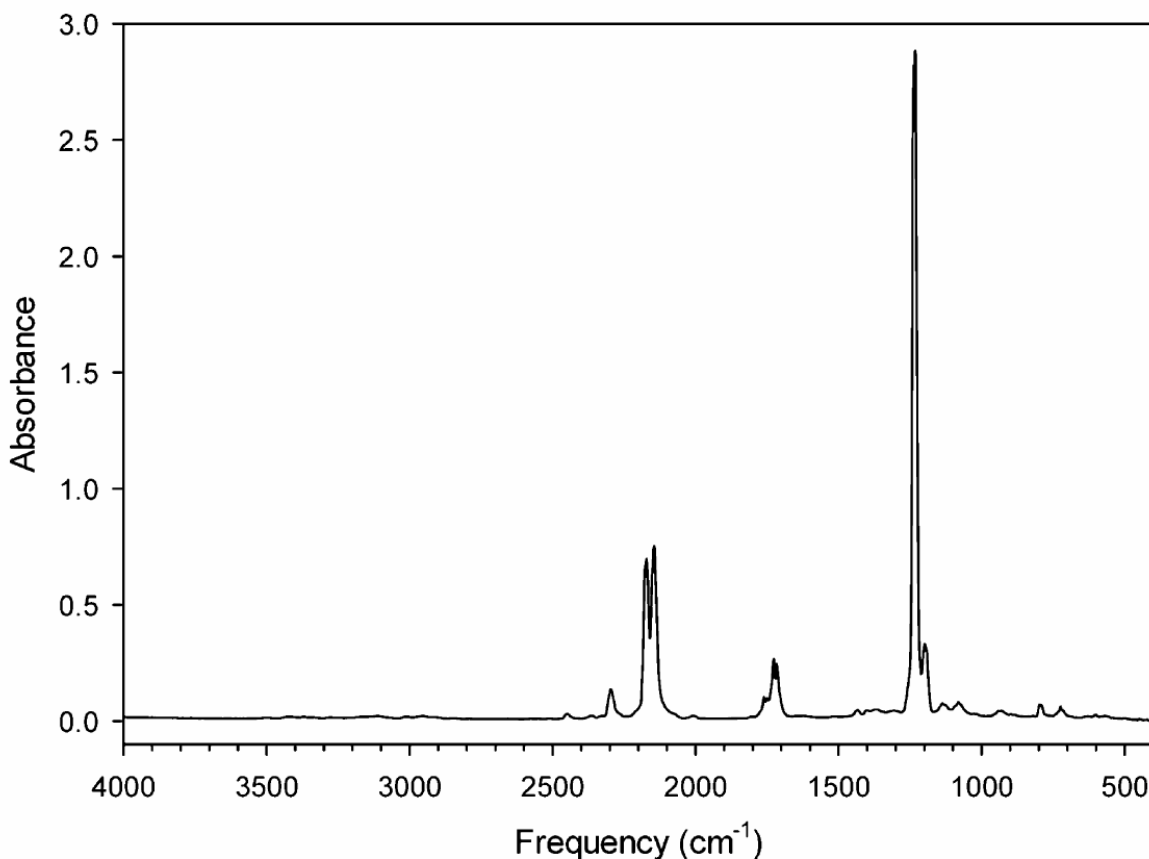


Figure 2.6 Infrared spectrum of carbonyl diazide from 400 to 4000 cm^{-1} collected at ~ 2 Torr pressure in a 15 cm length cell with KRS-5 optical windows.

As can be seen, the harmonic calculations are insufficient for explaining several absorptions, notably 2297, 2171, and 1200 cm^{-1} . At a high-level method the anharmonic cubic and quartic force constants were calculated, and second-order vibrational perturbation theory (VPT2) was used to compute the fundamental vibrational frequencies as well as the infrared intensities. Fermi resonances were also analyzed (VPT2 + F) at this level. The results of this anharmonic analysis are in striking agreement with observation (see Table 2.1, Table 2.2, and Figure 2.7). The cluster of features seen from 2000 to 2300 cm^{-1} results from a strong and extensive Fermi resonance in the *syn-syn* conformer of carbonyl diazide, whereby the combination

levels $\nu_4+\nu_{14}$, $\nu_4+\nu_{15}$, and $\nu_3+\nu_{15}$ borrow intensity from the very strong asymmetric $-\text{N}=\text{N}=\text{N}$ stretching mode, ν_{13} . Similarly, the intrinsically strong ν_{14} asymmetric C-N stretching mode mixes with the combination level $\nu_7+\nu_{15}$. The high level computational treatment has allowed us to assign all of the principal features in the spectrum. It is remarkable that many of the strong lines in the spectrum result from two quantum overtone or combination levels. This underscores the problems associated with relying on the harmonic treatment for the analysis of the spectrum. Figure 2.7 elegantly shows how the combined results of the VPT2 + F calculations for the *syn-syn* and the *anti-syn* conformers account for all major features.

Table 2.1 Calculated and experimentally observed IR frequencies for the *syn-syn* conformation of carbonyl diazide. Calculated intensities are in parentheses.

Mode	Symmetry	CCSD(T)/ANO0 Harmonic	CCSD(T)/ANO1 Harmonic	CCSD(T)/ANO1 VPT2+F	Experimental
ν_1	a_1	2214 (63)	2228 (63)	2191 (31)	
ν_2	a_1	1782 (194)	1764 (194)	1731 (179)	1721
ν_3	a_1	1254 (4)	1226 (5)	1222 (4)	
ν_4	a_1	945 (19)	953 (20)	933 (16)	941
ν_5	a_1	553 (0)	553 (0)	544 (0)	
ν_6	a_1	407 (2)	408 (2)	403 (1)	
ν_7	a_1	122 (0)	122 (0)	114 (0)	
ν_8	a_2	569 (0)	570 (0)	557(0)	
ν_9	a_2	152 (0)	155 (0)	151 (0)	
ν_{10}	b_1	733 (29)	730 (25)	720 (28)	723
ν_{11}	b_1	580 (9)	581 (7)	571 (8)	569
ν_{12}	b_1	75 (1)	76 (1)	72 (1)	
ν_{13}	b_2	2198 (858)	2212 (875)	2140 (282)	2145
ν_{14}	b_2	1266 (1755)	1277 (1735)	1230 (1633)	1235
ν_{15}	b_2	1095 (17)	1107 (13)	1069 (4)	
ν_{16}	b_2	807 (23)	808 (26)	795 (21)	794
ν_{17}	b_2	500 (2)	503 (3)	496 (1)	
ν_{18}	b_2	206 (1)	206 (1)	204 (1)	
ν_3+ ν_{14}	b_2			2435 (11)	2450
ν_3+ ν_{15}	b_2			2286 (93)	2295
ν_4+ ν_{14}	b_2			2171 (441)	2172
ν_4+ ν_{15}	b_2			1998 (12)	2005
ν_7+ ν_{15}	b_2			1181 (40)	1200

Table 2.2 Calculated and experimentally observed IR frequencies for the *anti-syn* conformer of carbonyl diazide. Calculated intensities are in parentheses.

Mode	Symmetry	CCSD(T)/ANO0 Harmonic	CCSD(T)/ANO1 Harmonic	CCSD(T)/ANO1 VPT2+F	Experimental
ν_1	a'	2212(295)	2226 (308)	2169 (174)	2172
ν_2	a'	2192 (528)	2206 (552)	2142 (167)	2145
ν_3	a'	1813 (475)	1801 (482)	1760 (198)	1756
ν_4	a'	1279 (766)	1290 (736)	1243 (583)	1257
ν_5	a'	1226 (354)	1237 (374)	1190 (177)	1200
ν_6	a'	1114 (148)	1125 (147)	1083 (80)	1082
ν_7	a'	894 (7)	901 (7)	884 (6)	
ν_8	a'	727 (34)	730 (33)	722 (30)	
ν_9	a'	611 (2)	613 (2)	600 (2)	
ν_{10}	a'	495 (1)	497 (1)	491 (1)	
ν_{11}	a'	433 (1)	436 (1)	430 (1)	
ν_{12}	a'	200 (2)	200 (2)	199 (2)	
ν_{13}	a'	127 (0)	126 (0)	127 (0)	
ν_{14}	a''	720 (27)	718 (24)	712 (18)	
ν_{15}	a''	576 (2)	576 (1)	567 (2)	
ν_{16}	a''	566 (11)	568 (10)	556 (7)	
ν_{17}	a''	135 (0)	138 (0)	134 (0)	
ν_{18}	a''	91 (0)	94 (0)	95 (0)	
$2\nu_5$	a'			2384 (23)	
$\nu_4 + \nu_6$	a'			2321 (40)	
$\nu_5 + \nu_6$	a'			2272 (28)	
$2\nu_6$	a'			2192 (31)	
$\nu_4 + \nu_7$	a'			2118 (54)	
$\nu_6 + \nu_8$	a'			1797 (55)	
$2\nu_7$	a'			1768 (178)	1756
$\nu_{14} + \nu_{16}$	a'			1269 (47)	
$\nu_8 + \nu_{10}$	a'			1215 (24)	
$2\nu_9$	a'			1199 (156)	1200
$2\nu_{15}$	a'			1133 (73)	1138
$\nu_{15} + \nu_{16}$	a'			1127 (40)	1138
$2\nu_{16}$	a'			1116 (13)	1138

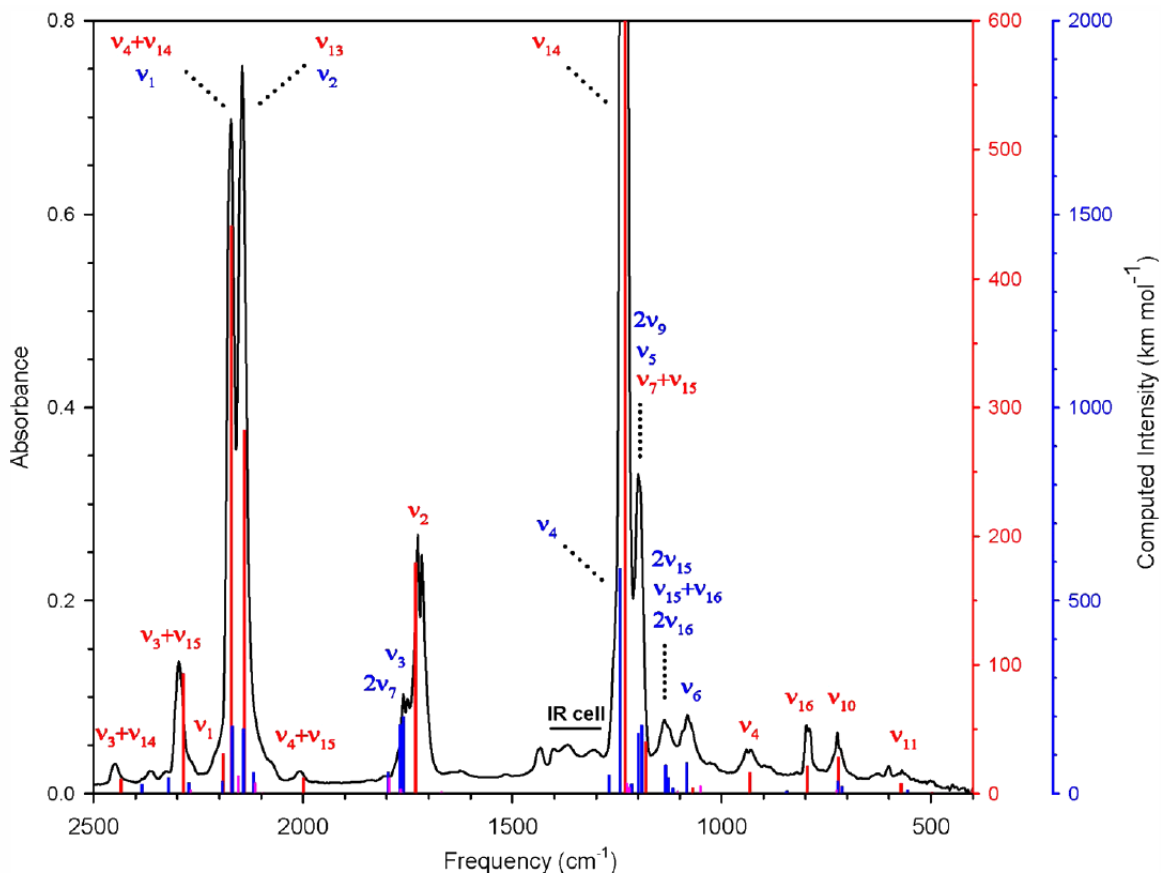


Figure 2.7 IR spectrum of carbonyl diazide from 400 to 2500 cm^{-1} with predicted transitions for both the *syn-syn* (red) and *anti-syn* (blue) conformers overlaid. The predictions are from an anharmonic VPT2 ANO1 calculation. The relative scaling of the conformers was adjusted to match the observed line intensities.

Millimeter-wave Spectroscopy

The observed spectra were dense with detectable absorptions throughout our frequency range. The most intense absorptions in our spectra were due to the impurities HN_3 , HNCO , and CO , that resulted from unintended products of the synthesis or decomposition products of carbonyl diazide. These three light molecules have intrinsically intense transitions relative to carbonyl

diazide because of their much smaller number of populated states, so even small concentrations of these impurities cause very strong absorptions. The spectra of these impurities are also relatively sparse (CO only has a single transition in our frequency range, at 345795.99 MHz), so these impurities were more of a nuisance than a true obstacle. Carbonyl diazide itself has a very dense and fairly strong rotational spectrum. We have been able to assign the most prominent features of the carbonyl diazide millimeter-wave spectrum, including ground vibrational spectra of the two lowest lying theoretically predicted conformational forms and the four lowest energy vibrational satellite spectra of the *syn-syn* form. Together, these account for most of the strong features in the spectrum. Transitions for the ground state and first excited state (ν_{12}) of the *syn-syn* form have been fit to near experimental error with a rigid rotor/centrifugal distortion model. The spectra observed in states ν_7 , ν_9 , and $2\nu_{12}$ present additional challenges, because they appear to show some effects of mutual Coriolis perturbations. Nevertheless, the rigid rotor/centrifugal distortion models we have used, i.e., ones not accounting for the perturbations, are adequate to assign a great majority of the observable transitions and to fit them with only small systematic errors in the highest J cases. The fit for the *anti-syn* form is successful in reproducing the many observed lines, but the variety of transition types and the accessible quantum number range is smaller than that of the *syn-syn* form, because of its less intense spectrum.

To collect spectra, the spectrometer chamber was charged with ~4 mTorr of sample and sealed. These fills were used for 2-3 hours before refreshing the sample. It was found that the intensity of carbonyl diazide lines slowly decreased over this period, either through decomposition or adsorption onto something in the spectrometer chamber. Refreshing the sample also mitigated

the effects of pressure creep as air slowly leaked into the chamber- depending on how leak tight the spectrometer is on a given day, the leak rate tends to be around 1-3 mTorr per hour.

Spectra were collected at both 293 K and 213 K. Due to the large number of low-lying vibrational states, including many combinations and overtones, the higher temperature spectrum is considerably more congested with excited state lines than the lower temperature spectrum. Less than 3% of the *syn-syn* conformation molecules are in the ground vibrational state at room temperature. This fraction increases to 8% at 213 K. The lowest lying vibrational satellites are also more intense at 213 K than at 293 K. Figure 2.8 shows a 200 MHz segment of the spectrum of carbonyl diazide. The primary feature in this segment is the $K_{prolate} = 17 \leftarrow 16$ Q-branch of the ground state of the *syn-syn* conformer from $J = 18$ to $J = 70$. Intermingled are transitions from the vibrational modes ν_{12} and ν_7 , as well as the *anti-syn* conformer. *Ab initio* calculations put these states at 72 cm^{-1} , 116 cm^{-1} , and 700 cm^{-1} above the ground state of the *syn-syn* isomer, respectively. As shown in Figure 2.8, the low temperature experiment gives a cleaner spectrum of the low-lying states, while the higher temperature spectrum was useful for studying the high energy *anti-syn* conformer.

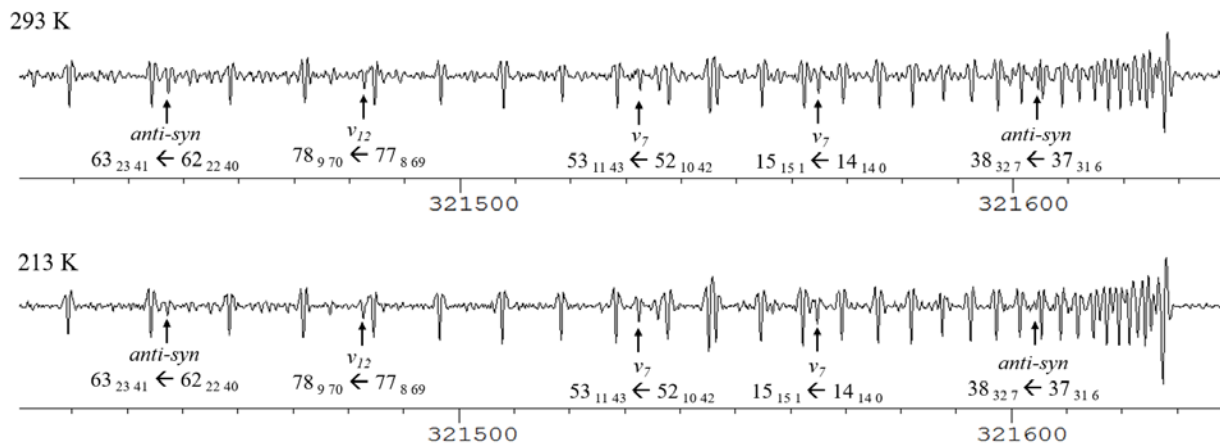


Figure 2.8 A 240 MHz segment of carbonyl diazide spectrum at both 293 K and 213 K. Most lines belong to a Q-branch series of the ground vibrational state of the *syn-syn* isomer, but lines from two vibrational modes and the *anti-syn* isomer are also present.

As temperatures are reduced below 213 K, the line intensities for transitions of the ground vibrational state of the *syn-syn* isomer begin to decrease as the effect of carbonyl diazide condensing on the walls of the spectrometer chamber seems to outweigh the effect of a more bottom-heavy distribution of states. Carbonyl diazide signal rapidly decreases as the temperature is lowered towards 200 K, which is a temperature our chiller system struggles to reach. It was found that at 200 K, the chamber could be evacuated of non-condensed gasses, resealed, and warmed, and the carbonyl diazide signal would partially return as it sublimed off of the walls. It was hoped that this strategy could be used to purify the sample in the chamber from non-condensable air that slowly leaks into the chamber, but the time it took for the chiller to reach low enough temperatures and the mediocre signal return after this ‘purification’ meant this was not a convenient strategy for sample conservation.

For the ground vibrational state of the *syn-syn* conformer, a very near prolate asymmetric top, the most apparent spectral features are the Q-branch series with fixed values of $K_{prolate}$, which have series origins occurring at roughly $(2K_{prolate} + 1)(A-(B+C)/2)$. The separation between these bands is therefore $\sim 2(A-(B+C)/2)$, or ~ 19.5 GHz.

As seen in Figure 2.9, the band origins are highly spectrally congested, and generally, the first few dozen lines of the series could not be sufficiently resolved to be independently measured. In the $K_{prolate}$ 17-18 series shown in Figure 2.9, the region between 341058 and 341081 MHz contains $J=19 - J = 54$. Most of these lines were excluded from the least-squares fitting. Like the other similar series, the lowest J lines increase in frequency as J increases, then turn towards lower frequency with further increase, forming a readily visible band head feature at the turn-around. Emerging from the congested band head regions are series of easily measured lines which gradually spread out as the lines progress to lower frequencies and higher J values.

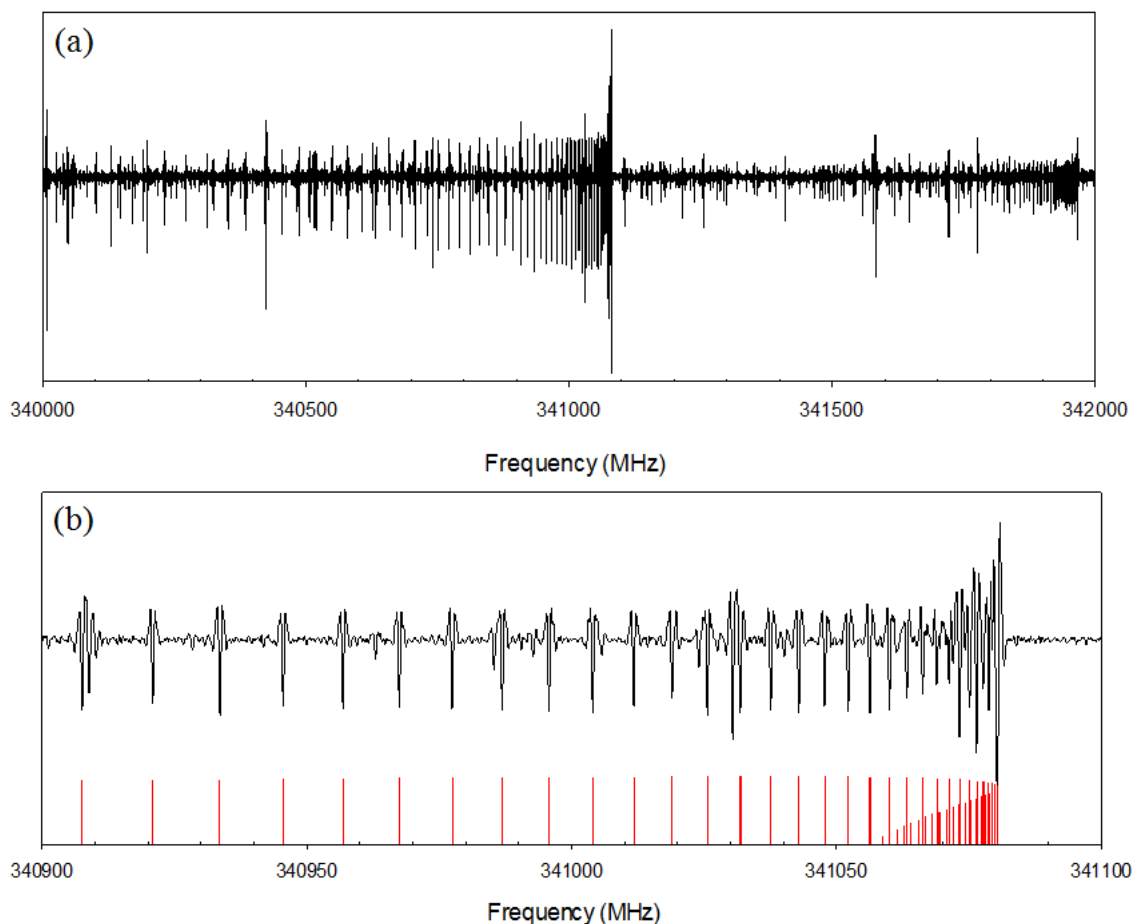


Figure 2.9 Panel a: A characteristic *b*-type Q-branch for the *syn-syn* conformer of carbonyl diazide. Panel b: a 10× zoom of the spectrum plotted with a stick spectrum of lines predicted from the final experimentally determined spectroscopic constants.

Initially, assigning the transitions of these Q-branches was very difficult because we did not appreciate the extent of the ‘turn around’. Because carbonyl diazide had not previously been studied by rotational spectroscopy, we had to rely on *ab initio* calculations to help guide our assignments. At the time of initial assignment we had not calculated the 4th order distortion terms. The extent (or existence) of the ‘turn around’ in the Q-branch depends primarily on D_{JK} , so our initial prediction, based on *ab initio* values for A , B , and C , had no ‘turn around’ at all, and it took

significant effort to correctly assign the J values progressing from the congested bandhead to lower frequencies.

Once the Q-branch series emerge from the bandheads it is easy to follow the series for ~40-60 transitions over a few GHz, but assigning a J value to the first measurable transition to lower frequency of the bandhead required a systematic guess-and-check procedure. An ultimately successful technique for assigning J values to the transitions emerging from the Q-branch bandheads was to run numerous fits on these lines, with each fit using different J assignments; the fits that worked the best presumably had the correct J assignments. Figure 2.10 shows the results of 21 least-squares fits for 57 lines progressing out of the $K_{prolate} = 18 \leftarrow 17$ Q-branch bandhead (this is the bandhead shown in Figure 2.9). These fits used the *ab initio* rotational constants and 4th order distortion terms shown in Table 2.3 as starting parameters. Of these, only A , C , and D_{JK} were allowed to vary in the optimization of the fit, as the spacing within a Q-branch is sensitive to these. B was not allowed to vary because B and C cannot be independently determined without more diversity in transition types (it is the quantity $B-C$ that can be determined from these transitions). In Figure 2.10, the least-squares fit with the lowest error is the one where the first measurable line outside of the bandhead at 341063.2416 MHz is assigned as $53_{18\ 35} \leftarrow 53_{17\ 36}$ (and the degenerate $53_{18\ 36} \leftarrow 53_{17\ 37}$). As the assigned J values for this transition and the rest of the transitions in the series are increased or decreased, the resulting least-squares fits are progressively worse.

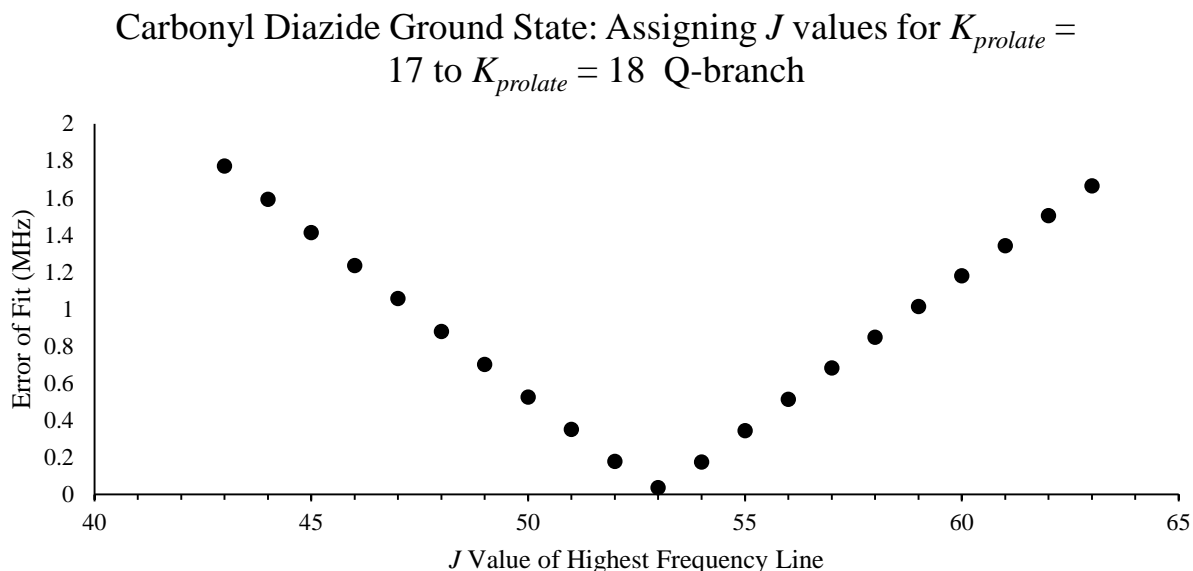


Figure 2.10 The errors (σ) in MHz of 21 least-squares fits for 57 doubly degenerate lines assigned to the $K_{prolate} = 18 \leftarrow 17$ Q-branch of the ground state of the *syn-syn* conformer of carbonyl diazide. Each fit has different J assignments for these lines; the X coordinate is the assigned J value for the highest frequency observed line at 341063.2416 MHz.

This iterative guess-and-check method of assigning the transitions could be applied to any Q-branch. Figure 2.11 shows the results of 21 least-squares fits for a dataset of 62 transitions belonging to the $K_{prolate} 15 \leftarrow 14$ Q branch. Again, there is a clear best fit to the data, in this case with the first measureable transition at 282701.8236 MHz being assigned as $33_{15\ 18} \leftarrow 33_{14\ 19}$ (and the degenerate $33_{15\ 19} \leftarrow 33_{14\ 20}$). A comparison of the results of Figure 2.10 and Figure 2.11 show a large difference in the J value of the first cleanly measureable transition outside of the bandhead. The $K_{prolate} 15 \leftarrow 14$ bandhead contains 18 mutually obscuring lines, while the $K_{prolate}$

18 \leftarrow 17 contains 35 obscured lines, again underscoring the difficulty in initial assignments. There is a general trend of higher Q-branch series having more complicated bandheads.

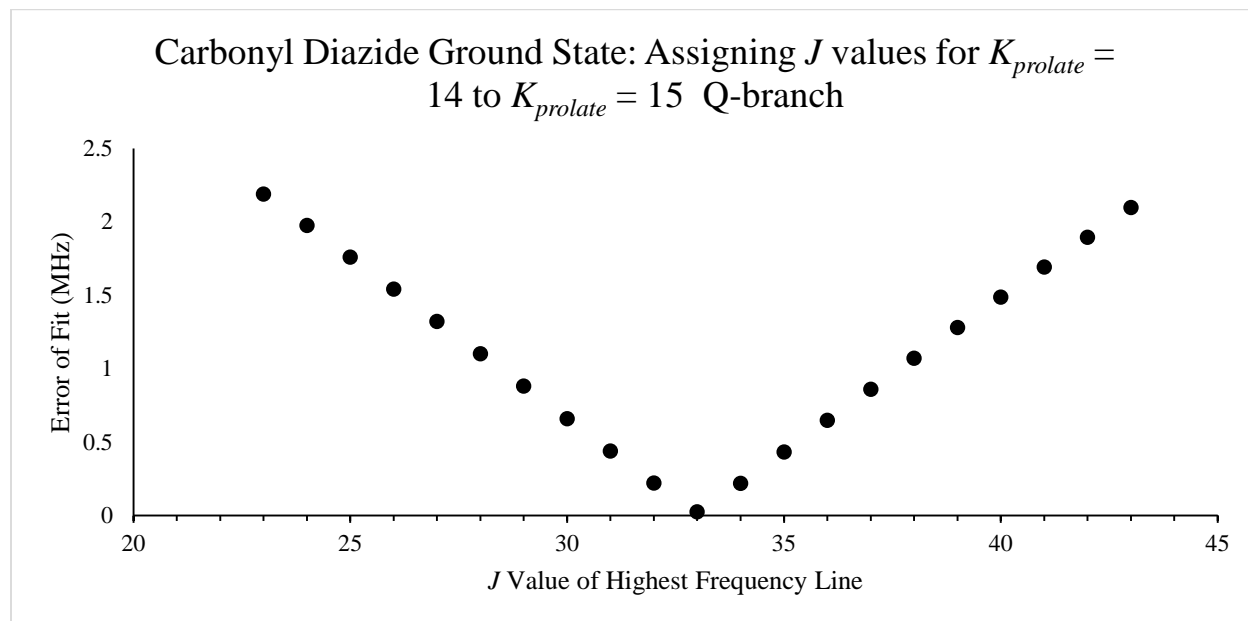


Figure 2.11 The errors (σ) in MHz of 21 least-squares fits for 62 doubly degenerate lines assigned to the $K_{prolate} = 15 \leftarrow 14$ Q branch of the ground state of the *syn-syn* conformer of carbonyl diazide. Each fit has different J assignments for these lines, the X coordinate is the assigned J value for the highest frequency observed line at 282701.8236 MHz.

If the assignments indicated by Figure 2.10 and Figure 2.11 are correct, all of the Q branches should be able to work together in a single fit. Good fits of multiple Q-branches could be obtained. These fits used a fixed value of B but allowed A , C , and all of the 4th order centrifugal distortion terms to vary. Once two Q-branches were fit together, the resulting constants could be used to find the correct assignments for the lines of the remaining three or four Q-branches in the frequency region of our spectrometer.

Least-squares fitting of the Q-branch series gave the difference $A-B$ and $B-C$. The assumption that the molecule was planar (or nearly so), and therefore had an inertial defect ($\Delta I =$

$I_C - I_B - I_A$) close to zero enabled us to get better approximations for all three rotational constants. Predictions of R-branch transitions based on the constants derived assuming an inertial defect of zero were good enough to find the R- Branch transitions.

The R-branch transitions exist as series of transitions with the same $K_{prolate}$ values and increasing J values with an approximate separation of $B+C$ between successive lines. For the *syn-syn* conformer in its ground vibrational state, a total of 1105 *b*-type transitions were observed, consisting of 628 Q-branch transitions from 6 different $K_{prolate}$ series and 477 R-branch transitions from 8 different $K_{prolate}$ series. As seen in Table 2.3, all of these transitions were fit to experimental accuracy ($\sigma = 0.038$ MHz) with an S-reduced, representation I', centrifugal distortion Hamiltonian with all five 4th order constants and the four diagonal 6th order constants. The very small observed inertial defect confirms that this molecule is planar. Also in Table 2.3 are the results of our coupled cluster calculation (ANO1 basis set) for the rotational constants and 4th order centrifugal distortion constants of this conformer. It can be seen that these theoretically predicted constants are in excellent agreement with the experimental results.

Table 2.3 Experimental and *ab initio* spectroscopic constants for the *syn-syn* and *anti-syn* conformers of carbonyl diazide in their ground vibrational states.

	<i>Syn-Syn</i>		<i>Anti-Syn</i>	
	Experimental	CCSD(T)/ANO1	Experimental	CCSD(T)/ANO1
<i>A</i> (MHz)	10807.32121(80)	10759	4860.3329(15)	4844
<i>B</i> (MHz)	1101.93922(32)	1100	1448.9307(80)	1447
<i>C</i> (MHz)	999.95107(39)	998	1115.7777(50)	1114
<i>D_J</i> (kHz)	0.076261(36)	0.075	0.19588(32)	0.19
<i>D_{JK}</i> (kHz)	-1.19632(16)	-1.17	-1.2477(18)	-1.18
<i>D_K</i> (kHz)	19.7585(40)	18.8	11.9279(28)	11.5
<i>d₁</i> (kHz)	-0.010738(34)	-0.0108	-0.0670(23)	-0.0659
<i>d₂</i> (kHz)	-0.000602(18)	-0.000566	-0.0090(30)	-0.00529
<i>H_J</i> (Hz)	0.0000469(31)		[0]	
<i>H_{JK}</i> (Hz)	-0.002860(17)		[0]	
<i>H_{KJ}</i> (Hz)	0.03728(43)		-0.01055(44)	
<i>H_K</i> (Hz)	-0.1393(71)		0.06943(82)	
σ (MHz)	0.038423		0.043777	
Δ_I (amu Å ²)	0.01415	-0.00013	0.1640	-0.00025
N lines	1105		786	

With an excellent fit for the ground vibrational state of the *syn-syn* conformer in hand, along with the theoretical predictions of vibration-rotation corrections, it was possible to assign the transitions for several excited vibrational states of the *syn-syn* conformer. These excited vibrational states all have distinctive Q-branch series with band heads quite similar to those already

described for the ground state. The $K_{prolate} = 19 \leftarrow 18$ Q-branch series band head for the $2\nu_{12}$ state is readily apparent at 341960 MHz in Figure 2.9. In a fashion similar to the ground state, the R-branch series for the excited vibrational states span a wide region of the spectrum, with analogous separations of approximately $B+C$. To assign and fit lines for these vibrationally excited states, the same general strategy as described for the ground state was successfully employed. Transitions (from both Q- and R-branch series) for states ν_{12} , ν_7 , $2\nu_{12}$, and ν_9 (calculated energies 71.5 cm^{-1} , 115.7 cm^{-1} , 143 cm^{-1} , and 150.6 cm^{-1} respectively) were identified, measured, and least-squares fit. As shown in Figure 2.12, ν_{12} is a B1 symmetric out-of-plane-twisting motion of the azide groups. Vibrational mode ν_7 is an A1 symmetric in-plane bending of the azide substituents. Vibrational mode ν_9 is an A2 asymmetric out-of-plane twisting movement of the azide substituents. As an overtone vibrational mode, $2\nu_{12}$ has A1 symmetry.

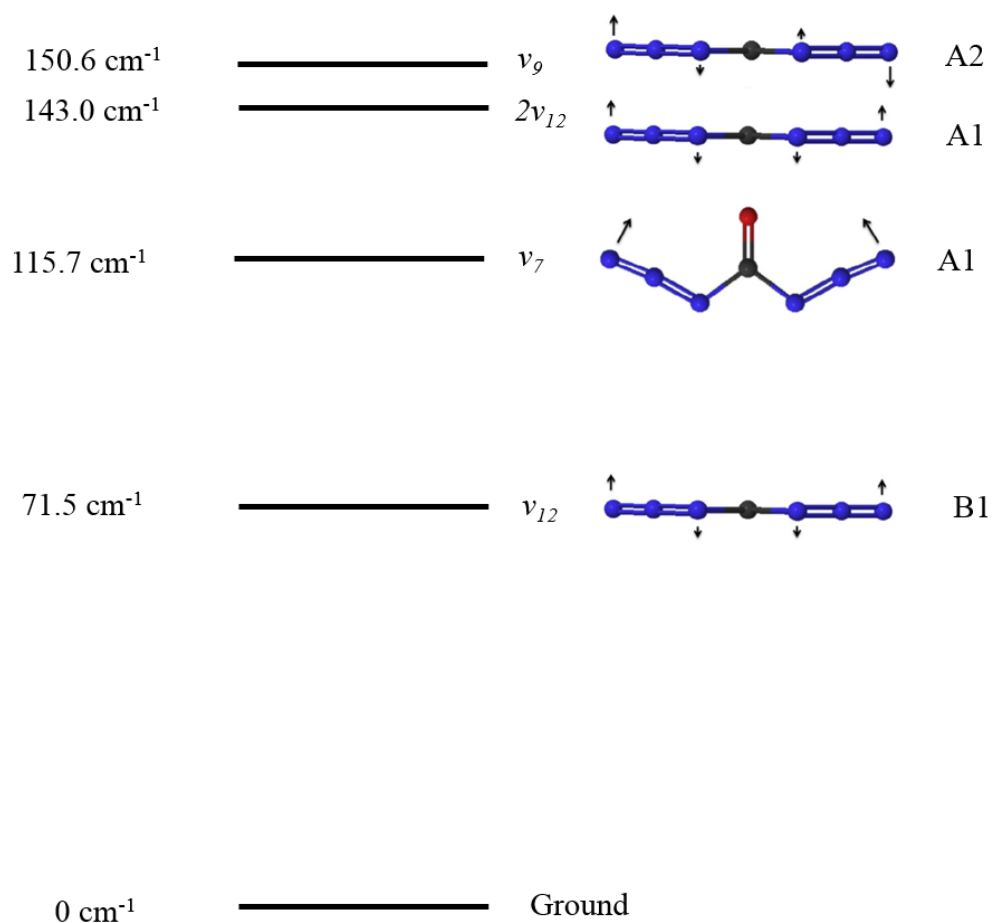


Figure 2.12 The vibrational modes of the *syn-syn* conformer of carbonyl diazide observed in the millimeter-wave spectra.

Unlike the ground state case, the incorporation of some 8th order centrifugal distortion terms in the Hamiltonian was necessary in order to acquire a satisfactory least-squares fit of these vibrational satellites. The need for these higher order terms likely goes hand-in-hand with the large inertial defects accompanying these vibrational modes (see Table 2.6), both attributable to the low frequency, large amplitude, nature of these bending motions of the two azide groups. Vibrational states ν_7 , ν_9 , and $2\nu_{12}$ all show clear signs of what is presumed to be Coriolis perturbation in two of their Q-branch series. Figure 2.13, Figure 2.14, and Figure 2.15 show

attempts to assign J values to the $K_{prolate} = 15 \leftarrow 14$, $17 \leftarrow 16$, and $18 \leftarrow 17$ Q-branches of ν_7 . Each of these figures shows 21 least-squares fits where each fit has a different set of J assignments for the lines progressing out of the Q-branch. The starting constants for these fits were the final fit parameters for the ground vibrational state of the *syn-syn* conformer, corrected with the *ab initio* values for the rotation-vibration interaction. Only A , C , and D_{JK} were allowed to vary. The $K_{prolate} = 15 \leftarrow 14$ series is well behaved, while the $17 \leftarrow 16$ and $18 \leftarrow 17$ series are perturbed.

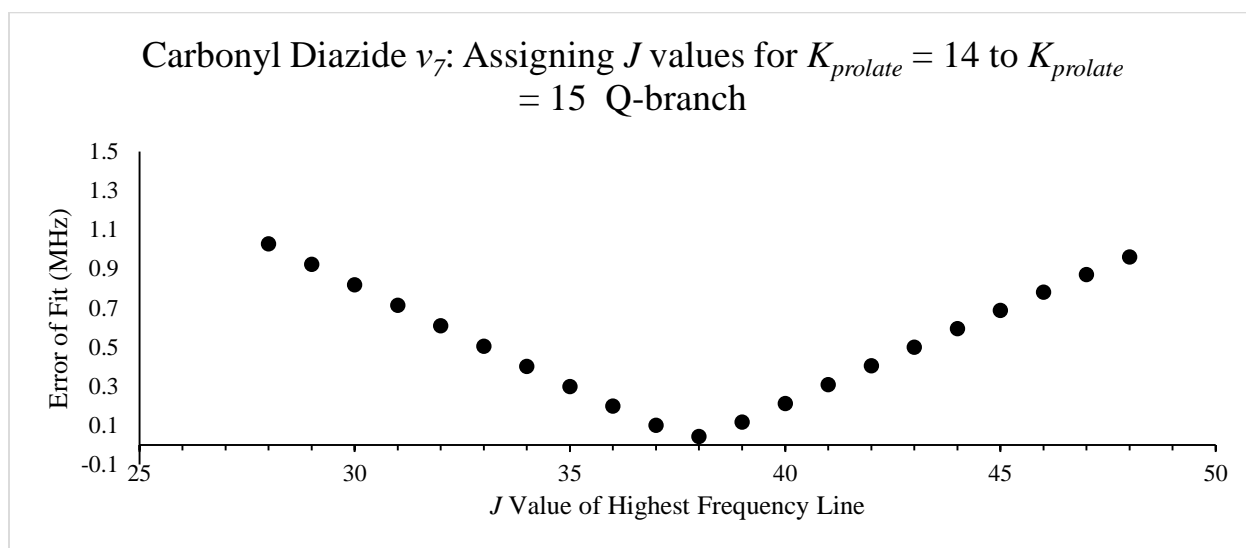


Figure 2.13 The errors (σ) in MHz of 21 least-squares fits for 47 doubly degenerate lines assigned to the $K_{prolate} = 15 \leftarrow 14$ Q-branch of the ν_7 state of the *syn-syn* conformer of carbonyl diazide. Each fit has different J assignments for these lines; the X coordinate is the assigned J value for the highest frequency observed line at 290014.0636 MHz.

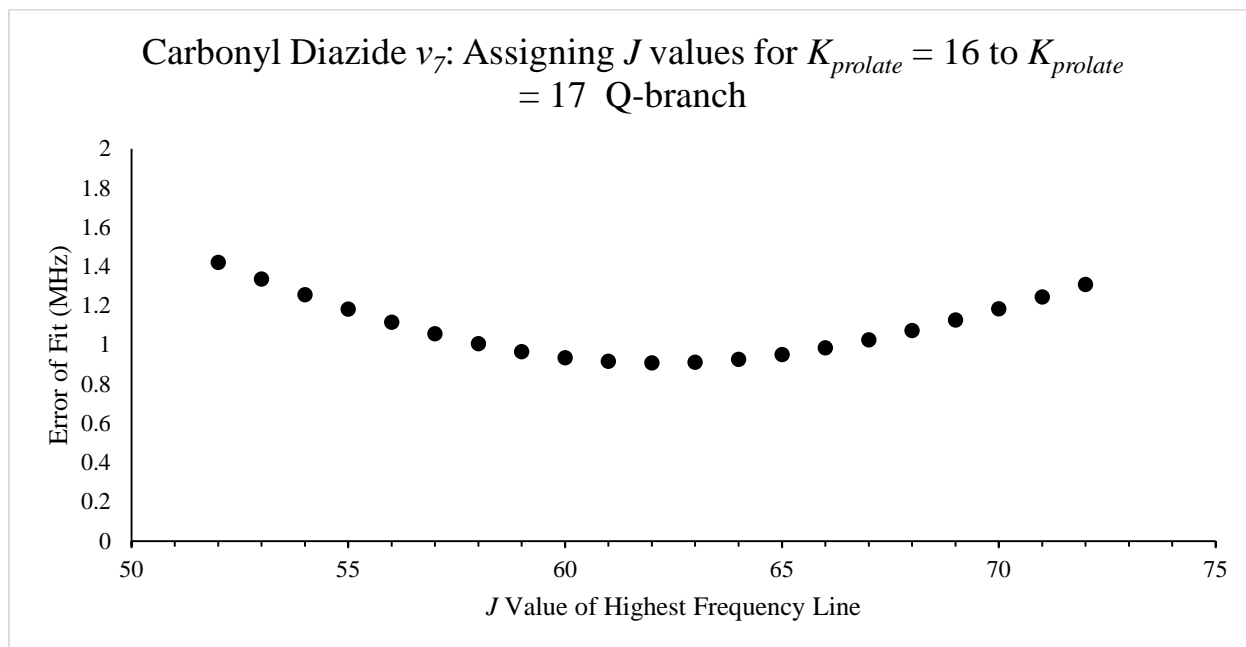


Figure 2.14 The errors (σ) in MHz of 21 least-squares fits for 58 doubly degenerate lines assigned to the $K_{prolate} = 17 \leftarrow 16$ Q-branch of the ν_7 state of the *syn-syn* conformer of carbonyl diazide. Each fit has different J assignments for these lines; the X coordinate is the assigned J value for the highest frequency observed line at 329756.9355 MHz.

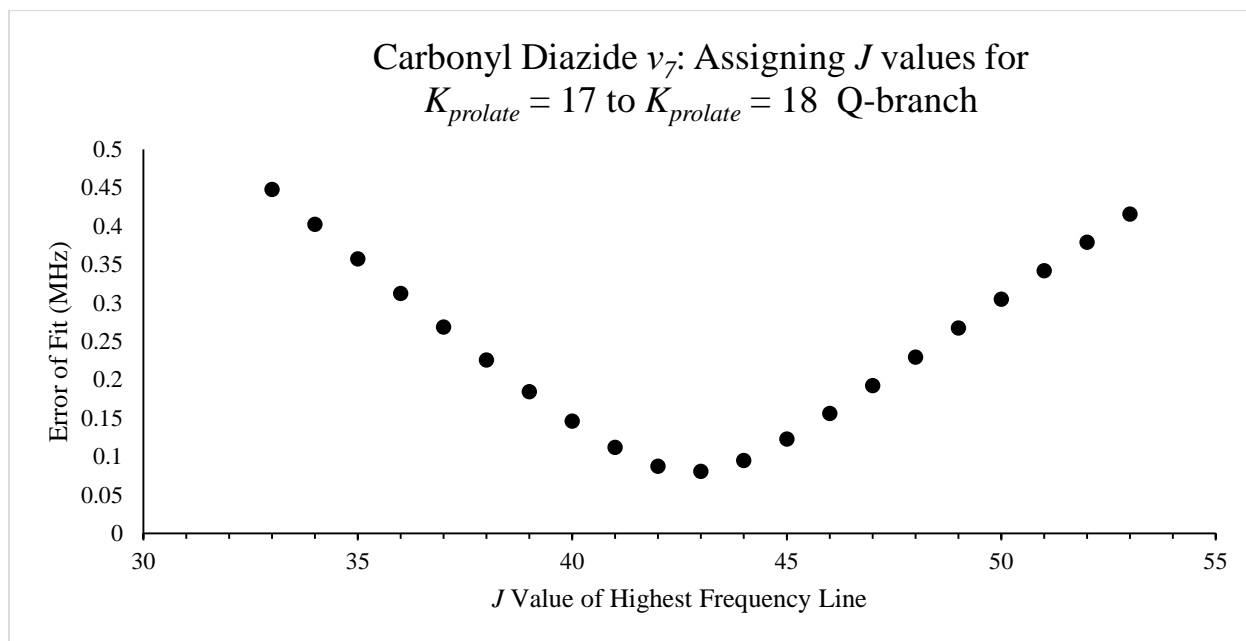


Figure 2.15 The errors (σ) in MHz of 21 least-squares fits for 37 doubly degenerate lines assigned to the $K_{prolate} = 18 \leftarrow 17$ Q-branch of the ν_7 state of the *syn-syn* conformer of carbonyl diazide. Each

fit has different J assignments for these lines; the X coordinate is the assigned J value for the highest frequency observed line at 349586.0318 MHz.

Figure 2.15 and especially Figure 2.14 show a less conclusive assignment preference than Figure 2.13, as evidenced by shallower curves and a higher error of the most preferred J assignment. It is also strange that the assignment preference for the first visible line outside of the bandhead for the $K_{prolate} 17 \leftarrow 16$ series is higher in J by 19 than the assignment preference for the first visible line in the $K_{prolate} = 18 \leftarrow 17$ series. This is strange because the higher $K_{prolate}$ series normally have more lines in their bandheads. Further evidence for perturbation lies in the optimized values of A , C , and D_{JK} in the fits with the preferred values of J . Table 2.4 shows the optimized values of these constants for the fits with the preferred J assignments for the three Q-branch series independently, as well as the value of these constants from the fit that includes three unperturbed Q-branches as well as the R-branches. Although there is no clear trend among the A values, the C and D_{JK} values for the unperturbed Q-branch are in good agreement with the overall fit, and the C and D_{JK} values for the perturbed branches are in poor agreement with the overall fit (in opposite directions too).

Table 2.4 Comparison of constants derived from single Q-branch fits and constants obtained from fit of all relatively unperturbed lines for ν_7 of the *syn-syn* conformer of carbonyl diazide. For the three single Q-branch fits the J assignments used are the preferred assignments from Figure 2.13, Figure 2.14, and Figure 2.15.

	Overall Fit (Table 2.6)	$K_{prolate} 15 \leftarrow 14$ (Figure 2.13)	$K_{prolate} 17 \leftarrow 16$ (Figure 2.14)	$K_{prolate} 18 \leftarrow 17$ (Figure 2.15)
A (MHz)	11083.48	11059.88	11062.85	11043.65
C (MHz)	1000.362	1000.01	1023.63	984.41
D_{JK} (MHz)	-0.00128	-0.00134	-0.00198	-0.00103
$A-B$ (MHz)	9981.08	9957.27	9960.24	9941.04
$B+C$ (MHz)	2102.77	2102.62	2126.24	2087.02
$A - \frac{B+C}{2}$ (MHz)	10032.10	10008.57	9999.73	10000.14
$B-C$ (MHz)	102.04	102.60	78.98	118.20

For ν_7 and $2\nu_{12}$, the Q-branch series $K_{prolate}$ 16-17 and $K_{prolate}$ 17-18 fit poorly into rigid rotor models, as do the Q-branch series for $K_{prolate}$ 13-14 and 14-15 for ν_9 . The implication is that the perturbed energy levels are the $K_{prolate} = 17$ states for ν_7 and $2\nu_{12}$ and the $K_{prolate} = 14$ states for ν_9 . To check this hypothesis we examined whether the corresponding R-branch lines were obviously perturbed. In general the R-branch lines in our frequency region have lower $K_{prolate}$ values than the Q-branches, but there is some overlap. For ν_7 we hypothesize that states with $K_{prolate} = 17$ are perturbed. R-branch transitions involving $K_{prolate} = 17$ of ν_7 are slightly too high frequency for our spectrometer. Likewise, for $2\nu_{12}$ we suspect the $K_{prolate} = 17$ state of being perturbed, but only 5 R-branch transitions involving $K_{prolate} = 17 \leftarrow 16$ are observable with our spectrometer below 360 GHz. In the ν_9 state, however, it is $K_{prolate} = 14$ we suspect of being perturbed based on the Q-branches $K_{prolate} = 14 \leftarrow 13$ and $K_{prolate} = 15 \leftarrow 14$, but the R-branch series involving these states work well with the overall least-squares fit. A summary of the lines we were able to fit for these three perturbed states is shown in Table 2.5. The five Q-branches which are observed to be perturbed do occur where they are expected $((2K_{prolate} + 1)(A - (B+C)/2))$, and their perturbation comes from the spacing of transitions within the band. It is confounding, therefore, that the $K_{prolate} = 18 \leftarrow 17$ of $2\nu_{12}$ could not be found at all, and it was not predicted to be in a particularly dense section of the spectrum. Further complicating this is the fact that $K_{prolate} = 19 \leftarrow 18$ was assigned and fit without incident, so the explanation for the disappearance of the $K_{prolate} = 18 \leftarrow 17$ band cannot be a massive perturbation of the $K_{prolate} = 18$ state.

Table 2.5 A summary of observed *b*-type transitions for the three vibrational states with apparent perturbations in some of the Q-branch series. A dash indicates that the series is outside of our spectrometer range, while asterisks indicate that the lines are noticeably perturbed and excluded from the least-squares fits.

	ν_7 A1 115.7 cm ⁻¹		ν_9 A2 150.6 cm ⁻¹		$2\nu_{12}$ A1 143 cm ⁻¹	
	Q	R	Q	R	Q	R
<i>K_{prolate}</i>						
9-8	-	46	-	-	-	21
10-9	-	45	-	15	-	35
11-10	-	40	-	34	-	40
12-11	-	38	-	44	-	48
13-12	26	35	-	33	-	43
14-13	60	28	*54*	21	43	36
15-14	47	17	*47*	23	69	24
16-15	56	7	50	14	57	16
17-16	*58*	-	56	4	*25*	5
18-17	*37*	-	24	-	*0*	-
19-18	-	-	18	-	57	-

All of the severely perturbed transitions have been omitted from the data sets used for the rotational/centrifugal distortion fits. The results of the fits for these vibrational states are summarized in Table 2.6. In the case of the lowest energy vibrational state (ν_{12}), however, it was possible to include all the measured transitions in the fit summarized in Table 2.6. As can be seen, a fit to within near experimental error is obtained for a rather large data set for the ν_{12} vibrational state.

Table 2.6 Experimentally determined spectroscopic constants for the four assigned excited vibrational states of the *syn-syn* conformer of carbonyl diazide.

	ν_{12}	ν_7	ν_9	$2\nu_{12}$
Relative E (cm⁻¹) CCSD(T)/ANO1	71.5	115.7	150.6	143.0
A (MHz)	10515.8293 (18)	11083.5749(61)	10687.5090(26)	10245.6949(37)
B (MHz)	1102.30411 (87)	1102.5248(39)	1102.3112(30)	1102.5814(33)
C (MHz)	1001.5272 (11)	1000.2230(42)	1000.5791(35)	1003.1971(33)
D_J (kHz)	0.077850 (65)	0.07475(16)	0.07586(20)	0.07675(33)
D_{JK} (kHz)	-0.90795 (64)	-1.3206(42)	-1.2848(21)	-0.5615(24)
D_K (kHz)	-42.116 (12)	83.086(55)	9.075(13)	-87.948(27)
d₁ (kHz)	-0.01219 (14)	0.0	-0.0449(19)	0.0
d₂ (kHz)	0.00305 (35)	0.0	0.137(10)	0.0
H_J (Hz)	0.0000479 (62)	-0.000073(16)	0.000680(46)	-0.000368(81)
H_{JK} (Hz)	-0.002216 (37)	0.00415(46)	-0.01184(93)	0.00096(14)
H_{KJ} (Hz)	0.1716(21)	0.150(20)	-0.0236(97)	0.5292(77)
H_K (Hz)	-24.515 (41)	25.69(22)	-1.792(22)	-36.641(89)
h₁ (Hz)	0.0000336 (67)	-0.001153(52)	-0.00270(19)	-0.000692(31)
h₂ (Hz)	0.0	0.00262(20)	0.0	0.0
h₃ (Hz)	-0.000123 (18)	-0.01505(28)	0.0	0.00340(35)
L_J (mHz)	0.0	0.0	0.0	0.0000233(67)
L_{JK} (mHz)	0.0	0.0	-0.001418(62)	-0.0000134(88)
L_{JK} (mHz)	0.0	-0.02002(82)	0.0226(16)	0.0
L_{KKJ} (mHz)	-0.0673 (25)	-0.395(35)	0.224(16)	-0.4258(84)
L_K (mHz)	7.967 (48)	-10.35(34)	0.0	11.06(10)
σ (MHz)	0.040047	0.04695	0.045508	0.05577
Δ_I (amu Å²)	-1.9256	1.2859	-0.6725	-3.9174
N lines	1119	720	672	768

In the ν_7 state spectrum we were able to assign 56 R-branch transitions where the asymmetry splitting was resolved, but when these were included in the fit the high- J , Q-branch

lines show some systematic residuals and the standard deviation of the residuals σ is slightly greater than the experimental error level (Table 2.6). If only the un-split R-branch lines and the non- $K_{prolate} = 17$ Q-branch lines are included, σ drops by a factor of two. In the cases of ν_9 and $2\nu_{12}$ we were not able to assign the weak split R-branch lines, because of the dense background spectrum, but if they could be measured and included in the fits, a similar increase in σ might be expected. Different combinations of centrifugal distortion constants were required to achieve the fits reported in Table 2.6 and only the D_J constants seems to be relatively invariant to vibrational state.

In Table 2.7 the vibration-rotation interaction constants and inertial defects for all four states from the experimental rotational constants and the coupled cluster calculations are compared. For ν_7 and ν_9 the agreement is reasonable, but the α_A and α_B values are in quite poor agreement in the case of ν_{12} . The α_i values and inertial defects for $2\nu_{12}$, however, are very close to two times the values of the same constants in the fundamental state ν_{12} , which was very helpful in assigning the spectrum of the overtone. The very large negative inertial defects observed for the out-of-plane modes and the large positive defects for the in-plane mode are very well predicted by the theoretical calculations and are consistent with our expectation for these low frequency bending vibrations.²⁸

Table 2.7 Comparison of vibration rotation interaction constants (α_i 's) for the four studied vibrationally excited states of the *syn-syn* conformer of carbonyl diazide determined by experiment and by *ab initio* calculations at the CCSD(T)/ANO1 level.

		α_A (MHz)	α_B (MHz)	α_C (MHz)	Δ_i (amu Å ²)
ν_{12}	experimental	-291.492	0.36489	1.57613	-1.9256
	CCSD(T)/ANO1	-263.41	-2.15	-0.36	-1.86
ν_7	experimental	276.2537	0.58558	0.27193	1.2859
	CCSD(T)/ANO1	270.95	0.67	0.16	1.35
ν_9	experimental	-119.812	0.37198	0.62803	-0.6725
	CCSD(T)/ANO1	-115.54	0.29	0.70	-0.72
$2\nu_{12}$	experimental	-561.626	0.64218	3.24603	-3.9174
	CCSD(T)/ANO1	-526.82	-4.3	-0.72	-3.8147
	$2 \times \nu_{12}$ values	-582.984	0.72978	3.15226	-3.9369

Identifying five vibrational states for the *syn-syn* conformer explained many of the stronger lines in our spectrum, making it feasible to search for transitions from the *anti-syn* conformer. Predictions for the *b*-type transitions showed widely spaced R-branch series spanning the length of our spectral range. A useful observation about these R-branch series is that the lines within a series are very evenly spaced, by roughly 2568.5 MHz ($2 \times A$). Additionally, separation between series was predicted to be regular with a spacing of approximately 9688.5 MHz ($B+C$). Using a particularly clean 310-330 GHz spectrum taken at 293 K, a list of all lines not already assigned to one of the vibrational states of the *syn-syn* isomer was compiled and a difference matrix of this list was created. The telltale recurring differences between some transitions were found, leading to the assignment of the *anti-syn* spectrum. Since our initial assignment we have learned to make use of Loomis-Wood²⁹ type plots, where copies of the spectrum are stacked, with each copy centered on a different frequency. In a typical use of Loomis-Wood plots, the stack of spectra are centered on the predicted frequencies for a series of transitions. If the prediction is good enough, the true lines can be seen in an obvious curve going through the Loomis-Wood plot. The rigid

spacing of the predicted R-branch lines in the *anti-syn* conformer make them good candidates to find with a Loomis-Wood plot. Such a plot is shown in Figure 2.16. The actual R-branch lines are found ~ 300 MHz lower in frequency than the calculated frequencies based on the *ab initio* constants. The dense spectrum makes the series somewhat difficult to see initially.

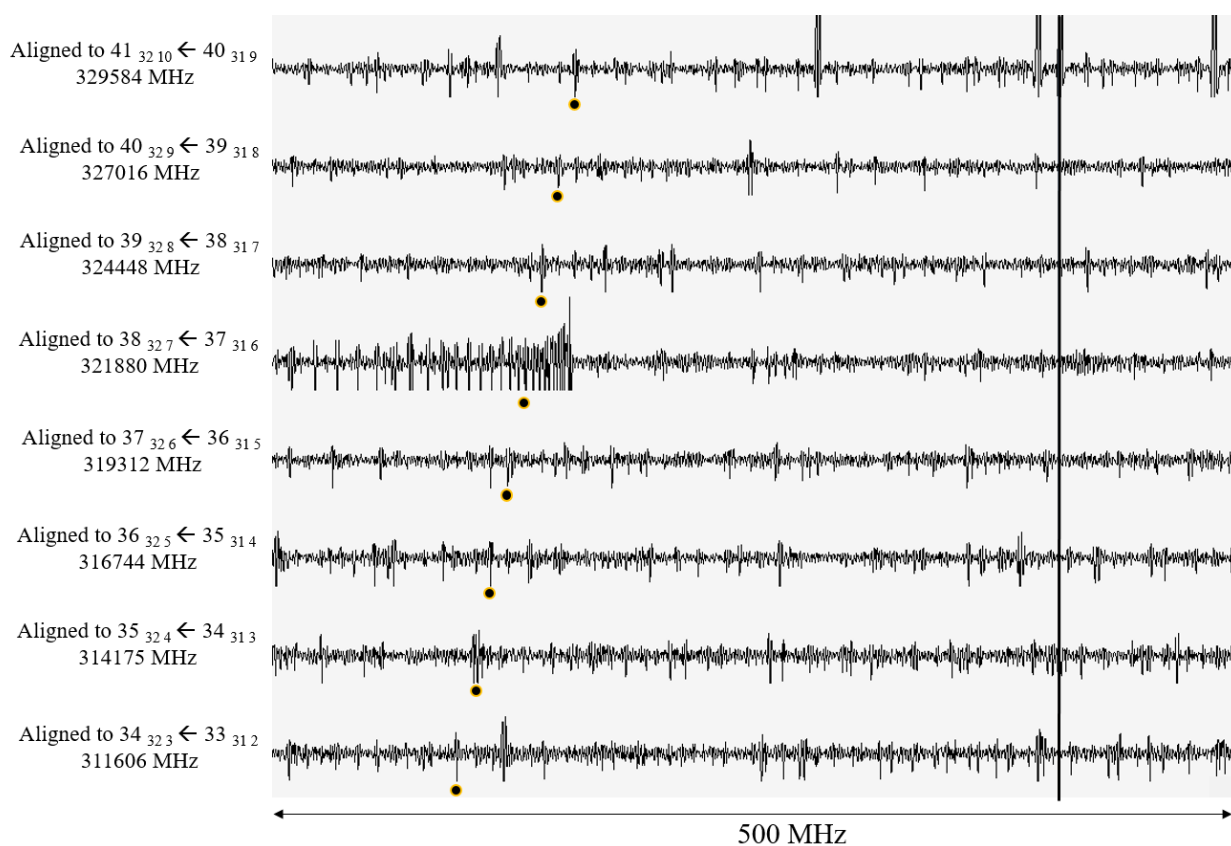


Figure 2.16 A Loomis-Wood plot of the millimeter-wave spectrum of carbonyl diazide at 293K. The stacked spectra are aligned with the predicted values for R-type lines of the *anti-syn* conformer based on *ab initio* predictions of the rotational constants. The predicted frequencies are on the vertical line. The experimentally observed frequencies for these lines are denoted with a dot.

The Q-branch series predicted in our spectral region for the *anti-syn* conformation all had $K_{prolate}$ values greater than 38, and they (and the non-degenerate R-branch transitions) were not

intense enough for us to distinguish them from the great many unassigned lines (presumably of higher vibrationally excited states). The spectroscopic constants from the fit of the *anti-syn* conformer are given in Table 2.3, along with the predictions of the same constants from coupled-cluster theory. As for the other conformer, the agreement of the rotational constants and the 4th order centrifugal distortion constants is excellent (somewhat less so for d_2), and the mean square of the residuals is near the experimental error limit. In spite of this low value of σ , the determination of the rotational constants is not as accurate as in the fit of the *syn-syn* conformer. The lack of transitions where the asymmetry splitting is resolved and of Q-branch transitions in the data set is the origin of this problem, and the somewhat large inertial defect in Table 2.3 is likely symptomatic of it. The inertial defect from the coupled cluster- calculation, however, is typical of what would be expected for a planar molecule. With the spectra of both conformers well fit, it was possible to estimate their relative energies based on peak intensities. We used a particularly clean segment of our 293 K spectrum between 310 and 330 GHz. To compensate for the gradual decrease in intensity during the course of a sample fill, intensities were compared in a matched pair fashion. Each well-measured *syn-syn* line was fit to a Gaussian line shape and compared with the nearest well-measured *anti-syn* line at both higher frequency and at lower frequency. The integrated intensity for each line was normalized with its computed integrated intensity (corrected for the statistical factor of two in favor of the *anti-syn*), and the ratio of the pair of normalized intensities was taken as the Boltzmann factor. In total, 118 of these pairs were used, a few outliers with ratios more than 3 standard deviations away from the mean having been dropped from the set. These 118 pairs gave an average Boltzmann factor of .0515, yielding

an energy difference of 2.4 ± 0.6 kcal/mol, which is consistent with the *ab initio* values presented in Figure 2.5.

Summary

Carbonyl diazide has been successfully synthesized from sodium azide and triphosgene, and the synthesis has been optimized for efficiency and safety. Anharmonic VPT2 calculations well predict the observed IR spectrum of carbonyl diazide. Pure rotational transitions in the millimeter-wave region have been assigned and fit for two conformers and four vibrationally excited states of carbonyl diazide. Three of the vibrationally excited states exhibit perturbed Q-branch series, and these perturbations are not well understood. Future work could involve the analysis of these perturbations. Overall this work has improved our understanding of the synthesis and spectroscopy of carbonyl diazide, and serves as an excellent starting point to further investigate its decomposition products.

Acknowledgements

We gratefully acknowledge the National Science Foundation (CHE-1011959) and the shared computing facilities at Wisconsin (CHE-0840494).

References

1. Curtius, T.; Heidenreich, K., Die Hydrazide und Azide der Kohlensäure. *Journal Fur Praktische Chemie* **1895**, *52*, 454-489.
2. Kesting, W., Hydrazidicarboxazide and its formation as a by-product in the diazotization of carbohydrazide. *Ber. Dtsch. Chem. Ges. B* **1924**, *57B*, 1321-4.
3. Curtius, T.; Bertho, A., Action of carbonyl azide, CON_6 , on aromatic hydrocarbons. *Ber. Dtsch. Chem. Ges. B* **1926**, *59B*, 565-89.
4. Chapman, L. E.; Robbins, R. F., Some reactions of carbonyl azide: N-Azidocarbonylazepine. *Chem. Ind. (London, U. K.)* **1966**, 1266-7.
5. Banert, K.; Joo, Y.-H.; Ruffer, T.; Walfort, B.; Lang, H., The Exciting Chemistry of Tetraazidomethane. *Angew. Chem. Int. Ed.* **2007**, *46* (7), 1168-1171.
6. Zeng, X.; Gerken, M.; Beckers, H.; Willner, H., Synthesis and Characterization of Carbonyl Diazide, $\text{OC}(\text{N}_3)_2$. *Inorg. Chem.* **2010**, *49* (20), 9694-9699.
7. Ball, D. W., Carbonyl diazide, $\text{OC}(\text{N}_3)_2$: Calculated thermodynamic properties. *Comp. Theor. Chem.* **2011**, *965* (1), 176-179.
8. Napolion, B.; Watts, J. D.; Huang, M.-J.; McFarland, F. M.; McClendon, E. E.; Walters, W. L.; Williams, Q. L., Accurate theoretical predictions for carbonyl diazide molecules: A coupled-cluster study of the potential energy surface and thermochemical properties. *Chem. Phys. Lett.* **2013**, *559* (0), 18-25.
9. Zeng, X.; Beckers, H.; Willner, H., Matrix Isolation of Two Isomers of N_4CO . *Angew. Chem. Int. Ed.* **2011**, *50* (2), 482-485.
10. Zeng, X.; Beckers, H.; Willner, H.; Stanton, J. F., Elusive Diazirinone, N_2CO . *Angew. Chem. Int. Ed.* **2011**, *50* (7), 1720-1723.
11. Zeng, X.; Beckers, H.; Willner, H.; Stanton, J. F., Fascinating Diazirinone: A Violet Gas. *Eur. J. Inorg. Chem.* **2012**, *2012* (21), 3403-3409.
12. Kim, Y. S.; Zhang, F.; Kaiser, R. I., Laboratory simulation of Kuiper belt object volatile ices under ionizing radiation: CO-N_2 ices as a case study. *PCCP* **2011**, *13* (35), 15766-15773.
13. Moss, R. A.; Chu, G.; Sauers, R. R., Unprecedented Chemistry of an Aryloxychlorodiazirine: Generation of a Dihalodiazirine and Diazirinone. *J. Am. Chem. Soc.* **2005**, *127* (8), 2408-2409.
14. Moss, R. A.; Sauers, R. R., The generation of diazirinone: a computational study. *Tetrahedron Lett.* **2010**, *51* (25), 3266-3268.

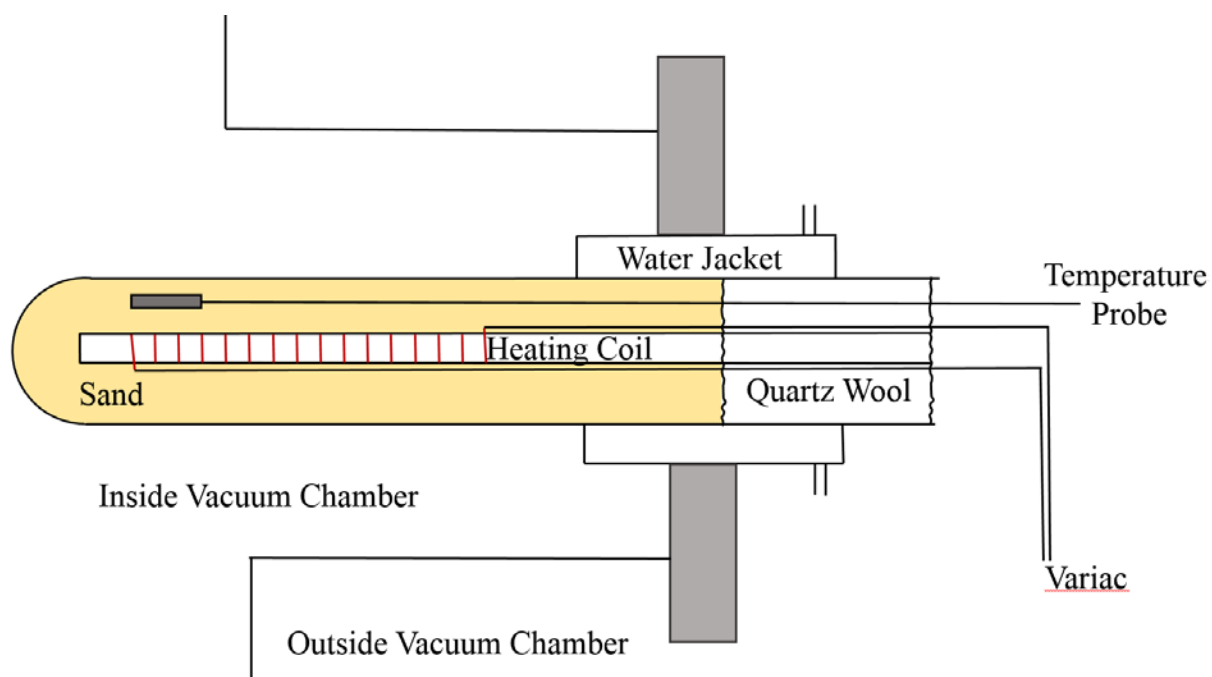
15. Perrin, A.; Zeng, X.; Beckers, H.; Willner, H., The first high-resolution infrared study of diazirinone, N₂CO: Analysis of the Fermi-coupled ν_1 and $2\nu_5$ bands. *J. Mol. Spectrosc.* **2011**, *269* (1), 30-35.
16. Shaffer, C. J.; Esselman, B. J.; McMahon, R. J.; Stanton, J. F.; Woods, R. C., Attempted Isolation and Characterization of Diazirinone (N₂CO). *The Journal of Organic Chemistry* **2010**, *75* (6), 1815-1821.
17. Shaffer, C. J.; Schröder, D., The Demise and Revival of Diazirinone. *Angew. Chem. Int. Ed.* **2011**, *50* (12), 2677-2678.
18. Hollis, J. M.; Remijan, A. J.; Jewell, P. R.; Lovas, F. J., Cyclopropenone (c-H₂C₃O): A New Interstellar Ring Molecule. *The Astrophysical Journal* **2006**, *642* (2), 933.
19. Cotarca, L., Comment on "Chemical Safety. Safe Handling of Triphosgene [bis(trichloromethyl)carbonate]". *Organic Process Research & Development* **1999**, *3* (5), 377-377.
20. Cotarca, L.; Delogu, P.; Nardelli, A.; unji, V., Bis(trichloromethyl) Carbonate in Organic Synthesis. *Synthesis* **1996**, *1996* (05), 553-576.
21. Pasquato, L.; Modena, G.; Cotarca, L.; Delogu, P.; Mantovani, S., Conversion of Bis(trichloromethyl) Carbonate to Phosgene and Reactivity of Triphosgene, Diphosgene, and Phosgene with Methanol. *The Journal of Organic Chemistry* **2000**, *65* (24), 8224-8228.
22. Brandstrom, A.; Lamm, B.; Palmertz, I., Use of tetrabutylammonium azide in the Curtius rearrangement. *Acta Chemica Scandinavica, Series B: Organic Chemistry and Biochemistry* **1974**, *28* (6), 699-701.
23. J.F. Stanton, J. G., M.E. Harding, P.G. Szalay; with contributions from A.A. Auer, R. J. B., U. Benedikt, C. Berger, D.E. Bernholdt, Y.J. Bomble, L. Cheng, O. Christiansen, M. Heckert, O. Heun, C. Huber, T.-C. Jagau, D. Jonsson, J. Jusélius, K. Klein, W.J. Lauderdale, D.A. Matthews, T. Metzroth, L.A. Mück, D.P. O'Neill, D.R. Price, E. Prochnow, C. Puzzarini, K. Ruud, F. Schiffmann, W. Schwalbach, S. Stopkowicz, A. Tajti, J. Vázquez, F. Wang, J.D. Watts and the integral packages MOLECULE (J. Almlöf and P.R. Taylor), PROPS (P.R. Taylor), ABACUS (T. Helgaker, H.J. Aa. Jensen, P. Jørgensen, and J. Olsen), and ECP routines by A. V. Mitin and C. van Wüllen. For the current version, see <http://www.cfour.de>.
24. Scuseria, G. E., Analytic evaluation of energy gradients for the singles and doubles coupled cluster method including perturbative triple excitations: Theory and applications to FOOF and Cr[_{sub 2}]. *The Journal of Chemical Physics* **1991**, *94* (1), 442-447.
25. Lee, T. J.; Rendell, A. P., Analytic gradients for coupled-cluster energies that include noniterative connected triple excitations: Application to cis- and trans-HONO. *The Journal of Chemical Physics* **1991**, *94* (9), 6229-6236.

26. Stanton, J. F.; Lopreore, C. L.; Gauss, J., The equilibrium structure and fundamental vibrational frequencies of dioxirane. *J. Chem. Phys.* **1998**, *108* (17), 7190-7196.
27. Mills, I. M. In *Infrared spectra. Vibration-rotation structure in asymmetric- and symmetric-top molecules*, Academic: 1972; pp 115-140.
28. Watson, J. K. G., Approximations for the inertial defects of planar molecules. *J. Chem. Phys.* **1993**, *98* (7), 5302.
29. Loomis, F. W.; Wood, R. W., The Rotational Structure of the Blue-Green Bands of Na₂. *Physical Review* **1928**, *32* (2), 223-236.

Chapter 3: Equipment improvements and preliminary work towards the generation of diazirinone

Includes the work of collaborators:

Brian J. Esselman, Joshua D. Shutter, R. Claude Woods, and Robert J. McMahon



Abstract

Preliminary work on the pyrolysis of carbonyl diazide to form diazirinone for spectroscopic study in our millimeter-wave spectrometer is described. Diazirinone has been a molecule of interest to our group for many years now. Improvements to the spectrometer are outlined, both those specifically geared towards pyrolysis projects such as the generation of diazirinone, but also general improvements made to the instrument in the wake of its major renovation. Notably we have added a ‘hot-finger’ heater to our spectrometer for *in-situ* pyrolysis. A second, external, pyrolysis apparatus has also been constructed. Although we have not succeeded in generating diazirinone yet, we have found a signals for a planar molecule which may be another decomposition product of carbonyl diazide. We have thoroughly examined the spectrum of this decomposition product (or impurity), but despite knowing its rotational constants we have not been able to identify the molecule.

Introduction

Diazirinone (N_2CO), is a molecule of potential astrochemical interest, as it can conceivably be formed as an adduct of the extremely common CO and N_2 molecules. Diazirinone has been observed as a metastable product in irradiation of CO- N_2 ices at 10K, which may simulate the chemistry of similar mixed ices in space.¹ An $^{15}\text{N}_2\text{CO}^+$ fragment has also been observed in a neutralization-reionization mass spectrometry experiment involving the chemical ionization of a gaseous mixture of $^{15}\text{N}_2$ and CO.² Although diazirinone is ~ 100 kcal/mol higher in energy than CO and N_2 , the barrier to decomposition is large enough (~ 25 kcal/mol) to entertain the possibility of finding it in the interstellar medium (ISM).²⁻³ In 2005 Moss *et al.* reported the generation of

diazirinone from the reaction of *p*-nitrophenoxchlorodiazirine with a nucleophilic fluoride ion as shown in Figure 3.1.⁴

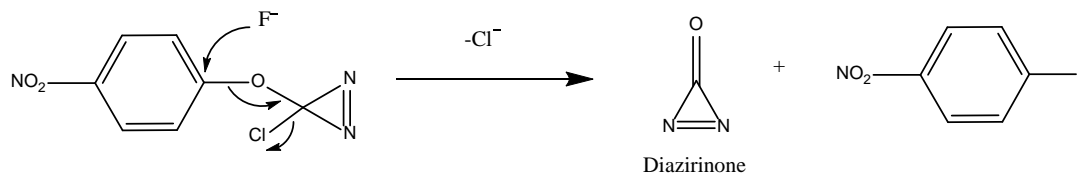


Figure 3.1. Synthetic Scheme for the generation of diazirinone as reported by Moss *et al.*

Attempts by members of our group to repeat this synthesis were unsuccessful. In the spectrum of the gaseous products of the reaction, a peak assigned by Moss *et al.*⁴ as the CO stretch of diazirinone was reassigned as carbon monoxide in a condensed or solution phase.⁵ Publication of these findings led Moss *et al.* to computationally re-evaluate their previous claims, ultimately concluding that although diazirinone was likely formed transiently in their reaction mixture, the presence of fluorine ions likely catalyzed a rapid decomposition of the diazirinone to N₂ and CO.⁶

An alternate path to diazirinone was found by Zeng *et al.* in 2011.⁷⁻⁸ Their approach was the pyrolysis of carbonyl diazide. The publication of this synthetic scheme renewed our group's long term goal of observing the rotational spectrum of this molecule and led us to our study of carbonyl diazide. During our studies of carbonyl diazide⁹⁻¹⁰ and pyridazine¹¹ we made numerous improvements to the spectrometer, with the intention of using our improvements and our acquired skills towards the eventual study of diazirinone and other more transient species.

Improvements to the spectrometer

In 2009 we received a grant for a major upgrade of the group's millimeter-wave spectrometer. A full explanation of the first wave of upgrades are documented in the thesis of

Brian Esselman.¹² In short, we upgraded the spectrometer's signal generation, the detector, the vacuum pumps, pressure gauges, mass flow controllers, valves, chiller system, GPS frequency standard, and the computer control system. A schematic for the current incarnation of the millimeter-wave spectrometer is shown in Figure 3.2. The new signal generation starts with an Agilent analog signal generator (generates microwave signals up to 20 GHz), the frequency modulated output of which is passed through an amplification multiplication chain and then into the chamber. This system is entirely computer controlled and requires no manual tuning by the operator at any point in the frequency range. The new detector is a diode, which operates at room temperature, in contrast to the indium antimonide bolometer it replaced, which required liquid helium to function. The computer control system was built in LabView on a modern Windows 8 PC. Most of the new valves, gauges, and the chiller unit can be controlled using the PC.

The newfound ability to completely automate our sample collection has been incredibly useful. A frequent mode of operation is to set a flow of sample through the chamber, or to charge the chamber with a static pressure of sample, and to set up a 100 GHz scan to run overnight. It takes approximately 12-14 hours to run this full scan. Once the scan is acquired, Kisiel's SView viewing program¹³ can be used to analyze the spectra on our office or home computers.

The instrument renovation process included a full dismantling of the Pyrex chamber, which is built from a series of thick walled 4 inch inner diameter tubes, tees, and crosses. Many of the pieces were coated in layers of carbon soot and other impurities from years of spectroscopy of molecules in an electric discharge. The pieces of the vacuum chamber were cleaned with acid baths and soap & water wherever possible. The main length of the chamber is more or less

permanently in place in the laboratory, so it was cleaned ramrod style with a very large brush attached to a power drill.

Disassembling the bulk of the vacuum chamber allowed the machine shop to build a platform on which we anchored the new turbomolecular fan vacuum pump which replaced a large oil diffusion pump. Upon reconstruction of the vacuum chamber, we had the opportunity to thoroughly leak check every joint using the department's helium-sensing vacuum leak detector. We were able to assemble the chamber and achieve a background leak rate of ~ 1 mTorr/hour, which was less than half the background rate before the renovation. The lower background leak rate results in cleaner full spectra when the chamber is given a static fill of sample for an overnight scan.

In all, this host of improvements has made millimeter-wave spectroscopy a very practical endeavor for our group. Since renovation, four graduate students and five undergraduate students have collected publishable results with the instrument.

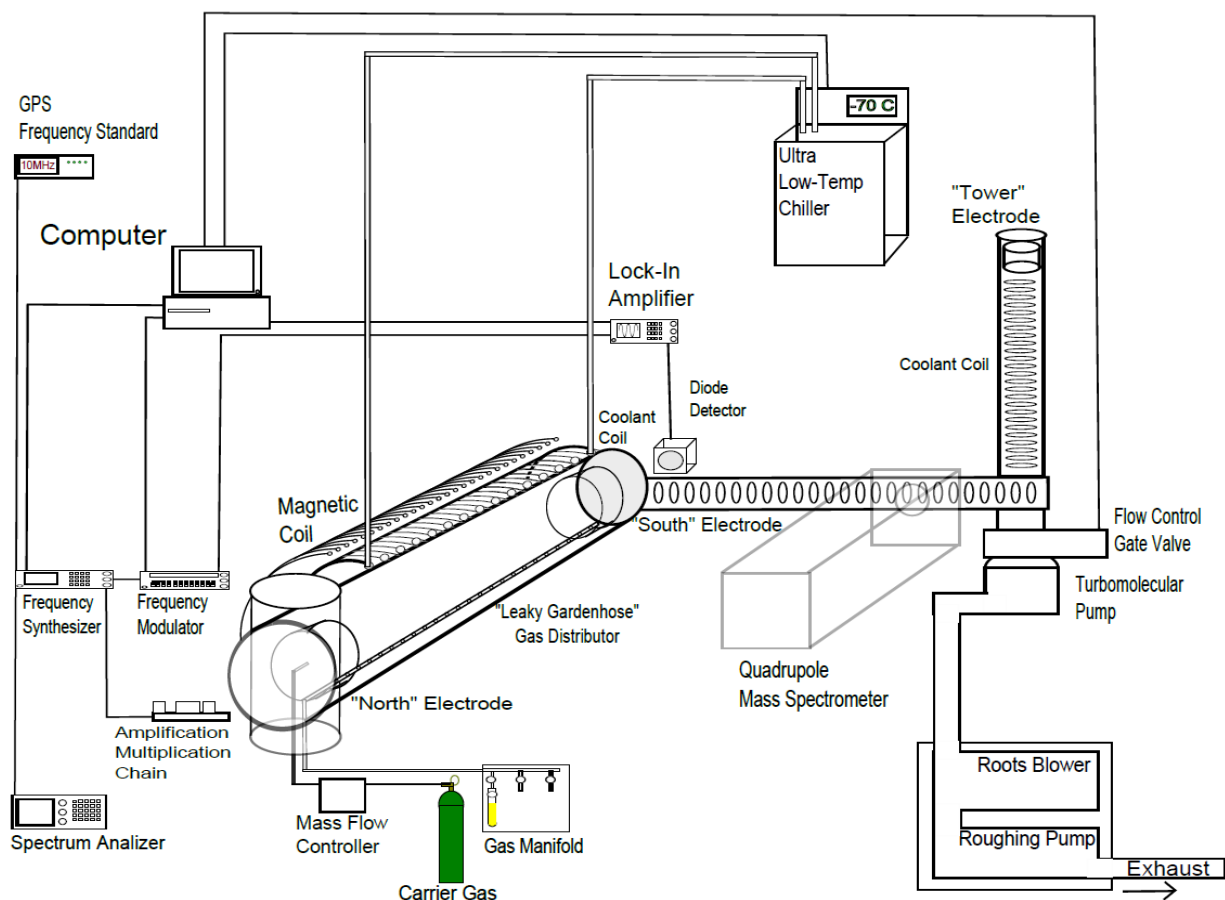


Figure 3.2 Schematic of our millimeter-wave spectrometer.

We have made numerous small improvements to the instrument since the major overhaul in 2010/2011. Figure 3.3 shows two safety features added to protect the turbomolecular pump. First, an automatic shutoff valve was added between the turbomolecular pump and the roots blower / Leybold mechanical pump that we use as backing pumps (Figure 3.3a). The shutoff valve is to protect the pump in case of a power outage. In a worst case scenario, in a blackout situation the turbomolecular pump could receive a burst of air from the backing pump / exhaust line while the turbomolecular fan is still spinning at close to 34,000 RPM due to its considerable angular momentum. The shutoff valve is pneumatically actuated and was incorporated into the system to prevent such a scenario. The pressure for this pneumatic action is the building's compressed air. A secondary solenoid controlled 3-way valve controls whether or not the pneumatic valve is pressurized. Disconnecting power from the solenoid valve results in the activation of the shutoff valve to isolate the turbomolecular pump.

A second improvement made to protect the turbomolecular pump is a constant nitrogen purge. Figure 3.3b shows a regulator which feeds house nitrogen into the purge port of the pump at ~25 psi. The regulator is equipped with both a coarse and a fine particle filter. The nitrogen purge is intended to protect the pump from corrosion when we study particularly reactive species, *e.g.*, when the electric discharge is activated.

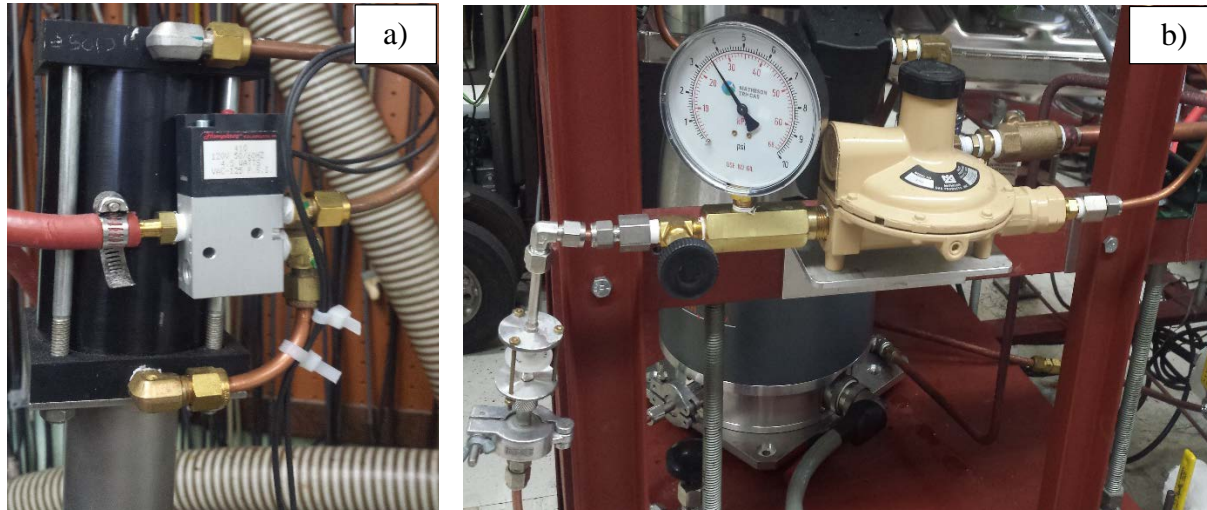


Figure 3.3 a) A pneumatic shut-off valve actuated by a three-way solenoid switch to protect the turbomolecular fan pump in case of a power outage. b) A constant flow nitrogen purge system to protect the turbomolecular fan pump.

Significant effort has also been put into improving our chiller and coolant plumbing system. As shown in Figure 3.2, the spectrometer is plumbed to an ultralow temperature chiller which cools its working fluid as low as $-90\text{ }^{\circ}\text{C}$, and pumps it through heat exchange coils wrapped around the spectrometer, and also through the two electrodes. Over the years this system has proven spectroscopically useful, as already described in Chapter 2. We expect cold spectra to be very valuable for the spectroscopy of diazirinone as well. Unfortunately the chiller system has proven incredibly frustrating to maintain. One problem is solvent choice. The solvent must be liquid in the temperature range $-90\text{ }^{\circ}\text{C}$ to $20\text{ }^{\circ}\text{C}$. It must be nontoxic, nonflammable, and, preferably, cheap. The first solvent we tried was the refrigerant R-123, which is chemically 2,2-dichloro-1,1,1-trifluoroethane. This worked reasonably well while the chiller was cold, but its high vapor pressure ($\text{bp} = 28\text{ }^{\circ}\text{C}$) meant that it evaporated quickly, and it was too expensive to tolerate the rapid loss we observed. By the rate of evaporation it became apparent that our ultralow

chiller was NOT a closed system. Indeed the solvent bath is essentially open to the air. It also became apparent that the plumbing system we had built was rife with leaks and developed them faster than we could fix them. We had been using a combination of standard half inch steel plumbing components to cross the room, and quarter inch plastic tubing with Swagelok unions as the heat transfer coils against the walls of the spectrometer chamber. A refrigerant 'sniffer' capable of detecting chlorofluorocarbons indicated that leaks were springing up at a great many points in our plumbing, likely the result of repeated cycling between -80 °C and room temperature. We found by trial and error that Cajon fittings (now Swagelok UltraTorr) handled the temperature change better than regular Swagelok tube fittings. We also found that standard plumbing ball valves were prone to catastrophic failure in these circumstances. When these valves are closed at cold temperatures, the solvent can expand by more than 10% as it warms to room temperature, destroying the valve. We were able to purchase, from Avco, specialty cryogenic ball valves which have an extra channel on one side of the ball to relieve this pressure. None of these valves have failed in the past three years. Figure 3.4 shows some of our current plumbing setup, which has been reasonably leak-proof.

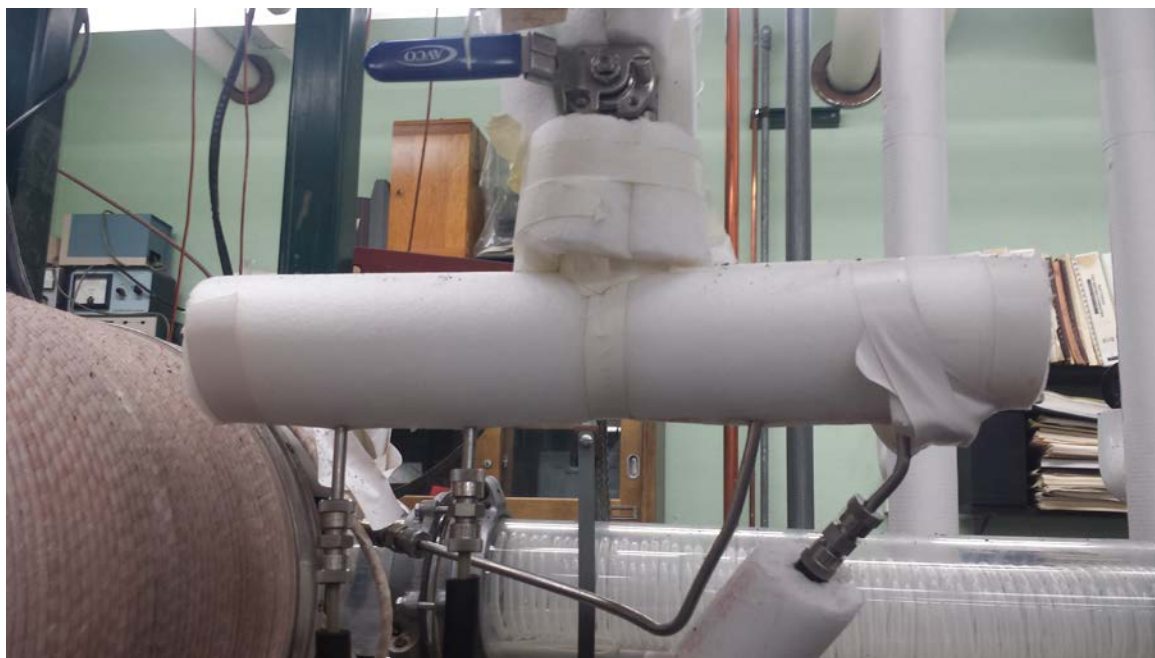


Figure 3.4 Our current setup for our chiller system

We made several attempts to leak-proof the chiller itself, but this is simply not possible based on several of the design choices the manufacturer made. With increasing prices of the R-123, we chose to try a different solvent. The solvent we currently use is Dow Syltherm XLT. This solvent is a silicone oil with the stated ability to work as a heat transfer fluid between $-100\text{ }^{\circ}\text{C}$ and $+260\text{ }^{\circ}\text{C}$. We have had no problems whatsoever with evaporation of this solvent, but a problem with the plumbing blocking up with ice has become much worse. Again, the open air design of the coolant bath is the source of the problem, with moisture in the air condensing into the solvent pool, and forming ice crystals that block flow. Unlike R-123, the Syltherm XLT is less dense than water and ice, and is more miscible with water. These differences likely contribute to the problems with ice crystals. We have experimented unsuccessfully with finding efficient ways to dry the solvent. We are currently building a canister filter to attempt to remove ice particles from our loop.

Pyrolysis apparatus

To generate diazirinone, Zeng *et al.* reported passing carbonyl diazide through a quartz tube at 400 °C and passing the gasses emerging from the tube through a U-trap at -100 °C, followed by a trap at liquid nitrogen temperature. The unreacted carbonyl diazide got trapped in the -100 °C trap, while diazirinone was trapped by liquid nitrogen. They reported passing the remaining carbonyl diazide through the pyrolysis multiple times until it was all consumed, either going to diazirinone, or to N₂ and CO, which pass through both traps. We designed an apparatus to parrot their synthesis, as shown in Figure 3.5. The design allows one to run the carbonyl diazide remnants back and forth through the pyrolysis tube by simply changing the valve settings and moving the dry ice to the warm trap. Initially we chose to build the traps out of several coils of Teflon tubing. This design allowed a larger path length and surface area in each trap, which we viewed as advantageous since we wanted to attempt setting the first trap at -78 °C (dry ice temperature) instead of -100 °C for practical reasons. Using Teflon for the traps instead of glass also minimized the risk of shrapnel in the event of an explosion. Indeed we did get an explosion the first time we tried passing a fresh batch of carbonyl diazide through the traps. During this trial the pyrolysis tube was at room temperature, because the purpose was simply to see if the dry ice trap would catch all of the carbonyl diazide, or if some would make it into the liquid nitrogen trap. The result was an explosion, which shredded the Teflon coil in the dry ice trap. The remnants are shown in Figure 3.6. Interestingly, the location of the detonation was at the precise point where the Teflon tube entered the dry ice/acetone bath. This indicates that a large portion of the sample condensed here, but it is unclear what set off the detonation.

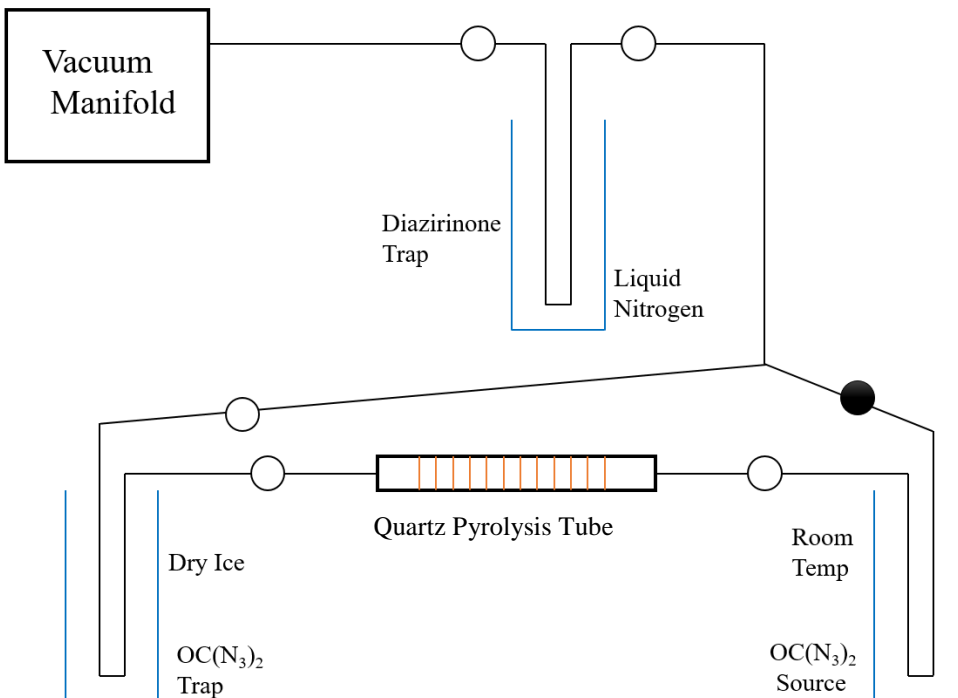


Figure 3.5 Schematic for our benchtop pyrolysis setup for the generation of diazirinone from carbonyl diazide.

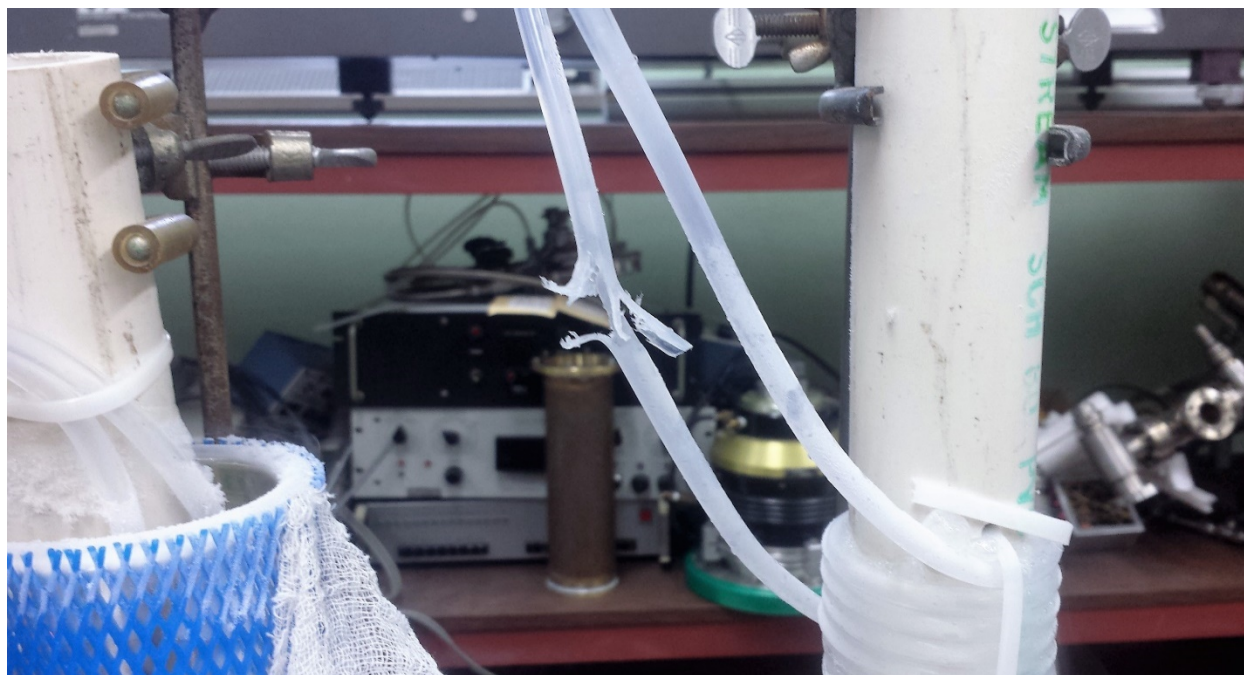


Figure 3.6 A trap made out of Teflon tubing intended to catch carbonyl diazide at dry ice temperature. On the first trial carbonyl diazide detonated, destroying the tubing.

The destruction of the Teflon tubing trap made us reconsider the pyrolysis design. Although there was no shrapnel in this case, we consider ourselves lucky that the dewar, almost directly touching that part of the tubing, did not implode. This detonation also posed a danger to the manifold's diffusion pump, because it was pumping on air for a few seconds before I was able to isolate it. For a second attempt at making the idea of Figure 3.5 a working piece of equipment in our laboratory, we chose to use stainless steel for the traps, as shown in Figure 3.7. In the event of a detonation, the 3/8" stainless steel tubing should be more resilient than either glass or Teflon. Additionally, we hypothesize that the buildup of pure carbonyl diazide in a very small area may be reduced for this tubing, because it is a thicker gauge which should result in spreading the condensed carbonyl diazide over a greater surface area. We have not yet tested this apparatus.



Figure 3.7 A pyrolysis apparatus using steel traps

We have also constructed an *in situ* pyrolysis apparatus. It is an electrically heated quartz tube, which sits inside the vacuum chamber, and whose temperature can be controlled by Variac. To incorporate this into our spectrometer, we added an extra Pyrex cross to the spectrometer to give us a new port for the heater. The new cross also afforded us a second auxiliary port, which we have put a thick walled glass trap in. The new Pyrex cross is shown in Figure 3.8. A schematic for the *in situ* pyrolysis heater is shown in Figure 3.9. This was constructed out of quartz by Tracy Drier. We have installed this apparatus, but have not tested it yet. In addition to the diazirinone project, we anticipate using this apparatus to generate ketene from diketene. We hope to make acylium ion in a ketene glow discharge.



Figure 3.8 A Pyrex cross added to the spectrometer to give new ports for a pyrolysis heater (right) and a thick-walled glass piece that can be used to condense sample (left).

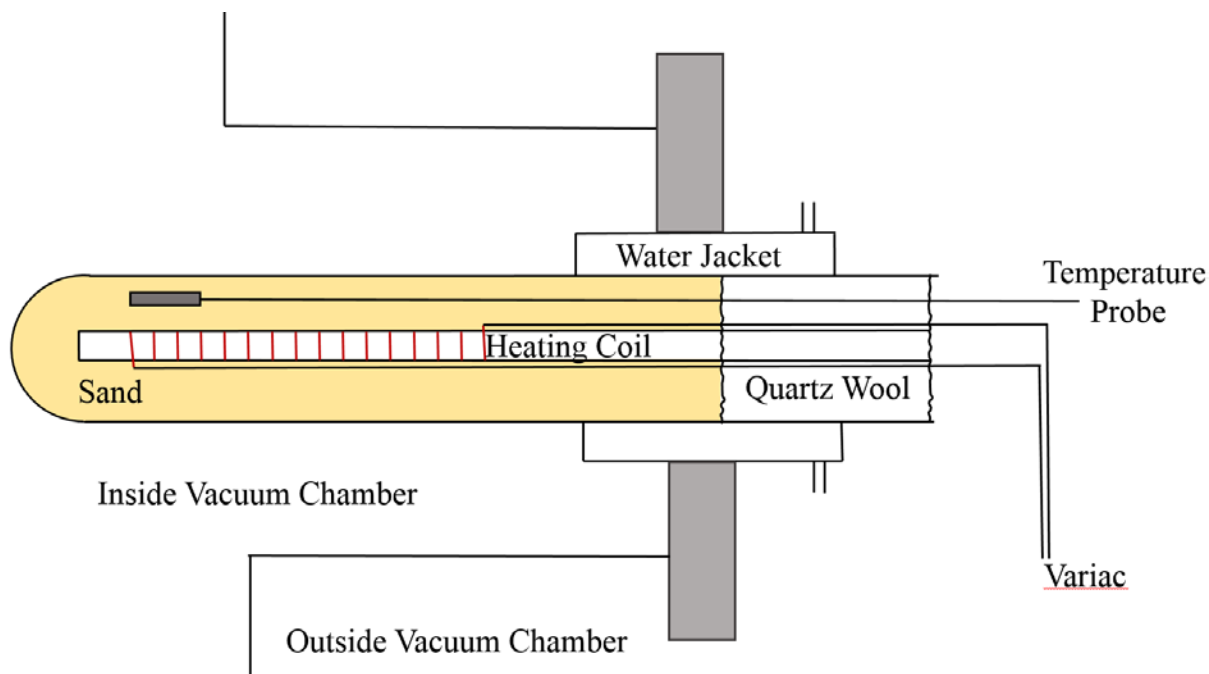


Figure 3.9 A schematic for our quartz-body in situ pyrolysis apparatus.

Impurity identification in carbonyl diazide sample

In the initial testing of one of our multi-trap pyrolysis setups, we attempted to use the dregs from an old (1 month) synthetic batch of carbonyl diazide to ascertain whether a dry ice/acetone trap would trap all of the carbonyl diazide, or whether some would make it through to the liquid nitrogen trap. What we found instead was an impurity with a distinct and strong rotational spectrum, as shown in Figure 3.10. Its appearance was surprising, and we spent a few weeks examining it, before identifying it as acetone. The distinctive pattern of patterns of patterns arises from the rotation of the molecule's two methyl groups. We are still not sure how this much acetone got into our sample, but we hypothesize that it was either adsorbed in one of our o-rings, or there was a relatively large leak in our gas line and acetone from the dry ice trap entered our sample flask or spectrometer that way.

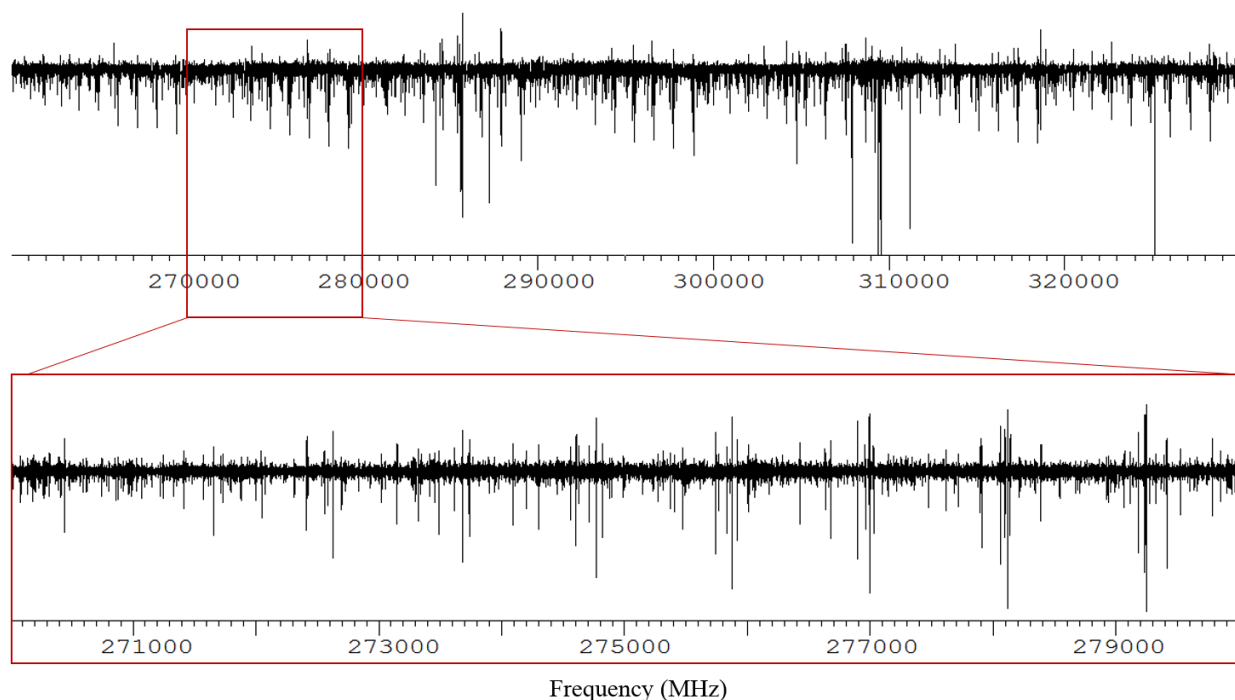


Figure 3.10 An impurity with a beautiful spectrum found in an old carbonyl diazide sample. It was eventually identified as acetone.

In the course of determining that the impurity was acetone (finally achieved by assigning the rotational spectrum and comparing the constants to reasonably sized molecules), we found a second impurity with much lower signal intensities. We found this impurity in a second fraction pulled out of the decrepit carbonyl diazide batch, which we exposed to 90 seconds of negative glow discharge. Because of the background leak rate we did not take a full 12 hour background scan of this fraction before turning on the discharge, so it is unclear whether the discharge is an important variable or not. We were able to completely assign the rotational spectrum (ground state only) of this second molecule, which consisted R- and Q-branch series like those shown in Figure 3.11 and repeated every ~ 10680 MHz. Despite weak line intensities when compared to the acetone transitions, the clear beginnings of their R-branches, shown in Figure 3.12 made the assignments possible.

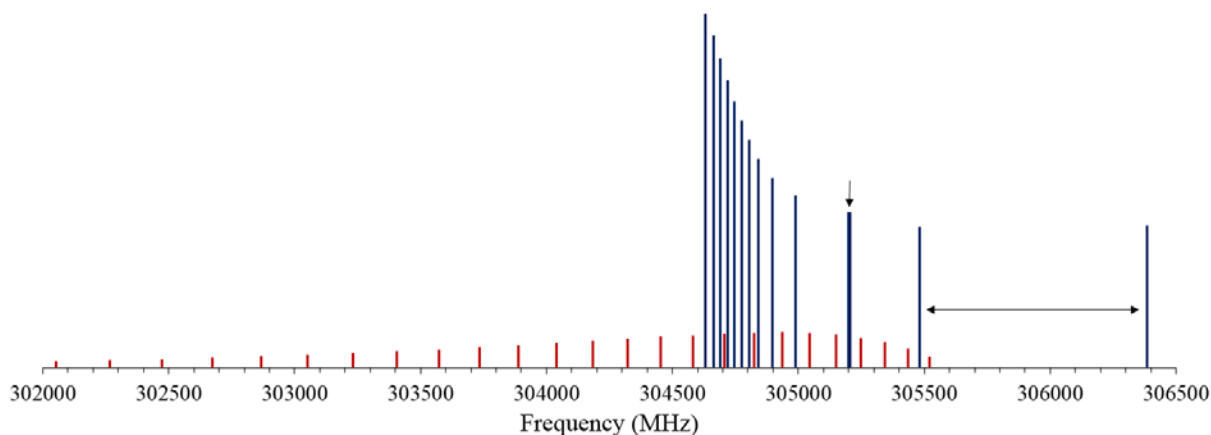


Figure 3.11 Stick spectrum of the unknown impurity showing an R-branch (blue) and Q-branch (red). The arrows call attention to the break in degeneracy later in the series.

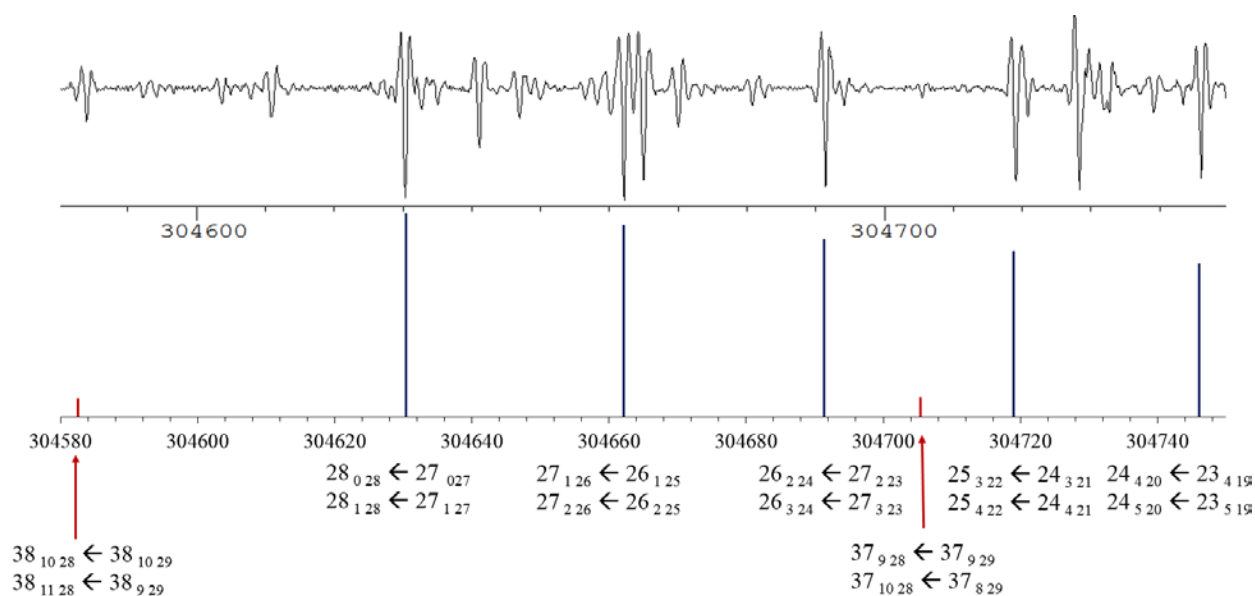


Figure 3.12 Stick spectrum and observed spectrum for the unknown impurity. The clear start of the R-branch made the spectral assignment reasonably straightforward.

In assigning the spectrum for the unknown impurity, we needed to determine whether the dipole moment was *a*-type, *b*-type, or a combination. At the beginning of the R-branch shown in Figure 3.12, predictions place the transitions $28_{0\ 28} \leftarrow 27_{0\ 27}$, $28_{1\ 28} \leftarrow 27_{1\ 27}$, $28_{1\ 28} \leftarrow 27_{0\ 27}$, and $28_{0\ 28} \leftarrow 27_{1\ 27}$ all at the same frequency. Indeed, through most of both the R-branches and the Q-

branches, the a - and b -type transitions are predicted to be degenerate, and therefore it is difficult to tell whether we are observing a - or b -type transitions. The clue comes where the 4 transitions break degeneracy, as shown in Figure 3.13. When comparing several of these ‘quartets’, it was repeatedly observed that there are lines where the a -type transitions should be, but not the b -type. We found that fits assuming a -type transitions worked better. Our best fit for this mystery impurity is shown in Table 3.1. The fit is really quite remarkable, considering that we have only ever seen the signals as low intensity impurity lines in a single spectrum, and possibly only ever had a few milligrams total of the sample.

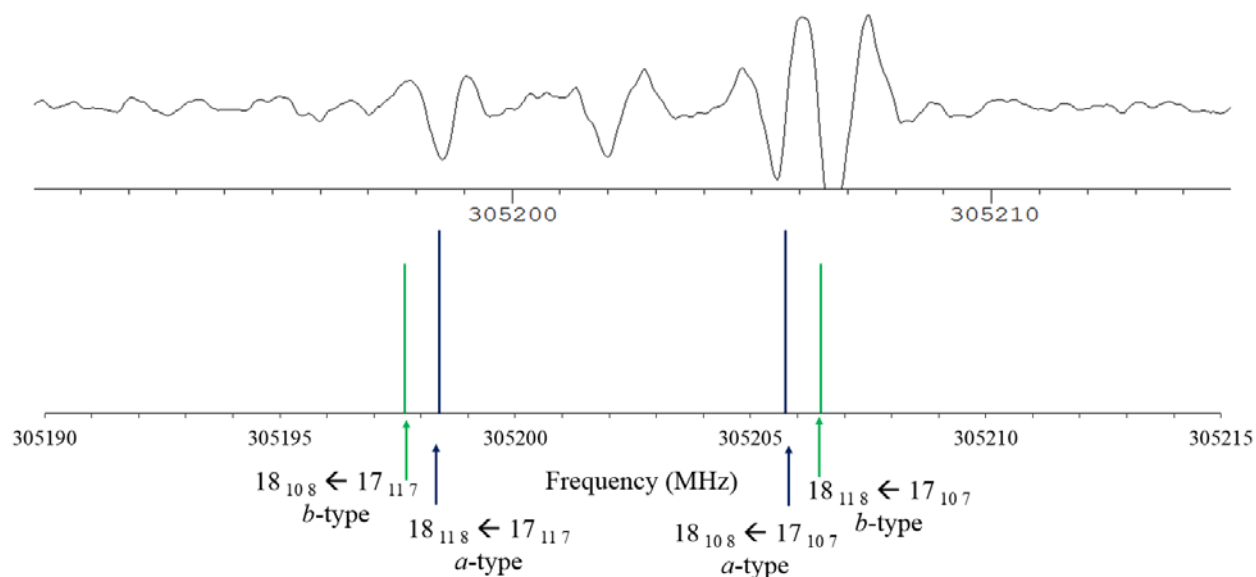


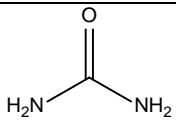
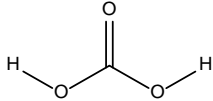
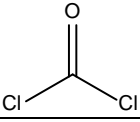
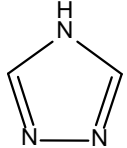
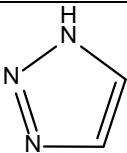
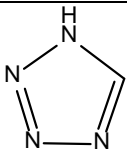
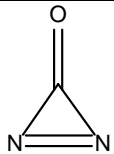
Figure 3.13 Predictions for a - and b -type R-branch transitions where degeneracy is lost, giving insight into the probable a -type dipole moment of the molecule.

Table 3.1 Spectroscopic constants for the unknown impurity

	Unidentified Impurity
<i>A</i> (MHz)	11002.5639(16)
<i>B</i> (MHz)	10428.9847(12)
<i>C</i> (MHz)	5345.37903(30)
<i>D_J</i> (kHz)	4.8080(17)
<i>D_{JK}</i> (kHz)	1.5161(45)
<i>D_K</i> (kHz)	7.8455(41)
<i>d_j</i> (kHz)	2.00747(86)
<i>d_k</i> (kHz)	5.6249(11)
<i>H_{KJ}</i> (Hz)	-0.0942(41)
<i>H_K</i> (Hz)	0.2057(43)
<i>Δ_i</i> (amu Å ²)	0.153
N lines	344
<i>Sigma</i> (MHz)	0.05549

The fit in Table 3.1 is very good, achieving a σ of 0.055 MHz while using relatively few centrifugal distortion terms. The rotational constants are determined to within a kHz. We still do not know what this molecule is, and although it may ultimately be as mundane as acetone, the rotational constants tell us enough to pique our interest. The inertial defect is a small positive number, showing planarity, and the relative magnitude of *A*, *B*, and *C* indicate a near oblate molecule. These conditions are possibly satisfied by a small ring, or perhaps a small planar carbonyl. Table 3.2 compares the experimentally determined rotational constants molecules of comparable shape and size. Experimental literature constants for the correct molecule should have constants within a MHz or two of ours, even if using a different representation or reduction. Larger molecules have smaller rotational constants, so if the molecule is a 5-membered ring it must have very few hydrogens attached, and therefore must have a large number of heteroatoms, which makes it potentially interesting. Of the molecules compared, urea is closest in rotational constants, but it is not close enough, and is known to be slightly non-planar.

Table 3.2 Rotational constants of molecules of similar size to our unknown impurity

		A (MHz)	B (MHz)	C (MHz)
Unknown Impurity	?	11002.5639(16)	10428.9847(12)	5345.37903(30)
Urea ¹⁴		11233.3431(85)	10369.3787(87)	5416.6451(85)
Carbonic Acid ¹⁵		11997.0550 (30)	11308.3803(19)	5813.8280(10)
Phosgene (³⁵ Cl ₂) ¹⁶		7918.7942(36)	3474.9594(17)	241.2064(14)
1,2,4-triazole ¹⁷		10245.14	9832.15	5015.22
1-H 1,2,3-Triazole ¹⁸		10030.62(15)	9870.95(15)	4972.98(10)
Tetrazole ¹⁹		10667.32(18)	10310.91(18)	5240.37(15)
Diazirine ²⁰		41588.(77)	8442.29(85)	7006.19(79)

Summary and Conclusions

We made numerous improvements to the spectrometer equipment, in a major renovation in 2010/2011. We have made many additional improvements since then. Particularly towards increasing the longevity of the turbomolecular pump, and towards reducing the marginal cost and labor expenditures in operating the chiller unit. Two new pieces of equipment are intended to

pyrolyze molecules to give access to new spectroscopic targets. One of these is attached to the vacuum manifold outside of the main spectrometer chamber, with the advantage of steel gas traps for trap-to-trap distillation prior to introducing the sample into the spectrometer. The second pyrolysis apparatus is a quartz sheathed heater, which is inside of our vacuum chamber. As an *in situ* heater, the advantage of this unit is our ability to monitor changes in our gaseous samples while the pyrolysis unit is in operation. In our early work towards diazirinone we have obtained an excellent fit for the spectrum of an impurity in one of our samples, but we have been unable to identify it.

References

1. Kim, Y. S.; Zhang, F.; Kaiser, R. I., Laboratory simulation of Kuiper belt object volatile ices under ionizing radiation: CO-N₂ ices as a case study. *PCCP* **2011**, *13* (35), 15766-15773.
2. de Petris, G.; Cacace, F.; Cipollini, R.; Cartoni, A.; Rosi, M.; Troiani, A., Experimental Detection of Theoretically Predicted N₂CO. *Angew. Chem. Int. Ed.* **2005**, *44* (3), 462-465.
3. Zhu, R. S.; Lin, M. C., Ab Initio Study on the Oxidation of NCN by O (3P): Prediction of the Total Rate Constant and Product Branching Ratios†. *J. Phys. Chem. A* **2007**, *111* (29), 6766-6771.
4. Moss, R. A.; Chu, G.; Sauers, R. R., Unprecedented Chemistry of an Aryloxychlorodiazirine: Generation of a Dihalodiazirine and Diazirinone. *J. Am. Chem. Soc.* **2005**, *127* (8), 2408-2409.
5. Shaffer, C. J.; Esselman, B. J.; McMahon, R. J.; Stanton, J. F.; Woods, R. C., Attempted Isolation and Characterization of Diazirinone (N₂CO). *J. Org. Chem.* **2010**, *75* (6), 1815-1821.
6. Moss, R. A.; Sauers, R. R., The generation of diazirinone: a computational study. *Tetrahedron Lett.* **2010**, *51* (25), 3266-3268.
7. Zeng, X.; Beckers, H.; Willner, H.; Stanton, J. F., Elusive Diazirinone, N₂CO. *Angew. Chem. Int. Ed.* **2011**, *50* (7), 1720-1723.

8. Zeng, X.; Beckers, H.; Willner, H.; Stanton, J. F., Fascinating Diazirinone: A Violet Gas. *Eur. J. Inorg. Chem.* **2012**, 2012 (21), 3403-3409.
9. Nolan, A. M.; Amberger, B. K.; Esselman, B. J.; Thimmakonda, V. S.; Stanton, J. F.; Woods, R. C.; McMahon, R. J., Carbonyl Diazide, OC(N₃)₂: Synthesis, Purification, and IR Spectrum. *Inorg. Chem.* **2012**, 51 (18), 9846-9851.
10. Amberger, B. K.; Esselman, B. J.; Woods, R. C.; McMahon, R. J., Millimeter-wave spectroscopy of carbonyl diazide, OC(N₃)₂. *J. Mol. Spectrosc.* **2014**, 295, 15-20.
11. Esselman, B. J.; Amberger, B. K.; Shutter, J. D.; Daane, M. A.; Stanton, J. F.; Woods, R. C.; McMahon, R. J., Rotational spectroscopy of pyridazine and its isotopologs from 235-360 GHz: Equilibrium structure and vibrational satellites. *J. Chem. Phys.* **2013**, 139, 224304 1-13.
12. Esselman, B. J. Computational and Spectroscopic Investigations of Species of Astrochemical Relevance. University of Wisconsin-Madison, Madison, Wisconsin, 2012.
13. Kisiel, Z. PROSPE: Programs for Rotational spectroscopy. <http://www.ifpan.edu.pl/~kisiel/prospe.htm>.
14. Godfrey, P. D.; Brown, R. D.; Hunter, A. N., The shape of urea. *J. Mol. Struct.* **1997**, 413-414, 405-414.
15. Mori, T.; Suma, K.; Sumiyoshi, Y.; Endo, Y., Spectroscopic detection of the most stable carbonic acid, cis-cis H₂CO₃. *J. Chem. Phys.* **2011**, 134 (4), 044319.
16. Carpenter, J. H.; Rimmer, D. F., Microwave spectrum of three isotopic species of carbonyl chloride. *Journal of the Chemical Society, Faraday Transactions 2: Molecular and Chemical Physics* **1978**, 74 (0), 466-479.
17. Bolton, K.; Brown, R. D.; Burden, F. R.; Mishra, A., The Microwave Spectrum and Structure of 1,2,4-Triazole. *J. Mol. Struct.* **1975**, 27, 261-266.
18. Stiefvater, O. L.; Jones, H.; Sheridan, J., Double-resonance -double-search assignment of the microwave spectrum of 1,2,3-triazole. *Spectrochim. Acta* **1970**, 26A, 825-833.
19. Krugh, W. D.; Gold, L. P., The Microwave Spectrum of Tetrazole. *J. Mol. Spectrosc.* **1974**, 49, 423-431.
20. Perrin, A.; Zeng, X.; Beckers, H.; Willner, H., The first high-resolution infrared study of diazirinone, N₂CO: Analysis of the Fermi-coupled v₁ and 2v₅ bands. *J. Mol. Spectrosc.* **2011**, 269 (1), 30-35.

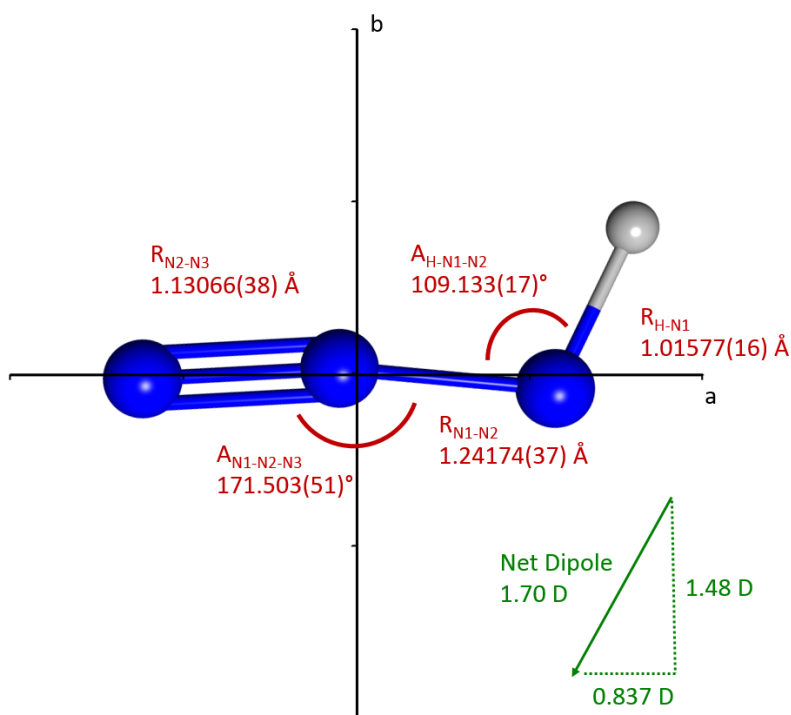
Chapter 4: Precise equilibrium structure determination of hydrazoic acid (HN_3) by millimeter-wave spectroscopy

Includes material from accepted work:

Amberger, B. K., Esselman, B. J.; Stanton, J. F.; Woods, R.C, McMahon, R. J., Journal of Chemical Physics, accepted.

Includes the work of collaborators:

Brian J. Esselman, R. Claude Woods, and Robert J. McMahon



Abstract

The millimeter-wave spectrum of hydrazoic acid (HN_3) was analyzed in the frequency region of 235–450 GHz. Transitions from a total of 14 isotopologues were observed and fit using the A-reduced or S-reduced Hamiltonian. Coupled-cluster calculations were performed to obtain a theoretical geometry, as well as rotation-vibration interaction corrections. These calculated vibration-rotation correction terms were applied to the experimental rotational constants to obtain mixed theoretical/experimental equilibrium rotational constants (A_e , B_e , and C_e). These equilibrium rotational constants were then used to obtain an equilibrium (R_e) structure using a least-squares fitting routine. The R_e structural parameters are consistent with a previously published R_s structure, largely falling within the uncertainty limits of that R_s structure. The present R_e geometric parameters of HN_3 are determined with exceptionally high accuracy, as a consequence of the large number of isotopologues measured experimentally and the sophisticated theoretical treatment (CCSD(T)/ANO2) of the vibration-rotation interactions. The R_e structure exhibits remarkable agreement with the CCSD(T)/cc-pCV5Z predicted structure, validating both the accuracy of the *ab initio* method and the claimed uncertainties of the theoretical/experimental structure determination. A manuscript describing this work has very recently been accepted for publication in the Journal of Chemical Physics. The present chapter is based largely on this manuscript, but contains some additional information that could not be included in that format.

Introduction

Hydrazoic acid (HN_3) has been of fundamental interest for more than a century. In 1890 Curtius reported this molecule as being highly toxic and explosive.¹ At the time, the nitrogen atoms of HN_3 were thought to be arranged in a three-membered ring. In 1935, Herzberg used the

overall shape of the partially resolved near-infrared overtone bands to conclude that the nitrogen backbone was linear, with the hydrogen atom bound either to the central nitrogen atom or to one of the terminal nitrogen atoms.² The H-N-N-N connectivity was firmly established by IR spectroscopy in 1940.³ The authors determined a 110.9° H-N-N angle while assuming a linear nitrogen backbone. An electron diffraction study in 1942⁴ found nitrogen-nitrogen bond lengths of 1.13 Å and 1.24 Å which were consistent with the IR work. In 1950 Amble and Dailey synthesized all four singly isotopically labeled HN_3 isotopomers and then found the corresponding values of $(B+C)$ from the $1_{10} \leftarrow 0_{00}$ pure rotational transitions.⁵ They determined a bent H-N-N angle of 112.6° and assumed a 180° N-N-N angle. The work of Amble and Daily is of particular interest because they are the only authors to observe HN^{15}NN through its direct synthesis. They heated labeled ammonium nitrate ($^{15}\text{NH}_4^{14}\text{NO}_3$) to generate labeled nitrous oxide (N_2O). This was then passed over sodium amide at 200°C to form labeled sodium azide. Fortuitously this method afforded them a mixture of labeled sodium azide that included NaN^{15}NN .

M. Winnewisser and coworkers obtained microwave and millimeter-wave spectra for H^{14}N_3 , D^{14}N_3 , H^{15}NNN and HNN^{15}N and obtained a substitution structure.⁶⁻⁹ Their work provided good values for many of the geometric parameters, but because HNNN is challenging to prepare, ambiguity remained in the position of the central nitrogen atom. B. Winnewisser used the center of mass condition to estimate the position of the central nitrogen and published an R_s structure with an N-N-N angle of 171.3° .¹⁰ Theoretical calculations have consistently supported this bent structure.¹¹⁻¹³

Evers *et al.* obtained the crystal structure of hydrazoic acid in 2011.¹⁴ Fundamental interest in the molecular geometry of HN_3 continues with Toyota *et al.* discussing the likely origins of the N-N-N angle as recently as 2013.¹³

In the 1980's and 1990's the rovibrational spectra for HN_3 and DN_3 were thoroughly studied by high resolution FTIR but the structure was not significantly refined.¹⁵⁻²⁷ This FTIR work will be discussed in greater detail in chapter 5. Of importance to our structure determination, there is a known centrifugal distortion perturbation between the higher K states of the ground vibrational state and the first excited vibrational state of hydrazoic acid. This perturbation exists for deuterated hydrazoic acid as well, but is not as severe. In the current analysis, we used only ground-state transitions that are unperturbed or only slightly perturbed; this allows the use of single-state fits. We excluded significantly perturbed lines even where they are well understood (for H^{14}N_3 and D^{14}N_3) for better continuity with our fits for isotopologues where analysis of these perturbations would be completely impractical.

Precise structural knowledge of hydrazoic acid is valuable in further understanding the family of tetratomic, 16 valence electron molecules, which includes HNCO , its isomers, and their heavier-element analogues. In this family, molecular geometries range from linear through quasilinear to manifestly non-linear.²⁸⁻³⁰ In comparative studies probing the origins of these geometries, the relative electronegativity of atoms in the backbone is an important variable. Hydrazoic acid is unique in this family in that all non-hydrogen atoms are identical. For this reason, HN_3 serves as a useful reference for untangling the subtle contributions which give rise to varying geometries in this family.

Hydrazoic acid was first observed in our spectrometer as an impurity in our samples of carbonyl diazide. In fact, in many of our carbonyl diazide spectra HN_3 transitions were the strongest overall lines (Figure 4.1).

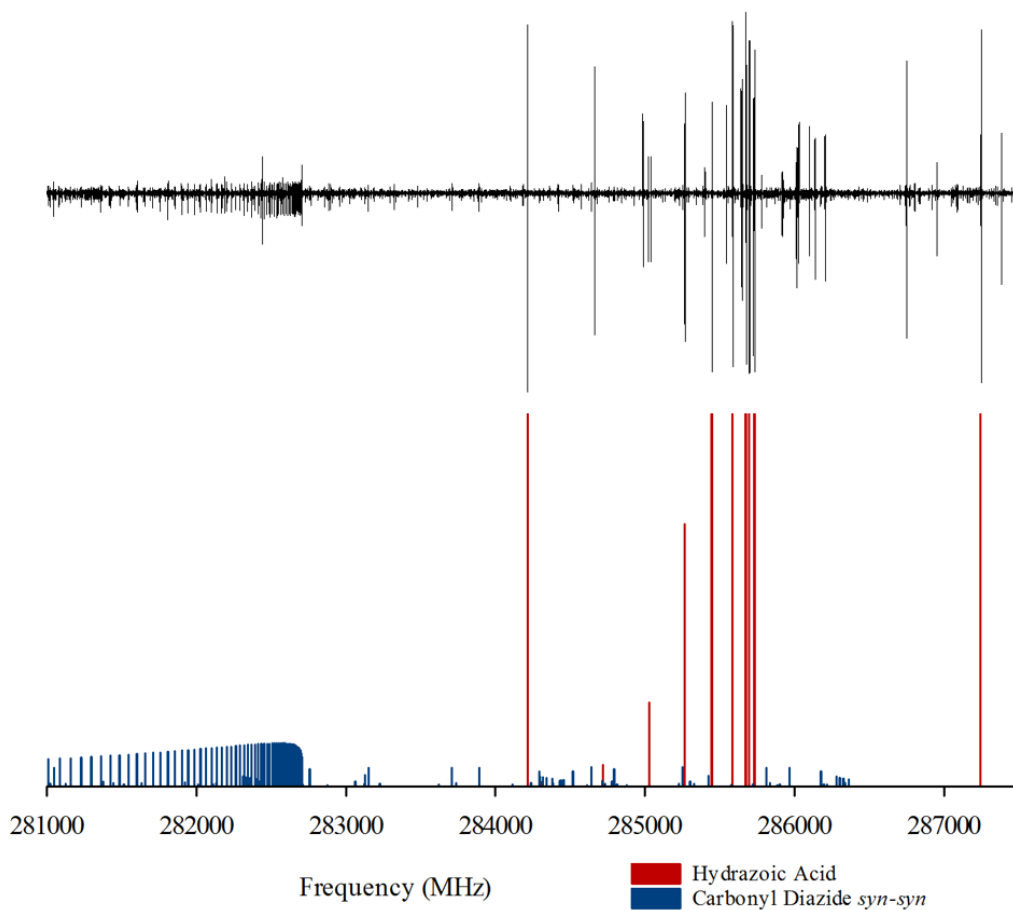


Figure 4.1 One of our spectra of carbonyl diazide in which hydrazoic acid is a major impurity. The spectrum clearly shows the $K_{prolate} = 15 \leftarrow 14$ *b*-type Q-branch of the *syn-syn* conformer of carbonyl diazide and the $J = 12 \leftarrow 11$ *a*-type R-branch of hydrazoic acid.

In our efforts to untangle the carbonyl diazide spectra we chose to take a ‘background’ spectrum of HN_3 . In this spectrum we were able to quickly identify all singly- ^{15}N substituted isotopologues at natural abundance. To our knowledge, HN^{15}NN had not been studied by rotational spectroscopy since 1950, and at that time only one transition was measured.⁵ The

difficulty in synthesizing this HN^{15}NN is why the best microwave structure to date¹⁰ relied on the center-of-mass condition to estimate the position of the central nitrogen. We found that a few simple variations on our synthesis, combined with the ability of our spectrometer to detect signals from isotopologues with a single ^{15}N at natural abundance gave us access to a total of 14 isotopologues. Six of the studied isotopologues contain a ^{15}N label on the central nitrogen, which eliminates most ambiguity about its location within the molecule.

The small size of hydrazoic acid allows for extremely high level computational treatment. The large number of observed isotopologues compared to the number of geometric parameters allows for highly redundant determination of structure. Hydrazoic acid thus presented an excellent opportunity for us to benchmark the level of agreement between pure theoretical, pure experimental, and mixed experimental/ theoretical structure determination methods.

Computational methods

A CCSD(T)/ANO2 optimized geometry was obtained and used in subsequent harmonic and anharmonic frequency calculations to calculate cubic and quartic centrifugal distortion constants and estimate the vibration-rotation interaction parameters for each isotopologue. An additional magnetic property calculation was performed to estimate the electron mass contributions to rotational constants. The vibration-rotation interaction constants (α_i 's) were used for the equilibrium structure determination.

All geometry optimizations and frequency calculations were carried out in CFOUR 2.0.³¹ CCSD(T)/ANO2³² optimized geometries were obtained using analytic gradients³³⁻³⁴ with the frozen core approximation. To determine the vibration-rotation interaction constants (α_i 's), the

cubic force constants were calculated by numerical differentiation of the analytic second derivatives at displaced points following the approach of Stanton *et al.*³⁵⁻³⁶ The VPT2 anharmonic frequency output allowed for a convenient calculation of the quartic distortion constants and the vibration-rotation interaction for each of the isotopologues. A very high level calculation of the equilibrium geometry was also completed at the all-electron CCSD(T) level with the cc-pCV5Z basis set by J. Stanton.

Synthesis

The synthetic procedure we use for generating HN_3 was modified from literature procedure in which sodium azide (NaN_3) was combined with acidified water.^{5, 8} In our case, sodium azide was dropped into an aqueous solution of phosphoric acid. The aqueous phosphoric acid was generated by adding phosphorous pentoxide (P_2O_5) to DI water. This source of phosphoric acid was chosen because it is easy to generate D_3PO_4 in D_2O (and thereby DN_3) analogously. The sodium azide can be either NaN_3 or Na^{15}NNN , giving access to many isotopologues. The phosphoric acid is placed in a multi-neck round-bottom flask and attached to the vacuum manifold.

The side-neck is used to attach a curved test tube containing the sodium azide (see Figure 4.2).

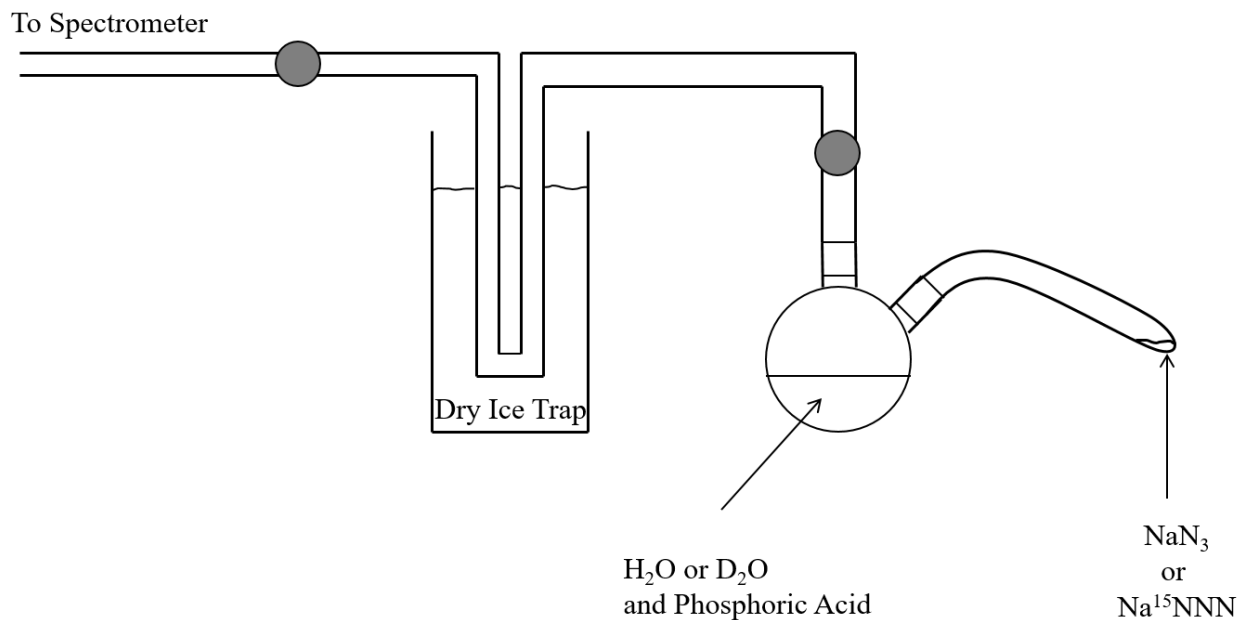


Figure 4.2 Synthetic apparatus for the generation of hydrazoic acid.

The apparatus is connected to the spectrometer's vacuum system via a dry-ice/ acetone trap. After evacuation of the apparatus, the tube containing the sodium azide is rotated 180° which drops the sodium azide powder into the acidic solution. For the next minute, all vapors (primarily H_2O and NH_3) bubbling out of the flask are caught in the dry ice temperature trap. The valves to the thick glass trap are then closed. It is observed that the water vapors remain condensed, and the hydrazoic acid has a moderate apparent vapor pressure of ~ 300 mTorr. At this pressure, the sample can easily be leaked into the spectrometer chamber until the desired pressure is achieved. We typically add ~ 5 mTorr of sample to our chamber. We have not attempted a flow system with HN_3 . The observed spectra appear to be pure. We have not attempted to measure a yield of this synthesis, but a typical synthetic batch (15 ml water, 0.5g P_2O_5 , and 0.1g NaN_3) provides enough

sample for several days of spectroscopy. We have stored hydrazoic acid in the glass trap at dry ice temperatures for a few weeks at a time without noticeable decomposition. One interesting observation about the behavior of HN_3 vapor in our system is that it appears to be adsorbed on something in the chamber. Immediately after addition into the chamber, the measured pressure will decrease by a few mTorr, which does not happen for most other gasses. Eventually (after 5-10 minutes) the rate adsorption drops below the background leak-rate of our spectrometer chamber and the overall pressure in the chamber slowly rises, as it does with most other samples. We have found that the signal strength of HN_3 has a half-life of ~ 90 minutes. To support the hypothesis that this pressure drop is the result of adsorption, when we evacuate the chamber and then isolate it from the vacuum pumps, HN_3 peaks slowly grow in. HN_3 has been found to remain an impurity in our spectrometer for several weeks after it is introduced. In one spectrum of H^{14}N_3 we have significant amounts of signal from isotopologues containing deuterium and ^{15}N at much greater than natural abundance— those isotopologues having been introduced to the chamber in previous weeks. To mitigate the signal loss due to this adsorption, we refresh our sample every hour. Glow discharges using oxygen gas have been used to clean residual HN_3 from the chamber with moderate success.

Increase in Spectrometer Range

During the course of our studies of HN_3 we developed two methods of extending the range of our spectrometer above 360 GHz. Our ordinary frequency generation involves the use of an amplification multiplication chain to multiply up the frequency-modulated output of our Agilent frequency generator by $18\times$. Because the maximum frequency output of our signal generator is

20 GHz, we assumed that our spectrometer had a hard upper limit of 360 GHz. There is no hard bottom limit to our range, but at frequencies below the nominal range of our equipment (270-360 GHz), signal strength drops off quickly, becoming unusable even for strong lines by ~230 GHz.

We have known for several years that spurious harmonics exist at the low end of our spectrum (below ~260 GHz target frequency). A common observation is phantom lines in our spectra at exactly 9/11ths of the actual transition frequency. For example, the $11_{11} \leftarrow 12_{012}$ transition of HN_3 occurs at 304728.3 MHz, but there is also a strong apparent absorption at “249323.2 MHz”. This phantom line results from a spurious harmonic in the up-multiplication of our signal frequency, which occurs while the software continues to assume an 18 \times multiplication.

We originally treated these phantom lines as nuisances, but in the last year we discovered that some of these lines are exactly 3/5ths of the actual transition frequencies. This is a large enough factor such that signals observed at the low end of our spectra may actually belong to signals above our previous hard ceiling of 360 GHz. For example, a signal which our spectrometer reports at 221176.4 MHz is actually the $16_{016} \leftarrow 15_{015}$ transition of HNN^{15}N at 368627.6 MHz (shown in Figure 4.3). An extremely weak signal observed at 276419.2 MHz is actually the $20_{20} \leftarrow 19_{019}$ transition for HNN^{15}N at 460698.7 MHz. Effectively a fraction of the power from our signal generator is being multiplied by 30 \times instead of 18 \times in these cases. This 30 \times only works well for strong transitions. We can use this technique to extend our frequency range by ~ 100 GHz in the case of strong transitions. There are several intensity dips throughout this range, with the strength of the 30 \times multiplication apparently oscillating somewhat. Figure 4.4 shows the intensity of a series of $K_{prolate} = 0$ lines for HNN^{15}N measured using this 30 \times harmonic. The line intensities

are normalized for predicted line intensity and compared against the strength of lines measured using our conventional 18× harmonic.

Recently the University of Wisconsin Chemistry Department has purchased a signal generator for the physical chemistry teaching laboratory that can operate as high as 40 GHz. We have borrowed this instrument and used it in conjunction with our amplification-multiplication chain to reach frequencies higher than 360 GHz. We have found that this method gives excellent spectra through 365 GHz, but that the signal strength drops off considerably by 370 GHz. Figure 4.3 shows two transitions above 360 GHz belonging to HNN^{15}N measured using the 30× harmonic, or by using the 18× harmonic with the borrowed frequency generator. The misshapen sidebands in the first trace are a clear hint that it was obtained using a harmonic multiplication other than the intended 18×.

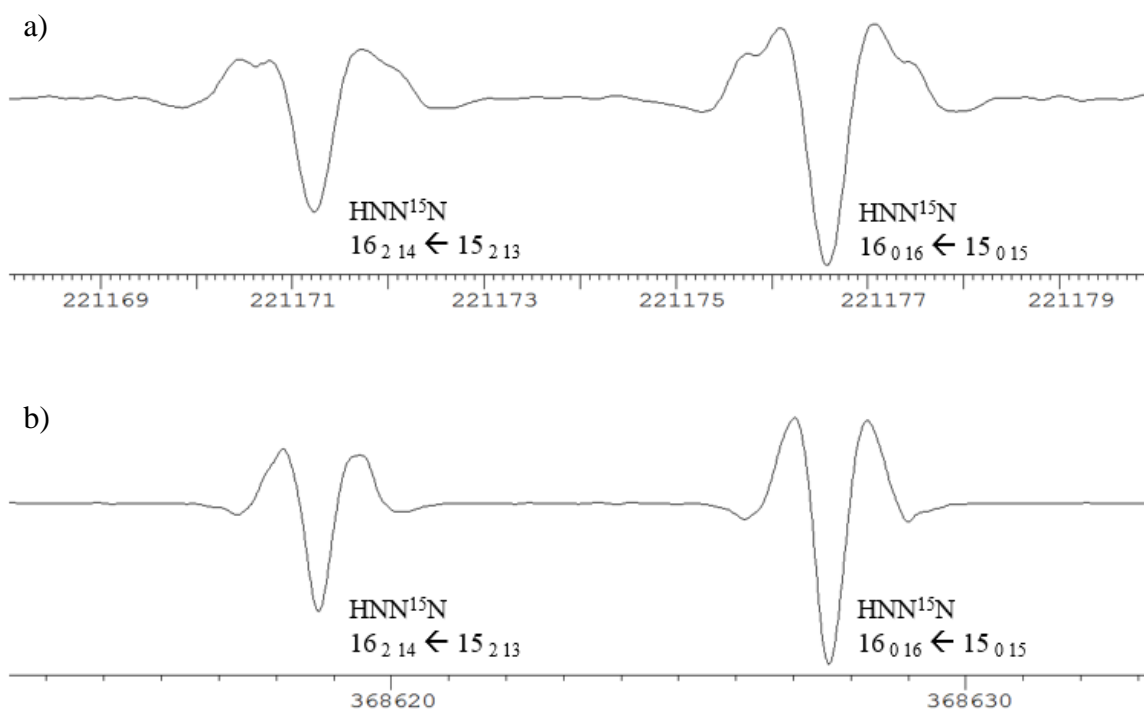


Figure 4.3 Two scans showing the transitions $16_{2\ 14} \leftarrow 15_{2\ 13}$ and $16_{0\ 16} \leftarrow 15_{0\ 15}$ of HNN^{15}N at using the intended $18\times$ harmonic (b) of the amplification multiplication chain, and the incidental $30\times$ harmonic (a). Because our software assumes an $18\times$ multiplication, transitions observed using the $30\times$ harmonic appear at $3/5$ ths of their actual frequency with misshapen sidebands.

A comparison of signal strengths of 11 lines belonging to $K_{prolate} = 0$ a -type R-branch transitions of HNN^{15}N is shown in Figure 4.4. It can be seen that transitions observed by utilizing the $30\times$ harmonic are substantially weaker than those observed with the $18\times$ harmonic. Ultimately the borrowed signal generator gives reasonably strong spectra up to ~ 370 GHz, while taking advantage of the spurious $30\times$ harmonic gives access to the wider range of frequencies at lower intensities.

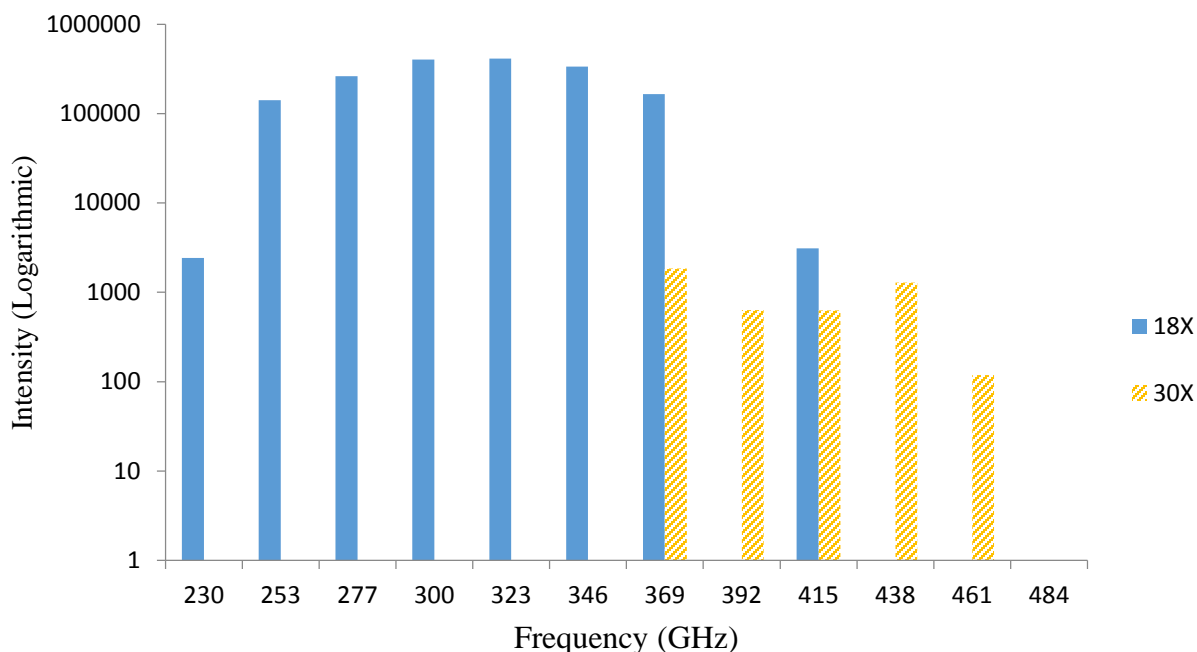


Figure 4.4 Line intensities of transitions belonging to $K_{prolate} = 0$ for HNN^{15}N on a logarithmic scale. The solid blue bars are intensities measured using the $18\times$ multiplication on the wider frequency range generator tuned above 20 GHz, utilizing the intended $18\times$ multiplier. The dashed orange bars are intensities of lines observed using the spurious $30\times$ harmonic.

Analysis of Rotational Spectra

The dipole in HN_3 is roughly parallel to the H-N bond, and thus not along any of the principal axes (Figure 4.13), resulting in strong a -type and b -type transitions ($\mu_a = 0.837 \text{ D}$ $\mu_b = 1.48 \text{ D}$).^{7,37} The predominant features in all of the spectra for hydrazoic acid are a -type R-branches which follow a typical pattern for near-linear molecules. For a series with a given $J+1 \leftarrow J$, transitions progress towards lower frequency with increasing $K_{prolate}$ value. The $K_{prolate} = 1$ lines are widely split by several gigahertz, the $K_{prolate} = 2$ lines are split by tens or hundreds of megahertz, and the $K_{prolate} = 3$ lines are typically split by less than a megahertz. Transitions for $K_{prolate} = 4$ and higher appear degenerate. The pattern of lines in the $J = 12 \leftarrow 11$ R-branch of HN_3 is shown in

Figure 4.5. The transition frequencies for the higher $K_{prolate}$ values are actually perturbed from what is shown. These were excluded from the fit and will be discussed in Chapter 5. For DN_3 , the pattern in a -type R-branch transitions is roughly the same as for HN_3 , but there is more of a ‘turn around’ in the series, with the $K_{prolate} = 0$ line generally appearing at lower frequencies than the $K_{prolate} = 2$ and $K_{prolate} = 2$ and $K_{prolate} = 3$ lines.

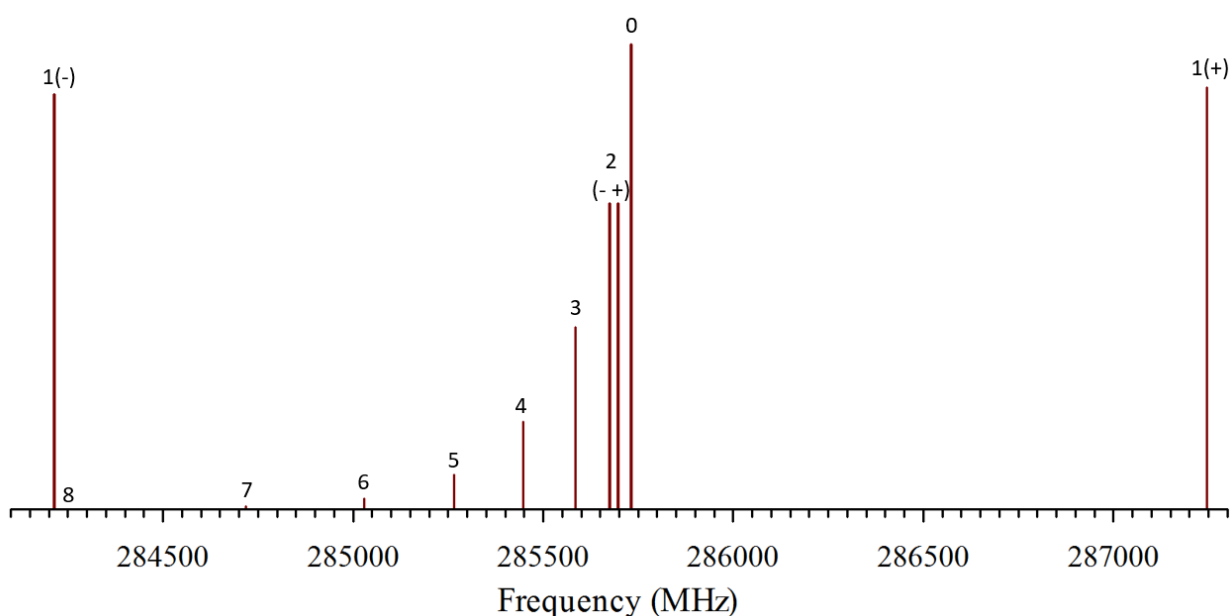


Figure 4.5 The pattern of expected transitions within an a -type R-branch for HN_3 . The branch shown belongs to the $J = 12 \leftarrow 11$ series. The labels are the $K_{prolate}$ values for the transitions. Note that $K_{prolate}$ values above $K = 6$ are actually quite perturbed.

For b -type transitions, HN_3 has a series of P-branch $K_{prolate} = 1 \leftarrow 0$ transitions which run through our spectrometer range from high to low frequency ($J_{upper} = 9-13$). Outside of our frequency range, the $K_{prolate} = 0$ states surpass the nearby $K_{prolate} 0 \leftarrow 1$ transitions which progress to high frequency and re-enter our range ($J_{upper} = 33-36$). A stick spectrum of the most intense features is shown in Figure 4.6. There is also a weak series of P-branch $K_{prolate} = 2 \leftarrow 1$ transitions

($J_{upper} = 52-55$). Finding these transitions proved critical in determining A and D_K (or A and Δ_K) independently of one another.

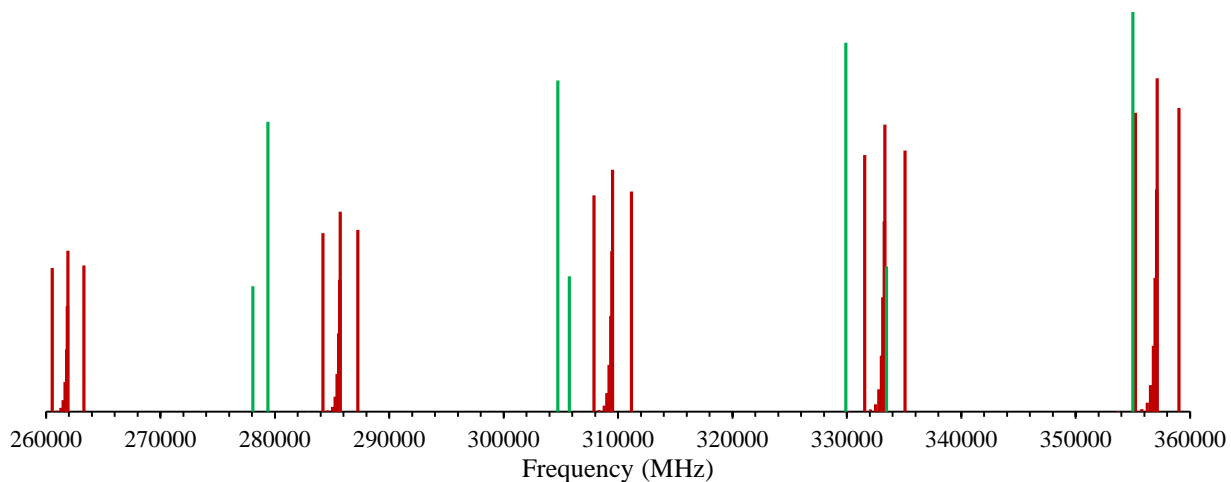


Figure 4.6 A stick spectrum describing the most intense features in the HN_3 rotational spectrum between 260 and 360 GHz.

HN_3 and DN_3 have somewhat dissimilar b -type spectra in our frequency range. This is the result of the hydrogen atom being the only mass appreciably off of the a -axis resulting in a substantial difference in the A constant between the two isotopologues (611 GHz for HN_3 and 345 GHz for DN_3). Hence, we observed more b -type transitions in the frequency range of our spectrometer for DN_3 than for HN_3 (Between 270 and 360 GHz there are 9 easily observed unperturbed b -type lines for HN_3 and 28 for DN_3). Most notably, a b -type Q-branch occurs (starting at 334 GHz) in our spectral range for DN_3 , while the same branch is too high in frequency (predicted to start at 599 GHz) for us to observe for HN_3 . A stick spectrum for the important features of the DN_3 spectrum is shown in Figure 4.7.

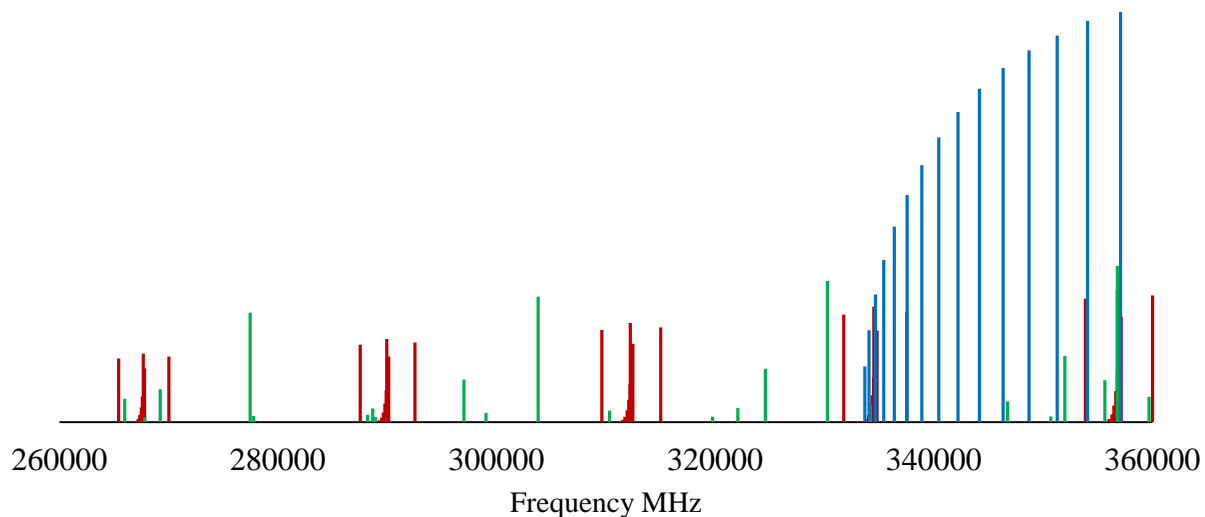


Figure 4.7 A stick spectrum describing the most intense features in the DN_3 rotational spectrum between 260 and 360 GHz. Red lines are a -type R-branch transitions, green lines are b -type R or P-branches, and blue lines are the b -type Q-branch.

We fit our spectral data using both the A-reduced and the S-reduced Hamiltonians in the Γ representation for each isotopologues. The choice of A- or S-reduction did not affect the quality of the fits; the spectroscopic constants obtained by S-reduction, when converted into the A-reduction,³⁸ were nearly identical to those obtained in our fit using the A-reduced Hamiltonian. As further proof of the quality of the A-reduction or S-reduction least squares fits, the rotational constants ($B_0^{(A)}$ or $B_0^{(S)}$) were converted into nearly identical determinable constants (B_0'') using the experimentally determined quartic distortion constants. The results of these checks for the constants of H^{14}N_3 are shown in Table 4.1.

Table 4.1 Checks to make sure that the A- and S- reduced fits are both accurate. $B_0^{(S)}$ values can be converted to $B_0^{(A)}$ values nearly identical to the experimental $B_0^{(A)}$ values. Additionally, $B_0^{(A)}$ and $B_0^{(S)}$ values can both be converted to nearly identical B_0'' values.

H ¹⁴ N ₃			A (MHz)	B (MHz)	C (MHz)
S-reduced constants		$(B_0^{(S)})$	611034.135	12034.1759	11781.4790
experimental					
A-reduced constants		$(B_0^{(A)})$	611034.132	12034.9838	11780.6713
experimental					
		$B_0^{(A)}$ converted from $B_0^{(S)}$	611034.135	12034.9829	11780.6722
		B_0'' converted from $B_0^{(A)}$	611034.142	12034.9836	11782.2871
		B_0'' converted from $B_0^{(S)}$	611034.145	12034.9836	11782.2871

For higher values of $K_{prolate}$, the energy levels are perturbed by a centrifugal distortion interaction with the first vibrationally-excited state.²⁰⁻²¹ For HN₃ we found evidence of slight perturbation in the $K_{prolate} = 4$ transitions, with the perturbation becoming progressively larger at higher $K_{prolate}$ values. Empirically, we found that including L_{KKJ} in our fits compensates for much of the perturbation in relatively low K states, and allows us to include a -type transitions up to $K_{prolate} = 5$ in single-state fits for HN₃ with satisfactory values of sigma, although the values of L_{KKJ} are unphysically large. For DN₃, we were able to include transitions up to $K_{prolate} = 7$ in our fits.

Transitions with $K_{prolate} = 1 \leftarrow 2$ are required in order to independently determine A and D_K (or A and Δ_K). More of these transitions occur in our frequency region for DN₃ than for HN₃, and they have greater intensity in DN₃. We were unable to positively identify any $K_{prolate} = 1 \leftarrow 2$ transitions in the four HN₃ isotopologues requiring a ¹⁵N atom at natural abundance. In our fits for HN¹⁵NN, H¹⁵N¹⁵NN, H¹⁵NN¹⁵N, and HN¹⁵N¹⁵N, we fixed D_K to reasonable values estimated based on ratios between the experimentally determined values of D_K for the other ten isotopologues.

Our spectroscopic constants from the fits for HN_3 and DN_3 are presented in Table 4.2 and Table 4.3, alongside our CCSD(T)/ANO2 and CCSD(T)cc-pCV5Z values for the rotational constants and quartic centrifugal distortion terms. In these tables, our data are presented in the A-reduction for easier comparison to previously reported values. Previously reported values for the rotational constants, determined by either microwave/millimeter-wave spectroscopy⁷⁻⁸ or far IR spectroscopy¹⁸⁻¹⁹ are presented side-by-side with our values. Because independent determination of A and Δ_K is not possible without adequate diversity of observed b -type transitions, the value of $A-\Delta_K$ is also presented in these tables. The apparent discrepancy between our A value for HN_3 in Table 4.2 and A from ref 7 is largely the result of a fixed value for Δ_K , as the values of $A-\Delta_K$ match well. Discrepancies in the higher order distortion terms are likely due, in part, to different subsets of these terms being used. Our choice of higher order distortion terms was based on which ones were beneficial to the fit and were determined to a value greater than their standard error for all isotopologues. With these caveats in mind, the general agreement is very good between the current work and previous works. The rotational constants determined at the CCSD(T)cc-pCVZ level were notably closer to our experimentally determined constants than were the CCSD(T)/ANO2 values. The 4th order centrifugal distortion constants determined by the CCSD(T)/ANO2 calculation were in good enough agreement with experimental values to be helpful in our assignments.

Table 4.2 Rotational constants for HN_3 from *ab initio* calculations, experimental spectroscopic data, and previous literature.

H^{14}N_3	CCSD(T)/ANO2 ^a	CCSD(T)/cc-pCV5Z ^a	This Work Millimeter-wave	Bendtsen & Nicolaisen Far-IR ¹⁸	Bendtsen & Winnewisser Microwave/Millimeter ⁷
A_0 (MHz)	605073.	610794.	611034.132(29)	611026.8(21)	610996.2(60)
B_0 (MHz)	11989.	12054.	12034.9838(62)	12034.78(27)	12034.1465(50)
C_0 (MHz)	11736.	11800.	11780.6713(66)	11780.49(27)	11781.4512(50)
Δ_J (kHz)	4.754		4.9174(10)	5.01(15)	4.673(35)
Δ_{JK} (kHz)	765.8		797.98(15)	789.1(27)	791.1858(11)
Δ_K (kHz)	217900		267559.(27)	268464(180)	[230000] ³⁹
δ_J (kHz)	0.07806		0.09118(22)	0.0809(90)	0.0888(27)
δ_K (kHz)	313.8		403.9(31)	104.9(90)	[0]
Φ_J (Hz)			[0]	0.006(45)	0.088(36)
Φ_{JK} (Hz)			1.19(10)	4.49(12)	40.6(8.6)
Φ_{KJ} (Hz)			255.(14)	-1199.(60)	-0.001210(35)
Φ_K (Hz)			[0]	383734.(6000)	[0]
L_{KKJ} (mHz)			-40010.(400)	[0]	[0]
Δ_i ($\text{u}\text{\AA}^2$)	0.0752	0.0743	0.079415223	0.079354396	0.073599658
$A-\Delta_K$ (MHz)	604855.		610766.6	610758.3	610764.2

^a The B_e values from the CCSD(T)/ANO2 and CCSD(T)/cc-pCV5Z calculations have been converted to B_0 values from the CCSD(T)/ANO2 vibration rotation corrections provided by the anharmonic frequency calculation.

Table 4.3 Rotational constants for DN₃ acid from *ab initio* calculations, experimental spectroscopic data, and previous literature.

D¹⁴N₃	CCSD(T)/ANO2^a	CCSD(T)/cc-pCV5Z^a	This Work Millimeter-Wave	Bendtsen & Nicolaisen Far IR¹⁹	Bendtsen & Winnewisser Microwave/ Millimeter⁸
<i>A</i>₀ (MHz)	340873.	344046.	344746.613(17)	344724.8(15)	344746.589(64)
<i>B</i>₀ (MHz)	11314.	11370.	11350.94041(96)	11351.55(24)	11350.983(16)
<i>C</i>₀ (MHz)	10927.	10984.	10964.82571(45)	10965.45(24)	10964.755(15)
Δ_J (kHz)	4.135		4.31494(72)	4.89(21)	4.281(16)
Δ_{JK} (kHz)	466.7		446.084(42)	435.9(21)	444.51(44)
Δ_K (kHz)	56910		91942.9(42)	91227.(30)	92242.(33)
δ_J (kHz)	0.1511		0.172965(33)	0.171(15)	0.1864(41)
δ_K (kHz)	263.9		338.82(28)	318.(12)	365.1(77)
Φ_J (Hz)			[0]	0.060(60)	[0]
Φ_{JK} (Hz)			1.248(19)	2.7(1.2)	-3.4(1.1)
Φ_{KJ} (Hz)			-213.7(26)	-606.(18)	-0.000308(21)
Φ_K (Hz)			[0]	86040.(300)	[.059] ⁴⁰
<i>L</i>_{KKJ} (mHz)			-3516.(42)	[0]	[0]
Δ_i (uÅ²)	0.0980	0.0969	0.1019	0.1016	0.1024
<i>A</i>-Δ_K (MHz)	340816.		344654.7	344633.6	344654.3

^a The B_e values of the rotational constants from the CCSD(T)/ ANO2 and CCSD(T)/cc-pCV5Z calculations have been converted to B_0 values using the CCSD(T)/ ANO2 vibration-rotation interactions from the anharmonic frequency calculation.

The ^{15}N -containing isotopologues exhibit spectra very similar to those for H^{14}N_3 and D^{14}N_3 . Transitions for the four synthetically ^{15}N -enriched species (H^{15}NNN , HNN^{15}N , D^{15}NNN , and DNN^{15}N) were observed at comparable intensity to their parent molecules. The characteristic *a*-type R-branches for these isotopologues were set several GHz away from the lighter all- ^{14}N isotopologues. Eight additional isotopologues were studied which contained a ^{15}N at natural abundance. Although line intensities were more than two orders of magnitude weaker than their lighter parent species, transitions were intense enough to observe $K_{\text{prolate}} = 0$ through $K_{\text{prolate}} = 5$ and most of the *b*-type features.

Because of the proximity of the center nitrogen atom to the center of mass, transitions for the six observed isotopologues with a label on the central nitrogen atom appeared as satellites to the corresponding transitions of the parent isotopologues. Because of this similarity of the six center-labeled isotopologues to the known spectra of their parent isotopologues, Loomis-Wood type plots proved very useful in assigning their spectra. Figure 4.8 shows a Loomis-Wood plot centered on the $K_{\text{prolate}} = 1(-)$ lines for HNN^{15}N . Each of these transitions shows a distinct satellite transition to lower frequency, which belongs to the $K_{\text{prolate}} = 1(-)$ transition for $\text{HN}^{15}\text{N}^{15}\text{N}$.

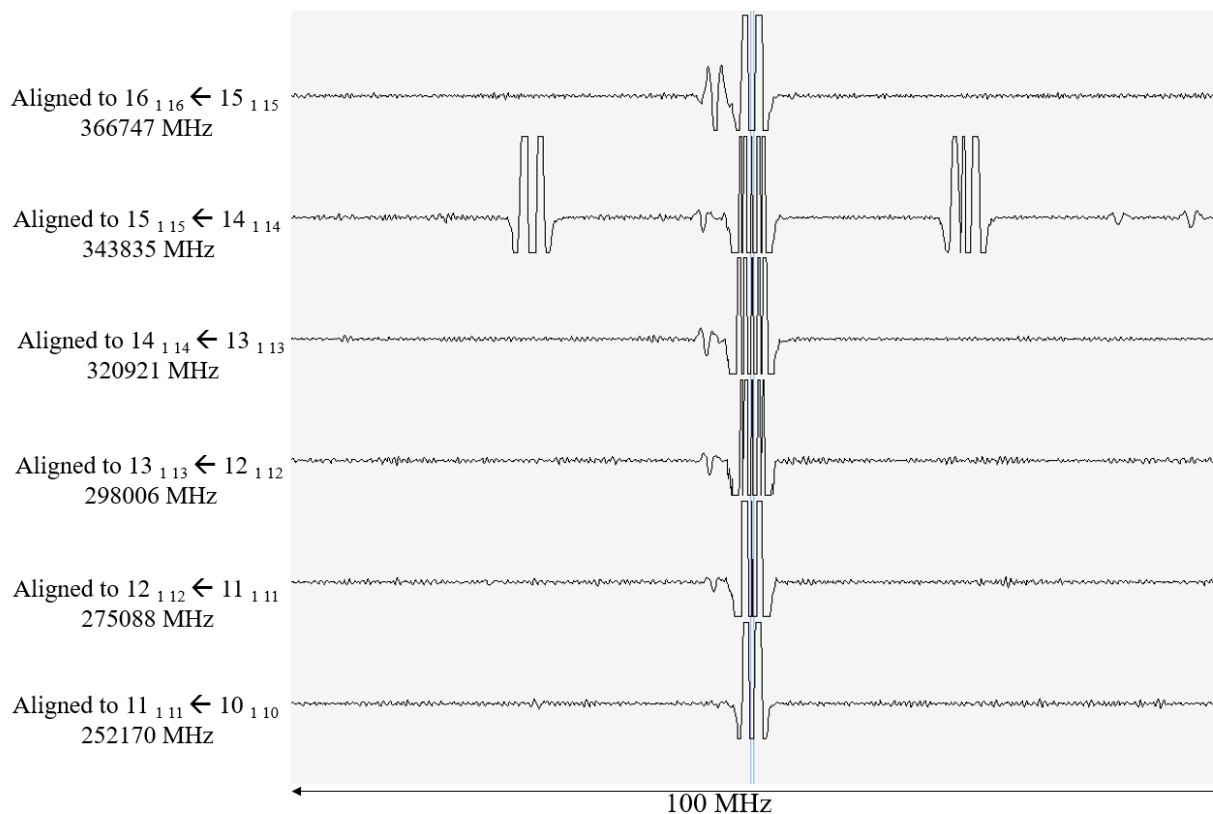


Figure 4.8 A Loomis-Wood plot centered on the $K_{prolate} = 1(-)$ transitions of HNN^{15}N . The small satellite transitions at ~ 5 MHz lower frequency are the analogous transitions for $\text{HN}^{15}\text{N}^{15}\text{N}$.

In the case of $\text{HN}^{15}\text{N}^{15}\text{N}$, transitions were sometimes too close to the significantly stronger transitions of HNN^{15}N to be observed or measured. At first our inability to find these lines was mystifying, but eventually we tried significantly reducing the size of our frequency modulation to pull the side-bands closer together, allowing us to find some of the $\text{HN}^{15}\text{N}^{15}\text{N}$ transitions as minor shoulders in the signals from the HNN^{15}N lines. The $K_{prolate} = 4$, $K_{prolate} = 5$, and $K_{prolate} = 1(+)$ transitions for $\text{HN}^{15}\text{N}^{15}\text{N}$ were entirely obscured by the HNN^{15}N transitions, regardless of the frequency modulation we chose. As a result, our set of measured transitions for $\text{HN}^{15}\text{N}^{15}\text{N}$ is the least complete, so we chose to fix the value of L_{KKJ} in the least-squares fitting. The returned values of H_{JK} and H_{KJ} do not closely match the values determined for the other HN_3 isotopologues. The rest of the fit parameters for $\text{HN}^{15}\text{N}^{15}\text{N}$ match nicely with expected values. Importantly, the

determinable constants (B'') and inertial defects for $\text{HN}^{15}\text{N}^{15}\text{N}$ with and without corrections for vibration-rotation interactions and electron mass were consistent with the other 13 isotopologues (see Table 4.6). The fits for the HN_3 isotopologues are presented in Table 4.4. The fits for the DN_3 isotopologues are presented in Table 4.5. The fits are presented in S I' reduction, as is more appropriate for a near-prolate molecule. It can be seen in Table 4.4 that the rotational constants for HNN^{15}N and $\text{HN}^{15}\text{N}^{15}\text{N}$ are very similar, which explains why their transitions are often so close to one another.

Table 4.4 Spectroscopic parameters for isotopologues of HN_3 in the S-reduced Hamiltonian Γ representation. The derived determinable constants (A_0'' , B_0'' , and C_0'') are also shown.

	HN_3	H^{15}NNN	HN^{15}NN	HNN^{15}N	$\text{H}^{15}\text{N}^{15}\text{NN}$	$\text{H}^{15}\text{NN}^{15}\text{N}$	$\text{HN}^{15}\text{N}^{15}\text{N}$
$A_0^{(S)}$ (MHz)	611034.135(29)	605576.892(35)	610032.993(90)	610977.569(30)	604507.434(46)	605510.183(32)	609961.086(60)
$B_0^{(S)}$ (MHz)	12034.17591(56)	11667.54336(74)	12033.3438(25)	11641.77520(65)	11665.5799(14)	11282.35889(93)	11641.8807(22)
$C_0^{(S)}$ (MHz)	11781.47899(83)	11427.8561(10)	11780.2941(24)	11405.07997(91)	11425.5693(19)	11058.0384(12)	11404.8190(32)
D_J (kHz)	4.8749(11)	4.6228(13)	4.8728(27)	4.5372(12)	4.6208(38)	4.3057(22)	4.5393(51)
D_{JK} (kHz)	798.23(15)	769.00(17)	796.07(20)	752.43(15)	765.97(29)	724.80(20)	751.93(68)
D_K (kHz)	267561.(27)	263929.(34)	[265241]	268092.(27)	[266172]	[263987]	[261923]
d_1 (kHz)	-0.09120(22)	-0.08397(26)	-0.0874(35)	-0.08247(23)	-0.08405(79)	-0.07473(49)	-0.0768(20)
d_2 (kHz)	-0.02127(16)	-0.01893(18)	-0.02351(99)	-0.01893(17)	-0.0232(11)	-0.01829(85)	-0.0238(15)
H_{JK} (Hz)	0.88(10)	0.64(11)	0.77(31)	0.73(11)	0.73(40)	0.75(27)	5.5(14)
H_{KJ} (Hz)	256.(14)	348.(16)	320.(18)	226.(14)	363.(25)	349.(16)	106.(37)
L_{KKJ} (mHz)	-40010.(399)	-35790.(439)	-43930.(501)	-39040.(388)	-38040.(662)	-35580.(462)	[-38040]
Δ_I ($\text{u}\text{\AA}^2$)	0.073655	0.073944	0.073708	0.073762	0.0740283	0.074040	0.073790
N_{lines}	78	84	49	88	42	56	32
σ_{fit} (MHz)	0.032213	0.040708	0.029478	0.036615	0.036002	0.030417	0.043468
A_0'' (MHz)	611034.145	605576.901	610033.003	610977.578	604507.443	605510.192	609961.095
B_0'' (MHz)	12034.98362	11668.32136	12034.14935	11642.53646	11666.35485	11283.09208	11642.64146
C_0'' (MHz)	11782.28707	11428.63444	11781.09999	11405.84156	11426.34459	11058.77189	11405.58007

Table 4.5 Spectroscopic parameters for isotopologues of DN₃ in the S-reduced Hamiltonian I' representation. The derived determinable constants (A_0'' , B_0'' , and C_0'') are also shown.

	DN₃	D¹⁵NNN	DN¹⁵NN	DNN¹⁵N	D¹⁵N¹⁵NN	D¹⁵NN¹⁵N	DN¹⁵N¹⁵N
$A_0^{(S)}$ (MHz)	344746.613(17)	340247.304(14)	344618.810(52)	344727.736(17)	340093.976(29)	340233.190(15)	344602.430(35)
$B_0^{(S)}$ (MHz)	11350.26267(51)	11045.06625(59)	11347.8911(15)	10979.46501(61)	11041.4039(13)	10679.69072(70)	10978.4955(13)
$C_0^{(S)}$ (MHz)	10965.50324(49)	10675.91653(51)	10963.1758(18)	10618.97971(57)	10672.3625(16)	10334.12862(86)	10617.9740(18)
D_J (kHz)	4.21746(66)	4.00210(73)	4.2157(35)	3.92948(78)	4.0000(30)	3.7217(15)	3.9302(34)
D_{JK} (kHz)	446.669(42)	446.986(49)	446.52(14)	420.523(40)	445.93(15)	420.302(78)	420.19(18)
D_K (kHz)	91942.1(42)	87571.1(34)	91145.(26)	92014.3(40)	86908.(16)	87592.9(89)	91358.(20)
d_1 (kHz)	-0.172982(32)	-0.155562(53)	-0.1754(13)	-0.155442(45)	-0.15735(73)	-0.14028(36)	-0.15595(94)
d_2 (kHz)	-0.048796(41)	-0.045163(53)	-0.0491(11)	-0.043371(57)	-0.04475(40)	-0.03963(19)	-0.04362(51)
H_{JK} (Hz)	0.890(19)	0.975(39)	0.80(18)	0.692(21)	0.59(20)	0.61(10)	0.65(30)
H_{KJ} (Hz)	-212.6(26)	-156.7(28)	-172.7(67)	-221.6(30)	-167.3(83)	-201.2(44)	-231.1(99)
L_{KKJ} (mHz)	-3516.(42)	-3411.(47)	-4873.(94)	-3379.(51)	-3709.(162)	-2580.(88)	-3598.(214)
Δ_1 (u.Å ²)	0.0963838	0.0968164	0.0963191	0.0965510	0.09673403	0.0969898	0.0964609
N_{lines}	136	143	60	135	46	61	41
σ_{fit} (MHz)	0.052628	0.0525370	0.0494997	0.0570679	0.038468	0.025424	0.042606
A_0'' (MHz)	344746.621	340247.312	344618.818	344727.744	340093.984	340233.197	344602.438
B_0'' (MHz)	11350.71723	11045.52075	11348.34550	10979.89291	11041.85734	10680.11803	10978.92306
C_0'' (MHz)	10965.95850	10676.37165	10963.63091	10619.40823	10672.81657	10334.55649	10618.40219

Hyperfine Splitting

Because nitrogen-14 has a nuclear spin of 1, there is the potential to observed hyperfine splitting of the rotational transitions. This splitting has been partially analyzed in the literature.⁴¹⁻
⁴² Although we did not observe splitting in the *a*-type R-branches, many of the *b*-type transitions did exhibit signs of this splitting. Figure 4.9 shows a Loomis-Wood plot where the *b*-type $K_{prolate} = 0$ to 1(-) P-branch transitions for HN^{15}NN were found based on the known locations for the analogous transitions for HN_3 . In this case, the isotopic satellites can clearly be seen ~ 1 GHz lower frequency than the transitions of the parent isotopologue. The lineshape of these *b*-type transitions in Figure 4.9 are noticeably asymmetric, the result of unresolved splitting.

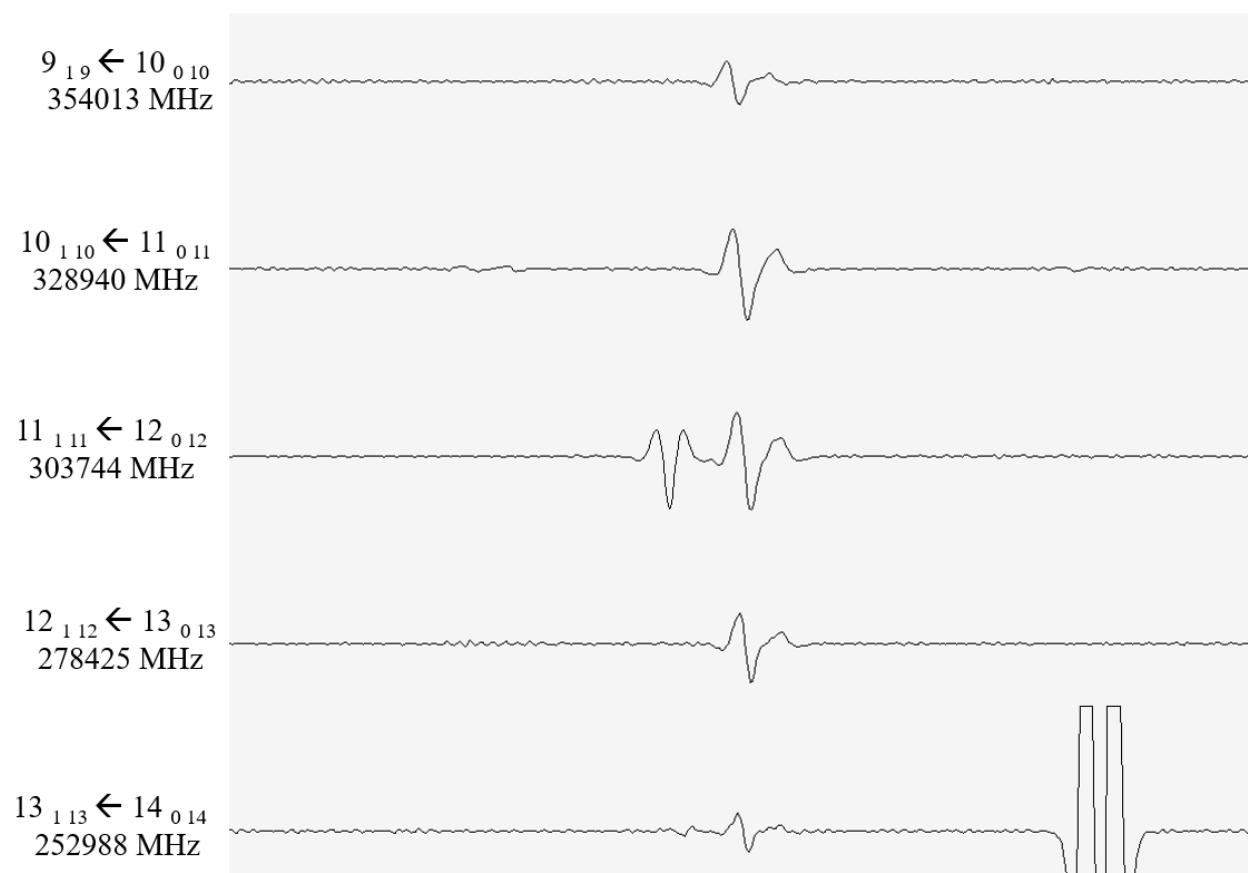


Figure 4.9 A Loomis-Wood plot showing *b*-type $K_{prolate} = 0-1(-)$ P-branch transitions for HN^{15}NN .

Only a few of the splitting patterns were resolved well enough to consider analyzing ($1_{10} \leftarrow 1_{01}$, $1_{11} \leftarrow 2_{02}$, and $1_{11} \leftarrow 0_{00}$), but the distortion of lineshapes could be used to help assign lines. The asymmetry could be used to help confirm that an observed line was a *b*-type line. Additionally, the degree of asymmetry in the lineshape was dependent on which nitrogens were substituted. Figure 4.10 shows a representative *b*-type line from each of the seven $^1\text{HN}_3$ isotopologues. Ideally this comparison would be made using transitions with the same quantum number, but compromises were made to find seven lines of intensity strong enough to be seen clearly without going off scale. In the lines we observed, the nitrogen farthest from the hydrogen seems to affect the lineshape the most, followed by the nitrogen closest to the hydrogen, with a nitrogen-14 at the center position affecting the lineshape the least.

The *b*-type Q-branch transitions for the DN_3 also showed signs of nuclear quadrupole coupling. A Loomis Wood plot showing the first 15 transitions in this series is shown in Figure 4.11. Although the pattern changes somewhat with increasing J , all 15 signals show signs of this coupling. To explore the hypothesis that the third nitrogen from the hydrogen has the nucleus that most effects line shape, a Loomis-Wood plot for the same transitions of DNN^{15}N is shown in Figure 4.12, and these transitions have a much more symmetric line shape.

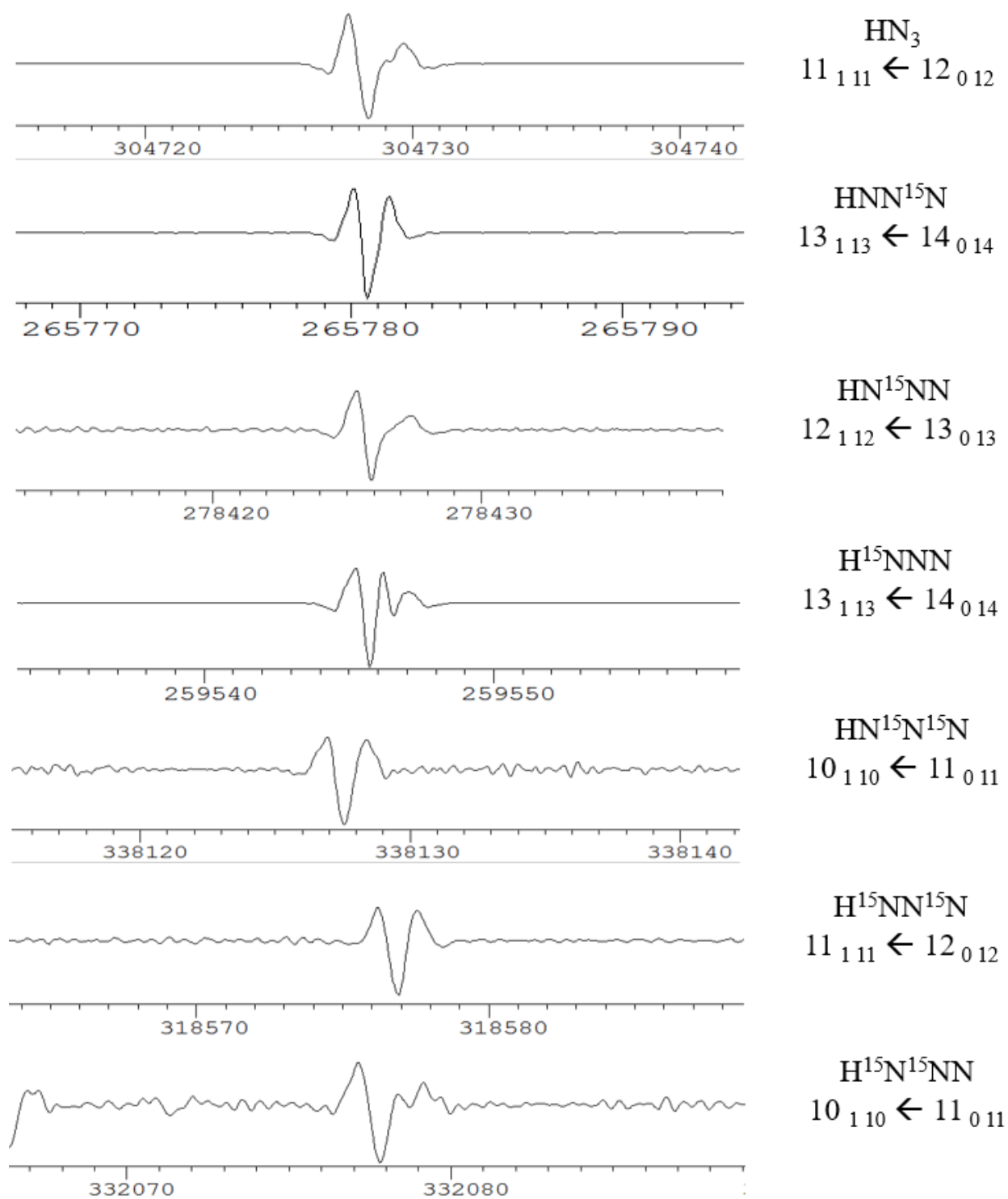


Figure 4.10 Representative $K_{prolate} = 0$ to 1(-) P-branch lines from each of the HN_3 isotopologues. The extent of splitting is a consequence of which nitrogens are substituted.

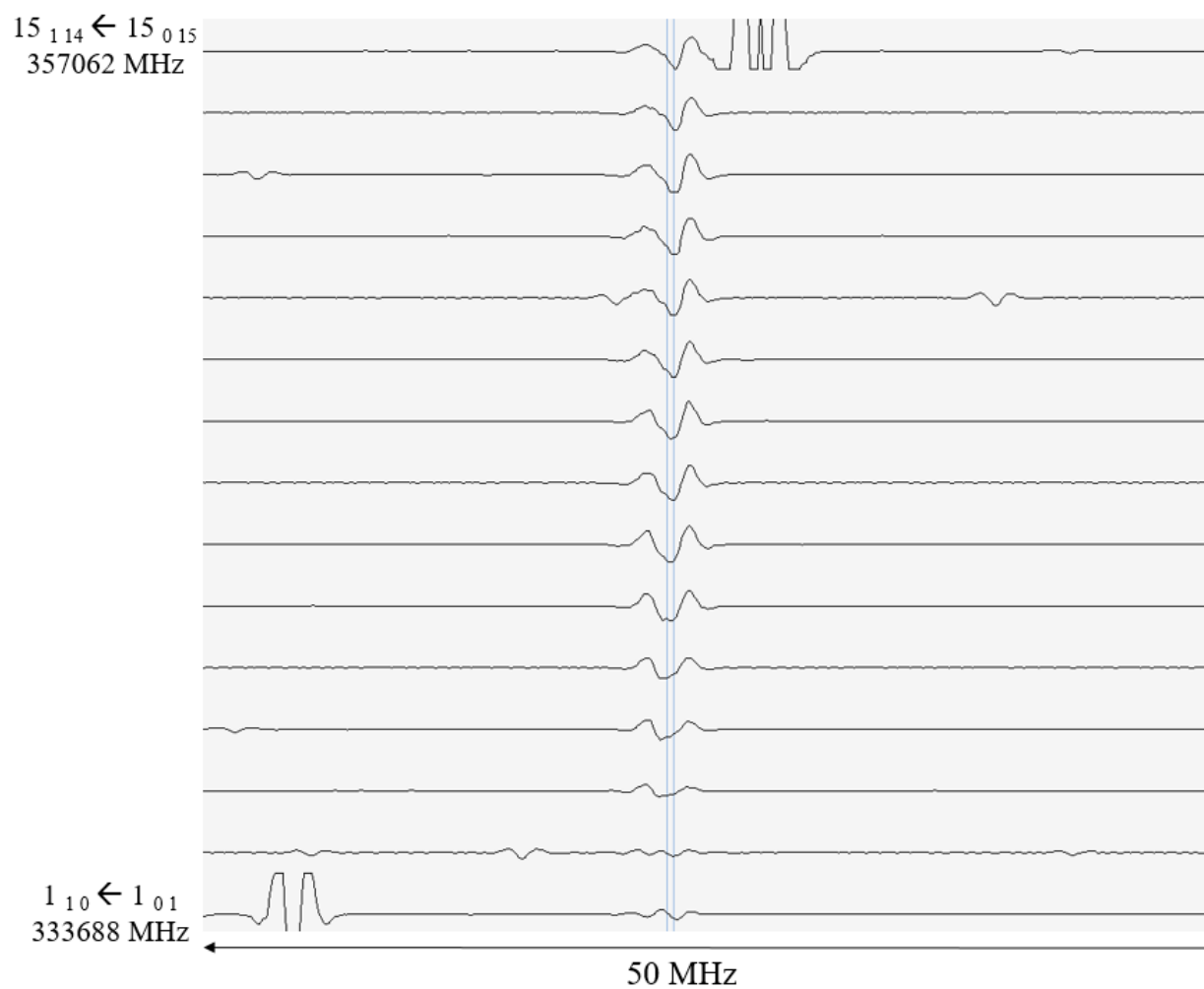


Figure 4.11 A Loomis-Wood plot displaying the first 15 lines in the $K_{prolate} = 1 \leftarrow 0$ Q-branch for $D^{14}N_3$. The misshapen lines are a result of hyperfine splitting.

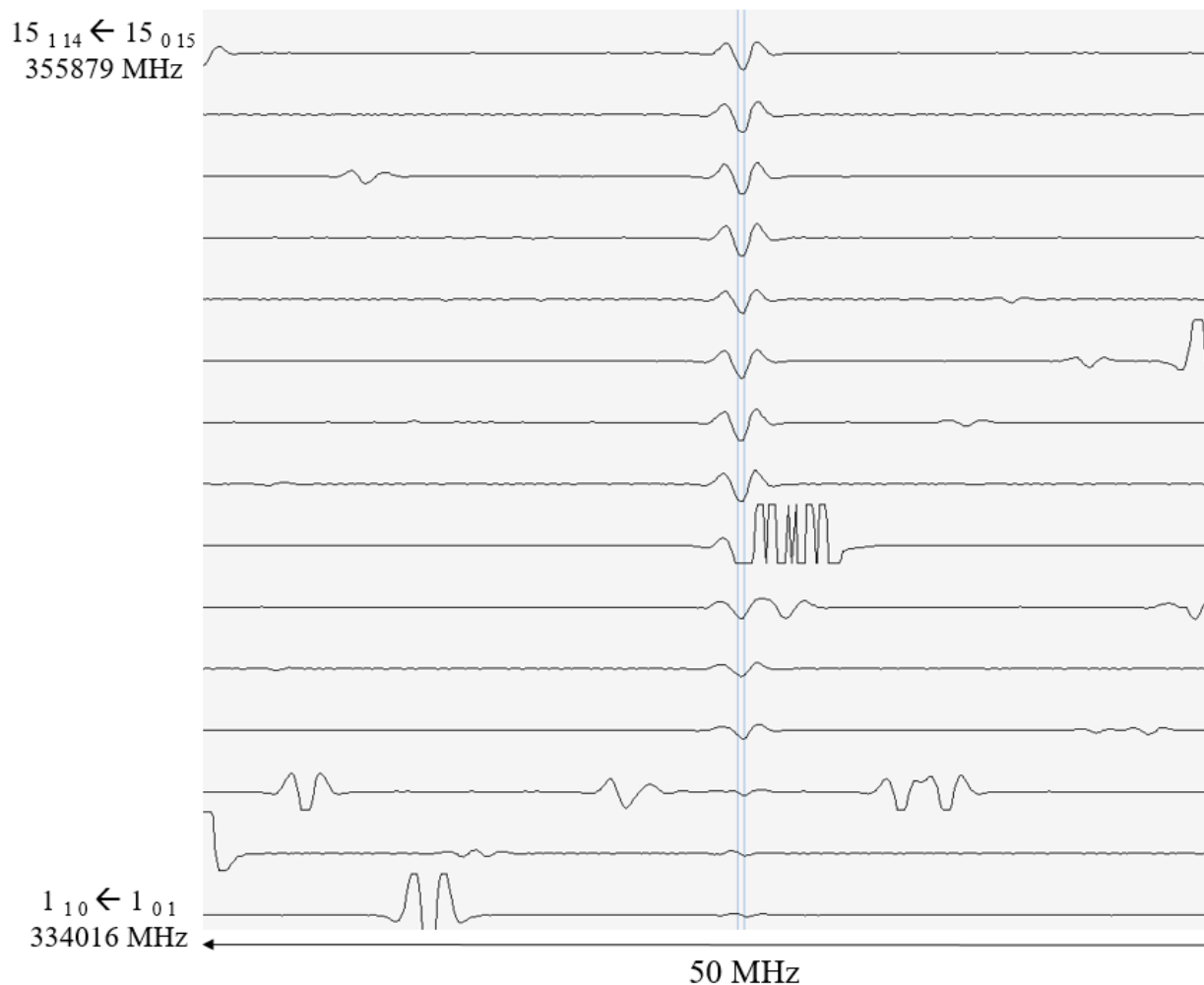


Figure 4.12 A Loomis-Wood plot displaying the first 15 transitions in the $K_{prolate} = 1 \leftarrow 0$ Q-branch for $DNN^{15}N$. The lines are considerably nicer looking than the analogous transitions for $D^{14}N_3$ shown in Figure 4.11.

Structure Determination

The structure of HN_3 was computed from the experimental rotational constants using several different methods. First, the rotational constants were corrected from the A- or S-reduced Hamiltonian constants ($B_0^{(A)}$ or $B_0^{(S)}$) to remove the impact of centrifugal distortion and obtain the determinable constants (B_0'') using Eqns. 1 - 6 below.³⁸ The determinable constants for each isotopologue are presented in Table 4.4 and Table 4.5. The average of the B_0'' values obtained

from A-reduced or S-reduced Hamiltonian constants was used in any structural determinations, but the two sets of values were virtually identical anyway.

$$A'' = A^{(A)} + 2\Delta_J \quad (4.1)$$

$$B'' = B^{(A)} + 2\Delta_J + \Delta_{JK} - 2\delta_J - 2\delta_K \quad (4.2)$$

$$C'' = C^{(A)} + 2\Delta_J + \Delta_{JK} + 2\delta_J + 2\delta_K \quad (4.3)$$

$$A'' = A^{(S)} + 2D_J + 6d_2 \quad (4.4)$$

$$B'' = B^{(S)} + 2D_J + D_{JK} + 2d_1 + 4d_2 \quad (4.5)$$

$$C'' = C^{(S)} + 2D_J + D_{JK} - 2d_1 + 4d_2 \quad (4.6)$$

The use of Kraitchman's equation (Eqn. 7) for single isotopic substitution⁴³ yields the absolute value of the Cartesian coordinates of the substituted atom (designated $|a_s|$) in the principal axis coordinate system of the reference isotopologue of HN_3 . An R_s structure, determined from the application of Kraitchman's equation, is presented in Table 7 using the average determinable constants for all 14 observed isotopologues. With our data, the analysis could be performed using eight separate coordinate systems (HN_3 , DN_3 and their six singly ^{15}N substituted isotopologues). Of these coordinate systems, HNN^{15}N was problematic because the center nitrogen was too close to the center of mass, resulting in an undetermined value of $|b|$ for the center nitrogen. The other seven coordinate systems worked effectively, and the geometric parameters for the R_s structure reported below is the average of the parameters from the seven calculations. The reported error is the standard deviation of the mean for those seven calculations.

$$|a_s| = \sqrt{\frac{I_{a_s} - I_a}{\mu} \left(1 + \frac{I_{b_s} - I_b}{I_b - I_a} \right)} \quad \mu = \frac{M^*(M_s - M)}{M + (M_s - M)} \quad (4.7)$$

Several R_0 and R_e structures were determined using xrefit (a module of CFOUR), which is a least-squares fitting program that optimizes the molecular structural parameters to fit all available moment of inertia data. The R_0 structure uses moments of inertia derived directly from the observable constants (B_0''). This optimized structure still does not include the contributions of vibration-rotation interactions or the electron mass on the observed rotational constants.

A purely experimental value for R_e is possible only if rotational constants are found for each vibrational fundamental for each isotopologue and there are no perturbations between the states. Without experimentally determined vibration-rotation interactions (α_i) for each vibrational mode, we determined a mixed experimental/theoretical equilibrium structure (R_e). The determinable rotational constants for each isotopologue were adjusted for the effects of vibration by correcting each of the rotational constants with one half of the sum of the corresponding vibration-rotation interaction parameters (α_i) obtained from a VPT2 calculation at the CCSD(T)/ANO2 level of theory. This basic approach has been used recently with great success for a variety of molecules, with various levels of theory for the vibration-rotation corrections.⁴⁴⁻⁴⁹ In our lab we have applied this method very successfully to pyrimidine and pyridazine. For a planar molecule like HN_3 , the vibration-rotation corrections to the rotational constants should adjust the inertial defects of all isotopologues to an ideal value of zero. As shown in Table 4.6, the inertial defects are much closer to zero for our vibration-rotation corrected constants, while the correction for electron mass does not further reduce the inertial defects. In previous studies, the electronic mass was shown to be important for the equilibrium structure determination of molecules which contain conjugated π systems.⁴⁹⁻⁵⁰

Table 4.6 Inertial defects for the isotopologues of HN_3 from various determinations of the moments of inertia.

Isotopologue	Experimental B_0'' $\Delta_i (\text{u}\text{\AA}^2)^a$	B_e from Vibration- rotation corrected B'' $\Delta_i (\text{u}\text{\AA}^2)^a$	B_e from Vibration-rotation and electronic corrected B'' $\Delta_i (\text{u}\text{\AA}^2)$
HNNN	0.0735	0.00353	0.00360
H ¹⁵ NNN	0.0738	0.00355	0.00363
HN ¹⁵ NN	0.0736	0.00350	0.00357
HNN ¹⁵ N	0.0736	0.00353	0.00362
H ¹⁵ N ¹⁵ NN	0.0739	0.00354	0.00362
H ¹⁵ NN ¹⁵ N	0.0739	0.00354	0.00363
HN ¹⁵ N ¹⁵ N	0.0737	0.00348	0.00356
DNNN	0.0963	0.00342	0.00343
D ¹⁵ NNN	0.0967	0.00345	0.00345
DN ¹⁵ NN	0.0962	0.00345	0.00346
DNN ¹⁵ N	0.0964	0.00343	0.00344
D ¹⁵ N ¹⁵ NN	0.0966	0.00346	0.00347
D ¹⁵ NN ¹⁵ N	0.0969	0.00346	0.00347
DN ¹⁵ N ¹⁵ N	0.0963	0.00343	0.00345

^aReported values are the average of determinable constants calculated from the $B^{(S)}$ and the $B^{(A)}$ values.

Our R_s , R_0 , and R_e structures are presented in Table 7 below along with the computed structures and the best previously published R_s structure.¹⁰ The R_e structural parameters in Table 4.7 are in very good agreement with the CCSD(T)/cc-pCV5Z results, and have unusually small uncertainty limits. Figure 4.13 shows the equilibrium structure of hydrazoic acid on its principal axes system. Figure 4.14 shows more clearly the relationship between the experimental, CCSD(T)/cc-pCV5Z, and CCSD(T)/ANO2 structural parameters. The small error bars in the experimental structural parameters make it possible to discern a dramatic improvement in the accuracy of the CCSD(T)/cc-pCV5Z *ab initio* results in comparison to the CCSD(T)/ANO2 values.

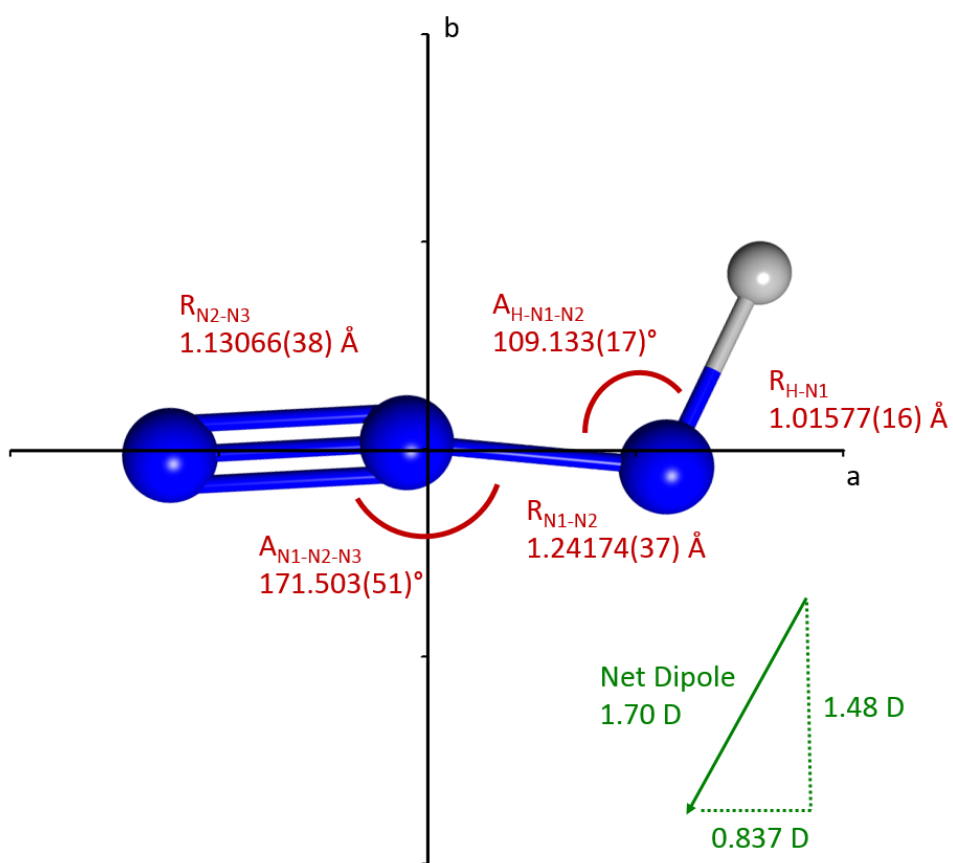


Figure 4.13 Hydrazoic acid in its principal axes system. The displayed dipole moment is from the literature, the structural parameters are the R_e values.

Table 4.7 Geometric parameters for HN_3 determined by various methods

	R_s Winnewisser 1980 ¹⁰	R_s B_0''	R_0 B_0''	R_e B_e, α_i corrected from B_0''	R_e B_e, α_i and electron corrected from B_0''	R_e CCSD(T)/cc-pCV5Z	R_e CCSD(T)/ANO2
$R_{\text{H-N1}}$ (Å)	1.0150(150)	1.01488(23)	1.0222(41)	1.01579(16)	1.01577(16)	1.01559	1.01722
$R_{\text{N1-N2}}$ (Å)	1.2430(50)	1.2293(14)	1.2453(89)	1.24175(36)	1.24174(37)	1.24153	1.24470
$R_{\text{N2-N3}}$ (Å)	1.1340(20)	1.1463(14)	1.1346(91)	1.13068(37)	1.13066(38)	1.13056	1.13271
$\angle_{\text{H-N1-N2}}$ (°)	108.80(400)	108.995(32)	108.58(39)	109.137(17)	109.133(17)	109.211	108.710
$\angle_{\text{N1-N2-N3}}$ (°)	171.30(500)	171.90(22)	170.91(115)	171.505(50)	171.503(51)	171.626	171.656

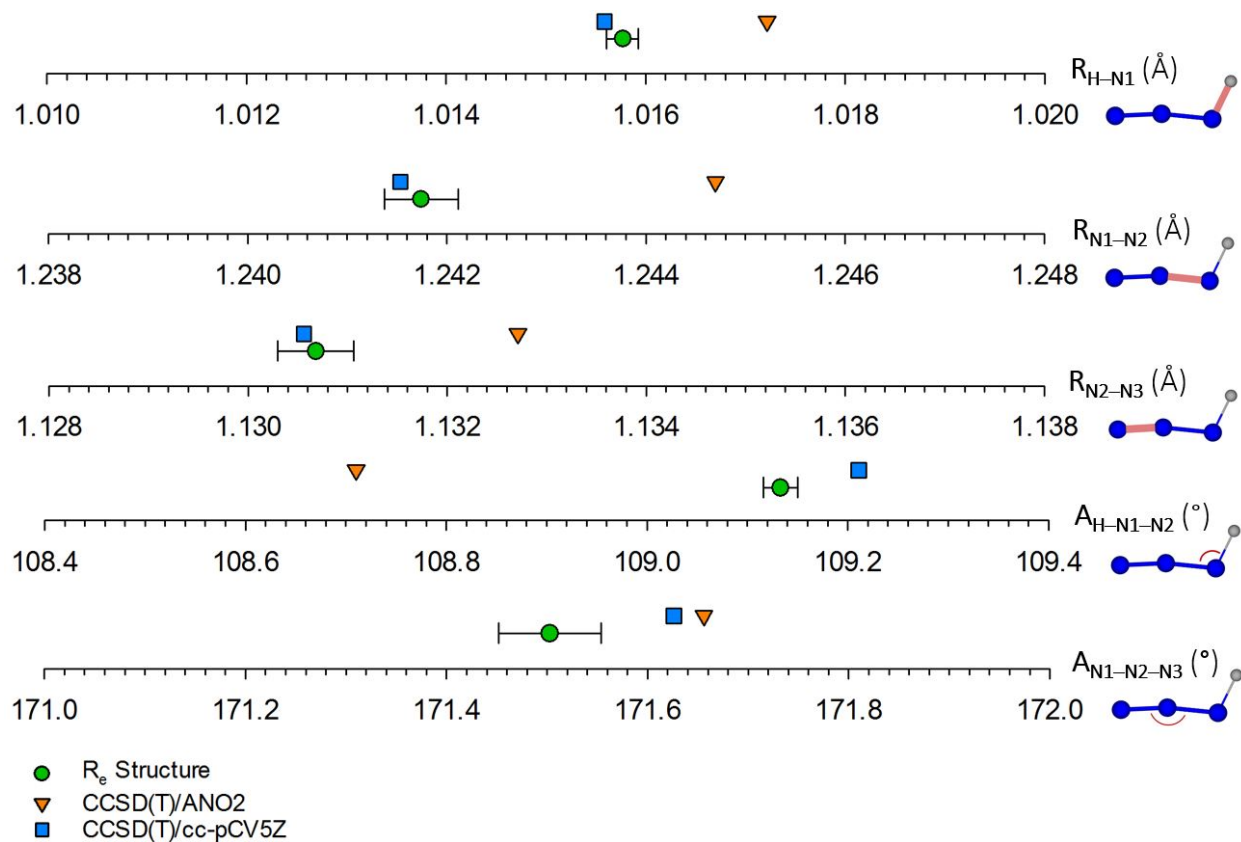


Figure 4.14 Graphical representation of the error bars for all 5 R_e structural parameters compared with the *ab initio* results from the CCSD(T)/ANO2 and CCSD(T)/cc-pCV5Z calculations.

Discussion

Although the potential of rotational spectroscopy to be the most accurate method for determining molecular structures has been recognized since its beginnings, the degree to which this accuracy has actually been achieved in published ‘microwave structures’ has varied widely.⁵¹ The measurement accuracy for spectral lines has always been very high, but the determination of bond distances and angles with great accuracy has usually been limited by two distinct issues: the

lack of sufficient isotopic data and/or the sophistication of the data analysis. Isotopic substitution at all atomic positions is critical – multiple substitutions leading to more accurate structures. Of comparable importance is the treatment (or lack thereof) of vibration-rotation interaction effects and, to a lesser extent, the centrifugal distortion and the non-spherical distributions of electron mass. In the present work we have endeavored to address all of these issues as completely as possible. Hydrazoic acid is a favorable case in that the simplicity of its synthesis and the sensitivity of current millimeter-wave spectrometers make practical the study of a great many isotopologues. On the other hand, it poses substantial challenges with respect to the interaction of vibration and rotation and moreover exhibits large values of the centrifugal distortion constants. The rotational level spacings are much more comparable with vibrational spacings than is the case for most molecules. Therefore, the vibration-rotation interactions are unusually strong and complex. Although there is high resolution spectral data for all six of the fundamental states of HN_3 and DN_3 ,^{12, 15-26, 52} using that data to extract the true α_i constants has proven intractable because of strong perturbations. Furthermore, finding experimental α_i 's for the rare isotopologues is not a realistic objective with current experimental methods. Hydrazoic acid thus provides an excellent test case for the method of combining experimental ground state rotational constants with *ab initio* sum of α_i constants to obtain a mixed equilibrium structure.⁴⁴⁻⁴⁹

Careful examination of the least-squares fits of the equilibrium moments of inertia to the structure (I_a^e , I_b^e , and I_c^e) reveals several things. The pattern of residuals among I_a^e , I_b^e , and I_c^e (denoted δI_a^e , δI_b^e , and δI_c^e) is nearly the same for all 14 isotopologues. In our R_e structure fit shown in Figure 4.13, the average of the residuals, δI_a^e , δI_b^e , and δI_c^e , over the 14 cases are, respectively, 0.00118(3), 0.00117(11), and -0.00118(10) $\text{u}\text{\AA}^2$. The very small standard deviations (in parentheses) confirm the precision of the experimental ground state rotational constants and

the precision of *ab initio* calculations of the isotopic variation for the sum of α_i 's at the level of theory employed. Most of these (albeit small) residuals are due to the remaining non-zero inertial defects found in Table 4.6. Indeed, $\delta I_a^e + \delta I_b^e - \delta I_c^e$ exactly match the remaining inertial defects of the theoretical/experimental I_e values input to the least-squares structure fit (shown in Table 4.6). The optimized R_e output structure by definition has an inertial defect of precisely zero.

The magnitude of the estimated statistical uncertainties given by xrefit for the five structural parameters can largely be attributed to this small but systematic deviation of the theoretical/experimental R_e inertial defects from zero. We tried xrefit structure fits where only I_a^e and I_b^e data, or only I_a^e and I_c^e data, or only I_b^e and I_c^e data were used. This approach serves to shunt the systematic error related to nonzero A_i into the third set of I_e 's, while still giving the fit more than ample degrees of freedom. The average of the parameters determined by these three two-moment fits is precisely the same as the parameters from the original three-moment fit. The parameter variation between the three two-moment fits is quite comparable to the reported statistical uncertainties produced by xrefit for the three-moment fit. The statistical error of the parameters determined by the two-moment fits is decreased by roughly a factor of ten compared to the original three-moment fit. The remaining statistical error in the two-moment fits should be the portion of error attributable to random variations in the moments of inertia rather than the systematic error caused by the non-zero inertial defects.

From the above discussion, it is clear that obtaining starting B_e 's with inertial defects even closer to the ideal value of zero would further improve the accuracy of the structural determination. The origin of these residual non-zero inertial defects is a matter of some speculation at this point. It is clear that electron mass effects are not an issue, because including them has little effect on the

inertial defects (Table 4.6). We have also observed that the use of a higher level of theory in the VPT2 calculation of the α_i 's does not solve the problem. Our suspicion is that the source of the trouble is our lack of inclusion of the next higher order terms in the vibration-rotation expansion (those quadratic in the vibrational quantum numbers, *i. e.*, the γ_i corrections). Future theoretical calculations, not currently implemented, will be required to test this hypothesis.

For achieving the level of accuracy sought here, careful consideration of the fairly large centrifugal distortion effects is also required. The xrefit routine of CFOUR can accept experimental A-reduction constants ($A_0^{(A)}, B_0^{(A)}, C_0^{(A)}$), S-reduction constants ($A_0^{(S)}, B_0^{(S)}, C_0^{(S)}$), or determinable constants (A_0'', B_0'', C_0''), and make internal conversions to equilibrium values (I_A^e, I_B^e, I_C^e) based upon supplied vibration-rotation interaction and electron mass corrections. We found that our equilibrium moments (I_e 's) derived from S-reduced moments ($I_0^{(S)}$'s) were in excellent agreement with our values calculated from the determinable moments (I_0'' 's). The agreement with the equilibrium moments deriving from our A-reduction moments ($I^{(A)}$'s) was still good but not to the same extent. For example, our I_e moments for H^{14}N_3 calculated from $I_0'', I_0^{(S)}$, and $I_0^{(A)}$ moments yielded inertial defects of 0.00353, 0.00354, and 0.00481 $\text{u}\text{\AA}^2$, respectively. Notably, the inertial defects for the $I'', I^{(S)}$, and $I^{(A)}$ moments for H^{14}N_3 before vibration-rotation correction are 0.0735, 0.0737, and 0.07942 $\text{u}\text{\AA}^2$ respectively. The source of this discrepancy is not entirely understood, although there would be an *a priori* expectation that the S-reduction might work better than the A-reduction for a molecule so close to being a prolate symmetric top. We have used the determinable moments (I_0'' 's) as the experimental moments in determining the R_e structure shown in Figure 4.13 and Figure 4.14.

The above issues notwithstanding, the accuracy reported in Table 4.7 is quite high for our R_e structures. The largest bond distance uncertainty is 0.00038 Å and the largest bond angle uncertainty is 0.05°. At this level of accuracy, the experimental structure becomes a significantly better benchmark for the quality of the *ab initio* predictions of molecular structure than has typically been the case. Although both of the theoretical methods reported here obtain excellent agreement with experiment by usually applied standards, the ANO2 frozen core structure does exhibit significant deviations from experiment in comparison to the claimed experimental uncertainty. On the other hand, the higher level all-electron quintuple zeta basis set coupled cluster calculation produces bond distances that fall within the experimental error bars and bond angles that are only slightly outside them— almost an order of magnitude better agreement. This improvement is clearly visible in Figure 4.14. The rather spectacular agreement between mixed experimental/theoretical structure with the very high-quality *ab initio* result is particularly gratifying, in that it serves to confirm both the reasonableness of our reported experimental error limits and also the power of the best modern theoretical methods to produce great accuracy in the prediction of molecular structure of small molecules.

Conclusions

We developed safe and efficient syntheses for HN_3 , HNN^{15}N , H^{15}NNN , DN_3 , DNN^{15}N and D^{15}NNN . Most of our syntheses resulted in inseparable (but perfectly usable) mixtures of these isotopologues. From these spectra we could observe isotopologues with one additional ^{15}N at natural abundance. We assigned the rotational spectra for all 14 accessible isotopologues. We calculated rotation-vibration interaction constants (α_i 's) for these isotopologues, and used them in conjunction with our experimental moments of inertia to arrive at a very accurate equilibrium

structure for HN_3 . In addition to this structure being a vast improvement over the previously published structure for HN_3 , we believe that this is one of the very best structural determinations ever completed for a molecule of this size.

Acknowledgments

We gratefully acknowledge funding from the National Science Foundation for support of this project (CHE-1362264 and CHE-1011959) and for support of shared Departmental computing resources (CHE-0840494). We thank Dr. Mark Wendt for access to the Agilent MXG Analog Signal Generator N5183B. JFS thanks the US National Science Foundation (CHE-1361031).

References

1. Curtius, T., Ueber Stickstoffwasserstoffsäure (Azoimid) N_3H . *Berichte der Deutschen Chemischen Gesellschaft* **1890**, 23, 3023- 3033.
2. Herzberg, G.; Patat, F.; Verleger, H., The geometric structure of the HN_3 molecule. *Z. Elektrochem. Angew. Phys. Chem.* **1935**, 41, 522-524.
3. Eyster, E. H., The Rotational Structure of the Hydrazoic Acid Bands in the Photographic Infra-Red. *J. Chem. Phys.* **1940**, 8 (2), 135-142.
4. Schomaker, V.; Spurr, R., The structure of nitrous oxide and of hydrogen azide. *J. Am. Chem. Soc.* **1942**, 64, 1184-1187.
5. Amble, E.; Dailey, B. P., The Structure and Dipole Moment of Hydrazoic Acid. *J. Chem. Phys.* **1950**, 18 (10), 1422-1422.
6. Winnewisser, M.; Cook, R. L., Centrifugal Distortion Effects and Structure of Hydrazoic Acid from the Millimeter Wave Rotational Spectra. *J. Chem. Phys.* **1964**, 41 (4), 999-1004.
7. Bendtsen, J.; Winnewisser, M., Ground state spectroscopic constants and dipole moment of hydrazoic acid, H^{14}N_3 . *Chem. Phys. Lett.* **1975**, 33 (1), 141-145.

8. Bendtsen, J.; Winnewisser, M., Absorption spectrum of deuterated hydrazoic acid, $D^{14}N_3$ in the microwave and millimeterwave region. *Chem. Phys.* **1979**, *40* (3), 359-365.
9. Kewley, R.; Sastry, K. V. L. N.; Winnewisser, M., Microwave and Millimeter Wave Spectra of Hydrazoic Acid. *J. Mol. Spectrosc.* **1964**, *12*, 387-401.
10. Winnewisser, B. P., The substitution structure of hydrazoic acid, HNNN. *J. Mol. Spectrosc.* **1980**, *82* (1), 220-223.
11. Lievin, J.; Breulet, J.; Verhaegen, G., *Ab initio* study of hydrazoic acid. *Theoret. Chim. Acta.* **1979**, *52* (1), 75-88.
12. Bendtsen, J., Raman spectrum of the ν_2 band of $H^{14}N_3$. *J. Raman Spectrosc.* **1980**, *9* (3), 162-165.
13. Toyota, A.; Muramatsu, T.; Koseki, S., *Ab initio* MCSCF study on several azide molecules: energy component analysis of the pseudo-Jahn-Teller effect. *RSC Advances* **2013**, *3* (27), 10775-10785.
14. Evers, J.; Göbel, M.; Krumm, B.; Martin, F.; Medvedyev, S.; Oehlinger, G.; Steemann, F. X.; Troyan, I.; Klapötke, T. M.; Eremets, M. I., Molecular Structure of Hydrazoic Acid with Hydrogen-Bonded Tetramers in Nearly Planar Layers. *J. Am. Chem. Soc.* **2011**, *133* (31), 12100-12105.
15. Yamada, K.; Takami, M., High-resolution infrared spectrum of hydrazoic acid: The ν_3 fundamental by a tunable diode laser. *J. Mol. Spectrosc.* **1980**, *84* (2), 431-446.
16. Bendtsen, J., Raman and infrared rotation-vibration spectra of the ν_1 Band of $D^{14}N_3$. *J. Raman Spectrosc.* **1984**, *15* (2), 113-119.
17. Bendtsen, J.; Hegelund, F.; Nicolaisen, F. M., Infrared spectrum of the Coriolis coupled vibrations ν_5 and ν_6 of hydrazoic acid. *J. Mol. Spectrosc.* **1986**, *118* (1), 121-131.
18. Bendtsen, J.; Nicolaisen, F. M., The pure rotational absorption spectrum of hydrazoic acid in the far-infrared region. *J. Mol. Spectrosc.* **1986**, *119* (2), 456-466.
19. Bendtsen, J.; Nicolaisen, F. M., The pure rotational absorption spectrum of deuterated hydrazoic acid (DN_3) in the far-infrared region. *J. Mol. Spectrosc.* **1987**, *125* (1), 14-23.
20. Hegelund, F.; Bendtsen, J., A simultaneous analysis of ν_5 , ν_6 , and the ground state of hydrazoic acid. *J. Mol. Spectrosc.* **1987**, *124* (2), 306-316.
21. Bendtsen, J.; Hegelund, F.; Nicolaisen, F. M., A simultaneous analysis of ν_5 , ν_6 , and the ground state of deuterated hydrazoic acid. *J. Mol. Spectrosc.* **1988**, *128* (2), 309-320.
22. Cheung, A. S. C.; Merer, A. J., The ν_1 and $\nu_2 + \nu_4$ bands in the infrared spectrum of HN_3 . *J. Mol. Spectrosc.* **1988**, *127* (2), 509-526.

23. Bendtsen, J.; Nicolaisen, F. M., Infrared spectrum of the ν_4 band of hydrazoic acid. *J. Mol. Spectrosc.* **1989**, *133* (1), 193-200.
24. Bendtsen, J.; Nicolaisen, F. M., High-resolution infrared spectrum of the ν_4 band of deuterated hydrazoic acid (DN_3). *J. Mol. Spectrosc.* **1991**, *145* (1), 123-129.
25. Bendtsen, J.; Nicolaisen, F. M., High-resolution infrared absorption spectra of the ν_3 and ν_4 hybrid bands of hydrazoic acid (HN_3). *J. Mol. Spectrosc.* **1992**, *152* (1), 101-108.
26. Bendtsen, J.; Guelachvili, G., High-Resolution Infrared Absorption Spectrum of the ν_2 Band of Hydrazoic Acid (HN_3). *J. Mol. Spectrosc.* **1994**, *165* (1), 159-167.
27. Hansen, C. S.; Bendtsen, J.; Nicolaisen, F. M., Analyses of the High-Resolution Infrared Absorption Spectra of the ν_2 and ν_3 Bands of Deuterated Hydrazoic Acid (DN_3). *J. Mol. Spectrosc.* **1996**, *175* (2), 239-245.
28. Gimarc, B. M.; Woodcock, D. A., A qualitative molecular orbital explanation of linear, quasilinear, and bent shapes for HABC molecules with 16 valence electrons. *J. Mol. Struct.* **1981**, *85* (1-2), 37-43.
29. Teles, J. H.; Maier, G.; Andes Hess, B.; Schaad, L. J.; Winnewisser, M.; Winnewisser, B. P., The CHNO Isomers. *Chem. Ber.* **1989**, *122* (4), 753-766.
30. Mladenović, M.; Elhiyani, M.; Lewerenz, M., Quasilinearity in tetratomic molecules: An ab initio study of the CHNO family. *J. Chem. Phys.* **2009**, *130* (15), -.
31. Stanton, T. J. o. M. S. F.; Gauss, J.; Harding, M. E.; Szalay, P. G.; with contributions from A.A. Auer, R. J. B., U. Benedikt, C. Berger, D.E. Bernholdt, Y.J. Bomble, L. Cheng, O. Christiansen, M. Heckert, O. Heun, C. Huber, T.-C. Jagau, D. Jonsson, J. Jusélius, K. Klein, W.J. Lauderdale, D.A. Matthews, T. Metzroth, L.A. Mück, D.P. O'Neill, D.R. Price, E. Prochnow, C. Puzzarini, K. Ruud, F. Schiffmann, W. Schwalbach, S. Stopkowicz, A. Tajti, J. Vázquez, F. Wang, J.D. Watts and the integral packages MOLECULE (J. Almlöf and P.R. Taylor), PROPS (P.R. Taylor), ABACUS (T. Helgaker, H.J. Aa. Jensen, P. Jørgensen, and J. Olsen), and ECP routines by A. V. Mitin and C. van Wüllen. For the current version, see <http://www.cfour.de>. *CFOUR*,
32. Pople, J. A.; Head-Gordon, M.; Raghavachari, K., Quadratic configuration interaction. A general technique for determining electron correlation energies. *J. Chem. Phys.* **1987**, *87* (10), 5968-5975.
33. Scuseria, G. E., Analytic evaluation of energy gradients for the singles and doubles coupled cluster method including perturbative triple excitations: Theory and applications to FOOF and Cr_2 . *J. Chem. Phys.* **1991**, *94* (1), 442-447.
34. Lee, T. J.; Rendell, A. P., Analytic gradients for coupled-cluster energies that include noniterative connected triple excitations: Application to *cis*- and *trans*-HONO. *J. Chem. Phys.* **1991**, *94* (9), 6229-6236.

35. Mills, I. M. In *Infrared spectra. Vibration-rotation structure in asymmetric- and symmetric-top molecules*, Academic: 1972; pp 115-140.
36. Stanton, J. F.; Lopreore, C. L.; Gauss, J., The equilibrium structure and fundamental vibrational frequencies of dioxirane. *J. Chem. Phys.* **1998**, *108* (17), 7190-7196.
37. White, K. J.; Cook, R. L., Millimeter-Wave Rotational Stark Spectra of HNCO, DNCO, and HN₃: Dipole-Moment Changes with K. *J. Chem. Phys.* **1967**, *46* (1), 143-151.
38. Gordy, W.; Cook, R., *Microwave Molecular Spectra*. 3rd. ed.; Wiley Interscience: New York, 1984; Vol. XVIII.
39. Krakow, B.; Lord, R. C.; Neely, G. O., A high resolution far infrared study of rotation in HN₃, HNCO, HNCS, and their deuterium derivatives. *J. Mol. Spectrosc.* **1968**, *27* (1-4), 148-176.
40. Bendtsen, J., Pure rotational Raman spectra of hydrazoic acid HN₃ and DN₃. *J. Raman Spectrosc.* **1977**, *6* (6), 306-313.
41. Forman, R. A.; Lide, D. R., Quadrupole Coupling Constants from the Microwave Spectrum of Hydrazoic Acid. *J. Chem. Phys.* **1963**, *39* (4), 1133-1134.
42. Gerry, M. C. L.; Heineking, N.; Maeder, H.; Dreizler, H., Resolution of the nitrogen-14 nuclear quadrupole hyperfine structure in the rotational spectrum of hydrazoic acid, HN₃, and evaluation of the rotational constants of H¹⁵NNN and HNN¹⁵N. *Z. Naturforsch., A: Phys. Sci.* **1989**, *44*, 1079-86.
43. Kraitchman, J., Determination of Molecular Structure from Microwave Spectroscopic Data. *American Journal of Physics* **1953**, *21* (1), 17-24.
44. Puzzarini, C.; Barone, V., Extending the molecular size in accurate quantum-chemical calculations: the equilibrium structure and spectroscopic properties of uracil. *PCCP* **2011**, *13* (15), 7189-7197.
45. McCarthy, M. C.; Cheng, L.; Crabtree, K. N.; Martinez, O.; Nguyen, T. L.; Womack, C. C.; Stanton, J. F., The Simplest Criegee Intermediate (H₂C=O-O): Isotopic Spectroscopy, Equilibrium Structure, and Possible Formation from Atmospheric Lightning. *Journal of Physical Chemistry Letters* **2013**, *4* (23), 4133-4139.
46. Womack, C. C.; Crabtree, K. N.; McCaslin, L.; Martinez, O.; Field, R. W.; Stanton, J. F.; McCarthy, M. C., Gas-Phase Structure Determination of Dihydroxycarbene, One of the Smallest Stable Singlet Carbenes. *Angew. Chem. Int. Ed.* **2014**, *53* (16), 4089-4092.
47. Kidwell, N. M.; Vaquero-Vara, V.; Ormond, T. K.; Buckingham, G. T.; Zhang, D.; Mehta-Hurt, D. N.; McCaslin, L.; Nimlos, M. R.; Daily, J. W.; Dian, B. C.; Stanton, J. F.; Ellison, G. B.; Zwier, T. S., Chirped-Pulse Fourier Transform Microwave Spectroscopy Coupled

with a Flash Pyrolysis Microreactor: Structural Determination of the Reactive Intermediate Cyclopentadienone. *J. Phys. Chem. Lett.* **2014**, *5* (13), 2201-2207.

48. Martinez, O.; Crabtree, K. N.; Gottlieb, C. A.; Stanton, J. F.; McCarthy, M. C., An Accurate Molecular Structure of Phenyl, the Simplest Aryl Radical. *Angew. Chem. Int. Ed.* **2015**, *54* (6), 1808-1811.

49. Esselman, B. J.; Amberger, B. K.; Shutter, J. D.; Daane, M. A.; Stanton, J. F.; Woods, R. C.; McMahon, R. J., Rotational spectroscopy of pyridazine and its isotopologs from 235-360 GHz: Equilibrium structure and vibrational satellites. *J. Chem. Phys.* **2013**, *139*, 224304 1-13.

50. Stanton, J. F.; Gauss, J.; Christiansen, O., Equilibrium geometries of cyclic SiC₃ isomers. *J. Chem. Phys.* **2001**, *114* (7), 2993-2995.

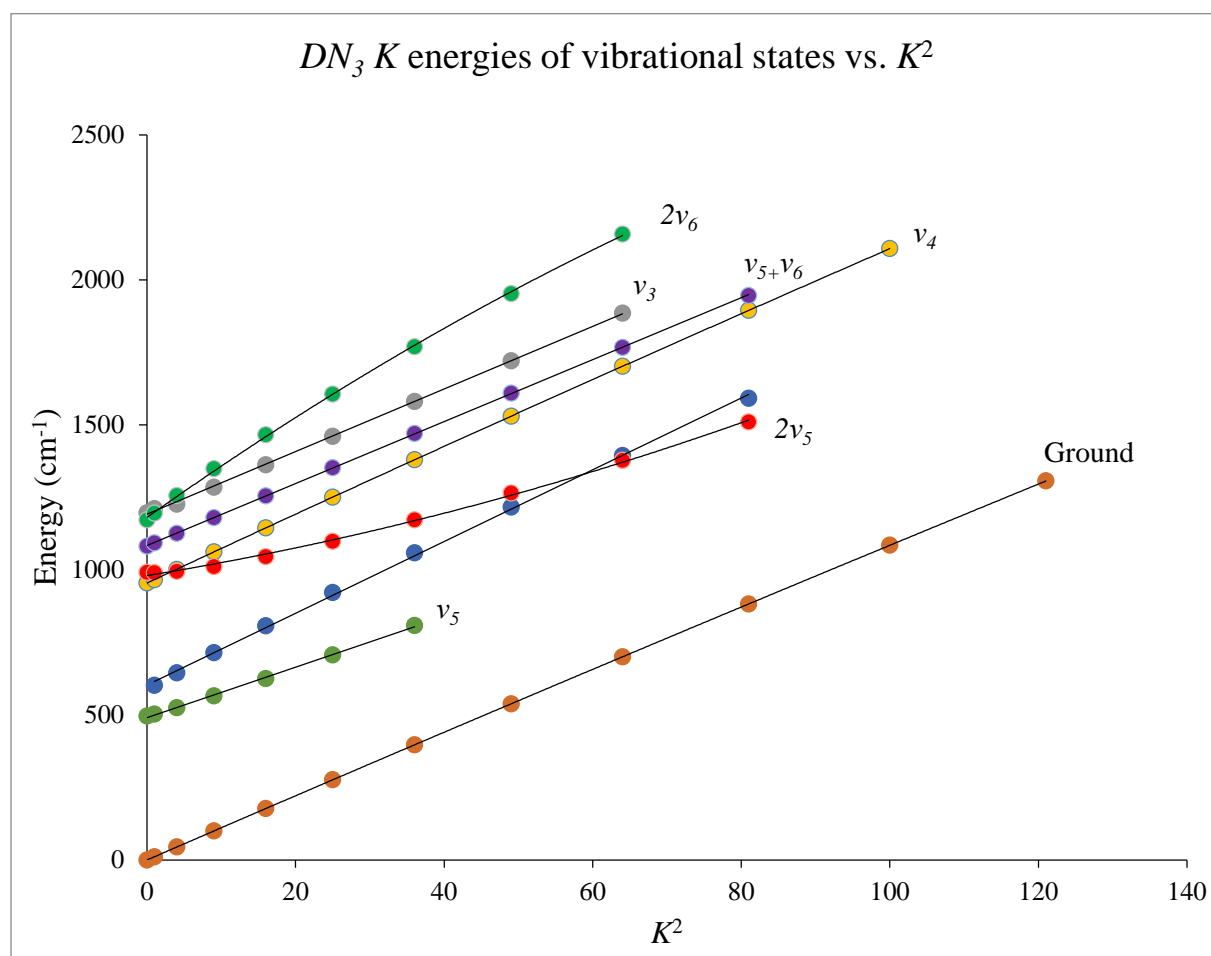
51. Groner, P., Chapter 3 The quest for the equilibrium structure of molecules. In *Vibrational Spectra and Structure*, James, R. D., Ed. Elsevier: 1999; Vol. Volume 24, pp 165-252.

52. Hansen, C. S.; Bendtsen, J.; Nicolaisen, F. M., Analyses of the High-Resolution Infrared Absorption Spectra of the ν_2 and ν_3 Bands of Deuterated Hydrazoic Acid (DN₃). *J. Mol. Spectrosc.* **1996**, *175* (2), 239-245.

Chapter 5: Analysis of the lowest eight vibrational states of hydrazoic acid (HN₃) and deuterated hydrazoic acid (DN₃) by millimeter-wave spectroscopy and FTIR data

Includes the work of collaborators:

R. Claude Woods, Brian J. Esselman



Abstract

Transitions from seven vibrationally excited states have been observed in our room temperature spectra for both HN_3 and DN_3 . In both of these isotopologues, the lowest energy polyad contains two states (ν_5 and ν_6). This lowest energy polyad is modestly perturbed by the ground state and by the five-state polyad above it (ν_4 , $2\nu_5$, $\nu_5+\nu_6$, $2\nu_6$, and ν_3). There are numerous strong perturbations within each polyad. The rotational and vibrational energy levels are different enough between HN_3 and DN_3 to provide unique challenges and advantages in the solving of their spectra. Our millimeter-wave data, published microwave data, and published FTIR data have been used in tandem to assign and fit transitions belonging to these vibrationally excited states. Presented are 3-state fits including the ground state, ν_5 , and ν_6 for both HN_3 and DN_3 . Also presented is a large body of work aimed towards the assignment of all eight studied states for both isotopologues and preliminary determinations of many of their spectroscopic constants.

Introduction

The spectra of hydrazoic acid (HN_3) and deuterated hydrazoic acid (DN_3) are strong enough to observe seven vibrationally excited states (four fundamentals, two overtones, and one combination) at room temperature in our millimeter-wave spectra. Deuterated hydrazoic acid has a significantly different A constant from HN_3 (345 GHz vs. 611 GHz). The drastic reduction in the A constant that comes with substituting the deuterium for hydrogen changes the rovibrational energy levels (and the interactions between them) appreciably. We have studied the rotational spectra of the vibrationally excited states of these two isotopologues in parallel. In general, DN_3 has more transitions in our frequency region and smaller perturbations.

Our work has been greatly aided by a body of published FIR and FTIR studies, primarily by Bendtsen and coworkers from the 1980's and 1990's.¹⁻¹⁰ The pure rotational spectra for the ground vibrational levels of HN₃ and DN₃ have also been previously studied in the microwave and millimeter-wave regions.¹¹⁻¹⁴

An overview of the fundamental states for HN₃ and DN₃, four of which are low enough in energy to be observed in our spectrometer, is presented in Table 5.1. An energy level diagram showing the lowest eight states (including overtones and combinations) for HN₃ and DN₃ is shown in Figure 5.1.

Table 5.1 Summary of the fundamental vibrational modes for HN₃ and DN₃

Fundamental	Symmetry	Description	Vibrational Energy (cm ⁻¹)	
			HN ₃	DN ₃
ν_5	A'	In-plane N-N-N bend	537.2663(8) ⁵	495.7479(10) ⁶
ν_6	A''	Out-of-plane N-N-N bend	606.3574(11) ⁵	586.4994(12) ⁶
ν_4	A'	In-plane N-N-H bend	1147.4075(5) ⁷	954.769(1) ⁸
ν_3	A'	Symmetric stretch	1266.6327(3) ⁹	1197.3864(1) ¹⁰
ν_2	A'	Antisymmetric stretch	2140.3258(4) ¹⁵	2110.1087(2) ¹⁰
ν_1	A'	H-N stretch	3339.8908(14) ¹⁶	2478.451(3) ¹⁷

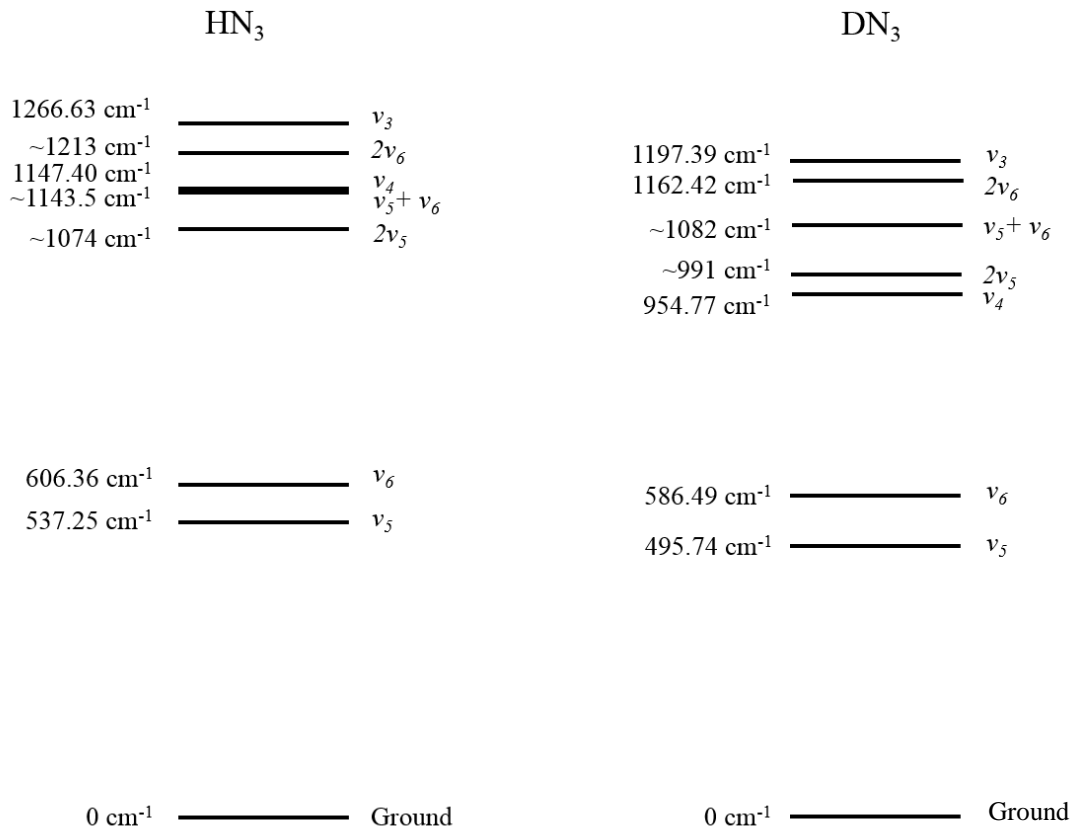


Figure 5.1 Vibrational energy level diagram for the eight lowest energy vibrational states of HN₃ and DN₃ (to scale).

The straightforward energy level diagram shown in Figure 5.1 is somewhat deceptive. The K energy levels within each vibrational state are widely spread due to the small size of the molecule, and while the $K = 0$ energy for the ground vibrational state of HN₃ is at 0 cm⁻¹ ($J=0$), the energy for $K = 10$ is at 1919 cm⁻¹ ($J=0$), and thus at higher energy than at least some K levels for every other state shown in Figure 5.1. In this chapter K will always refer to $K_{prolate}$ because hydrazoic acid is a very nearly prolate asymmetric top. In general in this chapter, rotational levels split by asymmetry will be distinguished as $K(-)$ for $K_{prolate} + K_{oblate} = J+1$ and $K(+)$ for $K_{prolate} + K_{oblate} = J$, according to the standard symmetry designation for the four group ($V=D_2$) of the asymmetric rotor problem. A more comprehensive energy level diagram showing the K energies

for all relevant K states is given in Figure 5.2 for HN_3 and in Figure 5.3 for DN_3 . The K energies refer to the hypothetical energy level corresponding to $J = 0$ for that K . In these figures and throughout the chapter, a K without a (-) or (+) designation refers to the average of $K(-)$ and $K(+)$.

Infrared data was only available for ν_5 , ν_6 , ν_4 , and ν_3 (for HN_3 and DN_3), and $2\nu_6$ (DN_3 only) so the K energies shown in Figure 5.2 and Figure 5.3 for $2\nu_5$, $2\nu_6$ and $\nu_5+\nu_6$ are estimated based on the ν_5 and ν_6 K energies. The energies for $\nu_5+\nu_6$ were estimated by the equation:

$$E_{K,\nu_5+\nu_6} \approx 2 \left(\frac{E_{K,\nu_6} + E_{K,\nu_5}}{2} - E_{K,\text{ground}} \right) + E_{K,\text{ground}} \quad (5.1)$$

The above comes from using the alpha approximation for the shift in $A - \frac{B+C}{2}$ without higher order terms. The energies for $2\nu_5$ and $2\nu_6$ were estimated as follows:

$$E_{K,2\nu_5} \approx E_{K,\nu_5+\nu_6} - (E_{K,\nu_6} - E_{K,\nu_5}) \quad (5.2)$$

$$E_{K,2\nu_6} \approx E_{K,\nu_5+\nu_6} + (E_{K,\nu_6} - E_{K,\nu_5})$$

These estimations assume that the dominant perturbation of $2\nu_5$, $\nu_5+\nu_6$, and $2\nu_6$ is the global A-type Coriolis perturbation (G_a), and possible interactions with ν_3 and ν_4 are not considered. Understanding Equation (5.2) is somewhat more complicated, but important. In the harmonic oscillator approximation, G_a changes to $\sqrt{2}G_a$ on going from the ν_5 / ν_6 interaction to $2\nu_5 / \nu_5+\nu_6$ or $\nu_5+\nu_6 / 2\nu_6$ interactions. The relevant matrices to be diagonalized to find the K energies are

$$\begin{bmatrix} E_{K,\nu_5}^0 & G_a K \\ G_a K & E_{K,\nu_6}^0 \end{bmatrix} \quad (5.3)$$

for the ν_5 and ν_6 case, and

$$\begin{bmatrix} E_{K,2\nu_5}^0 & \sqrt{2}G_a K & 0 \\ \sqrt{2}G_a K & E_{K,\nu_5+\nu_6}^0 & \sqrt{2}G_a K \\ 0 & \sqrt{2}G_a K & E_{K,2\nu_6}^0 \end{bmatrix} \quad (5.4)$$

for the overtone/harmonic case. The diagonal elements are the K energies before perturbation by the A-type Coriolis resonance. For the overtone levels these can be obtained with the same approximation used in Equation (5.1) for the combination states. The latter matrix factors into a one by one and a two by two and thus has an analytic solution for the eigenvalues, as does the matrix in Equation (5.3). Comparing these two solutions confirms Equation (5.1) and Equation (5.2). The splittings $E_{K,\nu_6} - E_{K,\nu_5}$, $E_{K,2\nu_6} - E_{K,\nu_5+\nu_6}$, and $E_{K,\nu_5+\nu_6} - E_{K,2\nu_5}$ all turn out to be

$$\sqrt{(E_{K,\nu_5}^0 - E_{K,\nu_6}^0)^2 + 4 G_a^2 K^2} \quad (5.5)$$

Fortunately, experimental K energies are available up to $K = 3$ for $2\nu_6$ of DN₃,¹⁰ and allow us to verify that these K energy level estimates are substantially correct (see below).

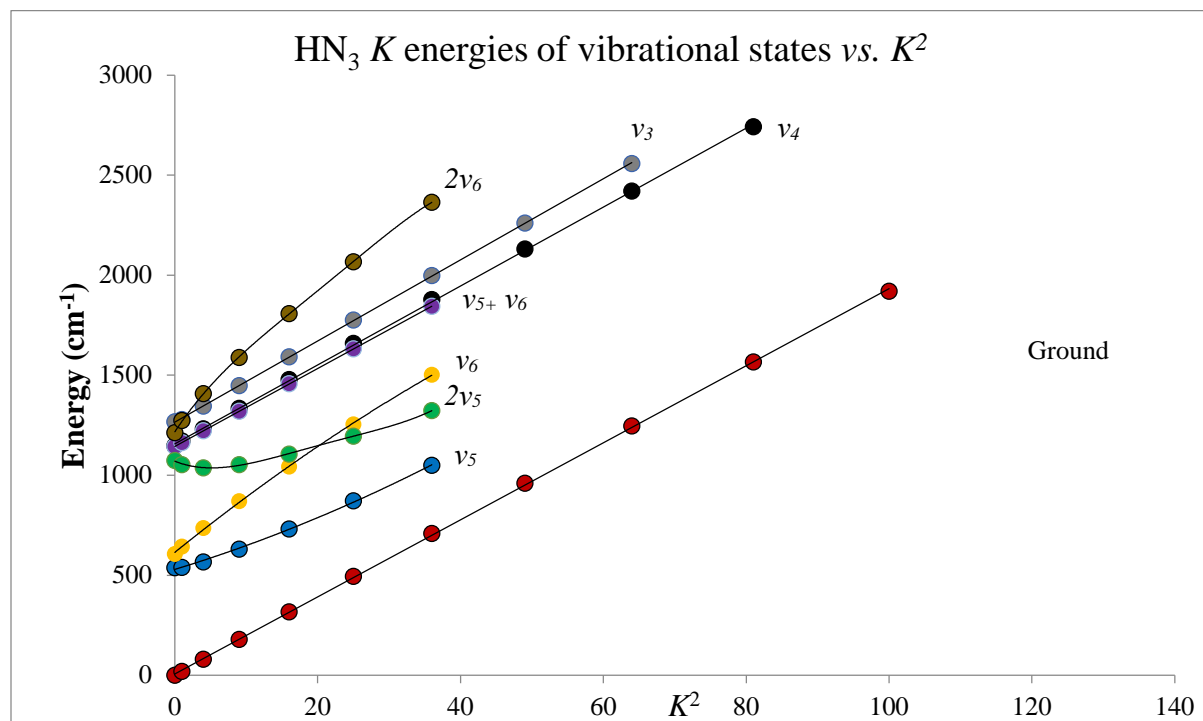


Figure 5.2 A plot showing the observed or calculated values for the K energies for the eight studied vibrational states of HN_3

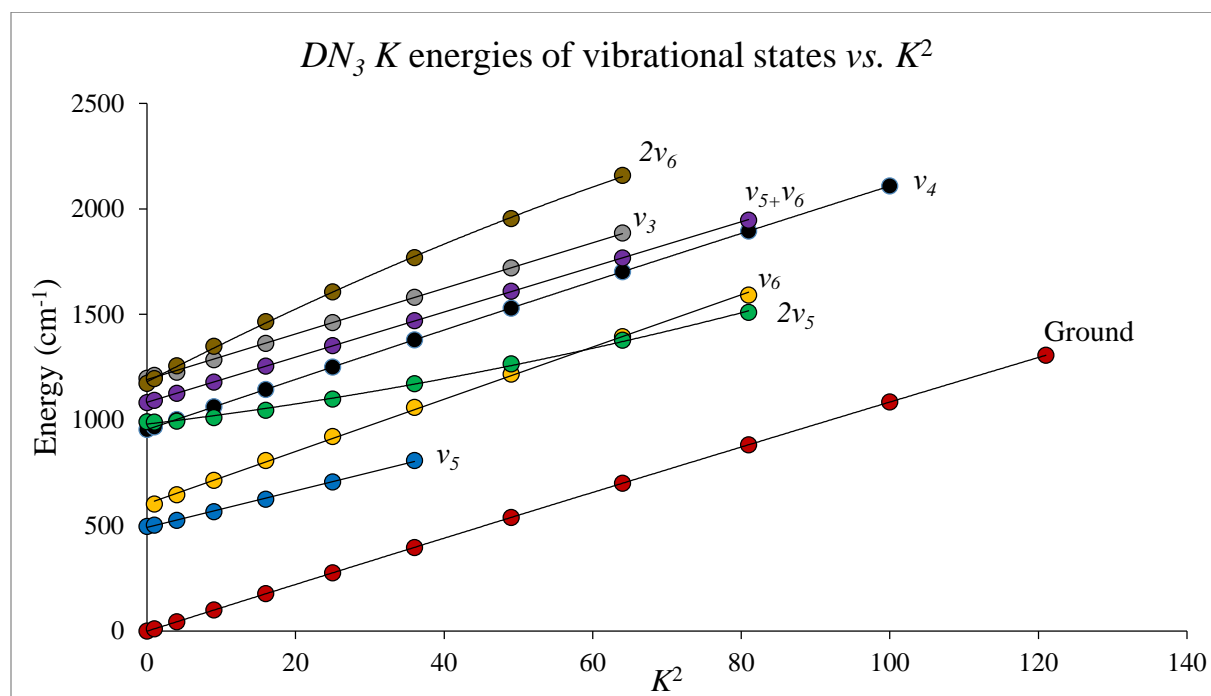


Figure 5.3 A plot showing the observed or calculated values for the K energies for the eight studied vibrational states of DN_3

Observation of Figure 5.2 and Figure 5.3 shows how significant the entanglement of the K energies from the eight vibrational states actually is. The separation between $K = 0$ of the ground vibrational state and ν_5 is 537 cm^{-1} and 496 cm^{-1} for HN_3 and DN_3 , respectively. This relatively large separation protects the lower K levels of the ground state from perturbations, and transitions involving these levels can be studied independently, as described in Chapter 4. The higher K levels of the ground vibrational state are perturbed via a centrifugal distortion interaction with the ν_5 state (parameter W_{05} , see below). State ν_5 is of course perturbed via the A-type Coriolis resonance with ν_6 discussed above. This global A-type Coriolis resonance causes the ν_5 and ν_6 states to repel each other, bringing the higher K levels of ν_5 to low enough energies to interact with levels in the ground vibrational state, enabling the observed perturbations in the ground state. As the ν_5 and ν_6 subband energies diverge as a result of their mutual perturbations, the ν_6 levels eventually ‘catch up’ with states in the second polyad.

The gap between the polyads is still large enough (468 cm^{-1} for HN_3 and 368 cm^{-1} for DN_3) for it to be reasonable to attempt to analyze the ground state, ν_5 and ν_6 in a three-state fit independently from the rest of the vibrational states at higher energy. This three-state least squares-fit approach was taken by Bendtsen *et al.* for both HN_3 ⁵ and DN_3 ⁶. The basic theory and the form of the Hamiltonian operator and its matrix elements are described in these publications. We have been partially successful with three-state fits of our millimeter-wave data. Simply from the steeper upward slope of ν_6 in Figure 5.2 and Figure 5.3, it is not surprising that the three-state fits are not entirely successful, as the polyads are not truly independent of one another.

As noted by Bendtsen *et al.* in the attempted 3-state fit of DN_3 ,⁶ there are Coriolis interactions between ν_6 and ν_4 which are too strong to be entirely ignored. These resonances

between ν_6 and ν_4 , along with expected centrifugal distortion interactions between ν_5 and $2\nu_5$ and ν_6 and $\nu_5+\nu_6$ create a bridge between the lower three states and the next highest polyad, which includes five states: ν_4 , $2\nu_5$, $\nu_5+\nu_6$, $2\nu_6$, and ν_3 . Of these, $\nu_5+\nu_6$ is the only state with A'' symmetry, and it has strong Coriolis interactions with $2\nu_5$ and $2\nu_6$, of which the G_a interaction has already been discussed. Additionally there are strong Fermi interactions between $2\nu_5$ and ν_4 , and $2\nu_6$ and ν_3 , which will be discussed further below. There is also a C-type Coriolis resonance between ν_3 and ν_4 . The full web of mutual perturbations is detailed later in Table 5.6 and Table 5.7.

The analysis of this upper polyad differs appreciably between HN_3 and DN_3 , because of a relative reordering of energy levels. Notably, ν_4 is lower in energy than both $\nu_5+\nu_6$ and $2\nu_5$ in DN_3 , because this bending mode involves a large movement of the hydrogen (or deuterium) atom. For both isotopologues, the state with the highest vibrational energy that we have observed is ν_3 (1266.6 cm^{-1} for HN_3 and 1197.4 cm^{-1} for DN_3). There is an energy gap of approximately 345 cm^{-1} to $3\nu_5$ in the next polyad for HN_3 . There is an energy gap of approximately 217 cm^{-1} to $\nu_4+\nu_5$ in the next polyad of DN_3 . Due to perturbations from these higher polyads it is unlikely that an eight-state least-squares fit will be entirely successful without attempting account for these interactions. Nonetheless, our goal is explore and understand these eight states as fully as possible with the available data, both published and from our spectrometer.

The challenge of simultaneously fitting the pure rotational transitions from multiple mutually-perturbing vibrational states is substantial. Our most successful fit to date, a three-state fit of the lowest three vibrational states of DN_3 including MW, MMW, & FTIR data, presented in Table 5.8, allowed for the optimization of 3 rotational constants and 10 centrifugal distortion

constants for each state, as well as the band origin energy for ν_5 and ν_6 , and 4 perturbation terms, for a total of 45 independent parameters, of which all but one were well determined in the fit. By necessity, a successful 8-state combined fit would involve upwards of 100 independent parameters. While we have favored Kisiel's ASROT and ASFIT¹⁸ programs for single-state fits, Pickett's SPFIT and SPCAT¹⁹ have the flexibility we require to simultaneously fit transitions from multiple states.

For single state fits of unperturbed molecules (such as the ground vibrational state of carbonyl diazide), the least-squares fit involves perhaps 6 to 15 parameters. In such a case, guessing and checking is a valid tool when assigning a new series of lines and adding it to a nascent fit file. The parameters will generally converge quickly, and the observed – calculated values for these lines in the output file will strongly suggest whether the new assignments are correct or not. On the other hand, when building a fit file with multiple perturbed states and dozens of parameters, it is of vital importance that the line assignments be correct and that the starting values for the parameters be good, otherwise there is very little chance that the fit will converge, and even if it does, the sheer number of parameters leaves a lot of 'wobble room' for incorrectly assigned lines to reside in the file without sticking out from the correctly assigned transitions. The bulk of this chapter details the lengths we have gone to correctly identify hundreds of series without the aid of the SPFIT non-linear least-squares fitting program. We have built considerable experience at making and confirming assignments by low tech methods, and using plots of these transitions, along with linear least-squares fits (straight line or polynomial) to extract valuable spectroscopic constants.

Assignment of lines.

The first step in understanding these eight vibrational states of HN_3 and DN_3 is the accurate assignment of transitions. This is a difficult task because many of the states are highly perturbed. Figure 5.4 shows a prediction for the transition frequencies in the $J = 12 \leftarrow 11$ a -type R-branch of the ground state of HN_3 . The prediction is based on the single state fit of transitions up to $K = 5$ described in Chapter 4. The actual transition frequencies for this series are shown in Figure 5.5. It can be seen that the $K = 6$ and 7 lines are moderately perturbed, while the $K = 8, 9$ and 10 lines are massively perturbed.

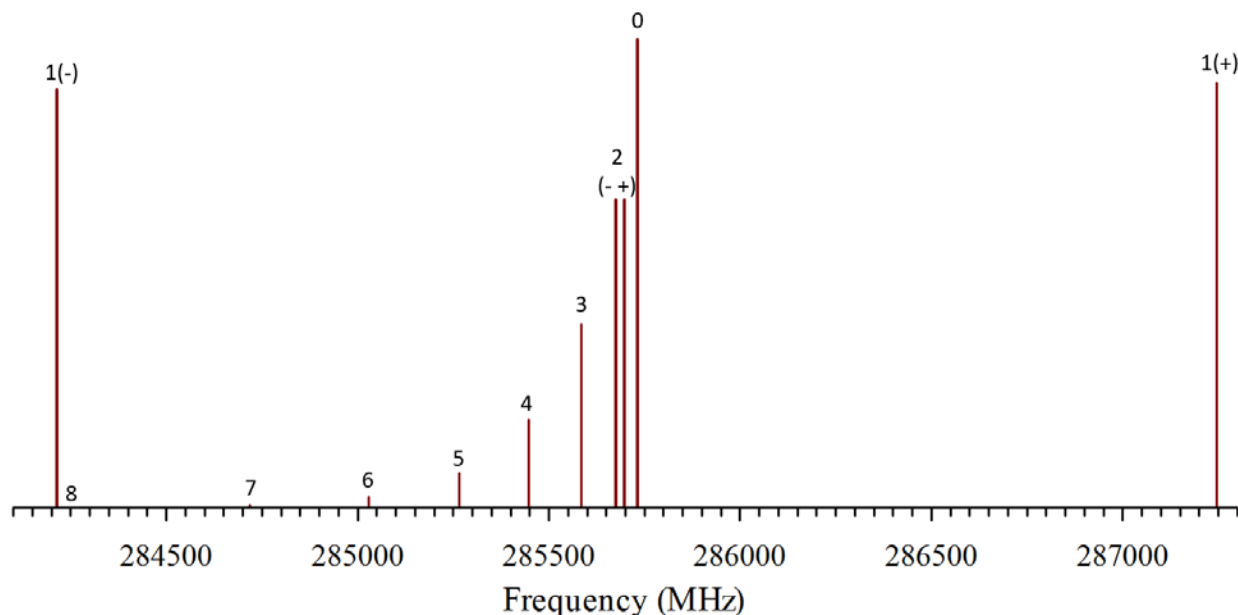


Figure 5.4 Predicted positions for lines in the $J = 12 \leftarrow 11$ a -type R branch. Constants used in the prediction are from a single-state rigid rotor/ centrifugal distortion model including a -type lines up to $K = 5$ and some b -type lines up to $K = 2$. Labels are the K values. The series is predicted to continue off scale to lower frequencies.

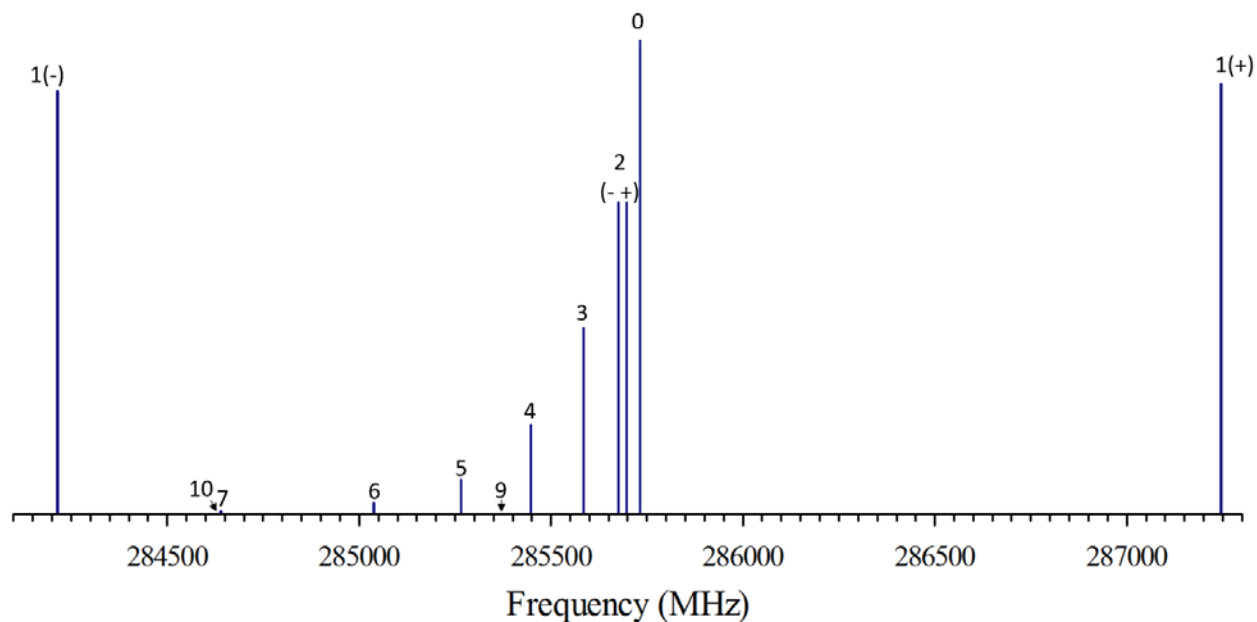


Figure 5.5 Assigned frequencies for lines in the $J = 12 \leftarrow 11$ a -type R-branch. Labels are the K values. The $K = 8$ line is off scale to low frequency at 282944 MHz.

The *a*-type series are largely intertwined for all eight states. Intensities are helpful in distinguishing states, but from Figure 5.2 and Figure 5.3 it can be inferred that each vibrational state has pure rotational transitions with a very wide range of intensities. The $K = 10$ *K* energy for the ground vibrational state of HN_3 is 1919 cm^{-1} higher than that of $K = 0$, and thus the energy levels are higher and their transition intensities are lower than most of the observed *K* energy levels for the seven excited vibrational states. One striking example of this intermingling of intensities is the challenge of distinguishing between the *a*-type R-branch series of $K = 5$ for ν_4 and $K = 7$ for ν_6 in DN_3 . The two series have similar intensities because their *K* energies are relatively close (34 cm^{-1}), despite the fact that the vibrational energy of ν_6 is 353 cm^{-1} lower than that of ν_4 . This proximity of $K = 5$ for ν_4 to $K = 7$ for ν_6 , also facilitates A-type Coriolis interactions (G_a and F_a) between these two states, making their frequencies more difficult to predict. An unfortunate coincidence in this example is that the series of transitions are also close in frequency, making the assignment ambiguous. The following sections outline strategies for assigning these perturbed and intermingled transitions.

Rotational Vibration Interaction Corrections

We have found the vibration-rotation corrections (α_i values) to be very useful for the assignment of vibrational states for carbonyl diazide²⁰ and pyridazine,²¹ as well as in the ongoing projects involving phenylisocyanate, pyrimidine, and formyl azide. Essentially, these α corrections (α_A , α_B , and α_C) are calculated and added on to the rotational constants of the ground state to give estimated values for the rotational constants of the excited vibrational states. Using these mixed theoretical/experimental rotational constants along with the centrifugal distortion constants from the ground state generally gives useful predictions of excited state transitions. The

calculated α_i 's for HN_3 and DN_3 are shown in Table 5.2 and Table 5.3. For ν_5 and ν_6 , experimental α values from both the literature and our own three-state fits are added to the list. These experimental values come from subtracting the excited state constants from the corresponding ground state constants.

Table 5.2 Vibration-rotation corrections for HN_3 . Literature values and our own experimental values are reported for ν_5 and ν_6 .

		α_A (MHz)	α_B (MHz)	α_C (MHz)
ν_5	CCSD(T)/ANO2	-612651.2	31.3	5.9
	Literature ⁵	-20801.7	26.5	9.7
	Experimental	-20557.6	33.9	2.8
ν_6	CCSD(T)/ANO2	608642.3	2.8	22.4
	Literature ⁵	12445.3	-5.8	26.4
	Experimental	11751.4	0.7	20.5
ν_4	CCSD(T)/ANO2	19140.8	-46.1	-61.6
ν_3	CCSD(T)/ANO2	17656.8	-4.4	-9.1
ν_2	CCSD(T)/ANO2	-2920.4	-88.3	-85.9
ν_1	CCSD(T)/ANO2	-26676.7	-13.2	-21.6

Table 5.3 Vibration-rotation corrections for DN₃. Literature values and our own experimental values are reported for ν_5 and ν_6 .

		α_A (MHz)	α_B (MHz)	α_C (MHz)
ν_5	CCSD(T)/ANO2	-129567.9	34.9	6.8
	Literature ⁶	-17133.6	35.5	6.9
	Experimental	-9398.4	36.2	5.8
ν_6	CCSD(T)/ANO2	123658.6	2.6	20.5
	Literature ⁶	16994.7	-2.5	22.4
	Experimental	1945.6	-0.5	20.4
ν_4	CCSD(T)/ANO2	22141.6	4.1	-19.0
	Literature ⁶	17222.6		
ν_3	CCSD(T)/ANO2	-2654.8	-52.6	-49.7
ν_2	CCSD(T)/ANO2	-1004.1	-82.1	-77.8
ν_1	CCSD(T)/ANO2	-11902.4	-10.1	-20.1

From the states where there is literature data available, it can be seen that some of the predicted values are very good, some are marginally good, and others are completely incorrect. In terms of assessing the viability of this approach, there are some worrying examples where the magnitude of the α constants look reasonable, but the values are different enough to be misleading in assigning lines. Ultimately we chose not to rely on the *ab initio* predictions of the vibration-rotation constants in the assignment of transitions.

Combination Differences

The published ro-vibrational data has been extremely useful as a starting point in the assignment of pure rotational lines in our spectra. For HN₃, FTIR ro-vibrational line lists have been published for the ν_5 , ν_6 , and ν_4 , bands^{5,7} in addition to pure rotational FIR lines for the ground

state.³ In addition, line lists for the ν_3 band from infrared diode laser spectroscopy have been published.¹ DN₃, line lists are published for the ground state pure rotational spectrum, and the ν_5 , ν_6 and ν_4 bands.^{6, 8} It is regrettable that additional FTIR line lists were deposited as SI for the HN₃ ν_3 band⁹ and the DN₃ ν_3 and $2\nu_6$ bands¹⁰ with the *Journal of Molecular Spectroscopy*, but have apparently been lost since that time and are unavailable to us.

Combination differences between four appropriate transitions were frequently utilized, when possible, in the initial assignment of lines. Because the IR data included both P and R-branches, two different combination differences could be readily tried to arrive at a single frequency. Because some rovibrational transitions were missing from the line lists, curves were fit to the observed lines to smooth and interpolate the full series of transitions. An example of this combination differences technique is shown in Figure 5.6. The $13_3 10 \leftarrow 12_3 9$ pure rotational transition in the ν_5 state was calculated using a measured pure rotational transition frequency from the ground vibrational state and two P or R-branch IR transitions. These two methods predicted $13_3 10 \leftarrow 12_3 9$ transition in ν_5 at 309933 MHz or 309937 MHz. We used this information to assign an observed line at 309932.86 MHz to this transition.

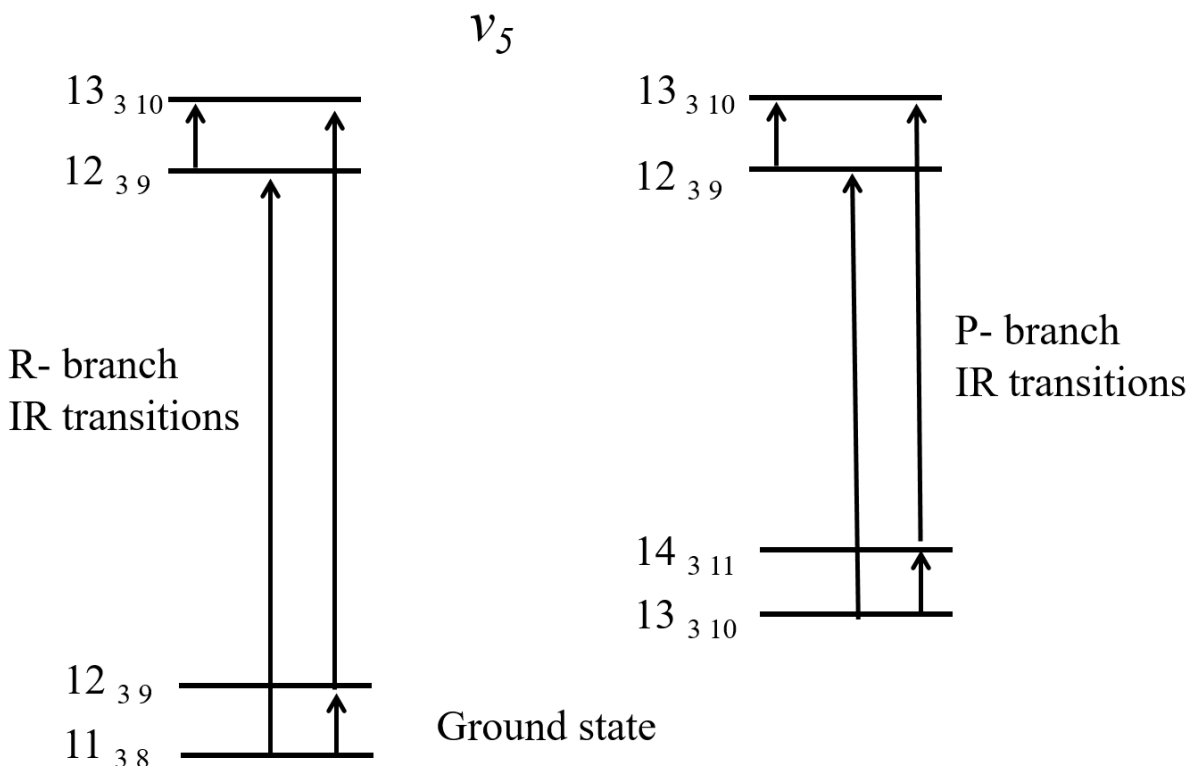


Figure 5.6 An energy level diagram showing two combination differences approaches to predict a pure rotational transition in the ν_5 state of HN_3 . The strategies utilize the frequency of a measured pure rotational transition in the ground vibrational state and either R-branch or P-branch vibrational-rotational transitions.

In some auspicious situations we were able to use combination differences of four pure rotational lines to solidly confirm our assignments. Figure 5.7 shows a beautiful example where the assignments for four lines in the $2\nu_6$ state of DN_3 are confirmed unambiguously. The four transitions are two *a*-type and two *b*-type transitions that link the states $13_{0,13}$, $14_{0,14}$, $12_{1,12}$, and $13_{1,13}$. Whether or not these states are perturbed does not matter. If the assignments are correct, combining these transition frequencies should give an ideal value of zero. In this case, the result was extremely satisfactory at 0.0223 MHz, well within the measurement error for a single transition and certainly within the combined measurement error for four transitions. As mentioned, situations where all four relevant transitions are in our frequency range are rare, but often

extrapolation of observed lines in a series could be used to predict those outside our region to create a working four state combination differences diagram.

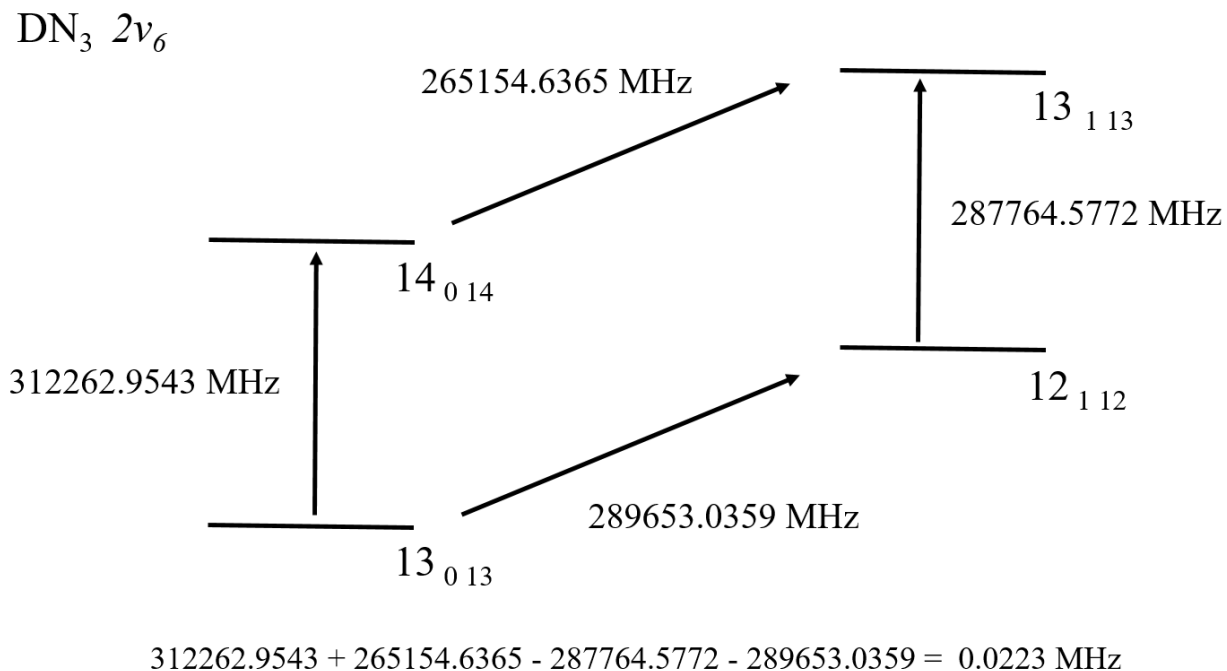


Figure 5.7 An energy state diagram showing a combination differences scheme which unambiguously confirms the assignments of four pure-rotational transitions in the 2ν₆ state of DN₃ which, fortuitously, all occur within the frequency region accessible to us.

Loomis-Wood plots

Loomis-Wood plots^{18, 22} were used extensively in our assignment process. Figure 5.8 shows a Loomis-Wood plot which is centered on the $K = 0$ frequencies for the ground vibrational state of hydrazoic acid.

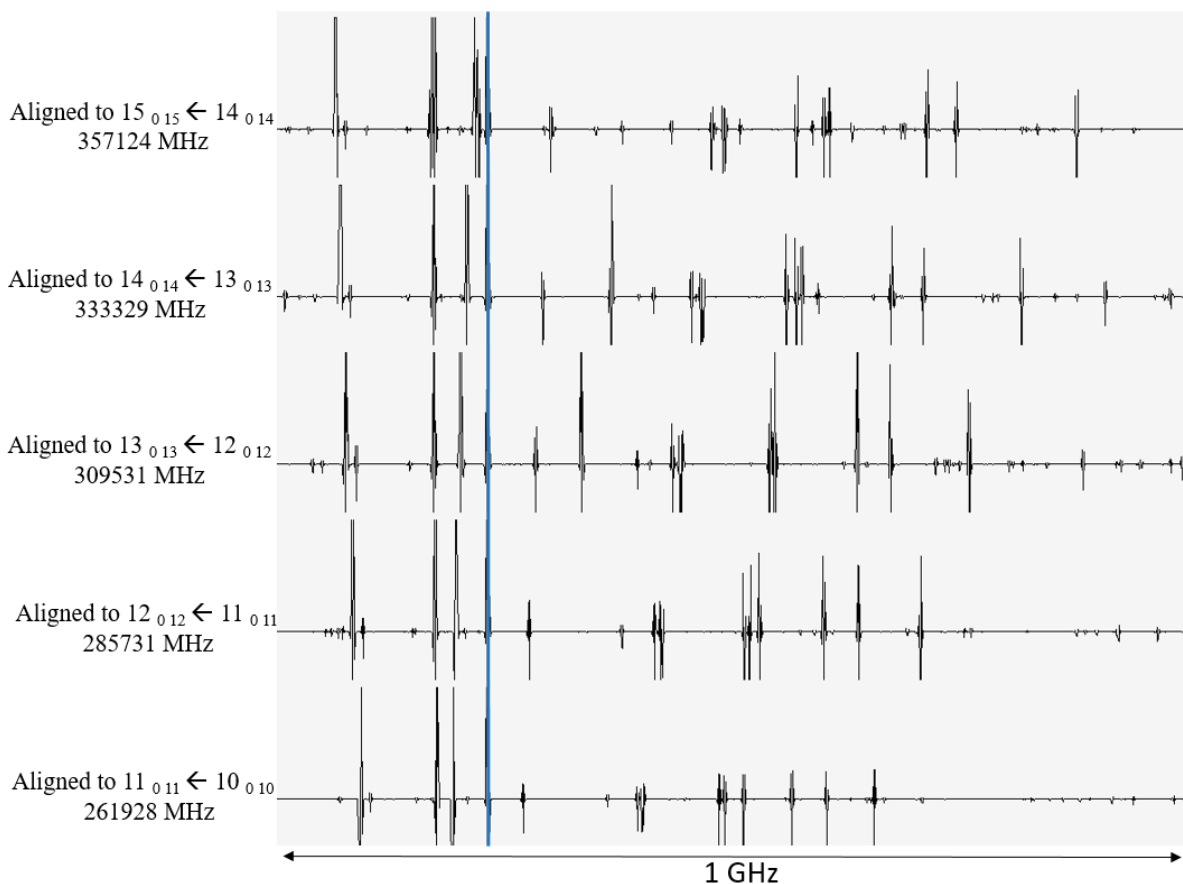


Figure 5.8 A Loomis-Wood plot with each trace of the spectrum centered on the $K = 0$ transitions for the ground vibrational state of HN_3 (vertical line). Numerous other series can readily be recognized in this plot, with each series being a specific K value in the a -type R-branches of either a vibrational satellite or isotopologue of HN_3 .

The Loomis-Wood plots built using our ~ 100 GHz long scans of HN_3 and DN_3 and centered on known or predicted a -type transitions allowed us to pick out roughly 100 series each for both HN_3 and DN_3 . Generally ~ 5 transitions for each series could be observed in our spectrometer's optimal range of 260-360 GHz, on which the Loomis-Wood plots were based. From these initial points, we could extrapolate and predict where to find additional transitions to higher and lower frequencies in the 'extended range' of our spectrometer. These series belong to a particular K value of a -type R-branches of either to an isotopologue (generally HN^{15}NN or

DN¹⁵NN), or to one of the eight observable vibrational states. Again, these series are mixed together, have a wide range of intensities, and are often heavily perturbed, but the Loomis-Wood plots are extremely useful for grouping individual unassigned transitions into series, which may or may not be assigned to a particular K and vibrational state at that point.

Linear plots of a -type R-branch transitions

A tool we have found to be useful in confirming that individual transitions belong to an a -type R-branch series and then assigning that series to the correct K value and vibrational state is a plot where the transition frequency of each transition is divided by J_{upper} and graphed vs. J_{upper}^2 . Fortunately there is a wide enough gap between the a -type R-branches, so that there is no ambiguity as to the J value for a given transition, and hypothetically, if there were, these graphs would quickly address that. An example of one of these transition frequency/ J_{upper} vs J_{upper}^2 plots is shown in Figure 5.9 for the $K = 0$ transitions of the ground vibrational state of HN₃. Internally we refer to these as ‘linear plots’ for the a -type R-branches, and indeed the points generally lie on straight line with a very high R^2 value, although occasionally a quadratic polynomial is a more accurate model. The slope and the intercept of the linear trendlines in these plots provide a useful fingerprint for each series. Firstly, the slope and intercept of these plots is dependent on the K value. Figure 5.9 through Figure 5.16 show plots for the series with $K = 0, 1(-), 1(+), 2(-), 2(+), 3(\text{average of } + \text{ and } -), 4, \text{ and } 5$ of the ground vibrational state of HN₃. These transitions are known from the previous chapter to suffer minimal perturbations, and thus they provide good examples of typical behavior for this type of plot for these series. As can be seen, the trendline for the $K = 0$ series has the steepest negative slope and $K = 2(+)$ has a distinctively shallow slope. For many vibrational states the $K = 2(+)$ slope is positive. The other series have similar moderate negative

slopes. The intercepts gradually decrease more or less linearly (slope $-2A_{JK}$) with increasing K . Figure 5.17 is a summary of all assigned a -type R-branch series for the ground vibrational state. The graphs of the intercepts vs. K^2 show characteristic, generally smooth curves. The graphs of the slopes vs K^2 show characteristic effects of asymmetry at $K = 0$, $K = 1$, and $K = 2$, and then settle into an almost flat (at $-4A_J$) straight line at higher K values. Those K states involved in strong local perturbations usually show clear departure from this general behavior for both the slope and intercept plots, and will be discussed in more detail below. It should be noted that the intercepts for $K = 2(+)$ and $K = 2(-)$ are equal (within experimental error) but those for $K = 1(+)$ and $K = 1(-)$ are very different. In the latter case, it is the average that is shown in all the subsequent plots. The smoothness of the curves for unperturbed states serves to confirm the assignment of the series to the correct vibrational state and K value. We have confidently assigned the a -type R-branch series for six vibrational states of HN_3 ; their summaries are shown in Figure 5.17 through Figure 5.22. We have confidently assigned the a -type R-branch series for all eight observable vibrational states of DN_3 ; those summaries are shown in Figure 5.23 through Figure 5.30. The previously discussed ambiguity in the assignment of the $K = 7$ lines for ν_6 and $K = 5$ lines for ν_4 is reflected in the missing data points in Figure 5.25 and Figure 5.26.

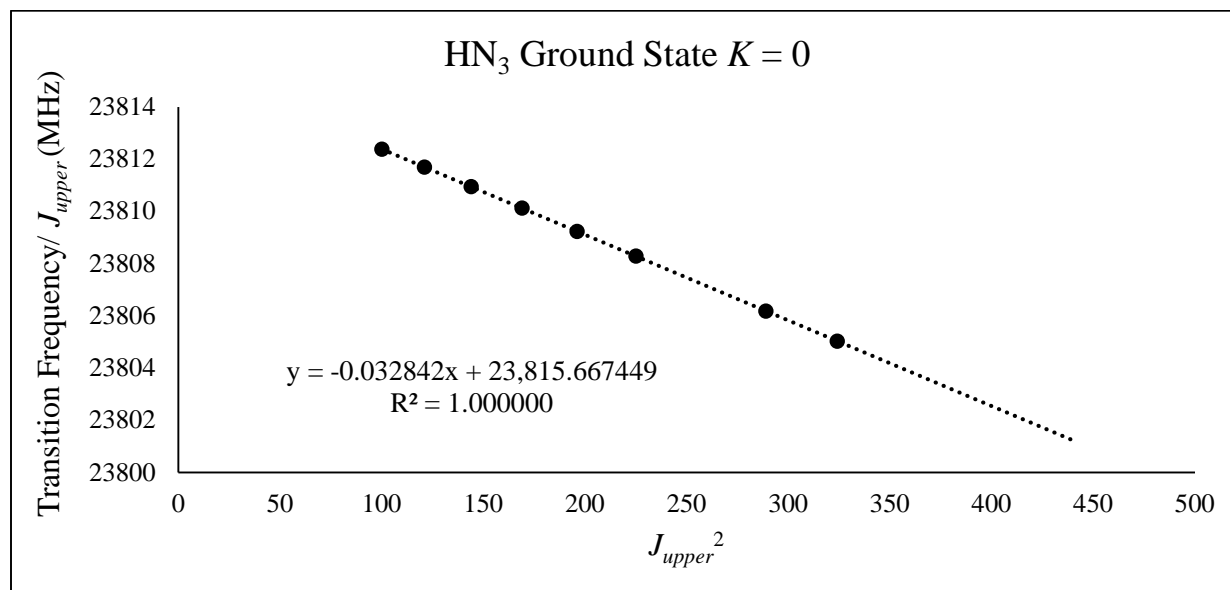


Figure 5.9 Plot of transition frequencies / J_{upper} vs. J_{upper}^2 for the $K = 0$ series for the ground vibrational state of HN₃.

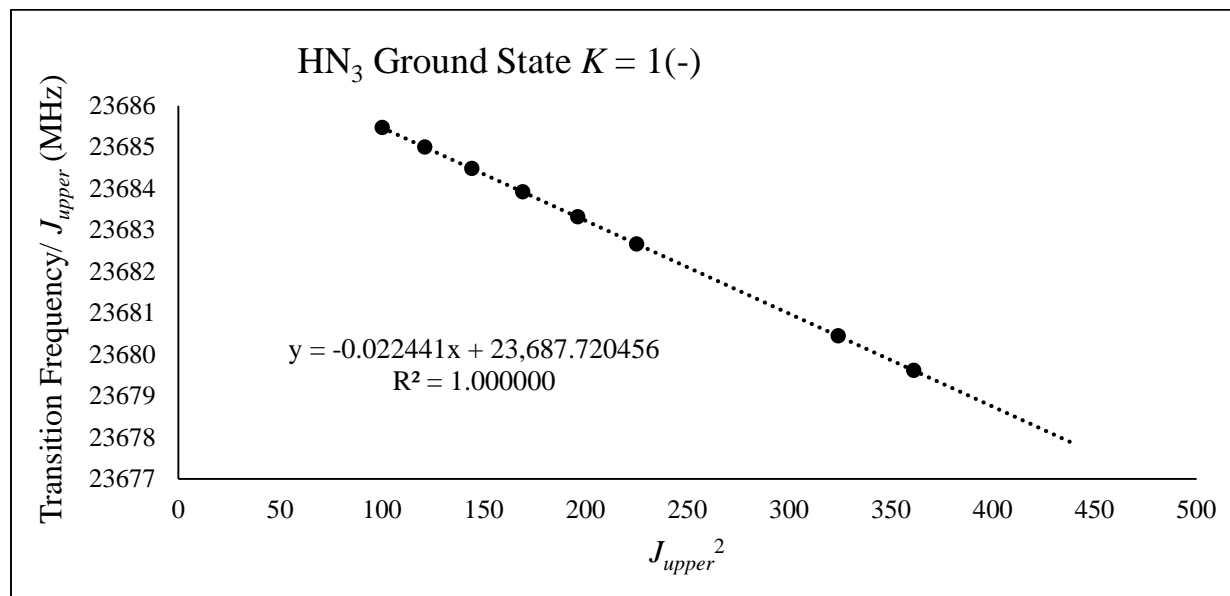


Figure 5.10 Plot of transition frequencies / J_{upper} vs. J_{upper}^2 for the $K = 1(-)$ series for the ground vibrational state of HN₃.

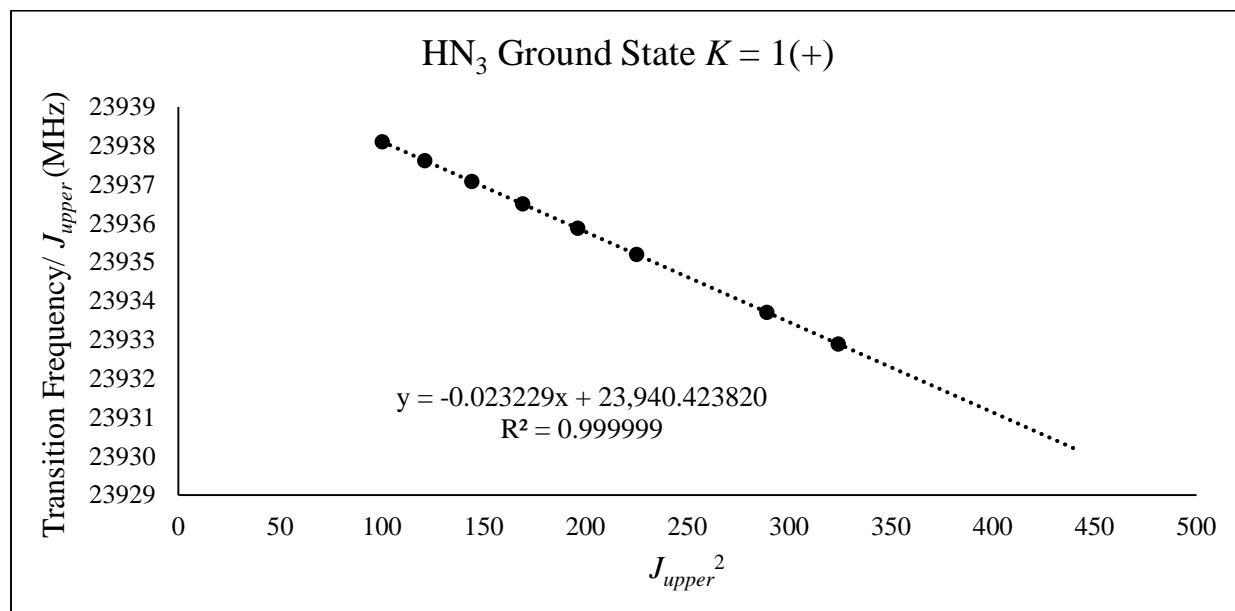


Figure 5.11 Plot of transition frequencies / J_{upper} vs. J_{upper}^2 for the $K = 1(+)$ series for the ground vibrational state of HN₃.

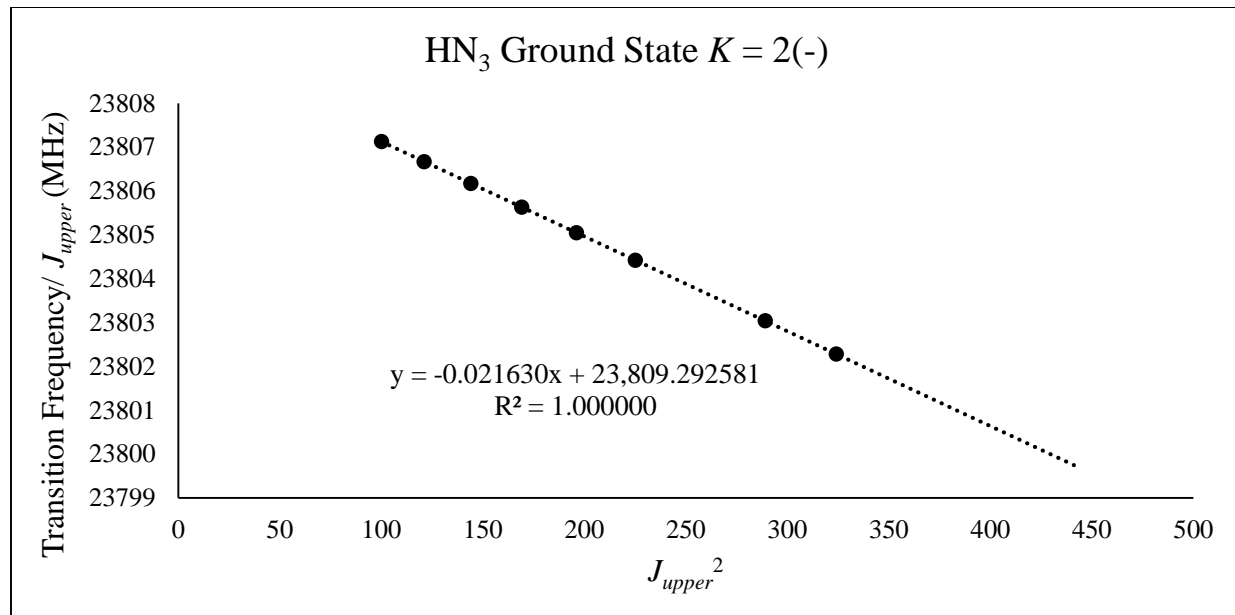


Figure 5.12 Plot of transition frequencies / J_{upper} vs. J_{upper}^2 for the $K = 2(-)$ series for the ground vibrational state of HN₃.

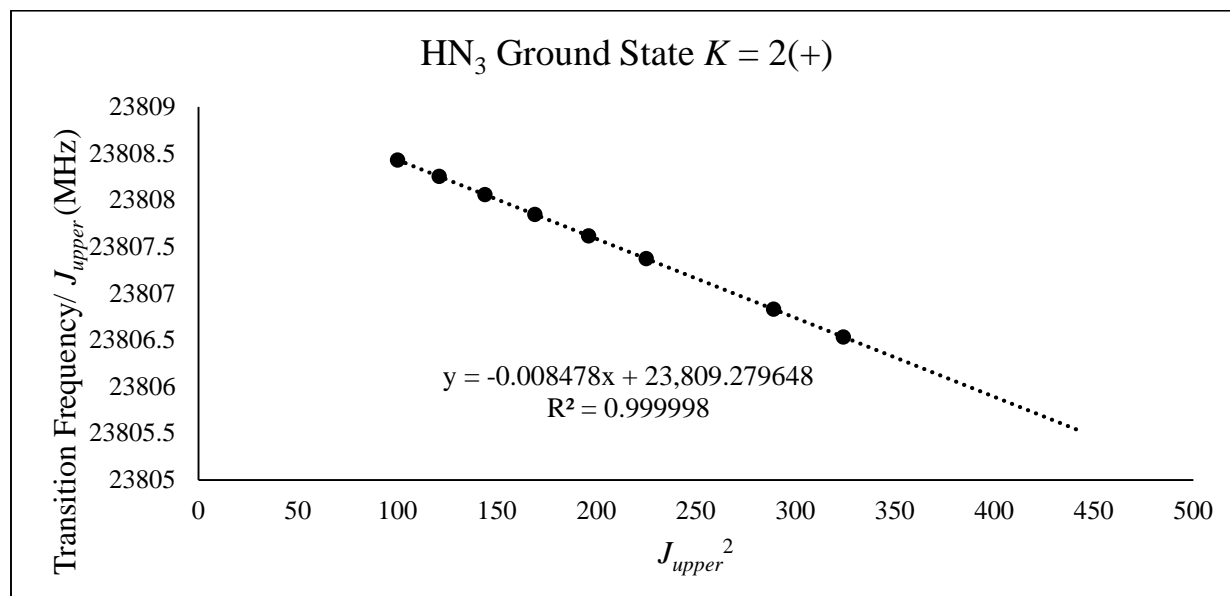


Figure 5.13 Plot of transition frequencies / J_{upper} vs. J_{upper}^2 for the $K = 2(+)$ series for the ground vibrational state of HN₃.

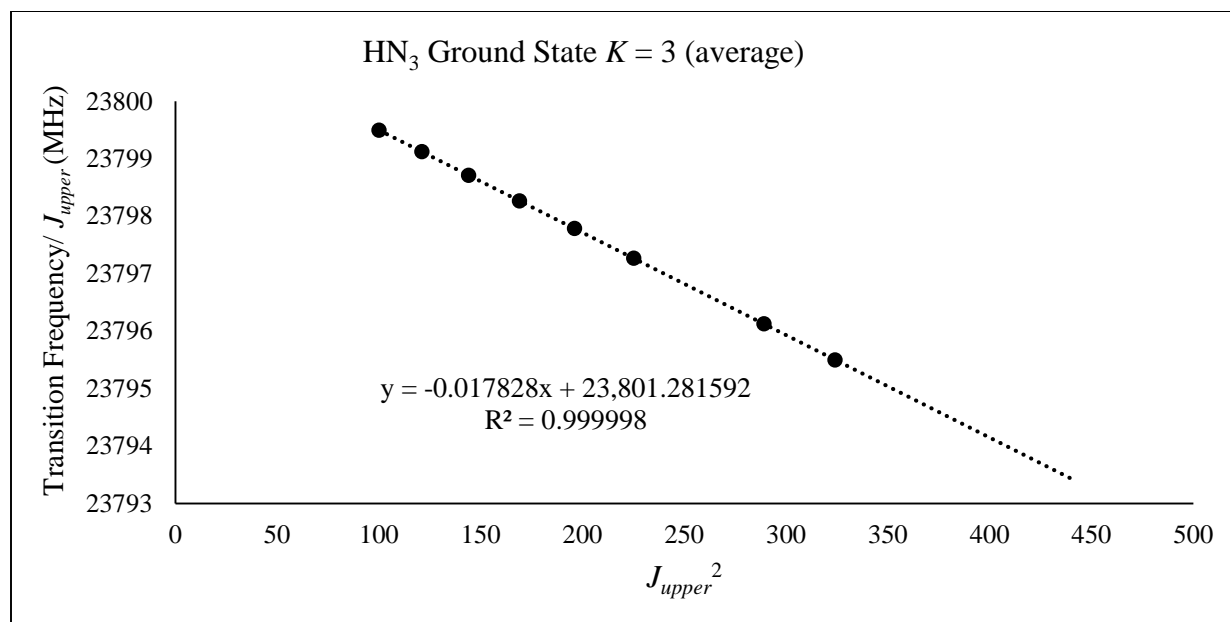


Figure 5.14 Plot of transition frequencies / J_{upper} vs. J_{upper}^2 for the $K = 3$ series for the ground vibrational state of HN₃.

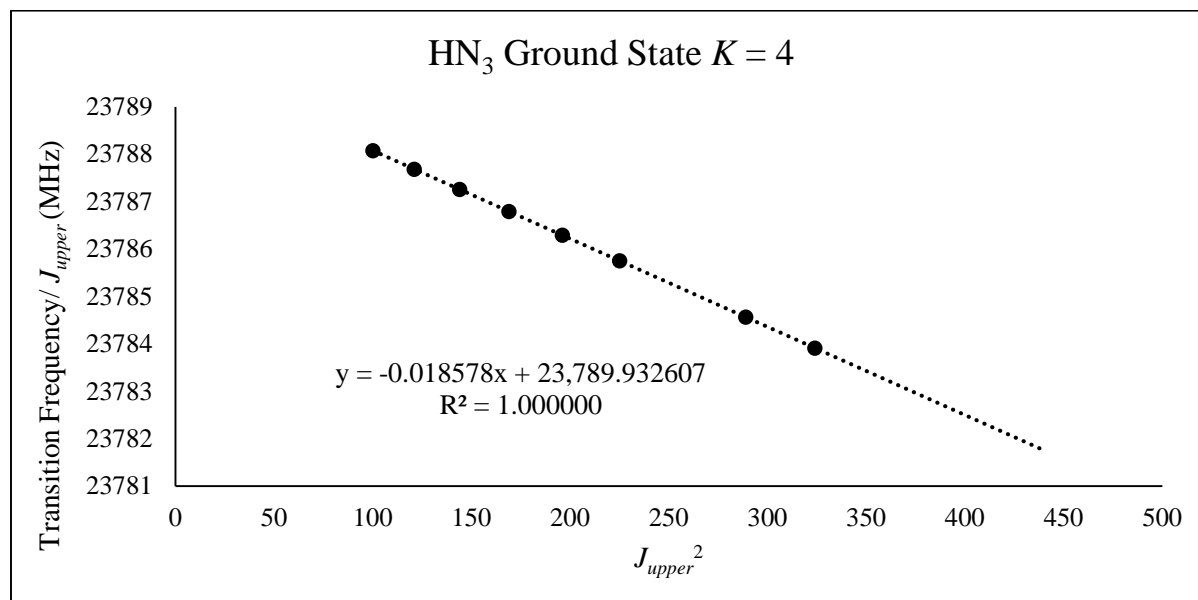


Figure 5.15 Plot of transition frequencies / J_{upper} vs. J_{upper}^2 for the $K = 4$ series for the ground vibrational state of HN₃.

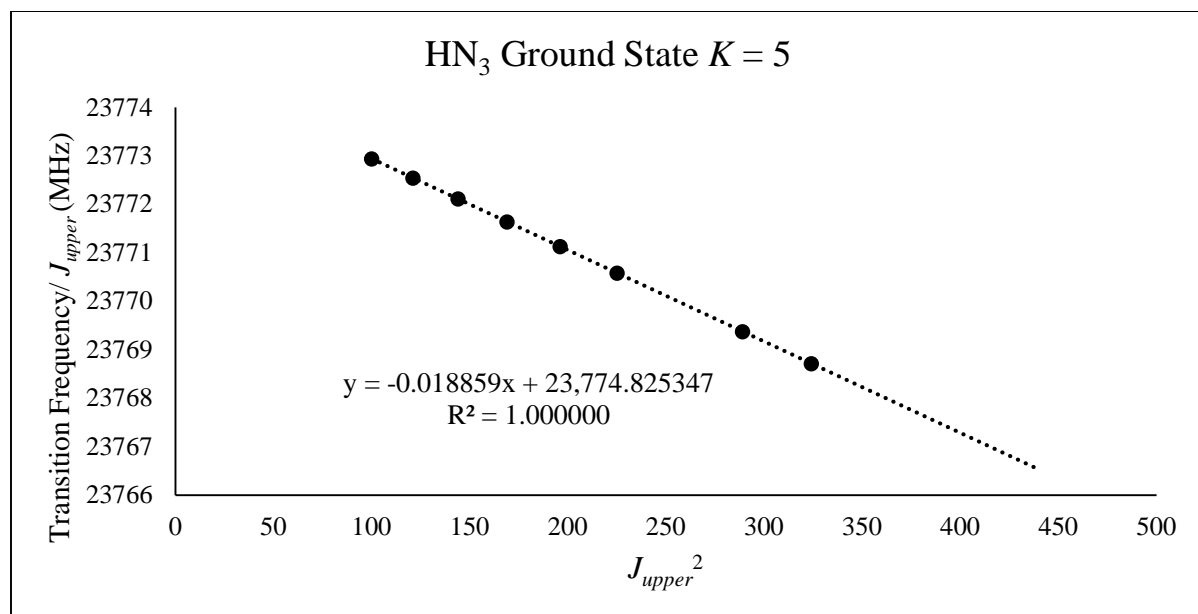


Figure 5.16 Plot of transition frequencies / J_{upper} vs. J_{upper}^2 for the $K = 5$ series for the ground vibrational state of HN₃.

HN₃ Ground State Summary

Series (K)	N lines	Slope of 'linear plot'	Intercept of 'linear plot'	Lowest frequency transition	Highest frequency transition
0	8	-0.03284	23815.67	238123.8149	428490.4688
1(-)	8	-0.02244	23687.72	236854.7728	449912.7743
1(+)	8	-0.023229	23940.42	239380.9898	430792.1128
2(-)	8	-0.02163	23809.29	238071.294	428441.0977
2(+)	8	-0.00848	23809.28	238084.3138	428517.5643
3	8	-0.01782	23801.28	237994.9794	428319.0310
4	8	-0.01858	23789.93	237880.7415	428110.4117
5	8	-0.01886	23774.83	237729.3884	427836.8656
6	6	-0.01877	23755.86	237539.7762	356274.4663
7	6	-0.01802	23722.55	237207.4759	355777.4642
8	5	0.02995	23574.35	259357.3838	353715.8947
9	4	-0.027706	23784.61	261594.0292	356675.9539
10	3	-0.02626	23723.93	284641.7563	355770.2455

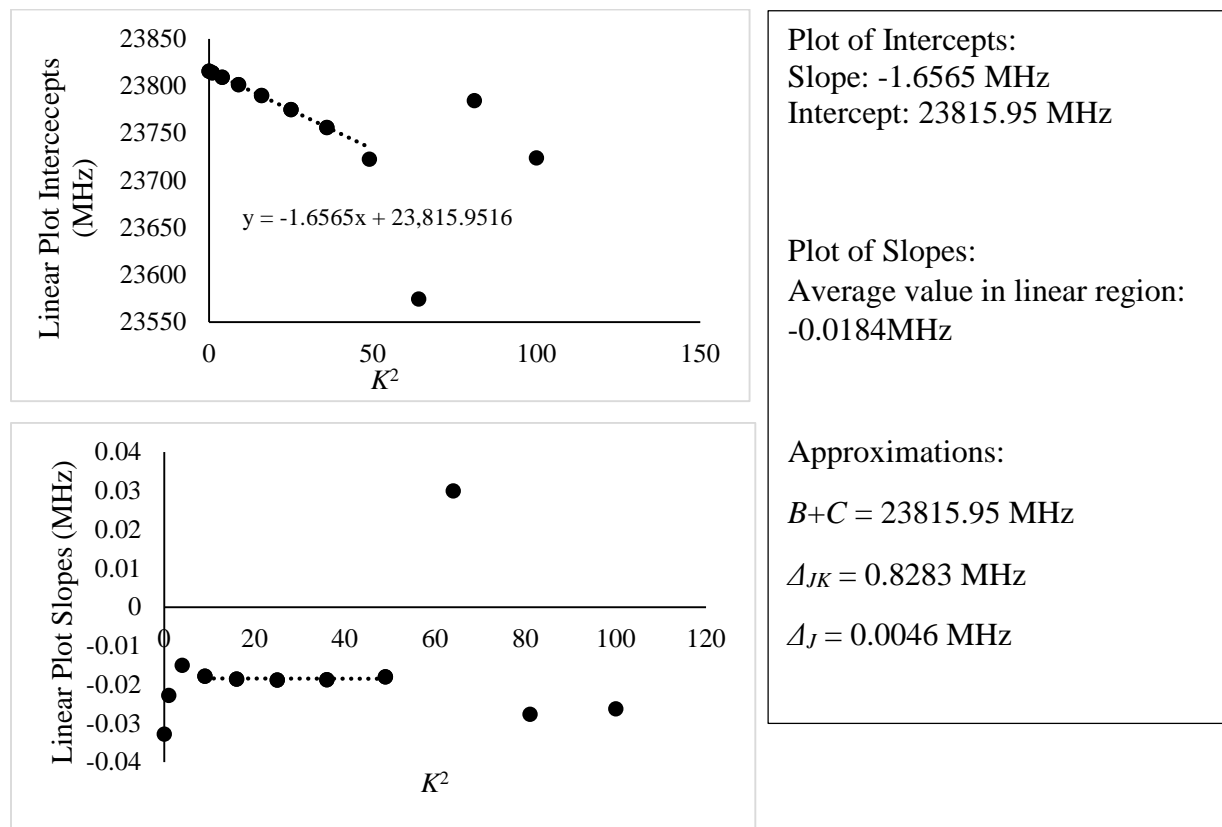


Figure 5.17 Summary of the *a*-type R-branch transitions assigned for the ground state of HN₃.

HN₃ ν_5

Series (K)	N lines	Slope of 'linear plot'	Intercept of 'linear plot'	Lowest frequency transition	Highest frequency transition
0	8	-0.06089	23844.34	238382.2828	428842.5802
1(-)	8	-0.02261	23752.02	237497.8395	427405.0188
1(+)	7	-0.02952	23952.66	239497.0917	407050.2015
2(-)	8	-0.02870	23848.67	238457.9842	429108.6725
2(+)	8	0.01023	23848.65	238496.6565	429335.1942
3	6	-0.01587	23843.67	238420.8593	357601.5281
4	8	-0.01867	23836.84	238349.7520	428954.2515
5	7	-0.01547	23828.99	238274.3378	405016.6407
6	6	-0.01861	23825.78	238239.1481	357323.8320
7	6	-0.06763	23928.93	239222.0368	358706.2966
8	5	-0.01040	23650.25	260138.9087	354718.6405
9	5	0.02665	23606.47	259706.2379	354186.4533

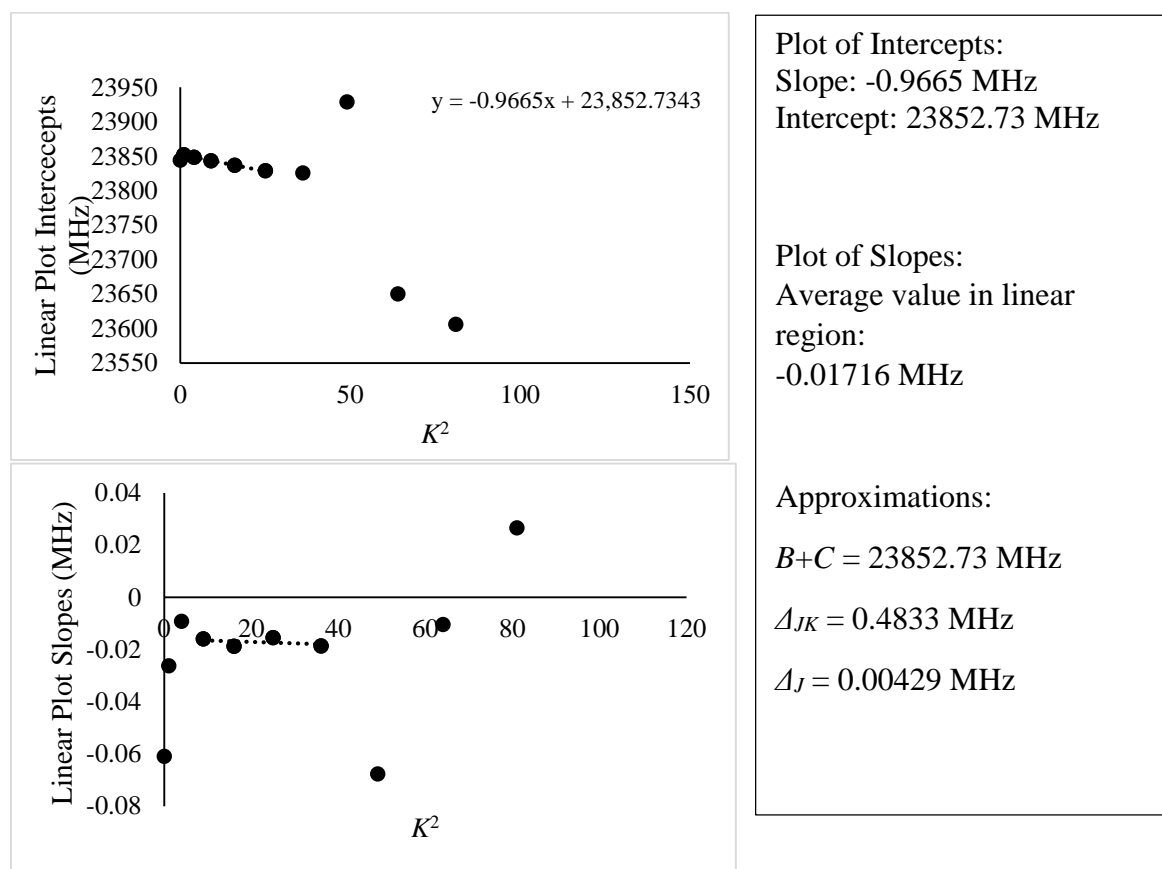


Figure 5.18 Summary of the a -type R-branch transitions assigned for the ν_5 state of HN₃.

HN₃ ν_6

Series (K)	N lines	Slope of 'linear plot'	Intercept of 'linear plot'	Lowest frequency transition	Highest frequency transition
0	8	-0.01993	23837.53	238355.3534	428959.3083
1(-)	8	-0.01878	23755.86	237539.7723	427495.8498
1(+)	8	-0.01958	23915.32	239133.6294	430361.5672
2(-)	8	-0.01926	23828.83	238269.0036	428806.4627
2(+)	8	-0.01551	23828.82	238272.7390	428828.2812
3	8	-0.02248	23817.92	238156.8067	428591.6070
4	8	-0.02064	23802.62	238005.5807	428326.8015
5	7	-0.02018	23783.55	237815.4084	404221.3306
6	6	-0.01853	23742.25	237403.9598	356071.1905

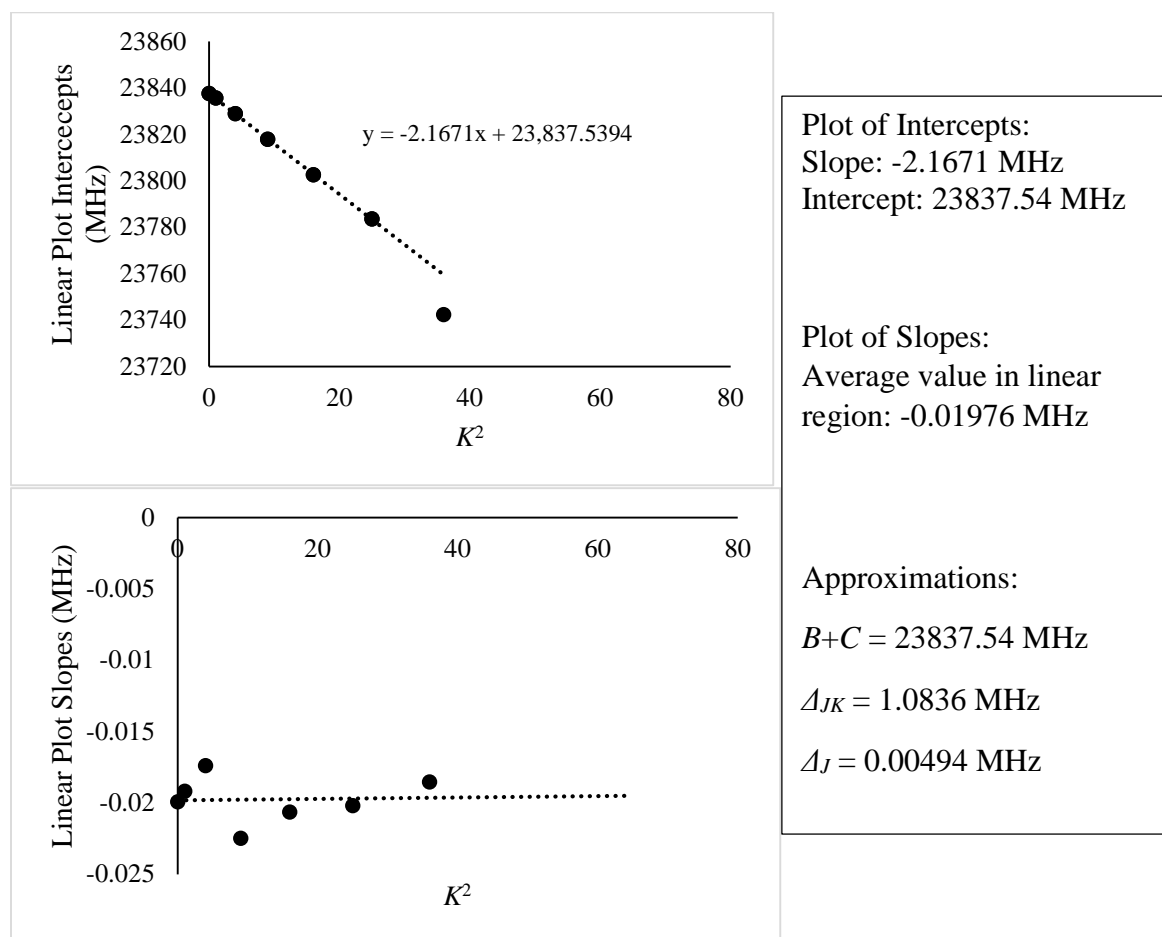


Figure 5.19 Summary of the *a*-type R-branch transitions assigned for the ν_6 state of hydrazoic acid.

HN₃ ν_4

Series (K)	N lines	Slope of 'linear plot'	Intercept of 'linear plot'	Lowest frequency transition	Highest frequency transition
0	7	-0.03535	23715.80	237122.6382	379308.2883
1(-)	6	0.02991	23656.95	236599.6909	354955.6379
1(+)	6	-0.00977	23850.34	238493.8789	357722.5033
2(-)	6	-0.01918	23706.49	237045.7439	355532.6609
2(+)	6	-0.00527	23706.45	237059.2957	355579.0840
3(-)	5	0.02266	23617.74	259824.9439	354342.0823
3(+)	5	0.02347	23617.66	259825.2454	354343.7733
4	5	-0.01671	23724.44	260946.5936	355810.2077
5	5	-0.01688	23682.22	260481.9209	355176.2793
6	4	-0.01831	23650.56	283775.1174	354696.6292

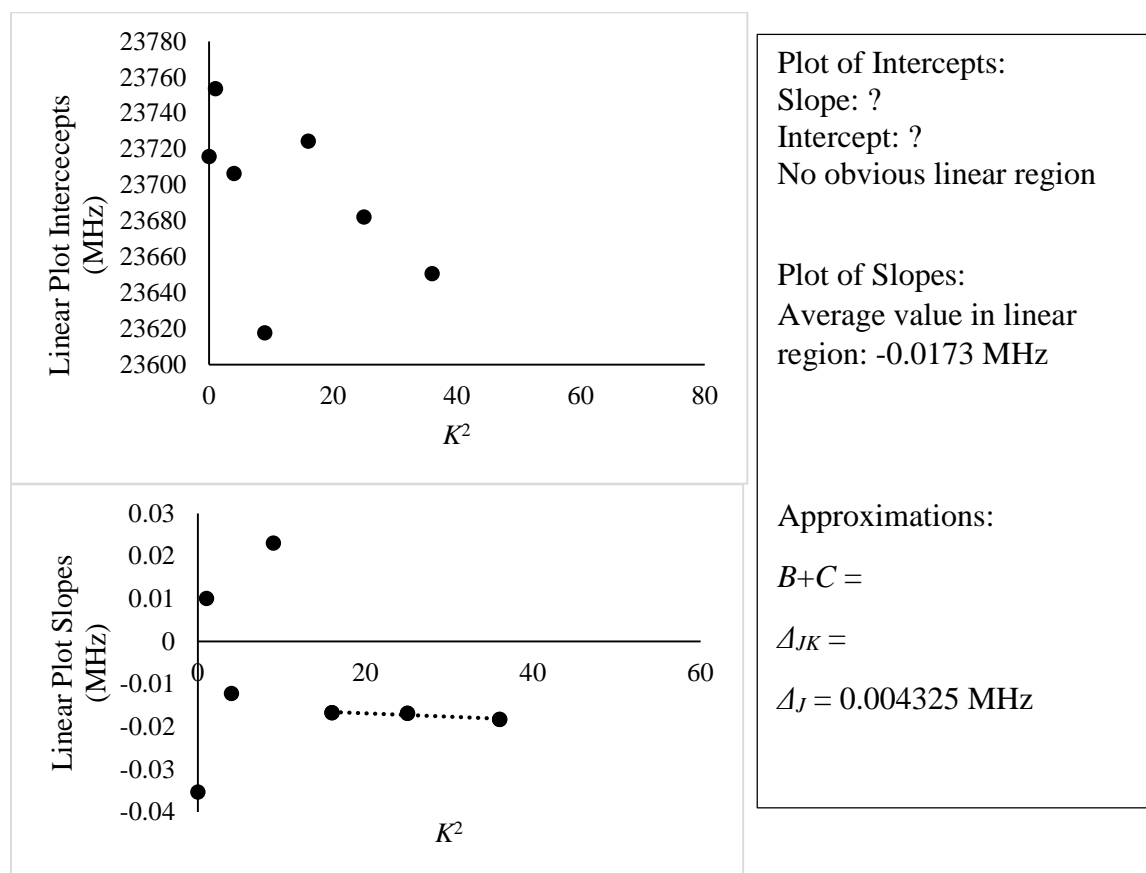


Figure 5.20 Summary of the a -type R-branch transitions assigned for the ν_4 state of HN₃

HN₃ 2ν₅

Series (K)	N lines	Slope of 'linear plot'	Intercept of 'linear plot'	Lowest frequency transition	Highest frequency transition
0	8	-0.07482	23882.40	238749.2912	429447.0462
1(-)	7	-0.03348	23751.25	237479.0536	403606.8238
1(+)	6	-0.03631	24010.37	264065.7054	407997.8588
2(-)	8	-0.02950	23884.44	238814.9159	429747.9503
2(+)	8	0.02212	23884.43	238866.3282	430047.9722
3(-)	8	-0.01432	23883.68	238822.3918	429822.7527
3(+)	8	-0.01375	23883.62	238822.3918	429827.0773
4	8	-0.01652	23877.52	238758.6365	429698.9002
5	7	-0.01757	23867.56	238658.2393	405662.2173
6	5	-0.02745	23853.78	238511.1724	357714.9746
7	5	-0.01568	23839.94	262218.4700	357546.1964
8	5	-0.01889	23825.31	262053.2849	357315.9553

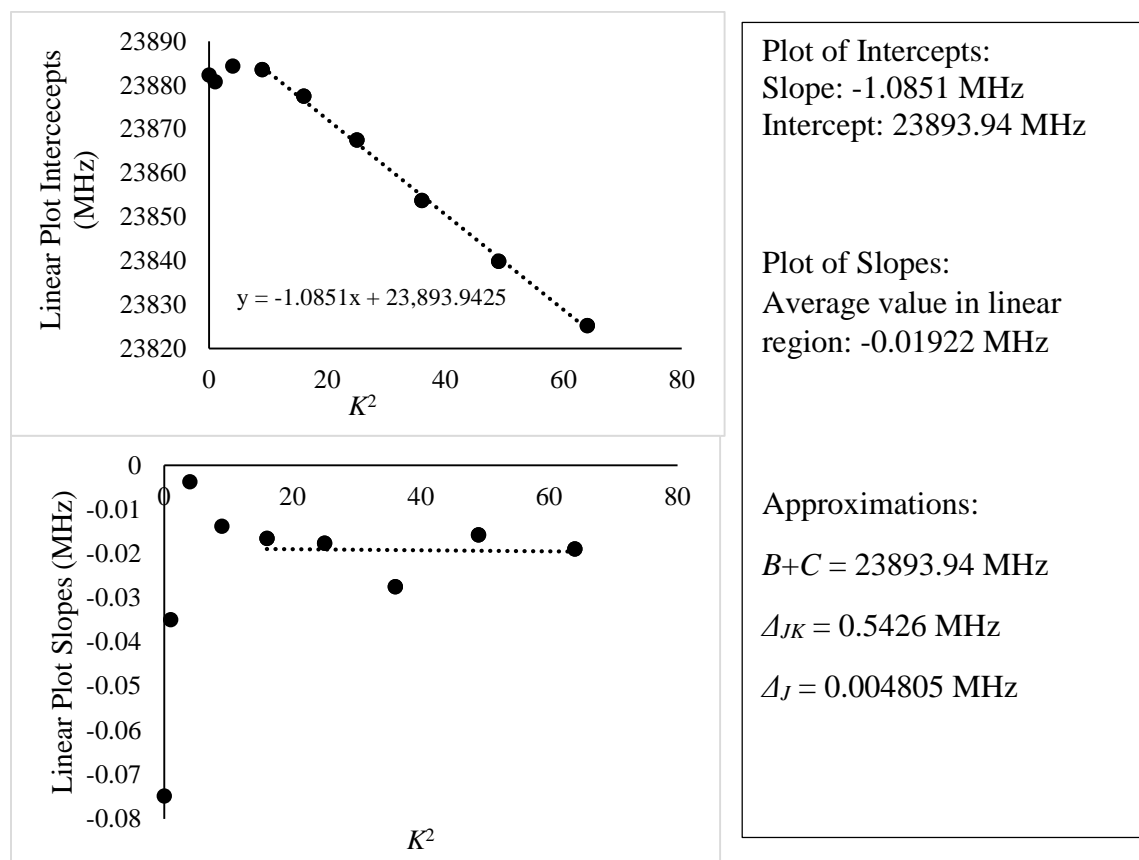


Figure 5.21 Summary of the *a*-type R-branch transitions assigned for the 2ν₅ state of HN₃.

HN₃ ν_3

Series (K)	N lines	Slope of 'linear plot'	Intercept of 'linear plot'	Lowest frequency transition	Highest frequency transition
0	6	-0.03211	23800.90	237976.8819	356905.1045
1(-)	6	-0.03039	23730.36	237273.3286	355852.9108
1(+)	6	-0.02317	23913.38	239110.6237	358622.4789
2(-)	6	-0.04853	23871.27	238664.2134	357905.3545
2(+)	6	-0.02782	23871.91	238691.0358	357984.4335
3	6	-0.01853	23742.25	237403.9598	356071.1905
4	5	0.01951	23727.61	261028.3635	355978.3902
5	5	-0.01873	23745.62	261176.8605	356121.0378
6	5	-0.01809	23729.17	260996.9857	355876.7917

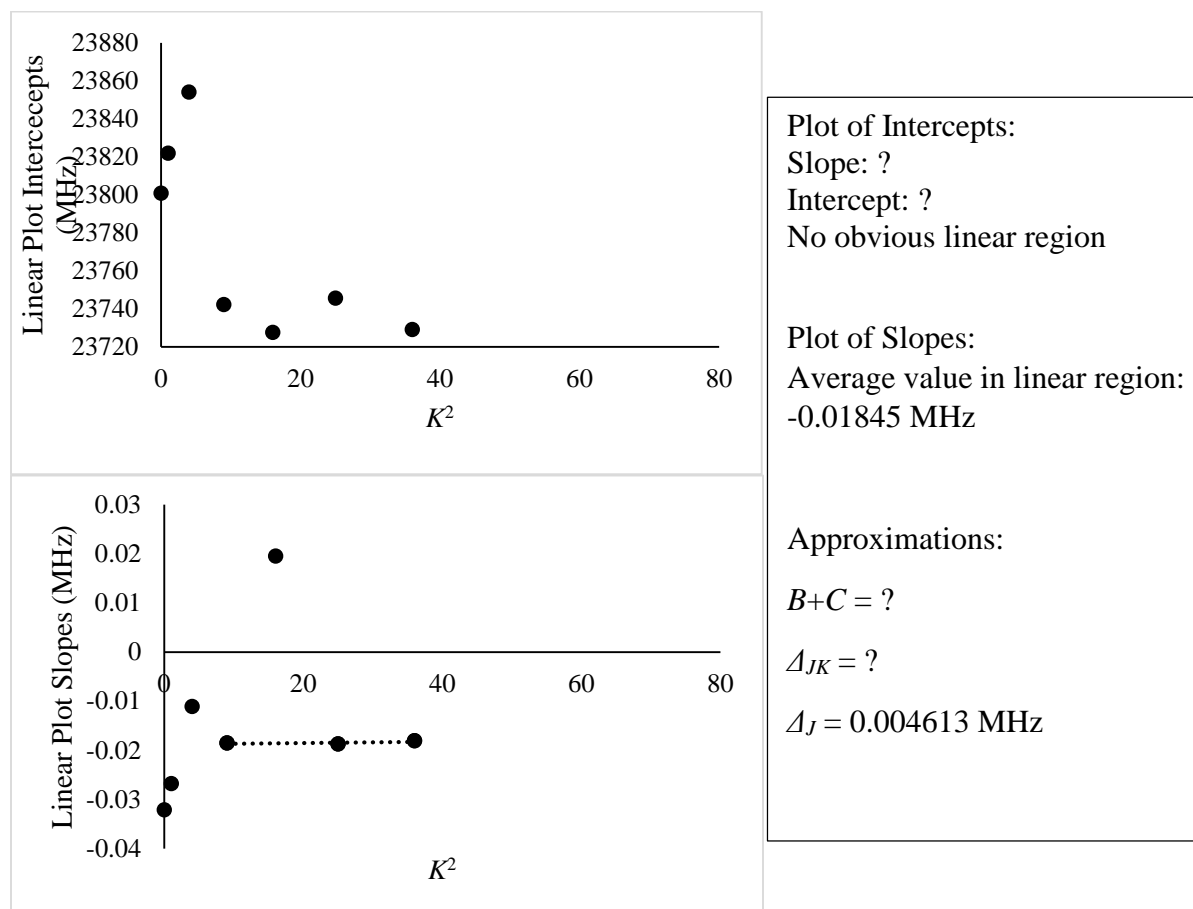


Figure 5.22 Summary of the a -type R-branch transitions assigned for the ν_3 state of hydrazoic acid.

DN₃ Ground

Series (K)	N lines	Slope of 'linear plot'	Intercept of 'linear plot'	Lowest frequency transition (MHz)	Highest frequency Transition (MHz)
0	10	-0.07210	22315.78	245377.71670	445739.05633
1(-)	10	-0.02967	22122.50	243308.1402	442213.01917
1(+)	10	-0.03182	22507.35	247538.3916	449892.28967
2(-)	10	-0.02595	22312.27	245400.4331	446037.71017
2(+)	10	0.02887	22312.26	245473.1892	446475.9095
3(-)	9	-0.01038	22307.81	267675.5935	446073.0728
3(+)	9	-0.00951	22307.68	267675.9359	446077.7355
4	10	-0.01316	22301.39	245297.8171	445922.6483
5	10	-0.01452	22293.12	245204.9621	445746.2018
6	10	-0.01519	22282.79	245090.4126	445534.2341
7	10	-0.01552	22270.19	244951.4284	445279.69167
8	9	-0.01571	22254.97	244783.7117	444973.6433
9	6	-0.01573	22236.42	244579.673	355718.2878
10	5	-0.01430	22213.08	266532.2924	355350.7632
11	4	-0.01418	22182.01	288334.9416	354853.9651

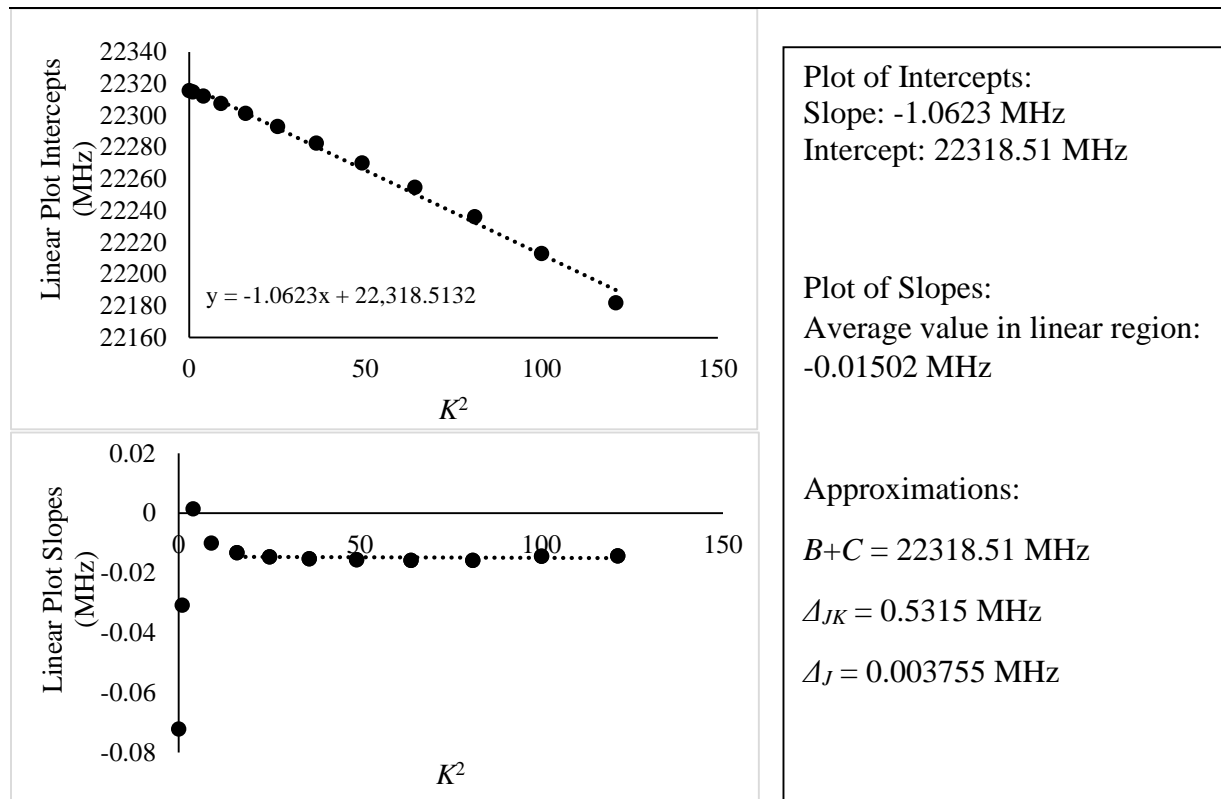


Figure 5.23 Summary of the *a*-type R-branch transitions assigned to the ground state of DN₃.

DN₃ ν_5

Series (K)	N lines	Slope of 'linear plot'	Intercept of 'linear plot'	Lowest frequency transition	Highest frequency transition
0	8	-0.10624	22356.64	245781.8391	424048.0748
1(-)	8	-0.03889	22163.25	243744.0949	420835.2750
1(+)	8	-0.04235	22548.72	247979.4581	428134.9656
2(-)	8	-0.03432	22353.80	245846.1501	424486.8785
2(+)	8	0.05613	22353.83	245966.6098	425107.2483
3(-)	9	-0.00678	22350.20	245842.9632	424603.1256
3(+)	9	-0.00586	22350.10	245843.4470	424612.0475
4	8	-0.01166	22345.31	245782.9367	424480.9768
5	8	-0.01369	22339.06	245711.4155	424348.2581
6	8	-0.01473	22331.45	245626.3367	424196.5013
7	6	-0.01531	22322.52	245527.3184	357097.6815
8	6	-0.01691	22312.61	245416.2294	356932.5214

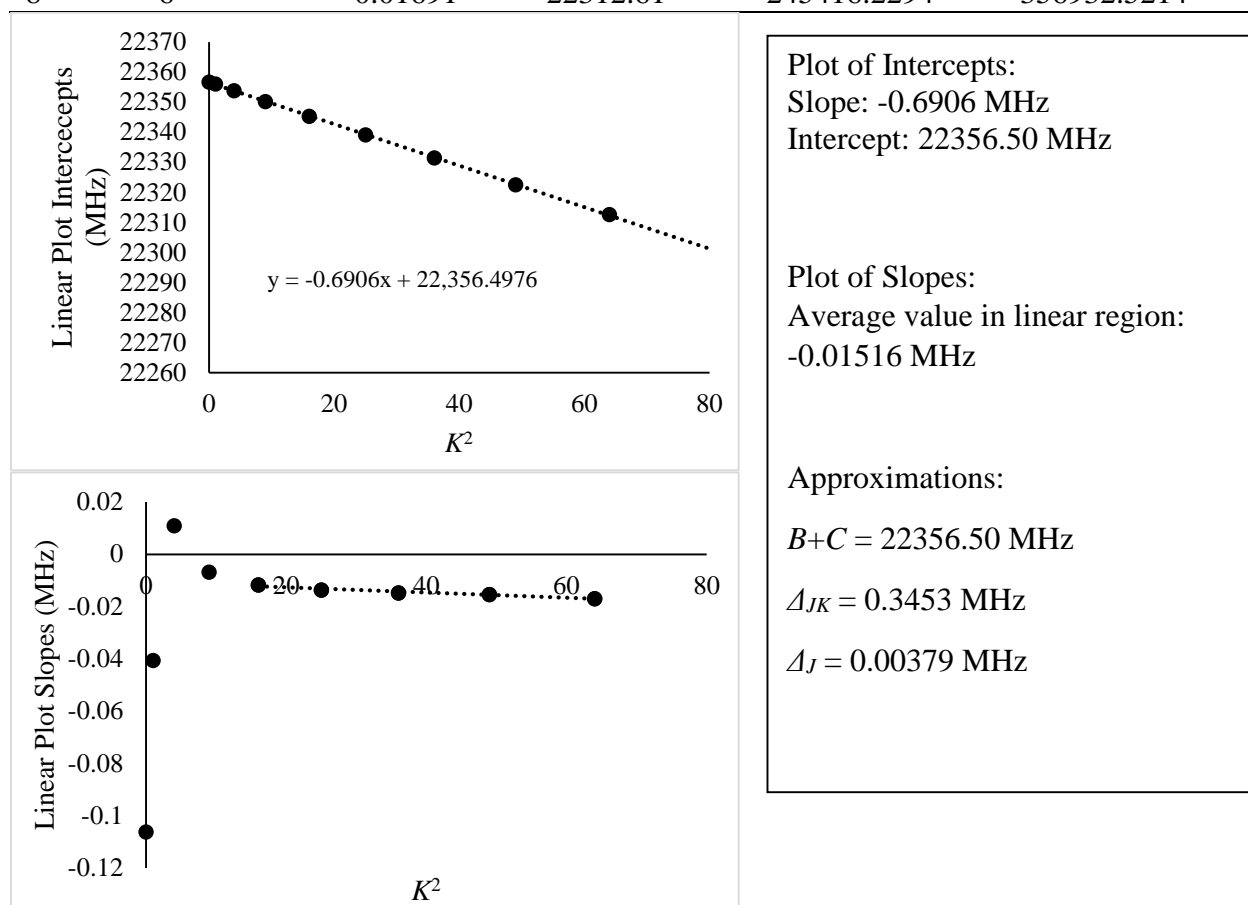


Figure 5.24 Summary of the a -type R-branch transitions assigned to the ν_5 state of DN₃.

DN₃ ν_6

Series (K)	N lines	Slope of 'linear plot'	Intercept of 'linear plot'	Lowest frequency transition	Highest frequency transition
0	9	-0.04695	22336.75	245641.7406	424076.1788
1(-)	9	-0.02284	22167.79	243815.32998	421031.43316
1(+)	9	-0.02459	22504.07	247512.00954	427408.535
2(-)	8	-0.02153	22333.13	245635.75337	424181.7981
2(+)	8	0.00988	22333.11	245677.32439	424396.8626
3(-)	7	-0.01283	22328.04	245591.26689	424144.7025
3(+)	6	-0.01249	22327.99	245591.26689	424146.10717
4	8	-0.01473	22320.57	245506.70964	423989.83867
5	7	-0.01556	22310.76	245397.61784	423797.74517
6	7	-0.01602	22298.35	245260.4926	423558.69717
7	?				
8	4	-0.01562	22266.82	267174.7543	333949.4601
9	5	-0.01573	22249.59	266967.8243	355928.7429

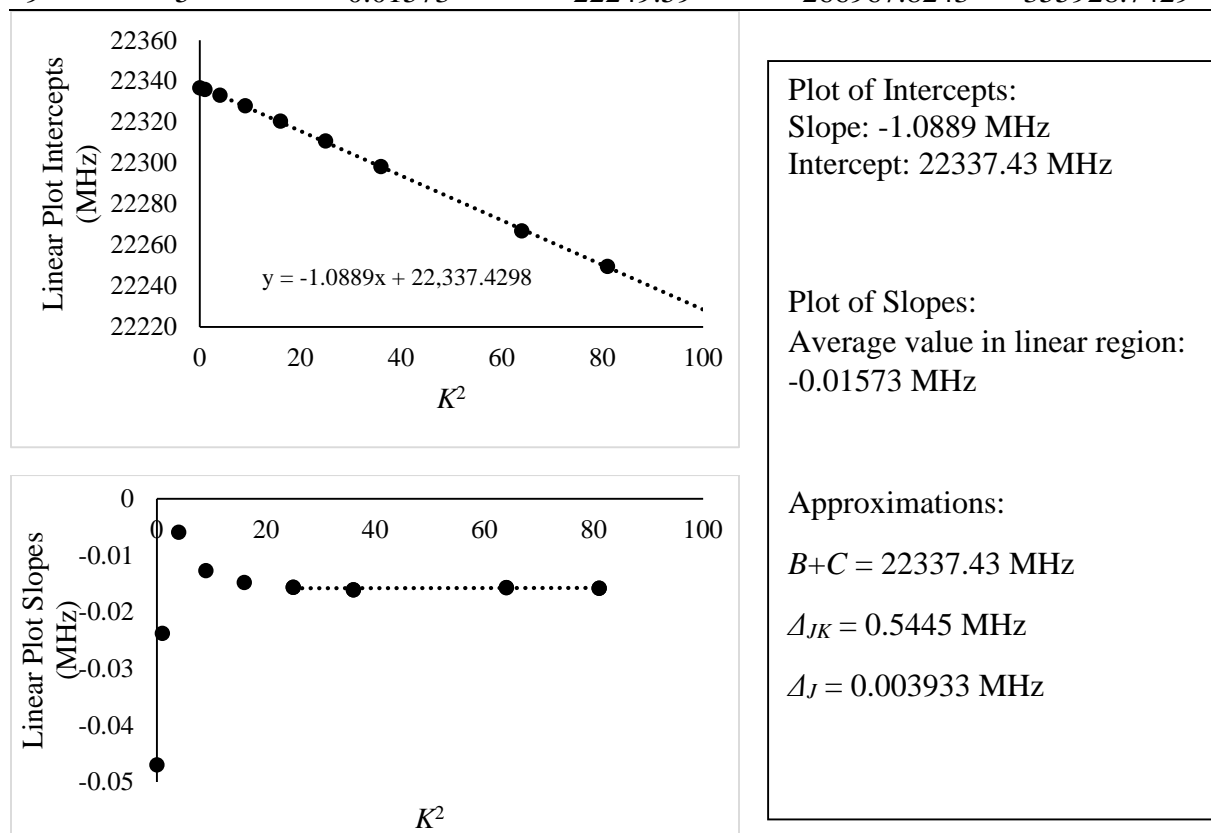


Figure 5.25 Summary of the a -type R-branch transitions assigned to the ν_6 state of DN₃

DN₃ ν_4

Series (K)	N lines	Slope of 'linear plot'	Intercept of 'linear plot'	Lowest frequency transition	Highest frequency transition
0	7	-0.07504	22301.18	245213.0781	356511.5141
1(-)	6	-0.03074	22096.97	243025.7523	353425.6757
1(+)	6	-0.03270	22504.24	247503.0842	359933.8645
2(-)	6	-0.02994	22306.03	245326.4254	356773.8449
2(+)	6	0.03490	22306.11	245413.6020	357040.6095
3(-)	6	-0.00981	22292.96	245209.4697	356647.2414
3(+)	6	-0.00893	22292.84	245209.4697	356648.0512
4	6	-0.01274	22283.58	25102.4566	356485.1345
5	6	-0.01580	22281.25	245072.7148	356435.3342
6	6	-0.01555	22265.38	244898.4897	356182.3782
7	4	-0.01371	22248.38	289199.2918	355918.4680
8	5	-0.01958	22226.80	266687.7211	355548.6202

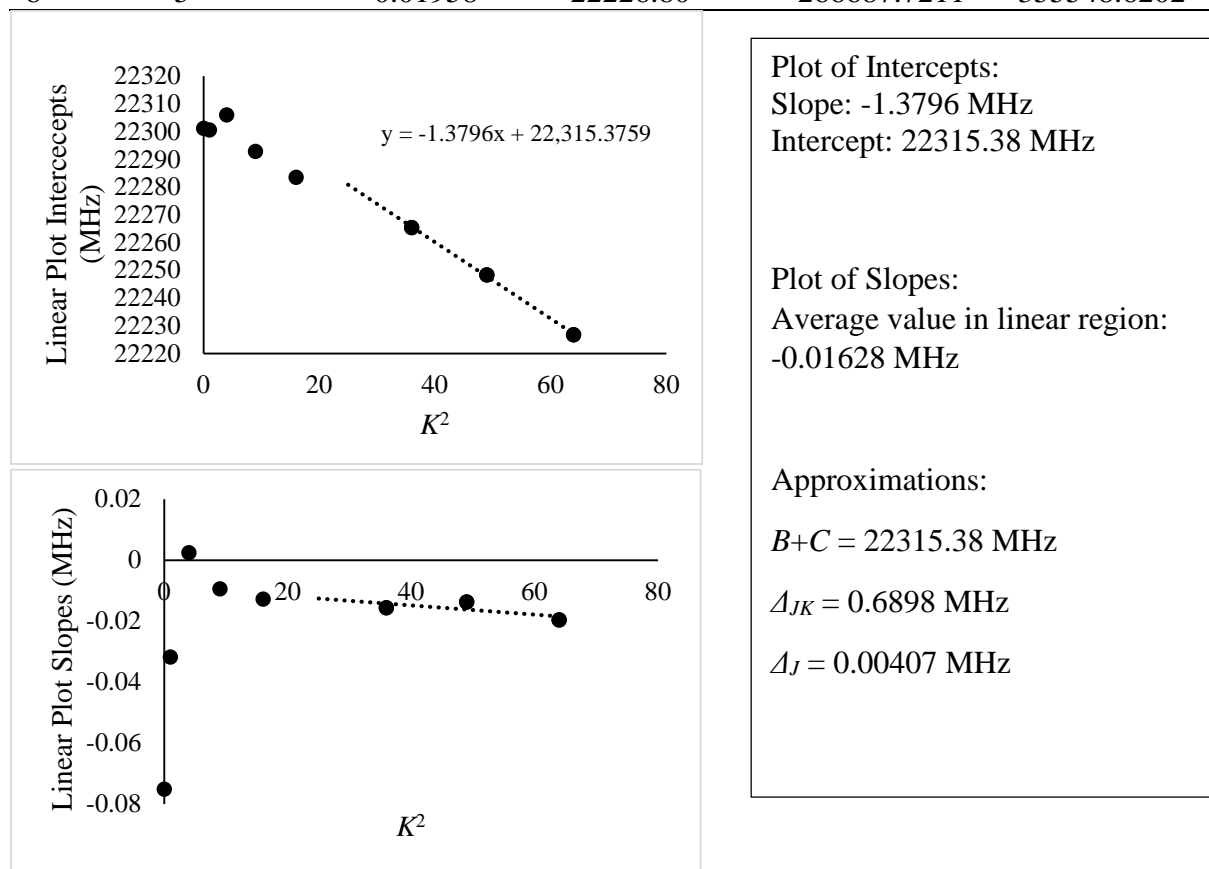


Figure 5.26 Summary of the a -type R-branch transitions assigned to the ν_4 state of DN₃

DN₃ 2ν₅

Series (K)	N lines	Slope of 'linear plot'	Intercept of 'linear plot'	Lowest frequency transition	Highest frequency transition
0	6	-0.14687	22396.05	246161.2961	357735.5944
1(-)	6	-0.04829	22189.98	244025.5351	354841.9318
1(+)	6	-0.05302	22600.57	248535.6512	361391.8657
2(-)	6	-0.03706	22385.28	246188.7811	358012.7121
2(+)	6	0.08490	22385.20	246350.1078	358510.7845
3(-)	6	-0.00407	22390.45	246289.4760	358230.4995
3(+)	6	-0.00132	22390.21	246290.6151	358238.0213
4	6	-0.00971	22387.79	246252.6960	358164.7298
5	6	-0.01293	22383.33	246199.4626	358080.3653
6	6	-0.01495	22378.97	246148.7869	358002.3201

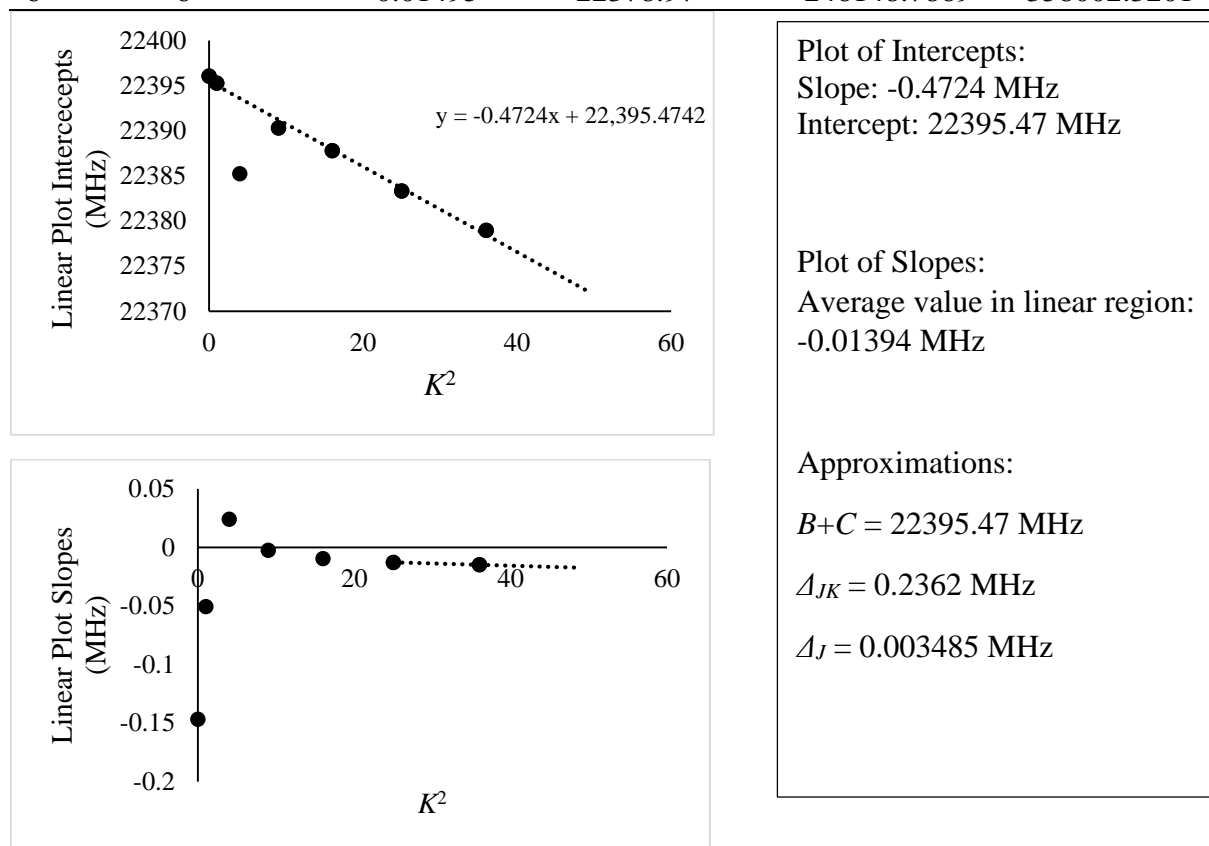


Figure 5.27 Summary of the *a*-type R-branch transitions assigned to the 2ν₅ state of DN₃

DN₃ $\nu_5+\nu_6$

Series (K)	N lines	Slope of 'linear plot'	Intercept of 'linear plot'	Lowest frequency transition	Highest frequency transition
0	6	-0.07848	22373.77	246007.0519	357658.9383
1(-)	6	-0.03293	22237.81	244572.0814	355670.0330
1(+)	6	-0.04286	22506.01	247528.2948	359961.7835
2(-)	5	-0.03617	22369.17	246012.7804	357758.5837
2(+)	5	0.03443	22369.01	246105.579	358045.1588
3					
4	5	-0.01601	22353.80	245870.4553	357595.1152
5	4	-0.01750	22342.19	290410.0284	357403.3961
6	5	-0.01588	22327.36	267900.8856	357172.7122

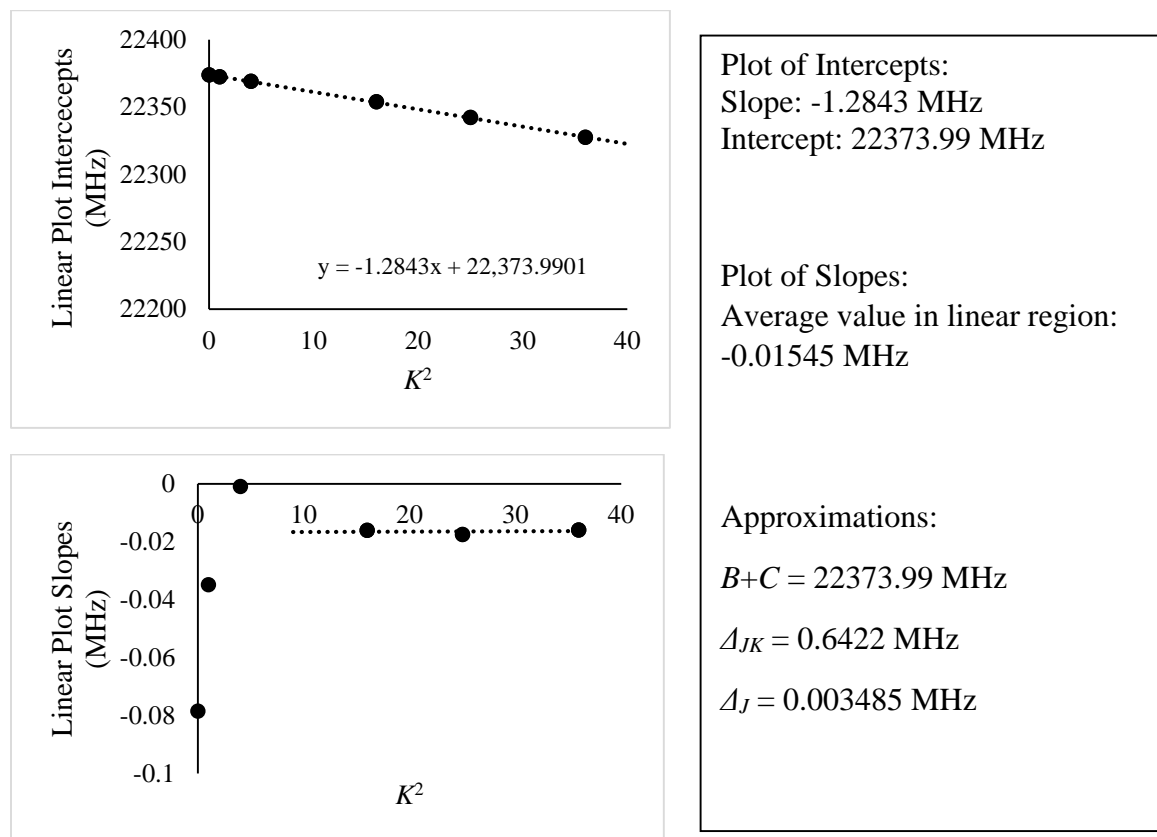
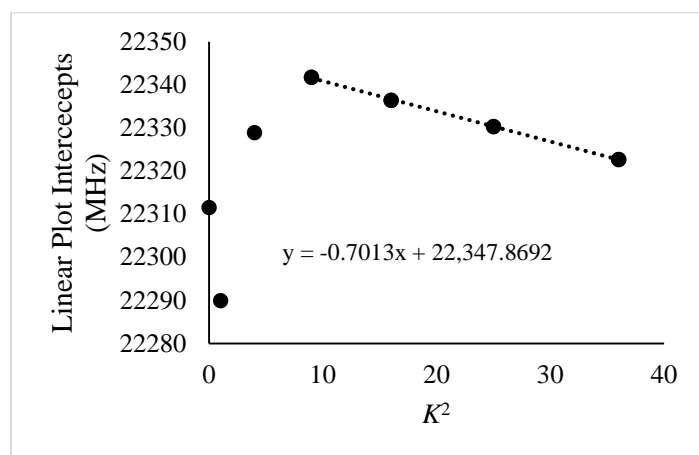


Figure 5.28 Summary of the a -type R-branch transitions assigned to the $\nu_5+\nu_6$ state of DN₃

DN₃ 2ν₆

Series (K)	N lines	Slope of 'linear plot'	Intercept of 'linear plot'	Lowest frequency transition	Highest frequency transition
0	4	-0.03598	22311.54	289970.691	356836.8041
1(-)	6	-0.02864	22140.58	243508.2009	354131.9412
1(+)	6	-0.02264	22439.27	246801.7766	358935.4947
2(-)	4	-0.01844	22328.99	245594.5315	357188.7
2(+)	4	0.00439	22328.75	245622.1317	357278.0244
3	6	-0.01409	22341.76	245740.7089	357410.5496
4	4	-0.01613	22336.38	268008.6578	357315.9593
5	5	-0.01137	22330.32	267944.2727	357238.6549
6	4	-0.01274	22322.70	267850.4015	334797.4847



Plot of Intercepts:
Slope: -0.7013 MHz
Intercept: 22347.87 MHz

Plot of Slopes:
Average value in linear region:
-0.01358 MHz

Approximations:

$$B+C = 22347.87 \text{ MHz}$$

$$\Delta_{JK} = 0.3507 \text{ MHz}$$

$$\Delta_J = 0.003395 \text{ MHz}$$

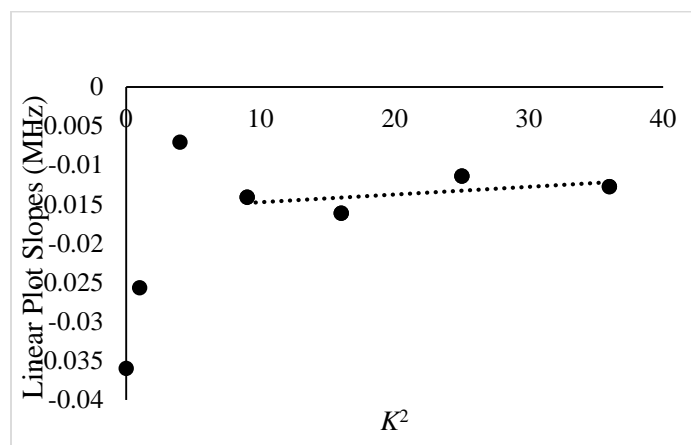
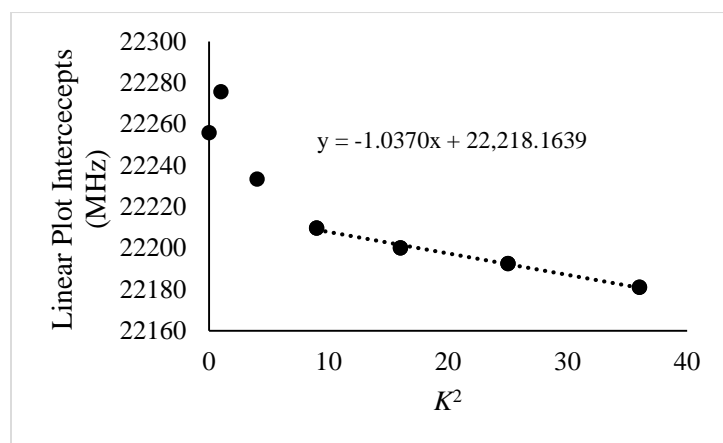


Figure 5.29 Summary of the a -type R-branch transitions assigned to the 2ν₆ state of DN₃

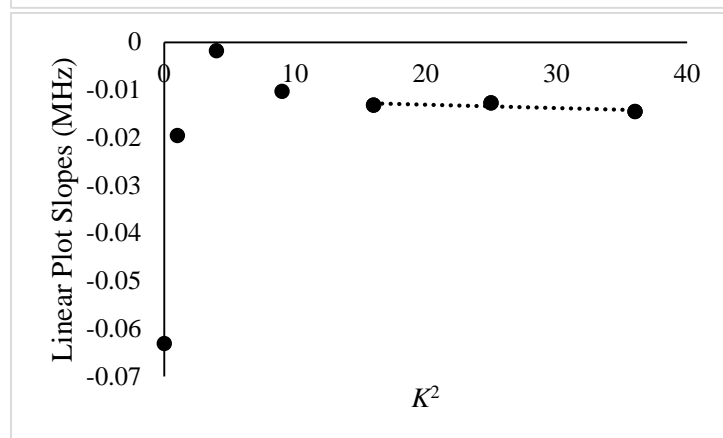
DN₃ ν_3

Series (K)	N lines	Slope of 'linear plot'	Intercept of 'linear plot'	Lowest frequency transition	Highest frequency transition
0	6	-0.06311	22255.83	244730.1832	355834.7209
1(-)	6	-0.01361	22105.77	243145.4396	353636.7075
1(+)	6	-0.02525	22445.53	246867.3133	359025.3007
2(-)	6	-0.02654	22233.35	244531.5249	355624.8806
2(+)	6	0.02303	22233.28	244596.7508	355826.7823
3(-)	6	-0.01072	22209.84	244293.9772	355313.6033
3(+)	6	-0.00990	22209.73	244293.9772	355315.0561
4	6	-0.01317	22200.10	244183.5513	355147.5794
5	6	-0.01272	22192.58	244101.4068	355029.3134
6	5	-0.01450	22181.01	266147.0877	354836.7794



Plot of Intercepts:
Slope: -1.0370 MHz
Intercept: 22218.16 MHz

Plot of Slopes:
Average value in linear region: -0.01346 MHz



Approximations:

$$B+C = 22218.16 \text{ MHz}$$

$$\Delta_{JK} = 0.5185 \text{ MHz}$$

$$\Delta_J = 0.003365 \text{ MHz}$$

Figure 5.30 Summary of the a -type R-branch transitions assigned to the ν_3 state of DN₃

Many of the plots of intercepts shown in Figure 5.17 through Figure 5.30 are linear or very nearly so, which indicates that the series involved in those plots are 1) correctly assigned and 2) not drastically perturbed. Likewise, many of the plots for the slopes vs. K^2 have a characteristic pattern where the $K = 0$ series has the most negative slope, the average of the $K = 2$ series has the least negative (or most positive) slope, and the slopes for subsequent K series become almost flat at $-4A_J$.

Confirming assignments of locally perturbed a -type series.

Many of the plots in Figure 5.17 through Figure 5.30 do not exhibit simple smooth behavior, and further examination is necessary to know whether the points that do not fit on a smooth curve are the result of incorrect assignments, or perturbations in correctly assigned series. Two major methods of verification are to compare these plots with published IR data, and to compare these plots with the plots of the suspected perturbing state. Figure 5.31 shows the plots of the intercepts for each K a -type R-branch series plotted against K^2 for both the ground and ν_5 states of HN_3 . The first 6 points for ν_5 and the first 7 points for the ground state fit on a straight line, indicating correct assignment and relatively low levels of perturbation. The final 4 points for each are off of this line (sometimes greatly off), and when each plot is examined individually it cannot be said whether the series are correctly assigned but perturbed, or simply incorrectly assigned. A direct comparison of the two states in Figure 5.31 strongly indicates that the two series are correctly assigned, that they are perturbing each other, and that the perturbation has a $\Delta K = 1$. Figure 5.32 is a plot of the average of the points on the two plots in Figure 5.31 with the K values offset by 1. A similar check can be done by examining the plots of slopes with a shift in K value of 1 (Figure 5.33) and the average of these plots (Figure 5.34) These plots lend additional weight

to the hypothesis that the two states perturb each other and provides strong evidence that the assignments of these series are correct. The perturbation is the centrifugal distortion perturbation (W_{05}). The selection rule for this perturbation is $\Delta K = \pm 1$ which explains the observed K value offset of 1 between the mirrored points of the two states.⁵ The final data point of Figure 5.34 does not lie on the expected curve. We do not know yet why this is.

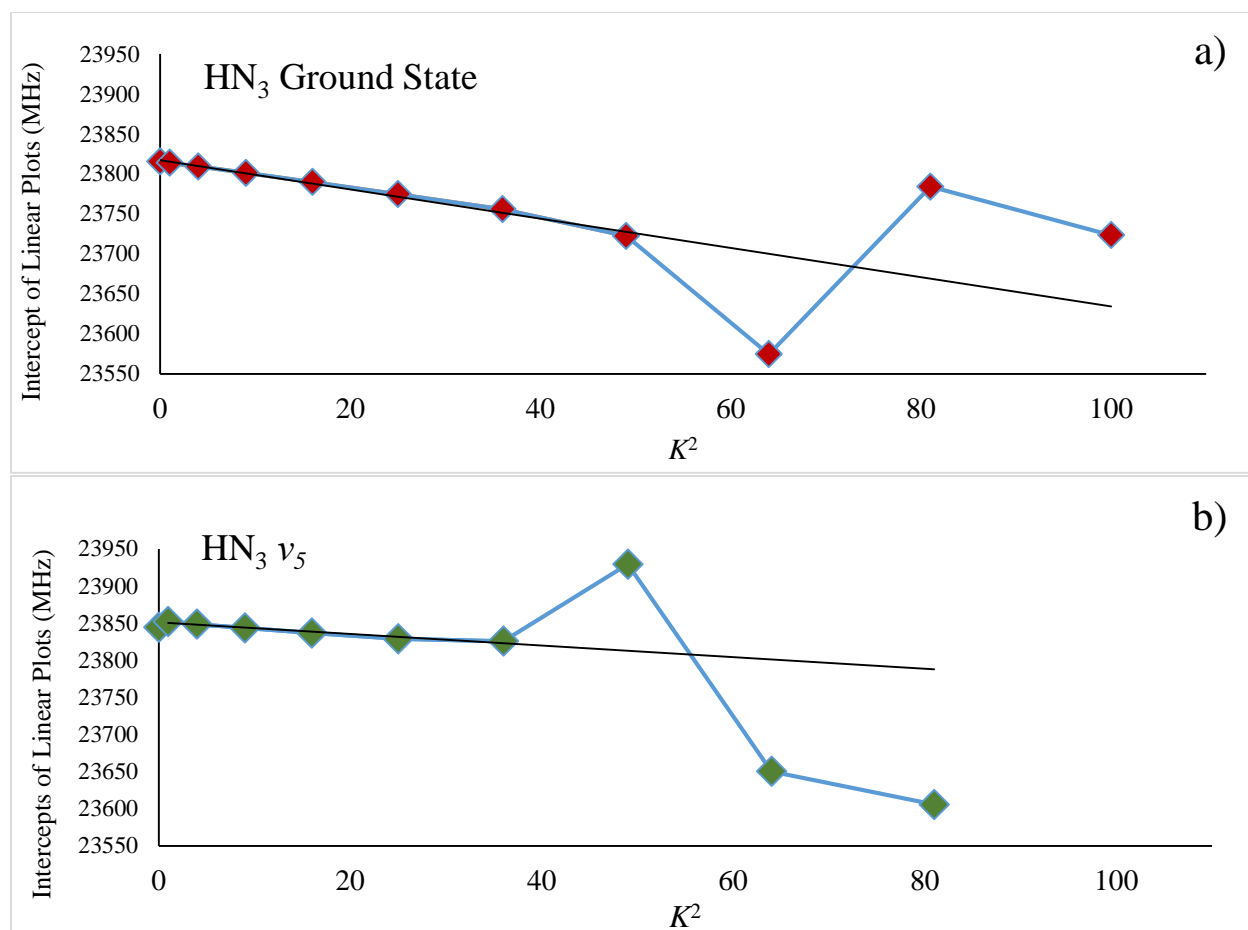


Figure 5.31 Plots of the intercepts for the ground state (a) and ν_5 (b) of HN_3 . If each plot is examined individually it is unclear whether the final three points are correctly assigned or not. When examined together, the mutual perturbation between the states becomes apparent.

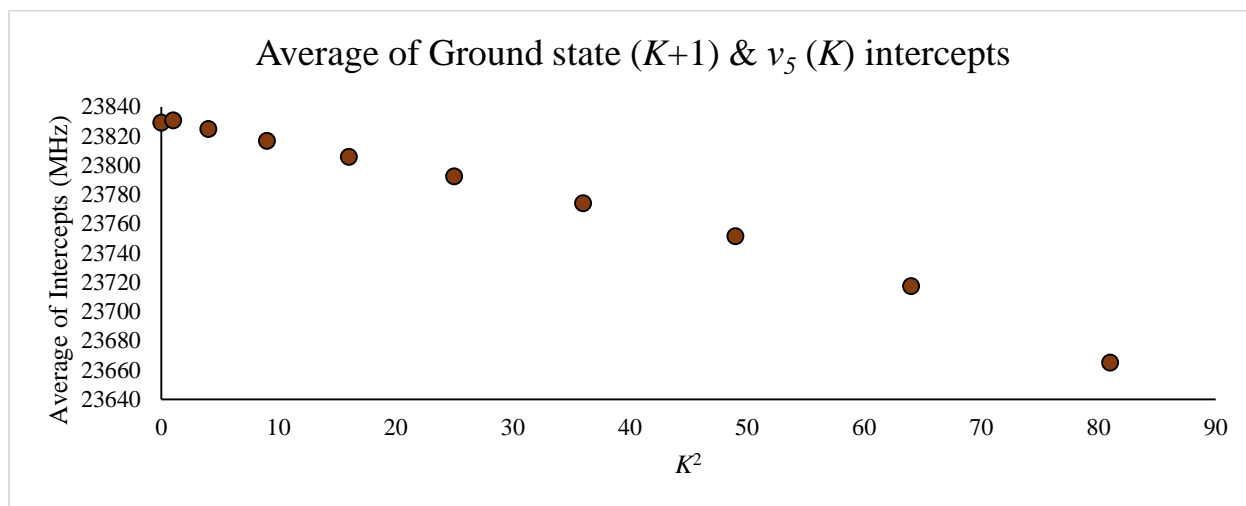


Figure 5.32 Average the intercept plots for the ground state and ν_5 of Figure 5.31. This is clearly a smoother curve than either of its components individually.

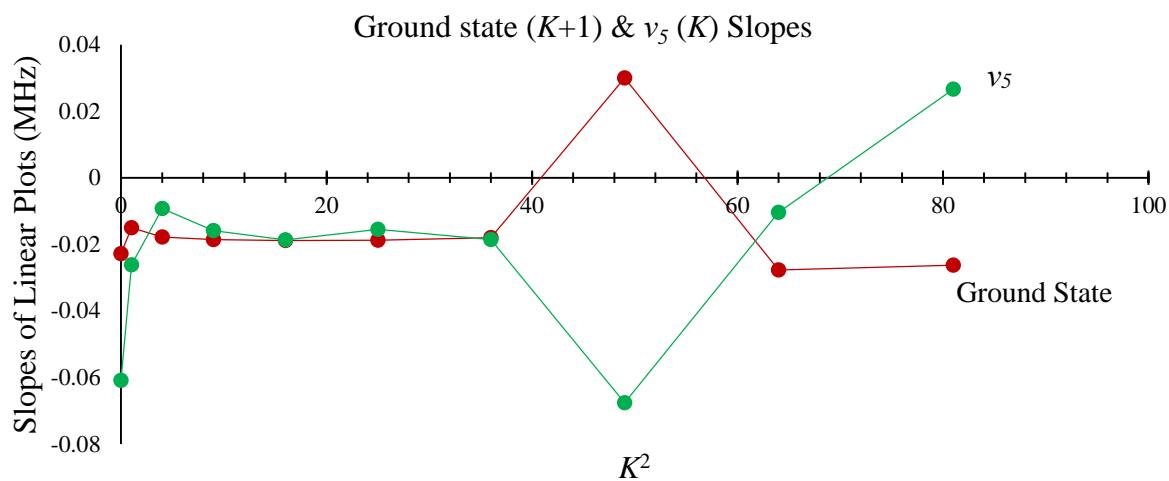


Figure 5.33 A plot of the slopes of the linear plots for each K value of ν_5 and the ground state of HN_3 vs K^2 . The ground state K values are shifted by one.

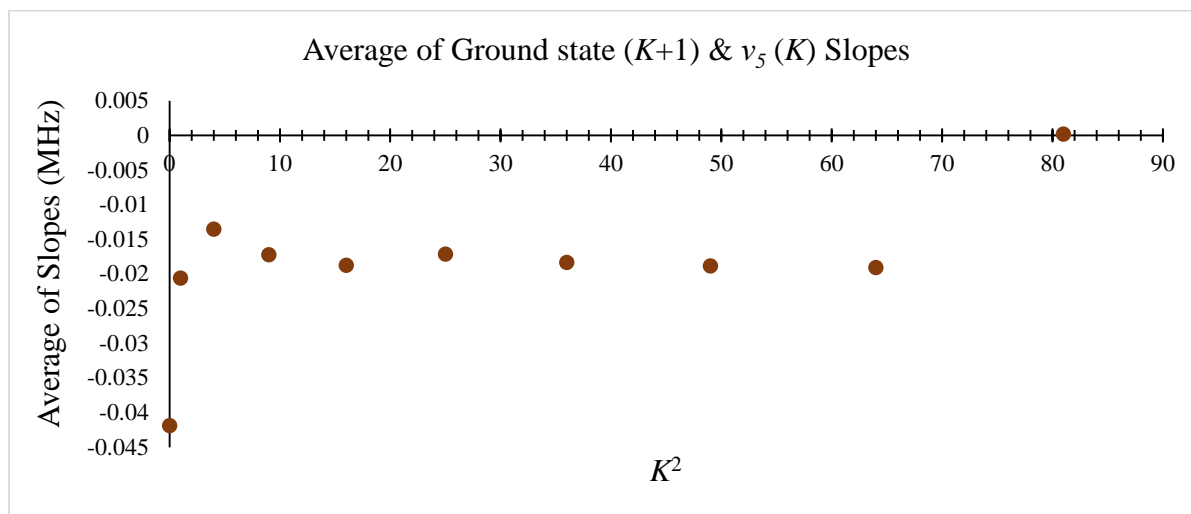


Figure 5.34 A plot of the average of the slopes for the linear plots for each K value of ν_5 and the ground state of HN_3 vs K^2 . The ground state K values were shifted by one before averaging

In Figure 5.35, we compare $\Delta B_{\text{effective}}$ (obtained by subtracting the slope of the ground state from the slope of the excited state) vs. K^2 for ν_3 and ν_4 to each other, and to a plot of the same quantity (in cm^{-1} instead of MHz) from the literature.⁹ When converted to the same units, the two plots not only have exactly the same shape, but lie on top of each other. This is an excellent confirmation of the assignment in the millimeter-wave spectrum and the corresponding assignments in the FTIR for both ν_3 and ν_4 . Despite the apparently erratic nature of the intercept plots for both of these states, a local C-type Coriolis perturbation (G_c) can explain most of the observed behavior. Figure 5.36 shows the average of the intercepts for ν_3 and ν_4 of HN_3 , with the K value offset by 1. The near-linear result confirms that source of most irregularity in the two states individually comes from the C-type Coriolis resonance between them. The selection rule for this perturbation is also $\Delta K = \pm 1$.

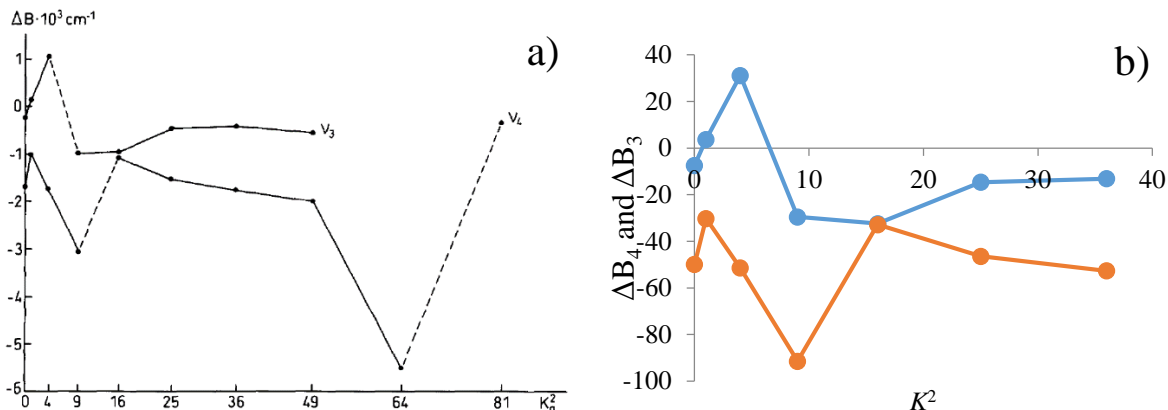


Figure 5.35 A plot of $\Delta B_{\text{effective}}$ vs. K^2 for ν_3 and ν_4 of HN_3 from the literature⁹ (a) and from our own data (b). $\Delta B_{\text{effective}}$ is closely tied to the intercept plots.

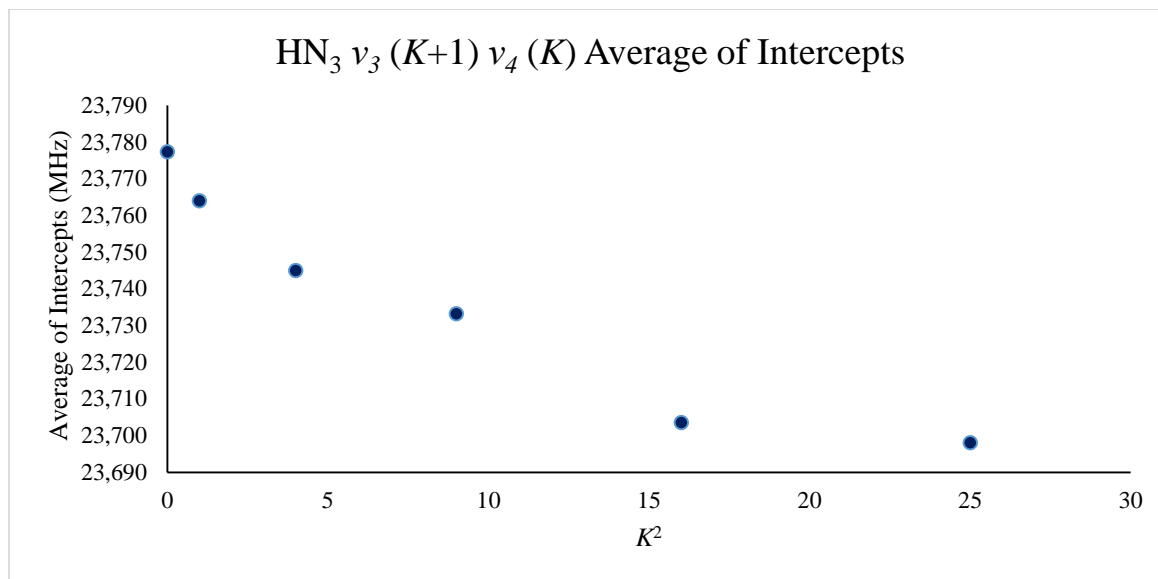


Figure 5.36 The average of the intercepts of ν_3 and ν_4 of HN_3 . There is a K offset of 1

There are two excellent examples of Fermi resonance in our DN_3 data. One is between $2\nu_6$ and ν_3 , and the other is between ν_4 and $2\nu_5$. The plots of the intercepts of the a -type R-branch series for these two pairs in DN_3 are shown in Figure 5.37 and Figure 5.38. Again these are situations where the individual plots look misshapen, but matching them with the analogous plot

from the perturbing state is extremely telling. The matrix elements for these perturbations are proportional to the cubic force constants, which have been calculated. The magnitude of the cubic force constant for the interaction between $2\nu_6$ and ν_3 is almost 6 times larger than for ν_4 and $2\nu_5$ ($k_{663} = -76.85$ and $k_{554} = 13.38$). Indeed, the stronger apparent perturbation is observed for $2\nu_6$ and ν_3 in Figure 5.37.

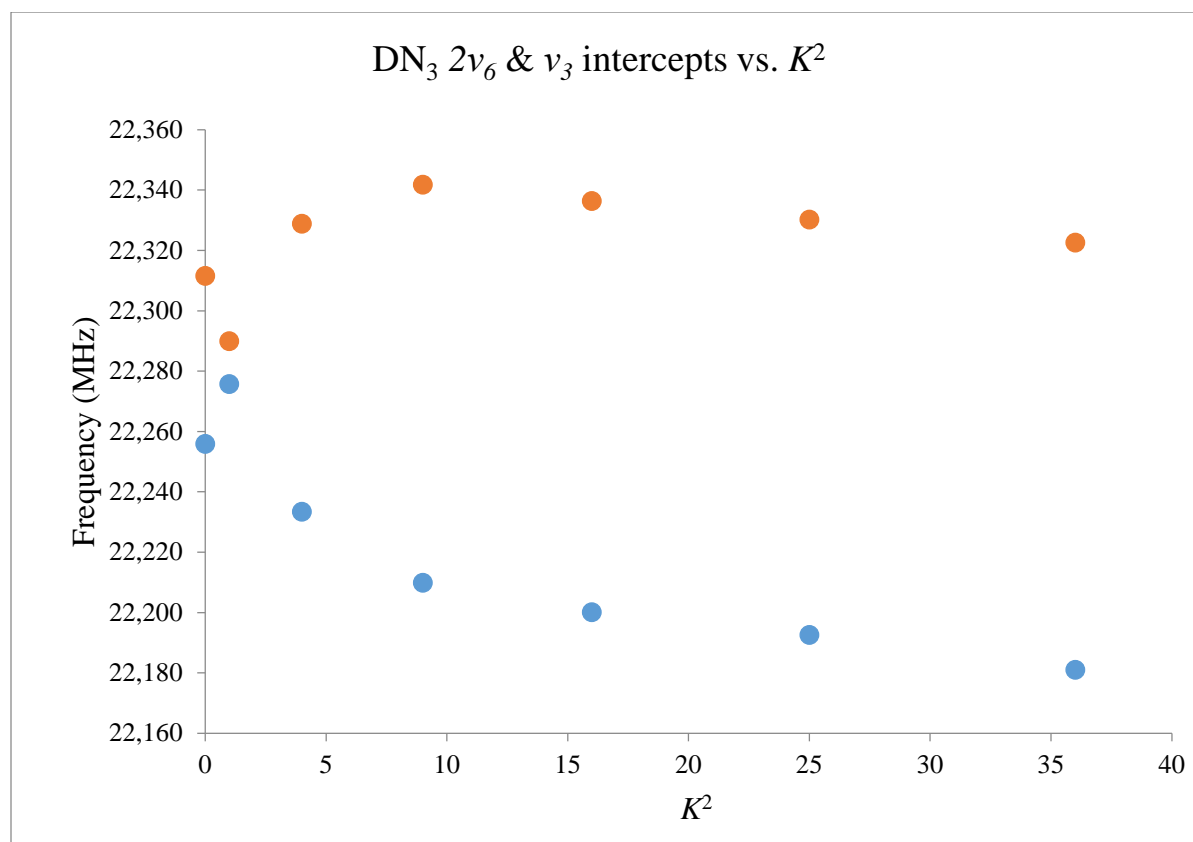


Figure 5.37 Plots of the intercepts from analysis of the a -type R-branch series of $2\nu_6$ and ν_3 of DN_3 . There is an apparent Fermi resonance between these two states.

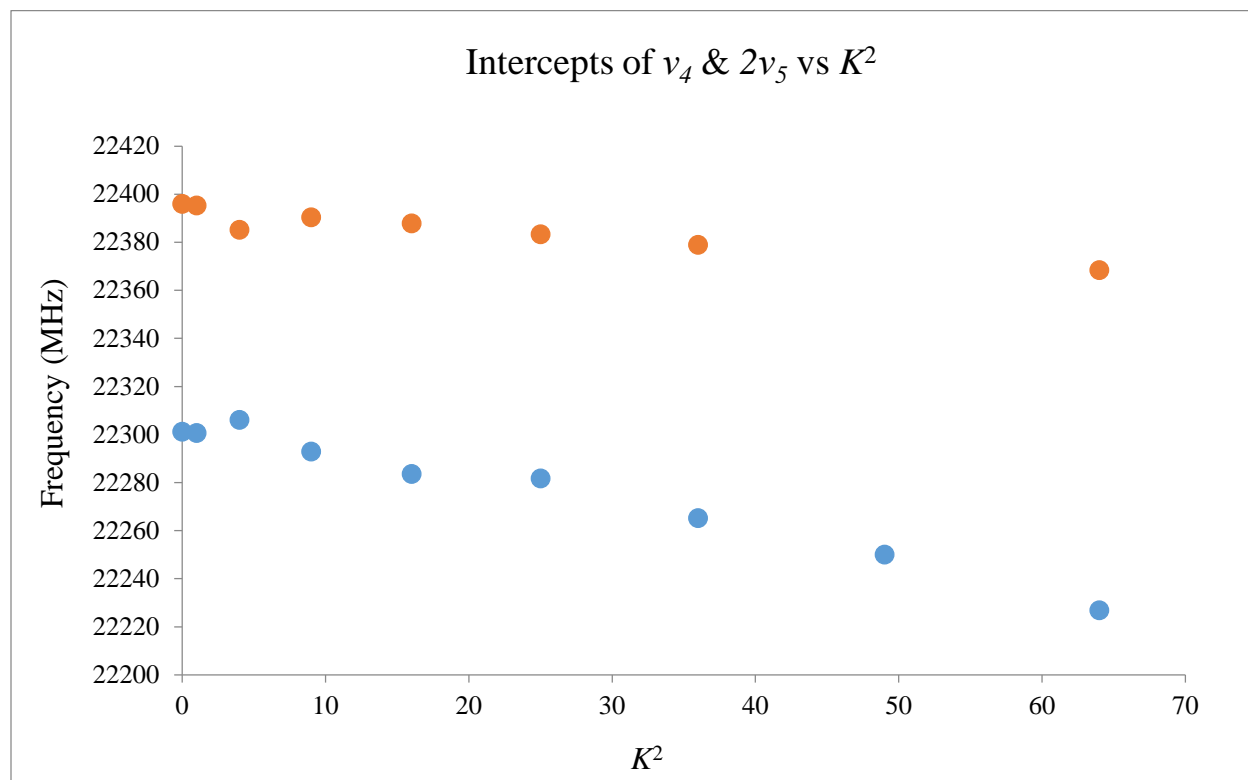


Figure 5.38 Plots of the intercepts from analysis of the a -type R-branch series of ν_4 and $2\nu_5$ of DN_3 . There is an apparent Fermi resonance between these two states.

The strong local Fermi resonance between the low K (0 through 3) states of $2\nu_6$ and ν_3 of DN_3 manifests itself in the millimeter-wave spectrum (Figure 5.37) and also in the ragged pattern of the observed K energies derived from analysis of the high resolution FTIR ν_3 and $2\nu_6$ bands (Figure 5.39).

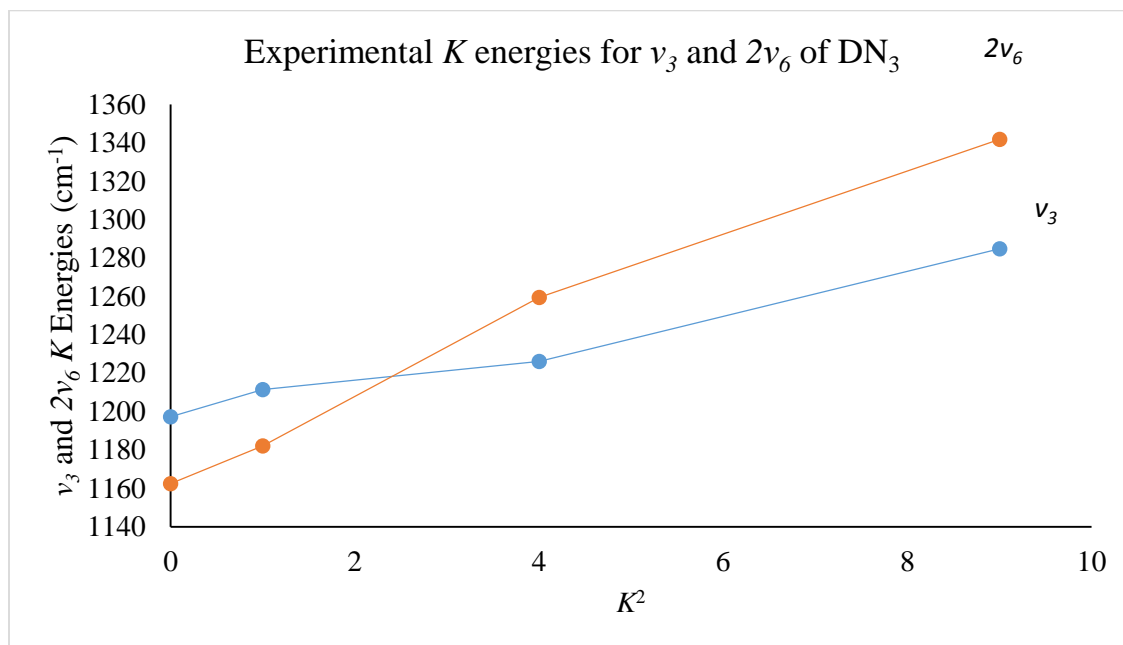


Figure 5.39 A closer view of the crossing of the $2\nu_6$ and ν_3 states of DN_3 between $K = 1$ and $K = 2$.

The resonance is particularly strong because of the large value of k_{366} and the K energy crossing of these two states between $K = 1$ and $K = 2$. The observed K energies for a particular K can be found by diagonalizing a two by two matrix

$$\begin{bmatrix} H_{\nu_3,K} & H_{Fermi} \\ H_{Fermi} & H_{2\nu_6,K} \end{bmatrix}$$

with the eigenvector matrix

$$\begin{bmatrix} -\cos \theta & \sin \theta \\ \sin \theta & \cos \theta \end{bmatrix}$$

The eigenvalues (the observed K energies) can be denoted $E_{\nu_3,K}$ and $E_{2\nu_6,K}$. For a property X , *e.g.*, the value of $\frac{B+C}{2}$ *effective* in state K , the Fermi perturbed values can be calculated from the unperturbed ones by

$$X_{\nu_3}^{Fermi} = X_{\nu_3} \cos^2 \theta + X_{2\nu_6} \sin^2 \theta \quad (5.6)$$

and

$$X_{2\nu_6}^{Fermi} = X_{\nu_3} \sin^2 \theta + X_{2\nu_6} \cos^2 \theta \quad (5.7)$$

It can be seen from these two equations that Fermi resonance always pulls the two properties together in this mixing of their wavefunctions. Because the unperturbed microwave intercepts for ν_3 are all below the corresponding ones for $2\nu_6$, they are pulled down by the Fermi resonance, while those for $2\nu_6$ are pulled up towards those of ν_3 , as is evident in Figure 5.37 (and for ν_4 and $2\nu_5$ in Figure 5.38).

The two above equations also lead to

$$\frac{X_{2\nu_6}^{Fermi} - X_{\nu_3}^{Fermi}}{X_{2\nu_6} - X_{\nu_3}} = \cos 2\theta \quad (5.8)$$

Theta can be determined from the data shown in Figure 5.40, which shows the subtraction of plots in Figure 5.37, which is essentially the numerator of the equation above. The K values 4,5, and 6 are reasonably unperturbed (at least by the Fermi resonance), and provide an acceptable approximation of the denominator in the equation above by their linear extrapolation. Using this value of θ for a given K , we can apply the inverse eigenvector transformation to the K energies shown in Figure 5.39 to reconstruct the undiagonalized matrix whose diagonal elements are the

deperturbed K energies $H_{\nu_3,K}$ and $H_{2\nu_6,K}$, and whose off diagonal elements are $H_{Fermi} = \frac{k_{366}}{4}$. We have carried out this analysis to give the deperturbed K energies shown in Figure 5.41 and to estimate the value of the cubic force constant k_{366} . The values obtained for $K=0$ and 1 are reasonably consistent (15.8 and 14.6 cm^{-1}) which corresponds to a k_{366} approximately equal to 61 cm^{-1} . This is in reasonable agreement with the magnitude of the previously mentioned *ab initio* value of 76.8 cm^{-1} .

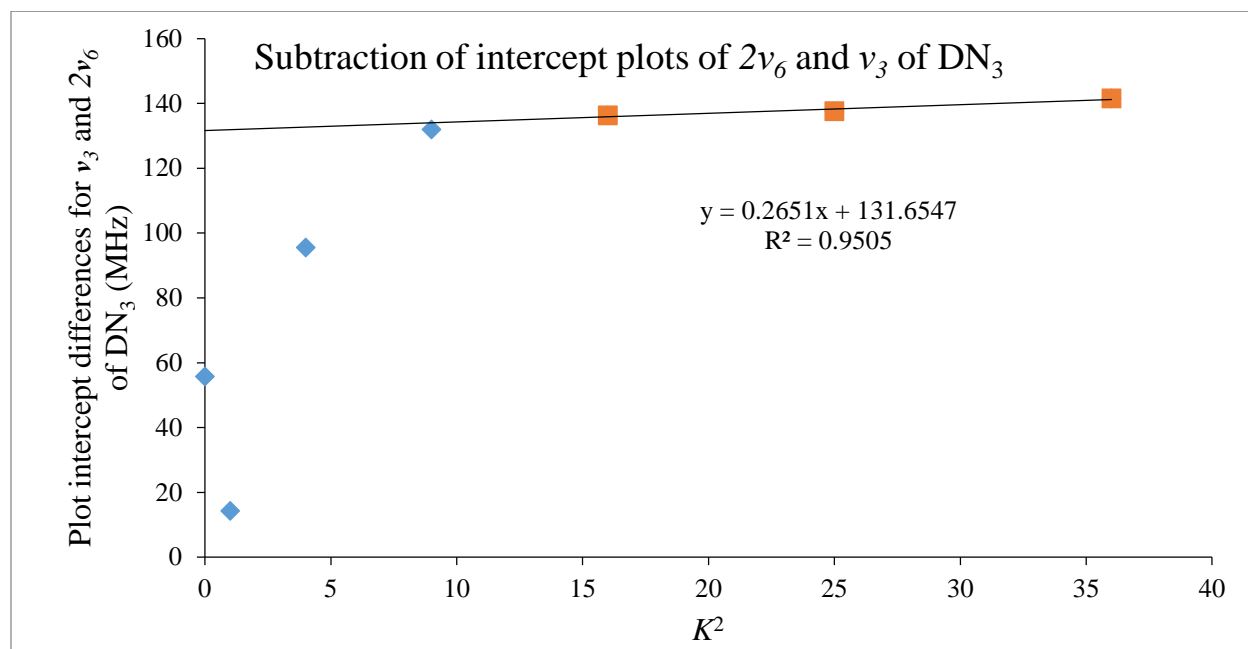


Figure 5.40 Plot showing the subtraction of the intercept plots for $2\nu_6$ and ν_3 shown earlier in Figure 5.37. A line has been fit to the values for $K=4, 5$ and 6 which are nearly unperturbed.

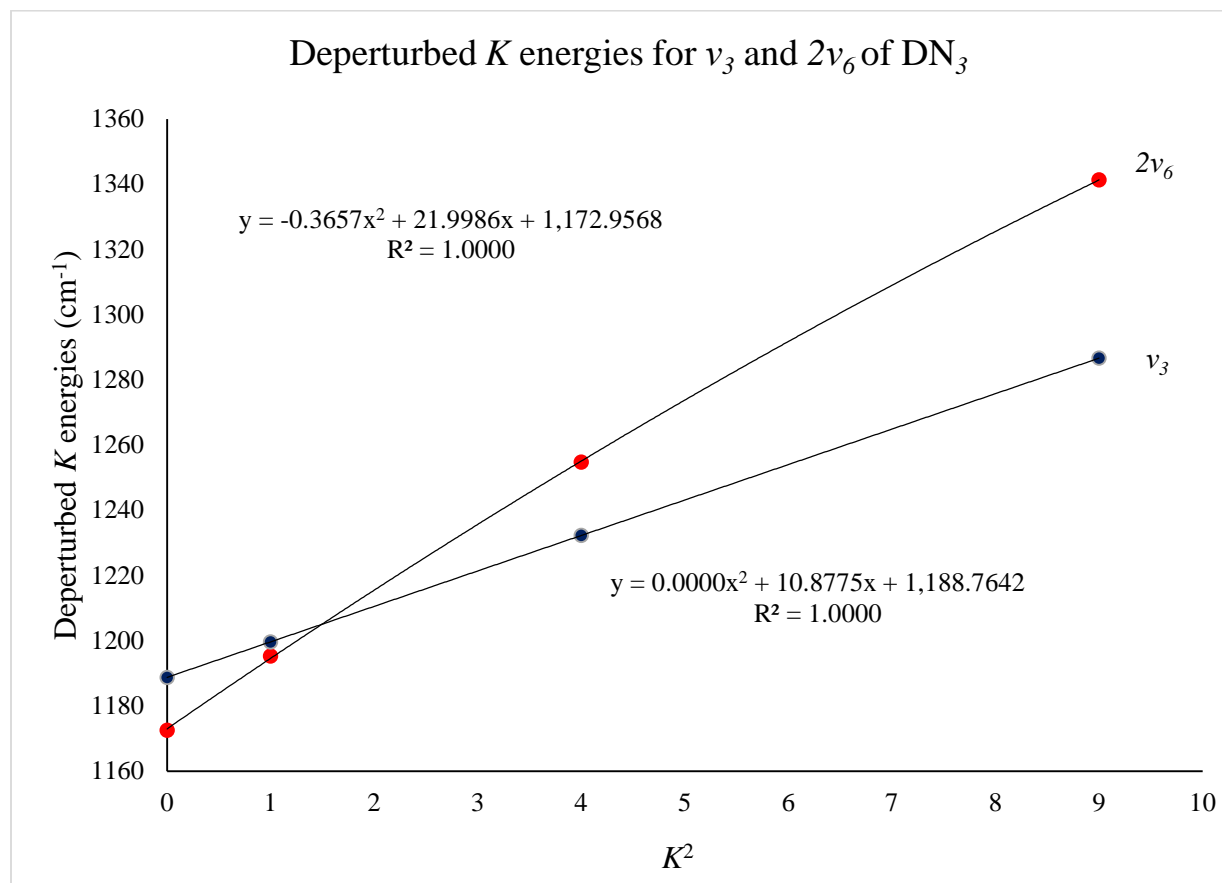


Figure 5.41 The deperturbed K energy levels for ν_3 and $2\nu_6$. The curves are dramatically smoother than the perturbed levels shown in Figure 5.39.

An examination of the deperturbed K energies in Figure 5.41 shows that the ν_3 K energies lie on a quite straight line, while those for $2\nu_6$ are more curved. This curvature is from the separate G_a perturbation, which is examined in detail elsewhere in this chapter. For the consideration of the G_a perturbation, these Fermi deperturbed K energies are the appropriate ones to use. This is obvious from Figure 5.42 which shows the deperturbed K energies, the experimental K energies, and the K energies predicted from Equation (5.1) and Equation (5.2) using G_a and other constants derived from ν_5 and ν_6 data. The close agreement between deperturbed and predicted K energies for $K = 0, 1,$ and 2 validates both equations and indicates that this prediction method will be very

useful for the other three overtone states. The agreement between the observed and predicted K energies is not nearly as good for these K levels.

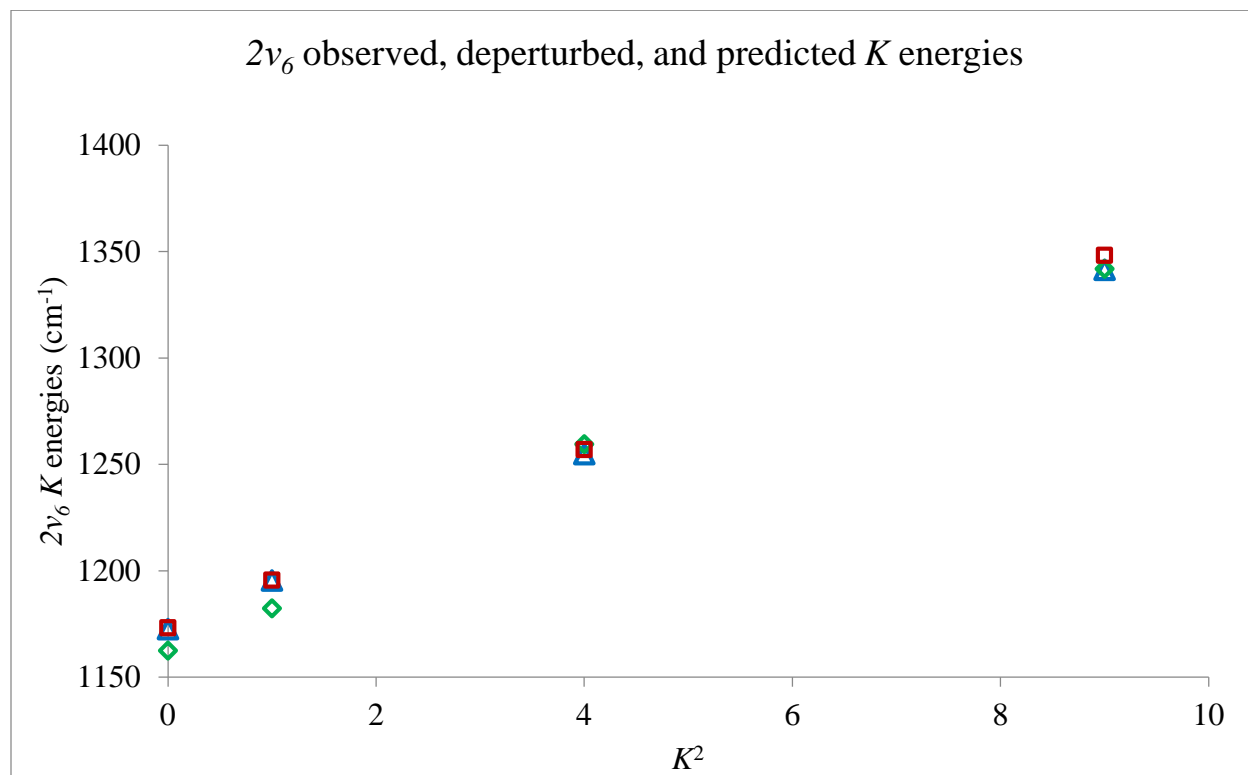


Figure 5.42 Plot of the observed $2\nu_6$ K energies for DN_3 (green diamonds), the deperturbed K energies (blue triangle), and K energies predicted with equations (5.1) and (5.2) (red squares)

Even though the crossing is very similar for ν_4 and $2\nu_5$, the wavefunction mixing is dramatically less, because of the small value of k_{455} compared to k_{366} . It should be remembered that the degree of mixing is proportional to the square of these cubic force constants. The Fermi resonances in HN_3 have the same cubic force constants, but different K energy positions, and are yet to be analyzed.

Head-to-head comparisons of the intercept plots for the two states believed to be perturbing each other have been useful in confirming line assignments, but comparison of our plots to literature data has also been useful. For several vibrational states, a value of $\frac{B+C}{2}$ has been

published for multiple K levels, but not the actual transitions. For example, in the case of $2\nu_6$, no IR transitions have been published, but the $B+C$ values for $K = 0$ through 3 were reported as 22312.39, 22291.72, 22333.64, and 22351.68 MHz respectively.¹⁰ Our assignments yielded linear plot intercepts of 22311.54, 22289.92, 22328.77, and 22,341.75 MHz for these states. A plot of the differences of these datasets is shown in Figure 5.43. The resulting straight line is clear confirmation that our assignments are in agreement with the results of the IR study. The origin of the non-zero slope is most likely an unreported distortion term used by the authors of the FTIR study. Similar subtraction plots were used for both ν_3 and ν_4 in both HN_3 and DN_3 with similarly straight but sloped straight lines, further confirming all of those assignments.

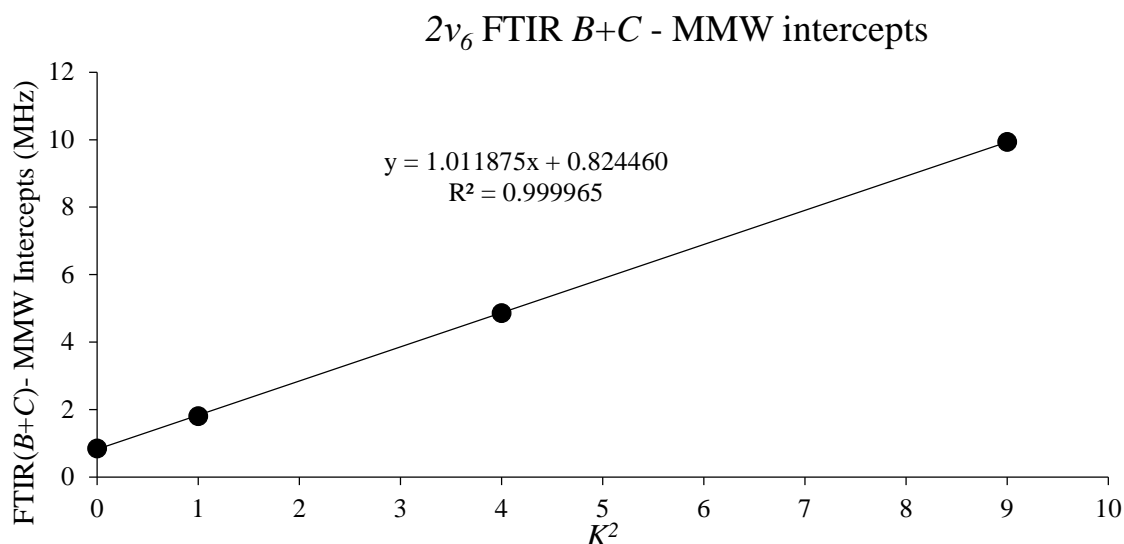


Figure 5.43 A plot of the differences between the literature $B+C$ values for K states of $2\nu_6$ ¹⁰ and our linear plot intercepts for these same states vs K^2 .

Analysis of splitting of a -type lines

A further tool in the assignment of lines belonging to the $K = 1$, $K = 2$, and $K = 3$ transitions was the analysis of the magnitude of the splitting between the non-degenerate $K(+)$ ($K_{prolate} + K_{oblate} = J$ for both states) and $K(-)$ ($K_{prolate} + K_{oblate} = J+1$ for both states) transitions. Figure 5.44 shows a graph of the differences between the non-degenerate pair of $K = 1$ a -type R-branch transitions for ν_5 of DN_3 . At the low end of our spectrometer's frequency range, the $J_{upper} = 11$ $K = 1(-)$ transition ($11_{111} \leftarrow 10_{110}$ at 243744.09 MHz) and the $J_{upper} = 11$ $K = 1(+)$ transition ($11_{110} \leftarrow 10_{109}$ at 247979.45 MHz) are separated by 4235.36 MHz. At the high end of our spectrometer's frequency range, the $J_{upper} = 19$ $K = 1(-)$ transition ($19_{119} \leftarrow 18_{118}$ at 420835.28 MHz) and the $J_{upper} = 19$ $K = 1(+)$ transition ($19_{119} \leftarrow 18_{118}$ at 428134.97 MHz) are separated by 7299.69 MHz. Figure 5.44 shows that the separation between these lines is directly proportional to the J_{upper} value.

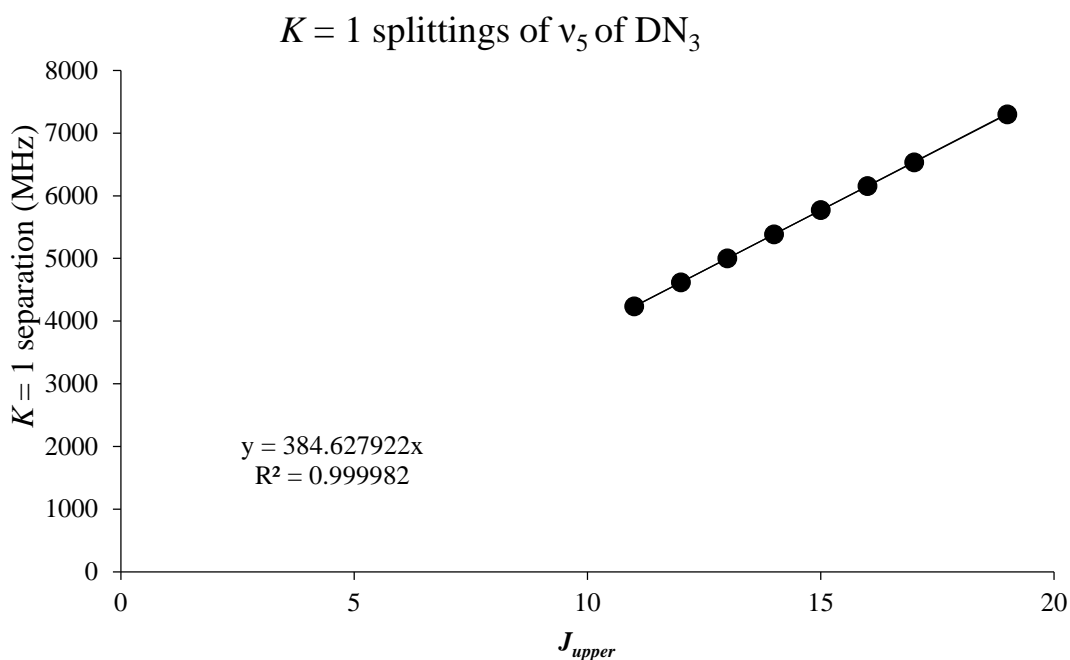


Figure 5.44 Splittings of $K = 1$ a -type R-branch lines plotted vs. J_{upper} .

The separations in the non-degenerate $K = 2$ a -type R-branch transitions are shown in Figure 5.45. At the low end of our spectrometer's frequency range, the $J_{upper} = 11$ $K = 2(-)$ transition ($11_{210} \leftarrow 10_{29}$ at 245846.15 MHz) and the $J_{upper} = 11$ $K = 2(-)$ transition ($11_{29} \leftarrow 10_{28}$ at 245966.61 MHz) are separated by 120.46 MHz. At the high end of our spectrometer range, the $J_{upper} = 19$ $K = 2(-)$ transition ($19_{218} \leftarrow 18_{217}$ at 424486.88 MHz) and the $J_{upper} = 19$ $K = 2(+)$ transition ($19_{217} \leftarrow 18_{216}$ at 425107.25 MHz) are separated by 620.37 MHz. The splitting in the $K = 2$ lines clearly increases faster with J than in the case of $K = 1$, with a linear plot achieved when the splitting is graphed vs. $(J_{upper}-1)J_{upper}(J_{upper}+1)$.

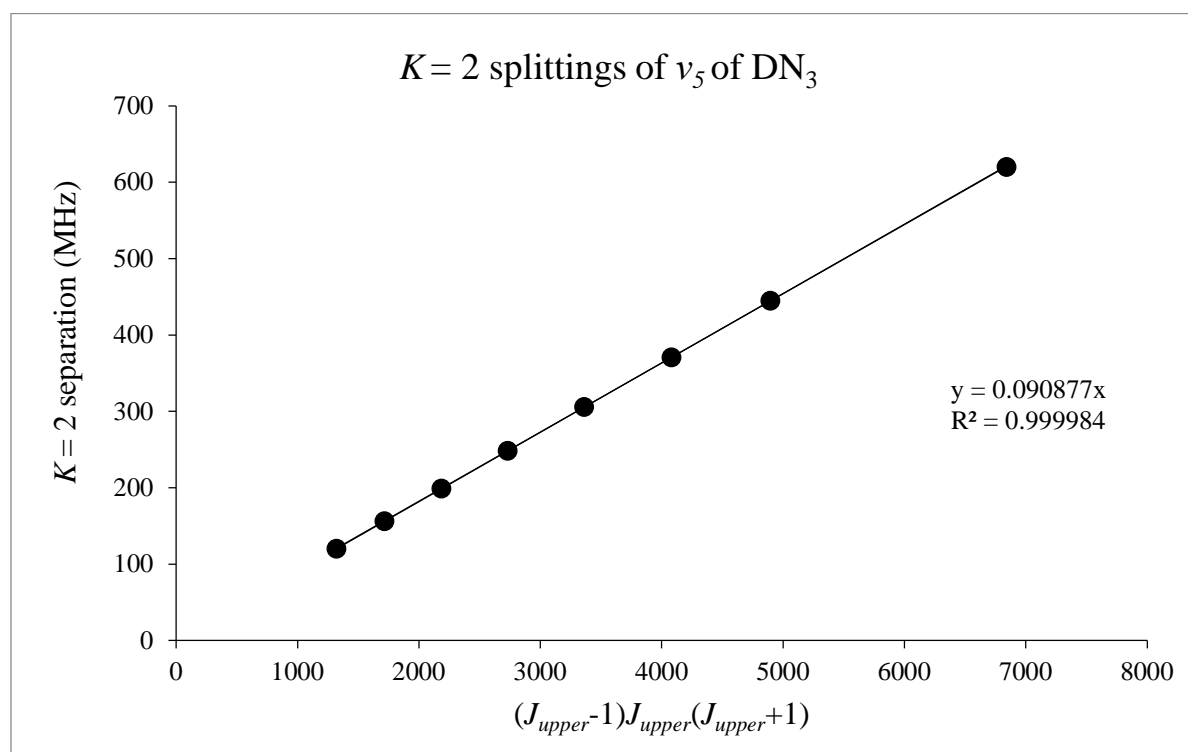


Figure 5.45 Splittings of $K = 2$ a -type R-branch lines plotted vs. $(J_{upper}-1)J_{upper}(J_{upper}+1)$.

The splittings in the $K = 3$ transitions in the a -type R-branches are measurable for some but not all J values. These splittings are generally larger in DN_3 than in HN_3 . Often the magnitude

of the splitting is close to our ability to resolve individual lines, so they may appear as a single line in the spectrum, a broad line, two intermingled lines, or two clearly resolved lines. Figure 5.46 shows the splittings in the *a*-type R-branch lines for ν_5 of DN_3 , where more of the lines are clearly resolved than for most other states, plotted vs. $(J_{upper}-2)(J_{upper}-1)J_{upper}(J_{upper}+1)(J_{upper}+2)$. At the low end of our spectrometer's range, the $J_{upper} = 11 K = 3(-)$ transition ($11_{39} \leftarrow 10_{38}$ at 245842.96 MHz) and the $J_{upper} = 11 K = 3(-)$ transition ($11_{38} \leftarrow 10_{37}$ at 245843.45 MHz) are separated by 0.49 MHz. At the high end of our spectrometer range, the $J_{upper} = 19 K = 3(-)$ transition ($19_{317} \leftarrow 18_{316}$ at 424603.13 MHz) and the $J_{upper} = 19 K = 3(+)$ transition ($19_{316} \leftarrow 18_{315}$ at 424612.05 MHz) are separated by 8.92 MHz. The excellent linear fits found in Figure 5.44, Figure 5.45, and Figure 5.46 all were constrained to have intercepts at zero.

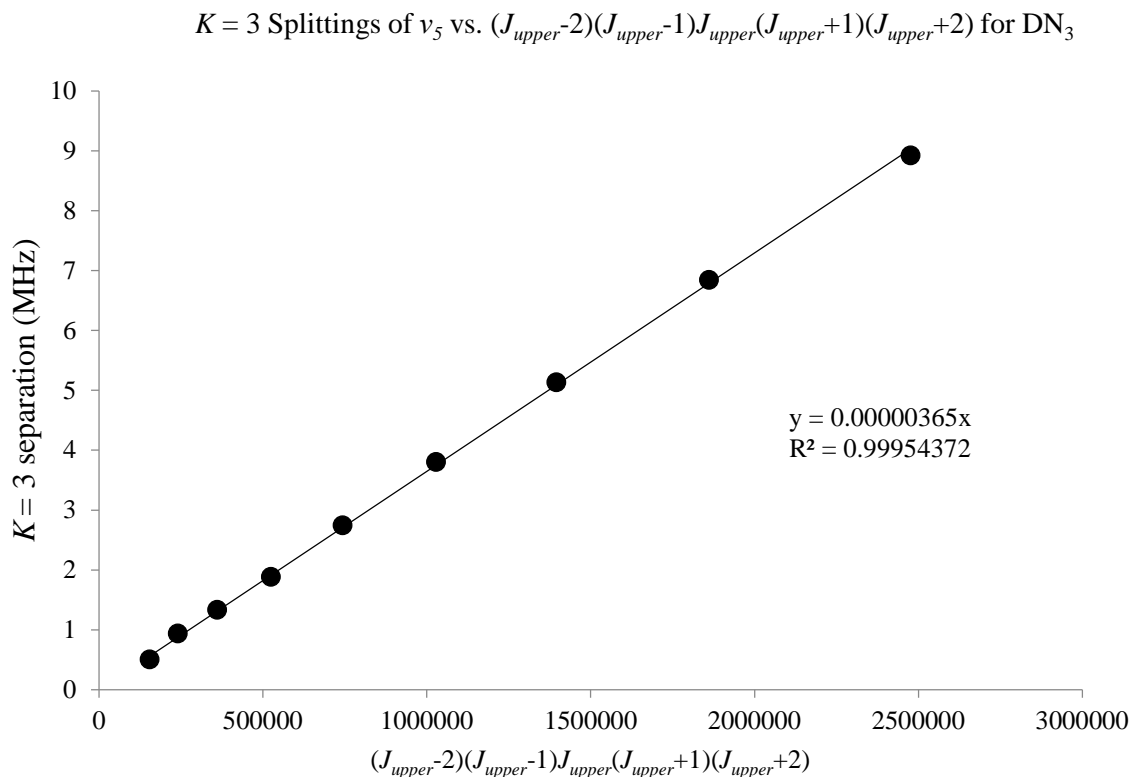


Figure 5.46 Splittings of $K = 3$ a -type R-branch lines plotted vs. $(J_{upper-2})(J_{upper-1})J_{upper}(J_{upper+1})(J_{upper+2})$.

An alternate way to plot this same splitting data is to divide the splittings by J_{upper} for $K=1$, $(J_{upper-1})J_{upper}(J_{upper+1})$ for $K=2$ and $(J_{upper-2})(J_{upper-1})J_{upper}(J_{upper+1})(J_{upper+2})$ for $K=3$, each series is then plotted vs. J_{upper} , and the intercepts deriving from $K = 1$, $K = 2$, and $K = 3$ can be called S_1 , S_2 , and S_3 , respectively. Many years ago, Wang²³ showed that for a rigid asymmetric rotor (unperturbed).

$$S_1 = B - C \quad (5.9)$$

$$S_2 = \frac{1}{8} \frac{(B-C)^2}{A - \frac{B+C}{2}} \quad (5.10)$$

$$S_3 = \frac{3}{2^{10}} \frac{(B-C)^3}{\left(A - \frac{B+C}{2}\right)^2} \quad (5.11)$$

These formulas apply directly to the ground states of HN_3 and DN_3 . The difference $B-C$ is determined directly from the $K = 1$ splittings (S_1) and if $A - \frac{B+C}{2}$ is known, $B-C$ can also be found from the $K = 2$ or $K = 3$ splittings (S_2 and S_3). In an early microwave paper, before $A - \frac{B+C}{2}$ was known from b -type transitions or FTIR data, Winnewisser and Cook¹¹ combined the $K=1$ and $K=2$ splitting data to determine $A - \frac{B+C}{2}$. In current analyses of the millimeter-wave data, the $K = 1$, $K = 2$, and $K = 3$ splittings provide all of the available information about the value of $B-C$.

In the presence of the A-type Coriolis perturbation (G_a), the formulas for S_1 and S_2 (and also S_3) must be modified. The analysis of the G_a perturbation plays out differently for $K = 1$ and $K = 2$, but in both cases the matrix of the perturbed asymmetric rotor must be expressed in the Wang basis. For $K = 1$, this Hamiltonian matrix is

$$\begin{array}{l} \nu_5 K = 1(+), \\ \nu_5 K = 1(-), \\ \nu_6 K = 1(+), \\ \nu_6 K = 1(-) \end{array} \begin{bmatrix} E_{1,\nu_5}^0 + W_{\nu_5} & 0 & 0 & G_a \\ 0 & E_{1,\nu_5}^0 - W_{\nu_5} & G_a & 0 \\ 0 & G_a & E_{1,\nu_6}^0 + W_{\nu_6} & 0 \\ G_a & 0 & 0 & E_{1,\nu_6}^0 - W_{\nu_6} \end{bmatrix} \quad (5.12)$$

Here $W = W_{1,-1}$ is the rigid rotor matrix element between $K = +1$ and $K = -1$. It may be noticed that the G_a element connects (+) to (-) and (-) to (+), which results from the a -type selection rules pertinent to the A-type Coriolis resonance ($\Delta K_{\text{oblate}} = \pm 1$). Applying second order perturbation theory to this matrix yields the following formulas for the perturbed splittings

$$S_{1,\nu_5}^{G_a} = S_{1,\nu_5} - \frac{G_a^2}{(E_{1,\nu_6}^0 - E_{1,\nu_5}^0)^2} (S_{1,\nu_5} + S_{1,\nu_6}) \quad (5.13)$$

$$S_{1,\nu_6}^{G_a} = S_{1,\nu_6} - \frac{G_a^2}{(E_{1,\nu_6}^0 - E_{1,\nu_5}^0)^2} (S_{1,\nu_5} + S_{1,\nu_6}) \quad (5.14)$$

where the unperturbed S constants on the right hand side of the equation are given by Wang's formula. These can be corrected for centrifugal distortion δ_K by substituting $(B-C)-4\delta_K$ for $B-C$. These equations show that the S for both states are shifted **down** by exactly the same amount.

To understand the splittings for $K = 2$, the Wang basis Hamiltonian matrix involving $K = 0$ and $K = 2$ must be considered.

$$\begin{bmatrix} H_{00,\nu_5} & \sqrt{2}H_{02,\nu_5} & 0 & 0 & 0 & 0 \\ \sqrt{2}H_{02,\nu_5} & H_{22,\nu_5} & 0 & 0 & 0 & 2G_a \\ 0 & 0 & H_{22,\nu_5} & 0 & 2G_a & 0 \\ 0 & 0 & 0 & H_{00,\nu_6} & \sqrt{2}H_{02,\nu_6} & 0 \\ 0 & 0 & 2G_a & \sqrt{2}H_{02,\nu_6} & H_{22,\nu_6} & 0 \\ 0 & 2G_a & 0 & 0 & 0 & H_{22,\nu_6} \end{bmatrix} \quad (5.15)$$

Applying second order perturbation theory to this matrix yields

$$S_{2,\nu_5}^{G_a} = S_{2,\nu_5} \left(1 + \frac{G_a^2}{(E_{2,\nu_6}^0 - E_{2,\nu_5}^0) \left(A - \frac{B+C}{2} \right)} \right) \quad (5.16)$$

$$S_{2,\nu_6}^{G_a} = S_{2,\nu_6} \left(1 - \frac{G_a^2}{(E_{2,\nu_6}^0 - E_{2,\nu_5}^0) \left(A - \frac{B+C}{2} \right)} \right) \quad (5.17)$$

These equations show that S_{2,ν_5} is shifted upwards, while S_{2,ν_6} is shifted downward by the same percentage. These equations for $K = 1$ and $K = 2$ have been tested for the ν_5 and ν_6 states of DN₃ with great success. For $2\nu_5$ and $2\nu_6$, the magnitude of the shifts are roughly twice as large because G_a must be replaced with $\sqrt{2}G_a$. This is confirmed by the actual splitting data for these states. For $\nu_5 + \nu_6$, and $K = 1$, the effects of the two perturbations are reinforcing, which leads to a large shift.

For $\nu_5+\nu_6$, and $K = 2$, the effects of the two perturbations tend to cancel, leading to splittings similar to those in the ground state. These expectations are also consistent with the observed splittings.

For HN_3 , G_a is larger, because of the larger A rotational constant and the vibrational separation between ν_5 and ν_6 is smaller, making these corrections all larger. Second order perturbation theory will also be less accurate in the case of HN_3 . We are hopeful, however, that this kind of analysis will be very helpful in the assignment of a -type R-branches for $\nu_5+\nu_6$ and $2\nu_6$.

Analysis of b -type transitions

Pure rotational P, Q, and R-Branches have been found for many of the vibrational states studied. The perturbation of individual K states drastically changes the frequency of b -type transitions, as does the massive difference in the A rotational constants between HN_3 and DN_3 , so there is a great deal of variation in the transitions observed for each state. Table 5.4 is a summary of the observed b -type lines for HN_3 . Table 5.5 is a summary of the observed b -type lines for DN_3 .

Table 5.4 Summary of observed J values (J_{upper} reported) for b -type lines for each state of HN_3

Branch	K_{upper}	K_{lower}	Ground	ν_5	ν_6	$2\nu_5$	$\nu_5 + \nu_6$	ν_4	$2\nu_6$	ν_3
P	1(-)	0(+)	6-13 33-40	13-20	30-33			14-18 41-46		1-3 25-29
R	1(-)	0(+)		7-16						
Q	1(+)	0(+)								1-17
Q	1(+)	1(-)		46-58						
P	2(-)	1(+)	52-55 72-75	14-21 41-46						
P	2(+)	1(-)		16-24 54-61						
P	2(+)	0(+)		22-26 53-60						

Table 5.5 Summary of observed J values (J_{upper} reported) for b -type lines for each state of DN₃

Branch	K_{upper}	K_{lower}	Ground	ν_5	ν_6	$2\nu_5$	$\nu_5 + \nu_6$	ν_4	$2\nu_6$	ν_3
Q	1(+)	0(+)	1-36	18-42				1-7		
P	1(-)	0(+)	1-3 24-31	19-26	1-8 29-35			2-4 25-29	9-13	2-5
R	1(-)	0(+)	1-5	2-11						
P	2(-)	1(+)	22-28 47-52	10-16 36-41	35-40 58-61					
P	2(+)	1(-)	27-45	11-20						
P	3(-)	2(+)		36-40						
P	3(+)	2(-)	60-64	38-42						

The b -type transition frequencies, like those for the a -type transitions, can be used to make plots with smooth curves that serve to confirm assignments, and can also be used to extract spectroscopic constants prior to attempting a full fit of the dataset. A Fortrat plot can be used to analyze b -type R-branch transitions and P-type transitions (both with ‘positive’ and ‘negative’

frequencies) simultaneously. The following equations show how a Fortrat plot is constructed, and how the coefficients of polynomial fits of these plots relate to observable spectroscopic constants.

Simple expressions for the energy of two rotational states are shown below. The B and D variables are the effective rotational constant and centrifugal distortion constant for the K state in question.

$$\text{Upper State energy } E'_{J'} = E'_0 + B'J'(J' + 1) - D'J'^2(J' + 1)^2 \quad (5.18)$$

$$\text{Lower State Energy } E''_{J''} = E''_0 + B''J''(J'' + 1) - D''J''^2(J'' + 1)^2 \quad (5.19)$$

The transition frequency between these states should simply be the difference in their energies.

$$\text{Transition Frequency } \nu(J) = E'_{J'} - E''_{J''} \quad (5.20)$$

Depending on the quantum numbers of the two states, the transition is classified as a P, Q, or R-branch transition. The P and R-branch transitions are most useful for Fortrat plots. Expressions for the energies of P- and R-branch transitions are shown below.

$$\text{R-branch: Lower state } J'' = J \quad \text{Upper state } J' = J + 1 \quad R(J) = E'_{J+1} - E''_J$$

$$R(J) = B.O. + (B' + B'')(J + 1) + (B' - B''D' + D'')(J + 1)^2 - 2(D' + D'')(J + 1)^3 - (D' - D'')(J + 1)^4 \quad (5.21)$$

$$\text{P-branch: Lower state } J'' = J \quad \text{Upper state } J' = J - 1 \quad P(J) = E'_{J-1} - E''_J$$

$$\begin{aligned}
 P(J) = B.O. + (B' + B'')(-J) + (B' - B''D' + D'')(-J)^2 - 2(D' + D'')(-J)^3 \\
 - (D' - D'')(-J)^4
 \end{aligned} \tag{5.22}$$

The previous equations can be generalized by substituting J terms as follows:

$$\begin{array}{ll}
 \text{For R-Branch:} & m = J + 1 \\
 \text{For P-Branch:} & m = -J
 \end{array}$$

$$\begin{aligned}
 \nu(m) = B.O. + (B' + B'')(m) + (B' - B'' - D' + D'')m^2 - 2(D' + D'')m^3 \\
 - (D' - D'')m^4
 \end{aligned} \tag{5.23}$$

This equation can be used to make a Fortrat plot to analyze both R and P-type transitions at the same time. For all of the Fortrat plots we have looked at, 4th order polynomials have given good fits to the data, but sometimes 6th order polynomials give even better fits. Spectroscopically, a 6th order polynomial represents the inclusion of H centrifugal distortion terms in the polynomial fit as follows:

$$\begin{aligned}
 \nu(m) = B.O. + (B' + B'')m + (B' - B'' - D' - D'')m^2 + [-2(D' + D'') + (H' + H'')]m^3 + \\
 [- (D' - D'') + 3(H' - H'')]m^4 + 3(H' + H'')m^5 + (H' - H'')m^6
 \end{aligned} \tag{5.24}$$

Figure 5.47 shows a Fortrat plot of the b -type transitions between the $K = 0(+)$ and $K = 1(-)$ states. The plot combines multiple datasets. The m values between 19 and 42 come from FIR R-branch transitions.⁴ The m values between 1 and 5 come from our MMW data of R-branch transitions. The m values between -2 and -4 come from our MMW data of P-branch transitions with ‘positive’ frequencies.¹⁴ The m values between -5 and -13 come from literature MMW/ MW P-branch transitions with ‘positive’ frequencies. The series then ‘passes through zero’ with the

relative energies of the $K = 0(+)$ states now above the energies for the $K = 1(-)$ states. The m values between -15 and -23 come from the MMW/MW P-branch transitions with ‘negative’ frequencies. The m values between -24 and -31 come from our MMW P-branch transitions with ‘negative’ frequencies. This impressive dataset can be fit well with either a 4th or 6th order polynomial.

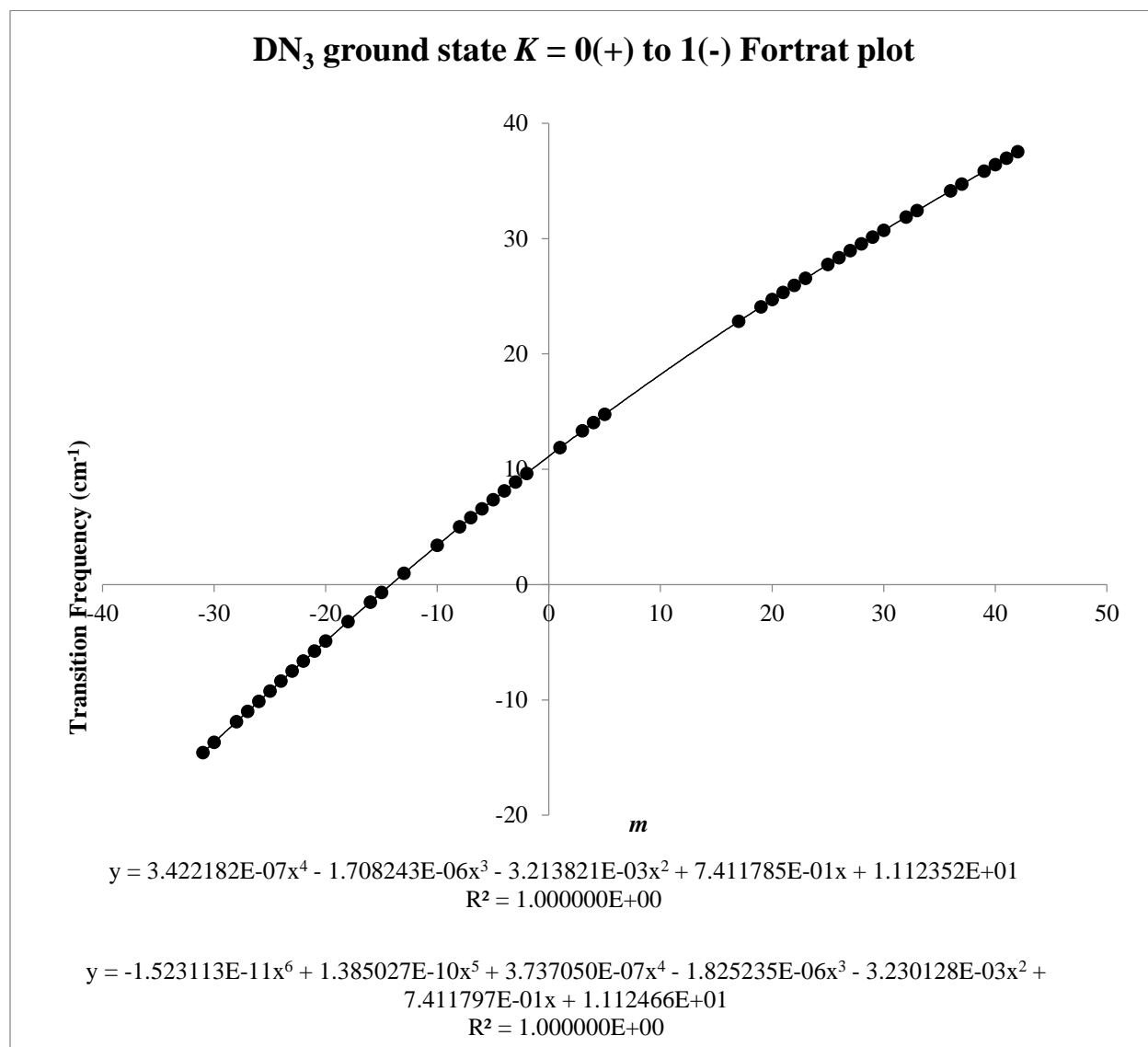


Figure 5.47 A Fortrat plot of pure rotational b -type transitions between $K = 0(+)$ and $K = 1(-)$ states spanning the microwave, millimeter, and infrared frequency regions.

Figure 5.48 shows a Fortrat plot for the $K = 0$ to $1(-)$ P-branch transitions in the ν_3 state of HN_3 . While the breadth of the dataset is less impressive than the Fortrat plot shown in Figure 5.47, a Q-branch involving the $K = 0$ and $1(+)$ levels is observed in our frequency region, which allows a fruitful comparison between Figure 5.48 and Figure 5.49 described below.

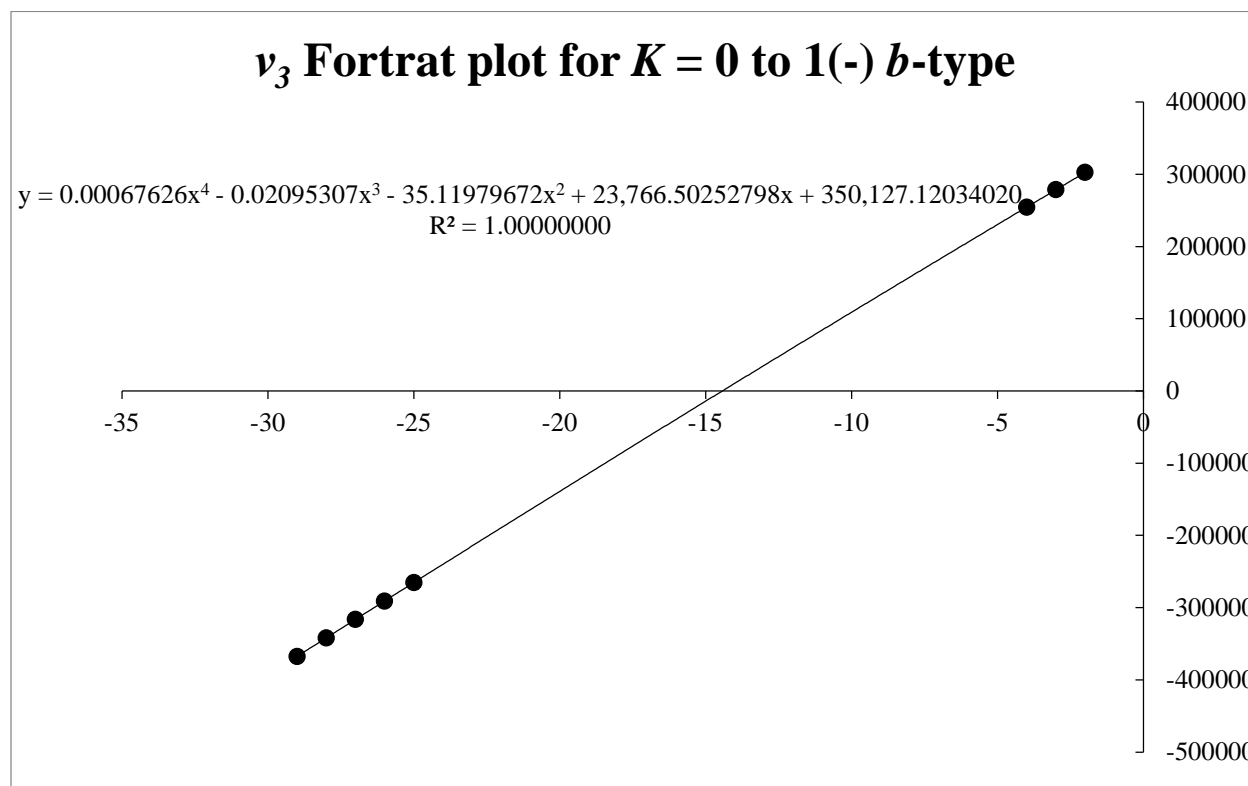


Figure 5.48 A Fortrat plot for the $K = 0$ to $1(-)$ P-branch transitions in the ν_3 state of HN_3 .

For Q-branch transitions, their energies can be expressed as follows below. The contributions from D , H , and L centrifugal distortion terms are neatly separated into the quadratic, cubic, and quartic coefficients, respectively.

Q-branch	Lower state $J'' = J$	Upper state $J' = J$	$Q(J) = E'_J - E''_J$
----------	-----------------------	----------------------	-----------------------

$$Q(J) = B.O. + (B' - B'')J(J + 1) - (D' - D'')J^2(J + 1)^2 + (H' - H'')J^3(J + 1)^3 - (L' - L'')J^4(J + 1)^4 \quad (5.25)$$

When The transition frequencies for the Q-branch transitions are plotted vs $J(J+1)$, the intercept is the band origin, the slope is the difference in effective rotational constants ($B'-B''$), the quadratic term is minus the difference in effective D constants ($D'-D''$), the cubic term is the difference in effective H constant ($H'-H''$) and the quartic term is minus the difference in the effective L value ($L'-L''$). Some of the same information can be extracted from the Fortrat plot, and some of this information can be extracted from the analysis of the a -type transitions in Figure 5.22. Figure 5.49 shows Q-branch transitions vs $J(J+1)$ for the Q-branch involving the $K = 0$ and $1(+)$ in the ν_3 state of HN_3 . In this case only a quadratic polynomial is required to fit the data. Note that the intercept of the Fortrat plot is 350,127 MHz and that for Q-branch plot is 350,126 MHz, which is the band origin for these transitions. This agreement is excellent in view of the the fact that both intercepts are outside the respective data ranges.

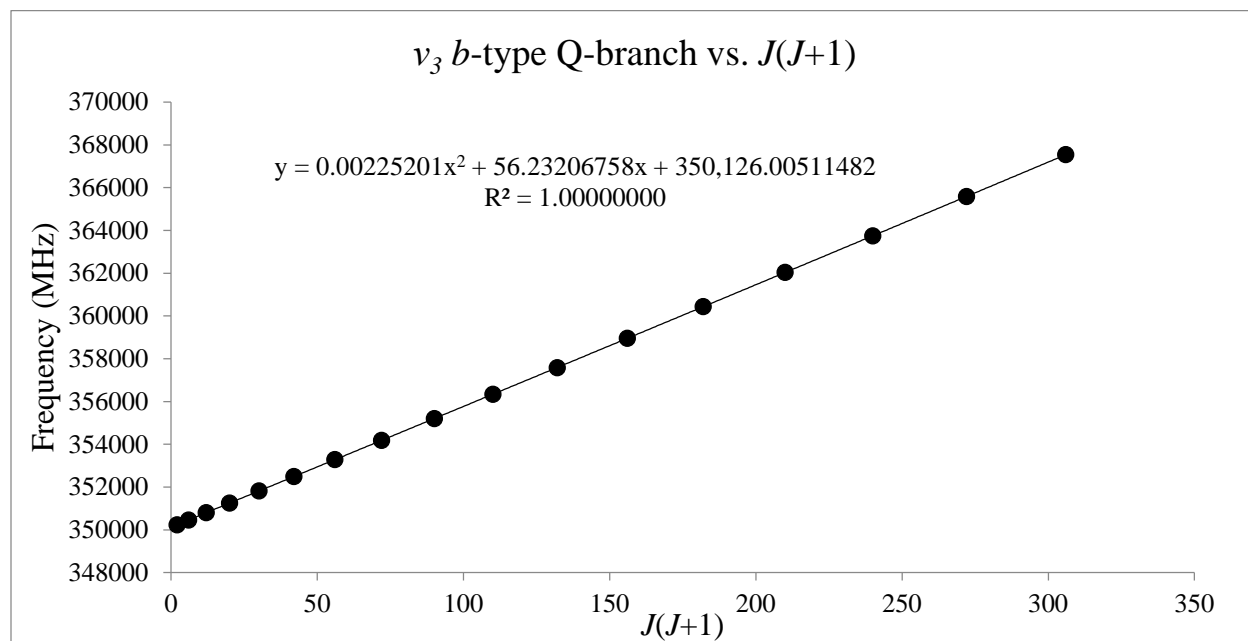


Figure 5.49 Plot of HN_3 ν_3 *b*-type Q-branch transitions between the $K = 0(+)$ and $1(+)$ states vs. $J(J+1)$.

Perturbation Analysis

In the above analyses we have confirmed initial assignments of hundreds of series of lines, including some very perturbed series. We have also extracted some spectroscopic constants from these analyses. To build working multi- vibrational state fits we need to also include appropriate perturbation terms with good starting values. We believe there are ~18 perturbation terms worth considering within the eight states studied for both HN_3 and DN_3 , occurring both within each polyad and between them. We have endeavored to get starting values for as many of these terms as possible, from the literature, from calculations, and from the analysis of various graphs of our assigned lines.

There is a centrifugal distortion interaction between the ground vibrational state and ν_5 , which we refer to as W_{05} . The effects of this interaction for HN_3 are shown in Figure 5.31. It is

clear that the perturbation exists between states with $\Delta K = 1$. For this perturbation $\Delta J = 0$. Literature values for this term are available for both HN_3 and DN_3 .⁵⁻⁶ Inclusion of this term in our three-state fits allowed us to successfully assign ground state transitions up to $K = 10$ for HN_3 and $K_p = 11$ for DN_3 (see Table 5.8 and Table 5.9). A similar perturbation term should occur between ν_5 and $2\nu_5$ as well as ν_6 and $\nu_5 + \nu_6$.

The A-type Coriolis (G_a) between ν_5 and ν_6 , ν_6 and ν_4 , $2\nu_5$ and $\nu_5 + \nu_6$, as well as $\nu_5 + \nu_6$ and $2\nu_6$ can be estimated. Estimating these terms requires knowing the calculated harmonic Coriolis coupling constant (ζ^A), the equilibrium A_e rotational constant, and the vibrational energies of the perturbing states (ω and ω').

$$G_a = \frac{\omega + \omega'}{\sqrt{\omega \times \omega'}} \zeta^A A_e \quad (5.26)$$

There are also local 2nd order A-type Coriolis interactions where $\Delta K = 2$. We refer to these as F_a . We have not yet implemented a practical way to estimate these terms.

There are local B-type Coriolis interactions between ν_5 and ν_6 , ν_6 and ν_4 , $2\nu_5$ and $\nu_5 + \nu_6$, as well as $\nu_5 + \nu_6$ and $2\nu_6$. These exist between vibrational states of different symmetry and rotational states of $\Delta J = 0$ and $\Delta K = 1$. These can be estimated from the calculated harmonic Coriolis coupling constant (ζ^B) for the pair of states, the equilibrium B_e rotational constant, and the vibrational energies of the perturbing states (ω and ω').

$$G_b = \frac{\omega + \omega'}{\sqrt{\omega \times \omega'}} \zeta^B B_e \quad (5.27)$$

The local C-type Coriolis interactions between ν_4 and ν_3 can be estimated from the calculated harmonic Coriolis coupling constant (ζ^C) for the pair of states, the equilibrium C_e rotational constant, and the vibrational energies of the perturbing states (ω and ω').

$$G_c = \frac{\omega + \omega'}{\sqrt{\omega \times \omega'}} \zeta^C C_e \quad (5.28)$$

The effects of this perturbation between ν_3 and ν_4 for HN_3 can be seen in Figure 5.35.

Table 5.6 A list of known or probable perturbations amongst the lowest eight vibrational states of HN_3 . Calculated (CCSD(T)/ANO2) or experimental values for these constants are given where known.

Centrifugal Distortion Perturbation (W_{05})		
$\Delta J = 0 \Delta K_{prolate} = 1$		
Ground	ν_5	Literature: ⁵ $0.04261(7) \text{ cm}^{-1} = 1277(2) \text{ MHz}$ 3-state fit: 1028.78(63) MHz
ν_5	$2\nu_5$	
ν_6	$\nu_5 + \nu_6$	
A-type Coriolis (G_a or Z^a) 1st order		
$\Delta J = 0 \Delta K_{prolate} = 0$ (different symmetry)		
ν_5	ν_6	Literature calculation: ^{5, 24} $38.06 \text{ cm}^{-1} = 1,141,600 \text{ MHz}$ 3-state fit: 1,140,413(293) MHz Calculation: 1,096,000 MHz
ν_6	ν_4	Calculation: 548900 MHz
$2\nu_5$	$\nu_5 + \nu_6$	Calculation: 1,094,000 MHz
$\nu_5 + \nu_6$	$2\nu_6$	Calculation: 1,094,000 MHz
A-type Coriolis (F_a or η^{bc}) 2nd order		
$\Delta J = 0 \Delta K_{prolate} = 2$ (different symmetry)		
ν_5	ν_6	Literature: $0.000322(8) \text{ cm}^{-1} = 9.65(24) \text{ MHz}$ 3-state fit: 6.87(54) MHz
ν_6	ν_4	
$2\nu_5$	$\nu_5 + \nu_6$	
$\nu_5 + \nu_6$	$2\nu_6$	
B-type Coriolis (G_b or Z^b) 1st order		
$\Delta J = 0 \Delta K_{prolate} = 1$ (different symmetry)		
ν_5	ν_6	Literature: $.06252 (13) \text{ cm}^{-1} = 1874 (4) \text{ MHz}$ 3-state fit: 1911.5 (11) MHz Calculation: -1173 MHz
ν_6	ν_4	Calculation: 1684.62 MHz
$2\nu_5$	$\nu_5 + \nu_6$	Calculation: -1171 MHz
$\nu_5 + \nu_6$	$2\nu_6$	Calculation: -1171 MHz
C-type Coriolis		
$\Delta J = 0 \Delta K_{prolate} = 1$ (same symmetry)		
ν_4	ν_3	Calculation: 5818 MHz
Fermi Resonance		
$\Delta J = 0 \Delta K_{prolate} = 0$		
ν_4	$2\nu_5$	Cubic force constant $k_{544} = 13.38$
$2\nu_6$	ν_3	Cubic force constant $k_{633} = -76.85$

Table 5.7 Summary of known or probable perturbations amongst the lowest eight vibrational states of DN₃. Calculated (CCSD(T)/ANO2) or experimental values for these constants are given where known.

Centrifugal Distortion Perturbation (W₀₅)		
$\Delta J = 0 \Delta K_{prolate} = 1$		
Ground	ν_5	Literature: ⁶ 0.0312(6) cm ⁻¹ = 935 (17) MHz 3-state fit: 1313(12) MHz
ν_5	$2\nu_5$	
ν_6	$\nu_5 + \nu_6$	
A-type Coriolis (G_a or Z^a) 1st order		
$\Delta J = 0 \Delta K_{prolate} = 0$ (different symmetry)		
ν_5	ν_6	Literature calculation: ^{6,24} 18.86 cm ⁻¹ = 565,400 MHz 3-state fit: 583,558.(405) MHz Calculation : 620,800 MHz
ν_6	ν_4	Literature calculation: ^{6,24} 9.43 cm ⁻¹ = 282,700 MHz Calculation : 304,083 MHz
$2\nu_5$	$\nu_5 + \nu_6$	Calculation: 619,200 MHz
$\nu_5 + \nu_6$	$2\nu_6$	Calculation: 619,000 MHz
A-type Coriolis (F_a or η^{bc}) 2nd order		
$\Delta J = 0 \Delta K_{prolate} = 2$ (different symmetry)		
ν_5	ν_6	Literature ⁶ : 0.00016(3) cm ⁻¹ = -4.79(90) MHz 3-state fit: 4.58(14) MHz
ν_6	ν_4	Literature: ⁶ -0.00251 (4) cm ⁻¹ = -75(1) MHz
$2\nu_5$	$\nu_5 + \nu_6$	
$\nu_5 + \nu_6$	$2\nu_6$	
B-type Coriolis (G_b or Z^b) 1st order		
$\Delta J = 0 \Delta K_{prolate} = 1$ (different symmetry)		
ν_5	ν_6	Literature: ⁶ 0.071(6) cm ⁻¹ 2130(180) MHz 3-state fit: -1650.(14) MHz Calculation: -1107 MHz
ν_6	ν_4	Calculation: 1556 MHz
$2\nu_5$	$\nu_5 + \nu_6$	Calculation: -1105 MHz
$\nu_5 + \nu_6$	$2\nu_6$	Calculation: -1104 MHz
C-type Coriolis (G_c)		
$\Delta J = 0 \Delta K_{prolate} = 1$ (same symmetry)		
ν_4	ν_3	Calculation: 5444 MHz
Fermi Resonance		
$\Delta J = 0 \Delta K_{prolate} = 0$		
ν_4	$2\nu_5$	Cubic force constant $k_{544} = 13.38$
$2\nu_6$	ν_3	Cubic force constant $k_{633} = -76.85$

Simultaneous fits of the ground, ν_5 , and ν_6 states of DN₃

Using the line assignments and approximations for spectroscopic constants derived from the literature and the body of work above, we have begun the task of fitting multiple vibrational states simultaneously. Table 5.8 shows our three-state fit of the ground vibrational state, ν_5 and ν_6 for DN₃. This fit uses FTIR ro-vibrational transitions from the literature,⁶ as well as MMW/MW/FTIR pure rotational transitions from the literature.¹⁴

Table 5.8 The results of a 3-state fit of the ground, ν_5 , and ν_6 states of DN₃. This fit used our millimeter-wave data, as well as published microwave,¹⁴ FIR,⁴ and FTIR⁶ data.

	Ground	ν_5	ν_6
A (MHz)	344746.37(14)	335348.(174)	346692.(174)
B (MHz)	11350.6411(67)	11386.827(94)	11350.181(88)
C (MHz)	10965.2163(84)	10971.062(95)	10985.614(80)
Δ_J (kHz)	4.2876(35)	4.360(10)	4.296(17)
Δ_{JK} (kHz)	226.2(42)	315.3(45)	793.2(17)
Δ_K (kHz)	92720.(30)	-83857.(708)	256865.(692)
δ_J (kHz)	0.17025(17)	0.17133(58)	0.1328(43)
δ_K (kHz)	196.6(26)	277.(16)	269.(14)
Φ_{JK} (Hz)	0.664(40)	0.31(80)	6.4(11)
Φ_{KJ} (Hz)	376.(15)	-693.(75)	-1711.(56)
Φ_K (Hz)	108592.(849)	-796330.(21873)	1182760.(18725)
L_{KKJ} (mHz)	977.(83)	-4883.(1038)	11738.(865)
L_K (mHz)	-145790.(5350)	6154600.(202995)	-9418700.(196701)
E (MHz)	0	14862133.8(17)	17583090.0(18)
N lines MMW	310	215	141
N lines IR	620	349	541
σ MMW(MHz)	0.352	1.23	2.02
σ IR (cm ⁻¹)	0.00246	0.00513	0.0159
G_a		583558.(405)	
F_a		4.58(14)	
G_b		-1650.(14)	
W_{05}	1313.(12)		

Kisiel's PIFORM program¹⁸ is a useful tool which reformats the output of SPFIT, showing the σ values for each state independently, and also differentiates between the σ value for microwave and IR transitions. PIFORM also corrects the statistical errors on the parameters to standard errors. It can be seen in Table 5.8 that the σ values are much higher than our measurement error. This can be rationalized, at least in part, by the Coriolis interaction between ν_6 and ν_4 , which is entirely unaccounted for in this three-state model. Indeed, the highest errors are seen in ν_6 , followed by ν_5 which is strongly coupled to ν_6 by the global G_a term. Hints of the importance of this G_a term can be seen elsewhere in Table 5.8. Notably, the ν_5 and ν_6 states share a large identical error in their A rotational constant of 174 MHz. Additionally, the Δ_K value for both the ν_5 and ν_6 states is wildly unphysical at -83.9 MHz and 256.9 MHz, but their average is 86.5 MHz, which is close to the ground state value for Δ_K of 92.7 MHz.

To better understand the G_a perturbation between ν_5 and ν_6 , we examine the two by two sub-block of the non J -dependent Hamiltonian matrix for ν_5 and ν_6 for a given fixed K . This is an extrapolation to a hypothetical $J = 0$ situation, so its eigenvalues should be equal to the intercepts of our 'linear plots' for ν_5 and ν_6 for that K .

$$\begin{bmatrix} E_6^0 + (A_6 - \frac{B_6 + C_6}{2})K^2 - D_{K,6}K^4 + H_{K,6}K^6 & G_a K \\ G_a K & E_5^0 + (A_5 - \frac{B_5 + C_5}{2})K^2 - D_{K,5}K^4 + H_{K,5}K^6 \end{bmatrix} \quad (5.29)$$

$$\lambda = \frac{E_6^0 + E_5^0}{2} + \frac{(A_6 - \frac{B_6 + C_6}{2}) + (A_5 - \frac{B_5 + C_5}{2})}{2} K^2 - \frac{D_{K,6} + D_{K,5}}{2} K^4 + \frac{H_{K,6} + H_{K,5}}{2} K^6 \quad (5.30)$$

$$\pm \sqrt{\frac{[(E_6^0 - E_5^0) + \left(A_6 - \frac{B_6 + C_6}{2}\right) - \left(A_5 - \frac{B_5 + C_5}{2}\right)]K^2 - (D_{K,6} - D_{K,5})K^4 + (H_{K,6} - H_{K,5})K^6]^2 + 4G_a^2 K^2}{2}}$$

$$\lambda_{average} = \frac{E_{K,6} + E_{K,5}}{2} \quad (5.31)$$

$$= \frac{E_6^0 + E_5^0}{2} + \frac{\left(A_6 - \frac{B_6 + C_6}{2}\right) + \left(A_5 - \frac{B_5 + C_5}{2}\right)}{2} K^2 - \frac{D_{K,6} + D_{K,5}}{2} K^4 + \frac{H_{K,6} + H_{K,5}}{2} K^6$$

$$\lambda_{difference} = E_{K,6} - E_{K,5} \quad (5.32)$$

$$= \sqrt{[(E_6^0 - E_5^0) + \left(A_6 - \frac{B_6 + C_6}{2}\right) - \left(A_5 - \frac{B_5 + C_5}{2}\right)]K^2 - (D_{K,6} - D_{K,5})K^4 + (H_{K,6} - H_{K,5})K^6]^2 + 4G_a^2 K^2}$$

$$\begin{aligned} (E_{K,6} - E_{K,5})^2 &\approx (E_6^0 - E_5^0)^2 + \left\{2(E_6^0 - E_5^0) \left[\left(A_6 - \frac{B_6 + C_6}{2}\right) - \left(A_5 - \frac{B_5 + C_5}{2}\right)\right] + 4G_a^2\right\} K^2 \\ &+ \left\{\left[\left(A_6 - \frac{B_6 + C_6}{2}\right) - \left(A_5 - \frac{B_5 + C_5}{2}\right)\right]^2 - 2(E_6^0 - E_5^0)(D_{K,6} - D_{K,5})\right\} K^4 \end{aligned} \quad (5.33)$$

$$\left\{2(E_6^0 - E_5^0)(H_{K,6} - H_{K,5}) - 2\left[\left(A_6 - \frac{B_6 + C_6}{2}\right) - \left(A_5 - \frac{B_5 + C_5}{2}\right)\right](D_{K,6} - D_{K,5})\right\} K^6 + \dots$$

The K energies $E_{K,6}$ and $E_{K,5}$ for high K are determined from the infrared sub-band origins for the ν_5 and ν_6 bands, respectively, and the E_K 's for the ground state, which come from the analysis of the FIR pure rotational spectrum. Those for low K are best determined from the band

origins of the Fortrat plots for MMW data. To extract the above J independent parameters from linear least-squares fits, one should make two plots: an average plot and a difference plot. The average of $E_{K,6}$ and $E_{K,5}$ should be plotted vs. K^2 and fit to a cubic polynomial. The successive coefficients yield the average of E_6^0 and E_5^0 , the average of $\left(A_6 - \frac{B_6+C_6}{2}\right)$ and $\left(A_5 - \frac{B_5+C_5}{2}\right)$, the average of $D_{K,6}$ and $D_{K,5}$, and the average of $H_{K,6}$ and $H_{K,5}$, respectively. For the difference plot, plotting $(E_{K,6} - E_{K,5})^2$ vs. K^2 followed by a cubic polynomial fit yields the following successive coefficients:

$$\begin{aligned}
 & (E_6^0 - E_5^0)^2 \\
 & \left\{ 2(E_6^0 - E_5^0) \left[\left(A_6 - \frac{B_6 + C_6}{2} \right) - \left(A_5 - \frac{B_5 + C_5}{2} \right) \right] + 4G_a^2 \right\} \\
 & \left\{ \left[\left(A_6 - \frac{B_6 + C_6}{2} \right) - \left(A_5 - \frac{B_5 + C_5}{2} \right) \right]^2 - 2(E_6^0 - E_5^0)(D_{K,6} - D_{K,5}) \right\} \\
 & \left\{ 2(E_6^0 - E_5^0)(H_{K,6} - H_{K,5}) - 2 \left(\left(A_6 - \frac{B_6 + C_6}{2} \right) - \left(A_5 - \frac{B_5 + C_5}{2} \right) \right) (D_{K,6} - D_{K,5}) \right\}
 \end{aligned} \tag{5.34}$$

The difference of the vibrational energies is straightforwardly determined from the square root of the constant coefficient of the difference plot. It can be seen from the last three coefficients of the difference plot that other difference parameters are highly correlated. The linear term depends on the rotational constant difference and the G_a perturbation parameter, as well as the vibrational energy difference, which is known from the constant term. The quadratic term depends on the rotational constant difference and the D_K difference as well as the vibrational energy difference. The cubic term depends on the rotational constant difference, the D_K difference, and the H_K difference, as well as the vibrational energy difference. In order to solve for these parameters, a simplifying assumption must be made, and the obvious choice is that $H_{K,6} - H_{K,5} = 0$. Having made

this assumption, the value of G_a and the two remaining difference terms can be found from solving the three equations. In the published infrared analysis, the authors chose to fix G_a to a previously published *ab initio* value.²⁴ Based on the above equations, this does not seem to be the optimal choice, since any error in the *ab initio* value will force the rotational constant difference to non-physical values.

It can be seen in Table 5.8 that the values for D_K in our 3-state DN₃ fit are clearly non-physical. This can be understood by the strong correlation of $D_{K,6} - D_{K,5}$ to the other difference parameters. That being said, the average of $D_{K,6}$ and $D_{K,5}$ is 86.5 MHz, which is in reasonable agreement with the ground state D_K value of 92.7 MHz. This is expected because the average of $D_{K,6}$ and $D_{K,5}$ is the quadratic coefficient in the plot of K -energy averages vs. K^2 .

Simultaneous fits of the ground, ν_5 , and ν_6 states of HN₃

A 3-state fit was also carried out for the lowest three vibrational states of HN₃. This fit proved more difficult to optimize than for DN₃, and in order to get the fit to converge to a reasonable set of parameters we needed to exclude all of the published mid and far IR FTIR data, but we were still able to include published microwave and millimeter-wave transitions. Without the IR transitions, we were unable to fit the relative vibrational energies of ν_5 and ν_6 , so we left them set to their literature values. This fit is shown in Table 5.9.

Table 5.9 A simultaneous three state fit of the ground, ν_5 , and ν_6 states of HN_3 . The fit includes our own millimeter-wave data as well as microwave and millimeter-wave data¹¹⁻¹³ from the literature.

	Ground	ν_5	ν_6
A (MHz)	610738.61(52)	590181.(325)	622490.(328)
B (MHz)	12034.54(50)	12068.42(99)	12035.2(10)
C (MHz)	11781.13(50)	11783.94(99)	11801.6(10)
Δ_J (kHz)	4.863(29)	4.758(46)	5.238(73)
Δ_{JK} (kHz)	670.47(78)	-963.5(53)	2690.0(56)
Δ_K (kHz)	-26395.(462)	-76880.(8526)	-887160.(14740)
δ_J (Khz)	0.0831(45)	-0.068(12)	-0.194(39)
δ_K (kHz)	196.(251)	595.(213)	566.(241)
Φ_J (Hz)	-0.031(11)	-0.122(42)	-0.143(85)
Φ_{JK} (Hz)	-0.79(99)	34.7(37)	-21.3(52)
Φ_{KJ} (Hz)	538.7(95)	-27921.(158)	26027.(189)
E (MHz)	[0]	[16106838.47]	[18178137.54]
N lines MM	188	136	82
σ (MHz)	0.38059	0.75078	1.04039
G_a (MHz)		1140413.(293)	
F_a (MHz)		6.87(54)	
G_b (MHz)		1911.5(11)	
W_{05} (MHz)	1028.78(63)		

With 3-state fits in hand for both HN_3 and DN_3 , we can compare the constants obtained with those from extracted from the linear plots of the a -type transitions (Figure 5.17 through Figure 5.30) As shown in Table 5.10, Generally the $B+C$ value derived from the value of the intercept of the intercept plots is very consistent with the value obtained in the non-linear least-squares fit. The values for Δ_J are also quite consistent. In the case of ν_5 and ν_6 of HN_3 , the values of Δ_{JK} from the three state fit do not match well with those obtained from the slope of the intercepts plots. Averaging the Δ_{JK} values of ν_5 and ν_6 gives 0.783 kHz for the plotting method, and 0.863 kHz for the 3-state fit, and is thus another example of the average of these constants being much better determined than their difference.

Table 5.10 A comparison of the constants derived from the linear plots of the *a*-type R-branch transitions and those found in the 3-state fits for the ground, ν_5 , and ν_6 states for HN₃ and DN₃.

		$B+C$ (MHz)	Δ_{JK} (kHz)	Δ_J (kHz)
HN ₃ Ground	from <i>a</i> -type plots	23815.95	0.8283	0.0046
	3-state fit	23815.67	0.6705	0.0049
HN ₃ ν_5	from <i>a</i> -type plots	23852.73	0.4833	0.0043
	3-state fit	23852.36	-0.963	0.0048
HN ₃ ν_6	from <i>a</i> -type plots	23837.54	1.0836	0.00494
	3-state fit	23836.8	2.69	0.005238
DN ₃ Ground	from <i>a</i> -type plots	22318.51	0.5315	0.00376
	3-state fit	22315.857	0.226	0.00429
DN ₃ ν_5	from <i>a</i> -type plots	23852.73	0.3453	0.00379
	3-state fit	22357.889	0.3153	0.00436
DN ₃ ν_6	from <i>a</i> -type plots	22337.43	0.5445	0.00393
	3-state fit	22335.79	0.7932	0.004296

Summary

We have observed transitions from eight vibrational states of both HN₃ and DN₃. The task of fitting these transitions to rotational constants is greatly complicated by the web of perturbations that exist between them. Excluding some transitions from the datasets allows for single-state fits of the ground vibrational levels, but analysis of the other states requires a multi-state fit. To get a functional multi-state fit, the transition assignments must be solid, and reasonable starting parameters for all of the constants, including the perturbation terms, must be known. In this chapter the numerous methods of assigning and confirming lines without resorting to an overall fit have been described. Numerous spectroscopic constants have also been estimated. We have been reasonably successful with 3-state fits of the three lowest vibrational levels. The five upper levels are strongly mutually perturbing, and it is critical for us to find the *b*-type transitions for $2\nu_5$ and $\nu_5+\nu_6$ of DN₃, as well as the *a*-type and *b*-type transitions for $\nu_5+\nu_6$ and $2\nu_6$ and the *b*-type transitions of $2\nu_5$ for HN₃, in order to be successful. Our extensive study of these states and the

perturbations between them make us optimistic about obtaining an eight-state fit for each isotopologue.

Acknowledgments

We gratefully acknowledge funding from the National Science Foundation for support of this project (CHE-1362264 and CHE-1011959) and for support of shared Departmental computing resources (CHE-0840494). We thank Dr. Mark Wendt for access to the Agilent MXG Analog Signal Generator N5183B.

References

1. Yamada, K.; Takami, M., High-resolution infrared spectrum of hydrazoic acid: The ν_3 fundamental by a tunable diode laser. *J. Mol. Spectrosc.* **1980**, *84* (2), 431-446.
2. Bendtsen, J.; Hegelund, F.; Nicolaisen, F. M., Infrared spectrum of the Coriolis coupled vibrations ν_5 and ν_6 of hydrazoic acid. *J. Mol. Spectrosc.* **1986**, *118* (1), 121-131.
3. Bendtsen, J.; Nicolaisen, F. M., The pure rotational absorption spectrum of hydrazoic acid in the far-infrared region. *J. Mol. Spectrosc.* **1986**, *119* (2), 456-466.
4. Bendtsen, J.; Nicolaisen, F. M., The pure rotational absorption spectrum of deuterated hydrazoic acid (DN_3) in the far-infrared region. *J. Mol. Spectrosc.* **1987**, *125* (1), 14-23.
5. Hegelund, F.; Bendtsen, J., A simultaneous analysis of ν_5 , ν_6 , and the ground state of hydrazoic acid. *J. Mol. Spectrosc.* **1987**, *124* (2), 306-316.
6. Bendtsen, J.; Hegelund, F.; Nicolaisen, F. M., A simultaneous analysis of ν_5 , ν_6 , and the ground state of deuterated hydrazoic acid. *J. Mol. Spectrosc.* **1988**, *128* (2), 309-320.
7. Bendtsen, J.; Nicolaisen, F. M., Infrared spectrum of the ν_4 band of hydrazoic acid. *J. Mol. Spectrosc.* **1989**, *133* (1), 193-200.
8. Bendtsen, J.; Nicolaisen, F. M., High-resolution infrared spectrum of the ν_4 band of deuterated hydrazoic acid (DN_3). *J. Mol. Spectrosc.* **1991**, *145* (1), 123-129.
9. Bendtsen, J.; Nicolaisen, F. M., High-resolution infrared absorption spectra of the ν_3 and ν_4 hybrid bands of hydrazoic acid (HN_3). *J. Mol. Spectrosc.* **1992**, *152* (1), 101-108.

10. Hansen, C. S.; Bendtsen, J.; Nicolaisen, F. M., Analyses of the High-Resolution Infrared Absorption Spectra of the ν_2 and ν_3 Bands of Deuterated Hydrazoic Acid (DN_3). *J. Mol. Spectrosc.* **1996**, *175* (2), 239-245.
11. Winnewisser, M.; Cook, R. L., Centrifugal Distortion Effects and Structure of Hydrazoic Acid from the Millimeter Wave Rotational Spectra. *J. Chem. Phys.* **1964**, *41* (4), 999-1004.
12. Kewley, R.; Sastry, K. V. L. N.; Winnewisser, M., Microwave and Millimeter Wave Spectra of Hydrazoic Acid. *J. Mol. Spectrosc.* **1964**, *12*, 387-401.
13. Bendtsen, J.; Winnewisser, M., Ground state spectroscopic constants and dipole moment of hydrazoic acid, H^{14}N_3 . *Chem. Phys. Lett.* **1975**, *33* (1), 141-145.
14. Bendtsen, J.; Winnewisser, M., Absorption spectrum of deuterated hydrazoic acid, D^{14}N_3 in the microwave and millimeterwave region. *Chem. Phys.* **1979**, *40* (3), 359-365.
15. Bendtsen, J.; Guelachvili, G., High-Resolution Infrared Absorption Spectrum of the ν_2 Band of Hydrazoic Acid (HN_3). *J. Mol. Spectrosc.* **1994**, *165* (1), 159-167.
16. Cheung, A. S. C.; Merer, A. J., The ν_1 and $\nu_2 + \nu_4$ bands in the infrared spectrum of HN_3 . *J. Mol. Spectrosc.* **1988**, *127* (2), 509-526.
17. Bendtsen, J., Raman and infrared rotation-vibration spectra of the ν_1 Band of D^{14}N_3 . *J. Raman Spectrosc.* **1984**, *15* (2), 113-119.
18. Kisiel, Z. PROSPE: Programs for Rotational spectroscopy.
<http://www.ifpan.edu.pl/~kisiel/prospe.htm>.
19. Pickett, H. M., The fitting and prediction of vibration-rotation spectra with spin interactions. *J. Mol. Spectrosc.* **1991**, *148* (2), 371-377.
20. Amberger, B. K.; Esselman, B. J.; Woods, R. C.; McMahon, R. J., Millimeter-wave spectroscopy of carbonyl diazide, $\text{OC}(\text{N}_3)_2$. *J. Mol. Spectrosc.* **2014**, *295*, 15-20.
21. Esselman, B. J.; Amberger, B. K.; Shutter, J. D.; Daane, M. A.; Stanton, J. F.; Woods, R. C.; McMahon, R. J., Rotational spectroscopy of pyridazine and its isotopologs from 235-360 GHz: Equilibrium structure and vibrational satellites. *J. Chem. Phys.* **2013**, *139*, 224304 1-13.
22. Loomis, F. W.; Wood, R. W., The Rotational Structure of the Blue-Green Bands of Na_2 . *Physical Review* **1928**, *32* (2), 223-236.
23. Wang, S. C., *Phys. Rev.* **1929**, *34*.

24. Levine, D. M.; Dows, D. A., Infrared Spectrum of HN₃ and DN₃: Assignment of the Coriolis-Coupled Bending Vibrations. *J. Chem. Phys.* **1967**, *46* (3), 1168-1172.

Appendix A

Rotational spectroscopy of pyridazine and its isotopologs from 235-360 GHz: Equilibrium structure and vibrational satellites

Brian J. Esselman
Brent K. Amberger
Joshua D. Shutter
Mitchell A. Daane
John F. Stanton
R. Claude Woods
Robert J. McMahon

Journal of Chemical Physics, 2013, *139*, 224304 1-13

Rotational spectroscopy of pyridazine and its isotopologs from 235–360 GHz: Equilibrium structure and vibrational satellites

Brian J. Esselman,¹ Brent K. Amberger,¹ Joshua D. Shutter,¹ Mitchell A. Daane,¹ John F. Stanton,² R. Claude Woods,¹ and Robert J. McMahon¹

¹Department of Chemistry, University of Wisconsin–Madison, Madison, Wisconsin 53706, USA

²Institute for Theoretical Chemistry, Departments of Chemistry and Biochemistry, The University of Texas–Austin, Austin, Texas 78712, USA

(Received 30 September 2013; accepted 8 November 2013; published online 10 December 2013)

The rotational spectrum of pyridazine (*o*-C₄H₄N₂), the *ortho* disubstituted nitrogen analog of benzene, has been measured and analyzed in the gas phase. For the ground vibrational state of the normal isotopolog, over 2000 individual rotational transitions have been identified between 238 and 360 GHz and have been fit to 13 parameters of a 6th-order centrifugal distortion Hamiltonian. All transitions in this frequency region can now be predicted from this model to near experimental accuracy, i.e., well enough for the purpose of any future radio-astronomical search for this species. Three isotopologs, [3-¹³C]-C₄H₄N₂, [4-¹³C]-C₄H₄N₂, and [1-¹⁵N]-C₄H₄N₂, have been detected in natural abundance, and several hundred lines have been measured for each of these species and fit to 6th-order Hamiltonians. Ten additional isotopologs were synthesized with enhanced deuterium substitution and analyzed to allow for a complete structure determination. The equilibrium structure (*R*_e) of pyridazine was obtained by correcting the experimental rotational constants for the effects of vibration-rotation coupling using interaction constants predicted from CCSD(T) calculations with an ANO0 basis set and further correcting for the effect of electron mass. The final *R*_e structural parameters are determined with excellent accuracy, as evidenced by their ability to predict 28 independent moments of inertia (*I*_a and *I*_b for 14 isotopologs) very well from 9 structural parameters. The rotational spectra of the six lowest-energy fundamental vibrational satellites of the main isotopolog have been detected. The rotational spectra of the five lowest-energy vibrational satellites have been assigned and fit to yield accurate rotational and distortion constants, while the fit and assignment for the sixth is less complete. The resultant vibration-rotation interaction (*α*) constants are found to be in excellent agreement with ones predicted from coupled-cluster calculations, which proved to be the key to unambiguous assignment of the satellite spectra to specific vibration modes. © 2013 AIP Publishing LLC. [<http://dx.doi.org/10.1063/1.4832899>]

INTRODUCTION

The existence of aromatic compounds in a variety of harsh reaction environments, including combustion, planetary atmospheres, and interstellar space, is a topic of considerable current interest.¹ Spectroscopic detection and characterization of molecular species in these environments rely on the availability of high quality laboratory spectra. Although the millimeter and submillimeter rotational spectra of nitrogen-substituted derivatives of benzene (C₆H₆), such as pyridine (C₅H₅N)² and pyrimidine (*m*-C₄H₄N₂)³ have been measured, the spectrum of pyridazine (*o*-C₄H₄N₂ shown in Fig. 1)^{4,5} at those frequencies has not. In the microwave (cm-wave) region (9–33 GHz), the rotational spectrum of pyridazine was first reported in 1967 by Werner *et al.*⁴ In addition to the normal isotopolog, they observed the [3-¹³C], [4-¹³C], and [1-¹⁵N] isotopologs in natural abundance and fit their spectra to a Hamiltonian with 4th-order centrifugal distortion. These cm-wave spectra are complicated by the presence of quadrupole hyperfine structure due to ¹⁴N atoms. A partial substitution structure (*R*_s) determination of the aromatic ring was completed using the isotopolog data, but a full structure determination was not possible. This was because the

Kraitchman⁶ analysis requires additional isotopic substitution (deuterium) to locate the hydrogen atom positions, and due to the proximity of carbon atoms C3 and C6 to the *b* principal axis, which made determination of the corresponding *a* coordinate very inaccurate. Lopez *et al.*⁵ provided a more precise measurement of the hyperfine coupling constants using molecular beam Fourier transform microwave spectroscopy. This investigation refined the rotational constants *A*, *B*, and *C*, but fixed the distortion constants to those determined in the original 1967 effort. Together these two papers provide rotational constants and distortion constants for a 4th-order Hamiltonian based upon rotational transitions with *J*_{upper} from 1 to 12. Much more accurate rotational and distortion constants, and thereby a more accurate structure determination, can be obtained if millimeter-wave rotational transitions with higher *J* values can be measured. These higher *J* transitions are ideal for laboratory or other detection, since the maximum absorption intensity for a molecule like pyridazine (*A* + *B* + *C* ≈ 15 GHz) at room temperature will occur for *J* ≈ 40.⁷

Aromatic species, like pyridazine, are of fundamental interest to the chemistry of the interstellar medium (ISM) and their detection would aid in the understanding of astrochemical abundances and reactions. Unfortunately, the

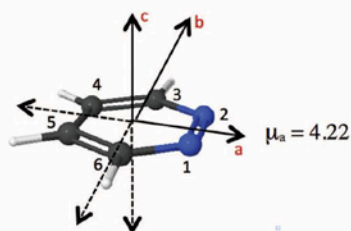


FIG. 1. Structure of pyridazine ($C_4H_4N_2$) with principal axes labeled. The midpoint between the two nitrogen atoms lies on the positive a axis. Image produced by WebMO.⁸

prototypical aromatic compound, benzene, possesses no permanent dipole moment (D_{6h} symmetry) and is therefore not observable by radio astronomy. The reported observation of the 673.9732 cm^{-1} infrared absorption of benzene in the interstellar medium with the Infrared Space Observatory (ISO)⁹ prompted an increased desire to detect related aromatic species. Unfortunately, to date, no six-membered aromatic benzene analogs or derivatives have been unambiguously detected,^{10,11} despite several searches in the ISM for similar species such as *o*-benzynes,¹² pyridine,¹³ and pyrimidine.¹⁴ Not only are these species interesting in their own right, but their presence would provide indirect evidence to support the infrared detection of benzene. To the best of our knowledge, pyridazine itself has not yet been the subject of an interstellar search, likely due in part to the lack of published laboratory millimeter and submillimeter-wave spectra. One could imagine that the nitrogen-containing benzene analogs could arise in the ISM from a substitution of HCN, HNC, or N_2 for acetylene, or cyanoacetylene for diacetylene, in the proposed pathways for the interstellar production of benzene.^{15,16} The two nitrogen atoms in pyridazine give rise to a dipole moment of $\mu = 4.22\text{ D}$,⁴ which is approximately twice that of pyridine ($\mu = 2.19\text{ D}$),¹⁴ and pyrimidine ($\mu = 2.39\text{ D}$),¹⁴ and much larger than *o*-benzynes ($\mu = 1.38\text{ D}$).¹⁷ This leads to an intrinsically very strong rotational spectrum, which is quite beneficial in detecting small abundances.

EXPERIMENTAL AND COMPUTATIONAL METHODS

The rotational absorptions presented here are the first measurements made using our newly upgraded millimeter-wave and submillimeter-wave spectrometer, which is based upon the instrument described previously.^{18,19} The new system uses tone-burst modulated radiation produced by a Fluke & Phillips PM 5193 SM programmable synthesizer, an Agilent MXG signal generator N5183A (0–20 GHz), and a Virginia Diodes $\times 18$ amplifier-multiplier chain. The 238–360 GHz radiation is passed through a 10 cm diameter by 3 m length free space absorption cell, and the transmitted radiation is detected by a Virginia Diodes zero-bias detector. This detector operates at room temperature, which offers advantages in terms of both convenience and cost relative to the earlier liquid-helium cooled InSb detector. The entire spectral range

exhibits a fairly flat frequency response and is accessible without requiring tuning by the operator. After passing through a Stanford Research Systems Model SR850 DSP Lock-In Amplifier, the signal is digitized and stored in a PC running custom software developed in LabVIEW 2010.²⁰ With the exception of blended lines that were not sufficiently resolvable to be included in a least-squares fitting routine (either our local version or that provided in the AABS package for *Assignment and Analysis of Broadband Spectra*²¹), all of the lines reported in this work are estimated to have an uncertainty of $\pm 50\text{ kHz}$, although much higher frequency accuracy is achievable with this apparatus when needed.

A typical absorption experiment occurred at room-temperature using a sample of pyridazine purchased from Aldrich (98% purity), used without purification at a pressure of 4.0 mTorr with continuous flow through the sample chamber. The custom LabVIEW software and spectrometer are automated, including automatic pressure control, so that very broad frequency scans without operator intervention are practical. In the latter stages of this work, we typically recorded an entire pyridazine or deuterium-enriched pyridazine spectrum from $\sim 235\text{ GHz}$ to 360 GHz (20 points/MHz) in a single unattended experiment spanning several days. The continuous spectrum in combination with the convenient AABS package allowed for a very large number of rotational transitions to be measured and analyzed for most of the vibration states and isotopic forms studied in this work. In total, frequencies of over 20 000 transitions were measured and fit and are reported here (the majority of which occur as degenerate pairs).

Pyridazine samples with enriched deuterium content were prepared using a method adapted from the work of Dauglius and co-workers using *t*-BuOLi/*t*-BuOD.²² The samples consist of mixtures of mono-, di-, tri-, and tetra-deuterio species, and the extent of deuterium incorporation may be controlled as a function of reaction time. In this work, three samples were prepared, employing reaction times of 1 h, 3.5 h, and 19 h. The preference for incorporation of deuterium at the *meta* position was monitored by $^1\text{H-NMR}$ spectroscopy, as reported previously by Katritzky *et al.*²³ These reactions were sufficient to observe ten deuterium-containing isotopologs: [$3\text{-}^2\text{H}$], [$4\text{-}^2\text{H}$], [$3,4\text{-}^2\text{H}$], [$3,5\text{-}^2\text{H}$], [$3,6\text{-}^2\text{H}$], [$4,5\text{-}^2\text{H}$], [$3,4,5\text{-}^2\text{H}$], [$3,4,6\text{-}^2\text{H}$], [$3,4,5,6\text{-}^2\text{H}$], [$4\text{-}^2\text{H}, 3\text{-}^{13}\text{C}$]. Simple density functional theory calculations (B3LYP/6-31G(d), Table S2 of the supplementary material⁴⁷) provided sufficiently reliable predictions to assign these molecules' spectra by their estimated rotational constants. These assignments were later confirmed by the various structure determinations described in more detail below.

The transition frequencies for each species were fit and predicted using Kisiel's asymmetric rotor fitting and prediction programs, ASFIT and ASROT,²⁴ respectively. For each pyridazine isotopolog, a 6th-order Hamiltonian was fit to the spectrum. Depending on the number and types of transitions, different numbers of constants were determinable for each species. Least-squares fitting of rotational constants to determine a R_0 structure and two equilibrium structures were completed using xrefit, a module of the CFOR computational quantum chemistry program.²⁵

The B3LYP,^{26,27}/6-31G(d),²⁸ B3LYP/cc-pVTZ,²⁹ and MP2³⁰/cc-pVTZ optimization and frequency calculations of pyridazine were completed in Gaussian 09³¹ using the WebMO⁸ interface. The nature of the optimized stationary point was confirmed by anharmonic, vibration-rotation interaction frequency calculations indicating it was a minimum on the potential energy surface. These calculations were completed with *verytight* optimization criteria using an ultrafine grid as recommended to predict the vibration-rotation interactions for other 5- and 6-membered heterocycles.³² At the higher levels CCSD(T)³³/cc-pVTZ, CCSD(T)/ANO0, CCSD(T)/ANO1, and CCSD(T)/ANO2,³⁴ optimized geometries were obtained using CFOUR²⁵ using analytic gradients^{35,36} with the frozen core approximation, GEO_CONV = 7, SCF_CONV = 10, and CC_CONV = 9. To determine the vibration-rotation interaction coupling constants, the cubic force constants were calculated by numerical differentiation of the analytic second derivatives at displaced points following the approach of Stanton *et al.*^{37,38} These DFT and *ab initio* computational results provided the foundation for assigning the various pyridazine isotopologs and the vibrationally excited states. While the shifts in the rotational constants (*A*, *B*, and *C*) were reasonably well described by B3LYP or MP2 calculations for the isotopologs, they were of little use for the vibrationally excited states. Fortunately, the coupled-cluster calculations did provide an experimentally useful estimation of the shifts for the vibrationally excited species. Output summaries of each of the theoretical calculations and our analysis can be found in the supplementary material.⁴⁷

ANALYSIS OF ROTATIONAL SPECTRA OF PYRIDAZINE (C₄H₄N₂) AND ITS ISOTOPOLOGS IN THEIR GROUND VIBRATIONAL LEVELS

Pyridazine displays a rotational spectrum typical of a near-oblate asymmetric top similar to that of many other aromatic six-membered ring species, such as pyridine,² pyrimidine,³ and phenyl radical.³⁹ Our initial identification of pyridazine's ground-state rotational spectrum was based upon the published rotational and 4th-order distortion constants derived from measurements in the cm-wave region.⁴ These data provided predictions for higher *J* transitions in the millimeter and submillimeter-wave that were typically accurate within ± 8 MHz for Q-branch transitions, ± 0.3 MHz for the lead R-branch transitions for a band, and ± 5 MHz for isolated R-branch transitions. The high-*J* transitions that are reported in this work do not exhibit any observable hyperfine structure arising from the quadrupole coupling with nitrogen. The hyperfine structure of pyridazine has already been thoroughly investigated in the cm-wave spectra described earlier.⁵ We did see a few examples of small hyperfine splittings in the lowest *J* lines we found (*J* values in the low 20s), but these lines were not included in our work. For the vibrational ground-states of the normal isotopolog and each of the ¹³C and ¹⁵N isotopologs, we combined our data sets of high-*J* transitions with those for the low-*J* transitions (corrected to remove hyperfine splitting) from Werner *et al.*⁴ and Lopez *et al.*⁵ As shown in Table I, our spectra contain many intense *a*-type, R-branch (^aR_{0,1}, ^aR_{2,-1}, ^aR_{2,3}, and ^aR_{4,-3}) transitions which were measured from *J*_{upper} = 16 to 57 for ground state pyridazine.

TABLE I. Transition types measured for pyridazine isotopologs (includes transitions reported in Ref. 4).

Type	C ₄ H ₄ N ₂	[3- ¹³ C]-	[4- ¹³ C]-	[1- ¹⁵ N]-	[3- ² H]	[4- ² H]		
^a Q _{0,-1}	738	186	210	79	0	397		
^b Q _{1,-1}	0	0	0	0	146	0		
^a Q _{2,-1}	743	181	204	71	0	397		
^a R _{0,1}	545	432	534	327	0	764		
^b R _{1,1}	0	0	0	0	207	0		
^b R _{1,-1}	0	0	0	0	22	0		
^b R _{-1,1}	0	0	0	0	193	0		
^a R _{2,-1}	138	7	1	0	0	54		
^a R _{-2,3}	10	0	0	0	0	0		
^b R _{3,-1}	0	0	0	0	0	0		
^a R _{4,-3}	1	0	0	0	0	0		
Total	2175	806	949	477	568	1612		
Type	[3,4- ² H]	[3,5- ² H]	[3,6- ² H]	[4,5- ² H]	[3,4,5- ² H]	[3,4,6- ² H]	[3,4,5,6- ² H]	[4- ² H,3- ¹³ C]
^a Q _{0,-1}	116	220	0	0	296	258	0	0
^b Q _{1,-1}	232	440	0	0	0	515	0	0
^a Q _{2,-1}	116	220	0	0	297	258	0	0
^a R _{0,1}	566	632	0	724	480	606	0	392
^b R _{1,1}	269	321	396	0	0	364	216	200
^b R _{1,-1}	25	52	0	0	0	64	41	1
^b R _{-1,1}	246	287	315	0	0	309	198	199
^a R _{2,-1}	13	23	0	1	58	4	0	0
^a R _{-2,3}	0	0	0	0	0	0	0	0
^b R _{3,-1}	4	7	1	0	0	12	17	0
^a R _{4,-3}	0	0	0	0	0	0	0	0
Total	1587	2202	712	725	1131	2390	472	792

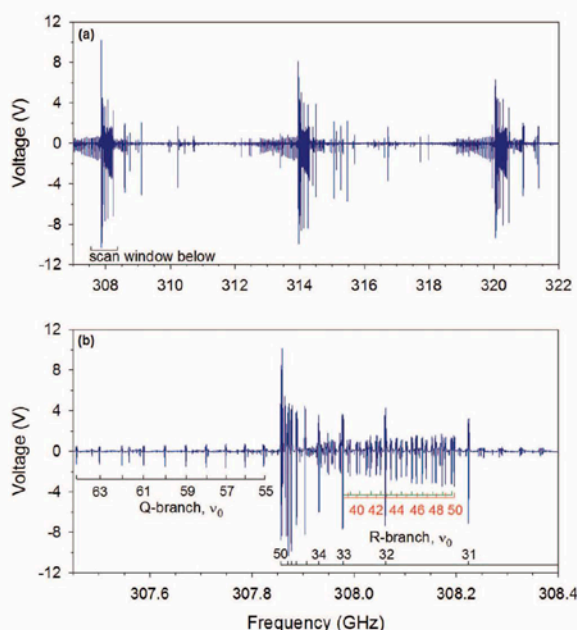


FIG. 2. Rotational spectra of pyridazine: (a) from 307 to 322 GHz taken in one experiment using an average of four scans of 64 000 points each, and (b) expansion of a single rotational bandhead ($J_{\text{upper}} = 50$). Full transition details can be found in the supplementary material.⁴⁷ The spectra were collected at a partial pressure of pyridazine of 4 mTorr and a temperature of approximately 289 K. The ground state pyridazine transitions are identified in black, R-branch excited state transitions are identified as ν_{16} red (lower) and ν_{13} green (upper). The J assignments are identical for the green and red series, but only labeled for the red case.

Unlike the transitions in the cm-wave region, the many observed Q-branch transitions in the newly measured frequency range appear as degenerate pairs, in which one transition is ${}^a\text{Q}_{0,-1}$ and the other is ${}^a\text{Q}_{2,-1}$. These transitions were measured from $J_{\text{upper}} = 44$ to 100 for pyridazine. For the ${}^{13}\text{C}$ and ${}^{15}\text{N}$ isotopologs, a similar range of a -type R-branch and Q-branch transitions was observed, though in somewhat smaller numbers due to the lower natural abundance of these species. The supplementary material⁴⁷ contains the ASFIT output files, which include all least-squares fit spectroscopic lines.

As is characteristic for near-oblate asymmetric tops of this type, many of the R-branch transitions collapse into easily identifiable bandlike patterns. These features (referred to as bands below) themselves are separated by roughly $2C$ (6097.4 MHz for ground state pyridazine) and are the three major spectral features observable in Fig. 2(a). An expanded display of the first band from 307 450 MHz to 308 400 MHz is shown in Fig. 2(b), beginning with degenerate $J = 50_{0,50} \leftarrow 49_{0,49}$ and $J = 50_{1,50} \leftarrow 49_{1,49}$ (${}^a\text{R}_{0,1}$) transitions at 307856.535 MHz. Each of the major lines progressing to higher frequency (labeled in black) is a degenerate pair of lines (${}^a\text{R}_{0,1}$) where J decreases by 1, K_{prolate} increases by 1, and K_{oblate} decreases by 2 for each successive ${}^a\text{R}_{0,1}$ line in the series. After ~ 20 transitions, the degeneracy breaks down and the two ${}^a\text{R}_{0,1}$ transitions become resolvable and then very widely separated. Progressing out of the bandhead to lower frequency are the corresponding Q-branch absorptions that

consist of degenerate pairs of ${}^a\text{Q}_{0,-1}$ and ${}^a\text{Q}_{2,-1}$ transitions, where the K_{oblate} is 50, matching J_{upper} for the first R-branch transition in the nearby series. The region around the ground state bandhead is further complicated by the presence of two additional obvious series of rotational transitions (labeled in green for ν_{13} and red for ν_{16}), which are R-branches associated with the two lowest-energy vibrationally excited states of the normal isotopolog (also starting with $J_{\text{upper}} = 50$). All of the other vibrationally excited states observed by us and discussed later are also present and visible in this spectral window, though they are less apparent due to their considerably smaller intensities.

The final data set for the ground state of the normal isotopolog of pyridazine contained over 2000 measured lines between 237–360 GHz and 83 of the cm-wave transitions reported by Werner *et al.*⁴ Two previously reported cm-wave transitions were excluded, due to errors greater than 100 kHz in their frequency measurements. The constants obtained from the least-squares fit of the measured transitions are presented in Table II, along with those from the previous works. These constants correspond to Watson's A-reduced Hamiltonian, Representation I', to allow for easy comparison to the previously published values. A limitation of our spectrometer in the configuration used in this work is its inability to operate below 235 GHz, which meant we could not observe any low- J transitions of pyridazine. The transitions we observe in our experiments are all heavily influenced by centrifugal distortion, so it was of critical importance to be sure we could obtain values of the rotational constants in good agreement with the published values from spectroscopy of low- J lines, hopefully without needing to include the latter in our analysis. We found that we were indeed able to obtain an excellent fit to the (partial) 6th-order Hamiltonian, with or without the previously published rotational transitions measured in the cm-wave region. The price of achieving this condition, however, is that many more (several hundred) rotational transitions are required than in the cm-wave region to obtain a satisfactory least-squares fit. Additionally, it is very important to measure different types of transitions, spanning a wide quantum number range, and, in particular, including as many non-degenerate ${}^a\text{R}_{0,1}$ transitions as possible in order to reduce the correlation between A and B in the fitting process. Only with extensive data sets were we able to predict unobserved lines within experimental error, so the large number of transitions reported here does not constitute the substantial over-determination that one might at first suspect. The excellent agreement between the constants for the normal isotopolog determined in previous works and those determined in this work is apparent in Table II. Our data refine the quartic (4th-order) distortion constants, but with the exception of Δ_{JK} which was the least well-determined 4th-order constant in the original work, the values were unchanged to 0.003 kHz. Comparison of the last two columns of the table clearly confirms that we obtain essentially identical spectroscopic constants, whether or not we include the cm-wave data in the fit. This behavior is critical for the analysis of the isotopologs for which ours is the only data available.

As a consequence of C_{2v} symmetry, pyridazine has five possible single-substitution isotopologs resulting from

TABLE II. Spectroscopic constants for pyridazine (Watson's A-reduced Hamiltonian, Representation F').

Spectroscopic constants	Werner <i>et al.</i> ⁴ (1967) ^a	Lopez <i>et al.</i> ⁵ (2002)	This work including Ref. 4	This work excluding Ref. 4
A (MHz)	6242.94	6242.95096 (38)	6242.95041 (14)	6242.95040 (15)
B (MHz)	5961.09	5961.09646 (40)	5961.09410 (13)	5961.09411 (14)
C (MHz)	3048.70	3048.71451 (25)	3048.71363 (20)	3048.71363 (20)
Δ_J (kHz)	0.7564	[0.7564] ^b	0.75676 (11)	0.75677 (12)
Δ_{JK} (kHz)	-0.1453	[-0.1453] ^b	-0.13558 (33)	-0.13562 (35)
Δ_K (kHz)	0.8329	[0.8329] ^b	0.82976 (32)	0.82977 (33)
δ_J (kHz)	0.3133	[0.3133] ^b	0.315715 (31)	0.315719 (35)
δ_K (kHz)	0.6868	[0.6868] ^b	0.68234 (10)	0.68234 (10)
Φ_J (Hz)			0.000233 (33)	0.000236 (34)
Φ_{JK} (Hz)			-0.00132 (27)	-0.00134 (28)
Φ_{KJ} (Hz)			0.00158 (32)	0.00160 (33)
Φ_K (Hz)			[0] ^a	[0] ^a
ϕ_J (Hz)			0.000190 (14)	0.000191 (14)
ϕ_{JK} (Hz)			-0.000252 (96)	-0.000258 (99)
ϕ_K (Hz)			0.002081 (16)	0.002081 (16)
Δ_1 ($\mu\text{Å}^2$)			0.0364	0.0364
κ			0.824	0.824
σ_{fit} (MHz)			0.034	0.036

^aEstimation of errors not provided.^b4th-order distortion constants for Ref. 5 were fixed at the previously measured values from Ref. 4.

mono-substitution by ^{13}C , ^{15}N , or ^2H . Three of these isotopologs were observed in natural abundance in our experiments, just as in the original cm-wave experiments: [$3\text{-}^{13}\text{C}$], [$4\text{-}^{13}\text{C}$], [$1\text{-}^{15}\text{N}$]. The signal intensity of each isotopolog is double the expected intensity due to natural isotopic abundance. The spectroscopic constants of the normal isotopic form and 12 substituted isotopologs we studied are presented in Table III. In these least-squares fits, we have used an S-reduced Hamiltonian, Representation III', which is the more appropriate method for analysis of a near-oblate asymmetric top.³ In contrast to the normal isotopolog, which was well predicted, the $^a\text{R}_{0,1}$ bandhead predictions for the [$4\text{-}^{13}\text{C}$] isotopolog from the previous work were in error by greater than 120 MHz due to the lower number of transitions observed in the cm-wave range. A comparison between spectroscopic constants from the original data set of Werner *et al.*⁴ and the newly measured transitions of this work in the S-reduced Hamiltonian, Representation III' can be found in Table S1 of the supplementary material⁴⁷ for each of the three heavy atom only isotopologs. The cm-wave transitions in the original study were insufficient in each of the three species, [$3\text{-}^{13}\text{C}$], [$4\text{-}^{13}\text{C}$], [$1\text{-}^{15}\text{N}$], to obtain a fit to a 4th-order Hamiltonian without fixing D_J . The newly measured lines allow us to determine all of the 4th-order distortion constants. The rotational constants (A , B , C) obtained in the original work agree with the present values to within 0.01 MHz for these three species. As with the normal isotopic form, many 6th-order constants must also be included in the fits to make them satisfactorily predictive of unmeasured lines.

The small changes in the rotational constants for each of the heavy-atom substitution isotopologs do not significantly alter the appearance of the R-branch series, and the same general pattern is observed as the main isotopolog. As expected, the inertial defect, Δ_1 (Eq. (1)) is fairly insensitive to isotopic substitution (Table III). On the other hand, the asymmetry

parameter, κ (Eq. (2)), varies over a fairly wide range from +0.612 to +0.919 for the observed isotopologs,

$$\Delta_i = I_c - I_b - I_a, \quad (1)$$

$$\kappa = \frac{2B - A - C}{A - C}. \quad (2)$$

The deuterated pyridazine species could not be observed without isotopic enrichment due to the low natural abundance of deuterium. Isotopic exchange reactions enabled the preparation of mixtures containing all nine of the possible deuterium-only substitution isotopologs: [$3\text{-}^2\text{H}$], [$4\text{-}^2\text{H}$], [$3,4\text{-}^2\text{H}$], [$3,5\text{-}^2\text{H}$], [$3,6\text{-}^2\text{H}$], [$4,5\text{-}^2\text{H}$], [$3,4,5\text{-}^2\text{H}$], [$3,4,6\text{-}^2\text{H}$], [$3,4,5,6\text{-}^2\text{H}$]. The number of spectral lines included in each fit is roughly related to the intensity of those transitions based upon the abundance (Table I) of the isotopolog in our prepared samples. Because the kinetics of the exchange reaction favor substitution at the 4-position (*meta*), the [$4\text{-}^2\text{H}$]- $\text{C}_4\text{H}_4\text{N}_2$ species is the most abundant (at low conversion as seen in the 1-h reaction sample) and the species with substitution at the 3-position, such as [$3,6\text{-}^2\text{H}$]- $\text{C}_4\text{H}_4\text{N}_2$ and [$3,4,6\text{-}^2\text{H}$]- $\text{C}_4\text{H}_4\text{N}_2$ are among the least abundant. In the deuterium enriched sample from the 3 h reaction, one mono- ^{13}C isotopolog, [$4\text{-}^{13}\text{C}$], [$3\text{-}^{13}\text{C}$]- $\text{C}_4\text{H}_4\text{N}_2$, was identified in natural abundance. The spectra of the deuterated samples also exhibited several additional unidentified isotopically substituted species, as well as vibrational satellite bands for the higher abundance species. In pyridazine, the orientation of the principal axes is dramatically sensitive to deuterium substitution, with rotations as large as 90° being observed. The isotopologs that have been studied thus involve species with *a*-type transitions, species with *b*-type transitions, and species with both *a*- and *b*-type transitions (of comparable intensity), as shown in Table I.

The second column of Table III gives the values of the rotational and centrifugal distortion constants we obtained from

TABLE III. Spectroscopic constants for pyridazine isotopologs (Watson's S-reduced Hamiltonian, Representation IIF).

Spectroscopic constants	C ₄ H ₄ N ₂	C ₄ H ₄ N ₂ predicted CCSD(T)/ANO0	[3- ¹³ C]	[4- ¹³ C]	[1- ¹⁵ N]
A (MHz)	6242.95134 (14)	6251.28	6112.22807 (85)	6217.71925 (61)	6218.91097 (66)
B (MHz)	5961.09283 (13)	5944.65	5961.31709 (85)	5848.36612 (60)	5857.40185 (51)
C (MHz)	3048.71390 (20)	3047.06	3017.24769 (37)	3013.02887 (23)	3015.70923 (32)
D _J (kHz)	1.473762 (92)	1.44551	1.44682 (21)	1.44448 (20)	1.44338 (29)
D _{JK} (kHz)	-2.449190 (38)	-2.39245	-2.40665 (21)	-2.39857 (27)	-2.39674 (46)
D _K (kHz)	1.100768 (55)	1.06981	1.08257 (15)	1.07706 (14)	1.07670 (25)
d ₁ (kHz)	-0.015682 (51)	-0.02119	-0.0062 (10)	-0.02311 (78)	-0.02001 (73)
d ₂ (kHz)	0.027114 (11)	0.02737	0.02196 (95)	0.01968 (53)	0.01949 (24)
H _J (Hz)	0.000525 (18)	-0.000251	0.00080 (11)	0.00040 (16)	-0.00042 (16)
H _{JK} (Hz)	-0.002696 (10)	0.00183	-0.00302 (22)	-0.00220 (33)	-0.00046 (34)
H _{KJ} (Hz)	0.003384 (16)	-0.00389	0.00344 (20)	0.00294 (27)	0.00147 (30)
H _K (Hz)	-0.001360 (12)	0.00232	-0.001295 (84)	-0.00121 (11)	-0.00061 (13)
h ₁ (Hz)	0.000030 (12)	-0.000103	0.00249 (94)	-0.00136 (71)	-0.00362 (58)
h ₂ (Hz)	[0] ^a	0.0000273	0.0027 (13)	-0.00121 (83)	[0] ^a
h ₃ (Hz)	-0.0000687 (82)	0.0000379	[0] ^a	-0.00040 (20)	[0] ^a
N lines	2175		806	949	477
Δ ₁ (μÅ ²)	0.0364		0.0370	0.0371	0.0369
κ	0.824		0.902	0.769	0.774
σ _{fit} (MHz)	0.037		0.044	0.040	0.041
Total A _{correction} (MHz)	52.813		51.486	52.212	52.159
Total B _{correction} (MHz)	43.626		43.360	42.692	42.788
Total C _{correction} (MHz)	24.670		24.310	24.246	24.261
Spectroscopic constants	[3- ² H]	[4- ² H]	[3,4- ² H]	[3,5- ² H]	[3,6- ² H]
A (MHz)	5962.40668 (41)	6192.44445 (15)	5854.14225 (16)	5889.76581 (36)	5959.19500 (34)
B (MHz)	5828.17973 (46)	5598.11888 (13)	5539.31505 (15)	5498.78296 (32)	5460.41809 (33)
C (MHz)	2946.68605 (33)	2939.56879 (11)	2845.68651 (15)	2843.27858 (12)	2848.96352 (12)
D _J (kHz)	1.33918 (22)	1.337213 (60)	1.215015 (85)	1.214997 (87)	1.22113 (10)
D _{JK} (kHz)	-2.21950 (40)	-2.206299 (79)	-2.00784 (13)	-2.00532 (12)	-2.01010 (25)
D _K (kHz)	0.99613 (22)	0.984774 (51)	0.898553 (76)	0.896253 (58)	0.89466 (14)
d ₁ (kHz)	-0.03792 (15)	-0.06243 (10)	-0.035556 (54)	-0.04783 (32)	-0.08169 (10)
d ₂ (kHz)	0.010701 (58)	-0.005308 (52)	-0.021522 (16)	-0.020212 (94)	0.000466 (29)
H _J (Hz)	0.000595 (48)	0.000714 (24)	0.000363 (15)	0.000727 (47)	[0] ^a
H _{JK} (Hz)	-0.00189 (10)	-0.002505 (49)	-0.001611 (31)	-0.002321 (94)	[0] ^a
H _{KJ} (Hz)	0.00233 (11)	0.003006 (46)	0.002206 (35)	0.002750 (74)	[0] ^a
H _K (Hz)	-0.000943 (52)	-0.001172 (20)	-0.000963 (17)	-0.001115 (29)	[0] ^a
h ₁ (Hz)	[0] ^a	0.000372 (56)	[0] ^a	0.00075 (17)	[0] ^a
h ₂ (Hz)	[0] ^a	0.000309 (47)	[0] ^a	0.000249 (84)	[0] ^a
h ₃ (Hz)	[0] ^a	0.0000196 (52)	[0] ^a	0.000042 (12)	[0] ^a
N lines	568	1612	1587	2193	712
Δ ₁ (μÅ ²)	0.0337	0.0341	0.0314	0.0314	0.0307
κ	0.910	0.635	0.791	0.743	0.679
σ _{fit} (Mhz)	0.035	0.026	0.022	0.029	0.033
Total A _{correction} (MHz)	43.834	51.784	46.690	46.773	43.743
Total B _{correction} (MHz)	47.845	40.299	40.853	40.725	43.824
Total C _{correction} (MHz)	23.500	23.343	22.293	22.268	22.392
Spectroscopic constants	[4,5- ² H]	[3,4,5- ² H]	[3,4,6- ² H]	[3,4,5,6- ² H]	[4- ² H, 3- ¹³ C]
A (MHz)	6002.7188 (12)	5622.36606 (24)	5732.55746 (16)	5385.76388 (45)	6079.770 (15)
B (MHz)	5388.7995 (11)	5385.21892 (23)	5299.11962 (15)	5275.67750 (46)	5587.211 (15)
C (MHz)	2839.10005 (55)	2750.18252 (30)	2753.23394 (14)	2664.70726 (65)	2910.9599 (10)
D _J (kHz)	1.2155 (10)	1.10397 (14)	1.109819 (63)	1.01033 (47)	1.3471 (31)
D _{JK} (kHz)	-2.0017 (23)	-1.82352 (10)	-1.826765 (77)	-1.6668 (15)	-2.2219 (61)
D _K (kHz)	0.8922 (12)	0.816310 (70)	0.813679 (52)	0.7457 (12)	0.9862 (28)
d ₁ (kHz)	-0.05310 (13)	-0.008860 (84)	-0.063096 (56)	-0.029026 (53)	-0.1958 (92)
d ₂ (kHz)	0.029260 (31)	0.019550 (11)	0.003944 (20)	0.010842 (16)	-0.2005 (35)
H _J (Hz)	0.00102 (32)	0.000354 (29)	0.000328 (11)	0.00062 (16)	0.00230 (71)
H _{JK} (Hz)	-0.0035 (10)	-0.001577 (16)	-0.001534 (14)	-0.00234 (72)	-0.0082 (20)
H _{KJ} (Hz)	0.0041 (10)	0.001934 (21)	0.001926 (16)	0.0028 (10)	0.0080 (19)
H _K (Hz)	-0.00159 (33)	-0.000773 (13)	-0.0007728 (94)	-0.00108 (49)	-0.00231 (60)

TABLE III. (Continued.)

Spectroscopic constants	[4,5- ² H]	[3,4,5- ² H]	[3,4,6- ² H]	[3,4,5,6- ² H]	[4- ² H, 3- ¹³ C]
h_1 (Hz)	[0] ^a	[0] ^a	[0] ^a	[0] ^a	[0] ^a
h_2 (Hz)	[0] ^a	[0] ^a	[0] ^a	[0] ^a	[0] ^a
h_3 (Hz)	[0] ^a	[0] ^a	[0] ^a	[0] ^a	[0] ^a
N lines	725	1131	2390	472	792
Δ_1 ($\mu\text{\AA}^2$)	0.0319	0.0292	0.0285	0.0262	0.0350
κ	0.612	0.835	0.709	0.919	0.689
σ_{fit} (MHz)	0.028	0.032	0.033	0.021	0.038
Total $A_{\text{correction}}$ (MHz)	49.758	45.401	42.684	38.036	50.465
Total $B_{\text{correction}}$ (MHz)	38.033	38.088	40.877	41.698	40.127
Total $C_{\text{correction}}$ (MHz)	21.186	21.186	21.270	20.260	23.019

^aThese 6th-order distortion constants were fixed at zero. When these parameters were included in the fit, they were not well determined, and their value was within the estimated uncertainty of zero. The total correction terms for each rotational constant are the result of adding one half of the sum of the corresponding vibration-rotation interaction constants (α) to an electronic mass correction of 0.309, 0.395, and 0.062 to A , B , and C , respectively. The correction terms are added to A , B , C to obtain A_e , B_e , and C_e .

a CCSD(T) calculation with an ANO0 basis set for the normal isotopolog. The set of predicted 4th-order constants is in excellent agreement with the experimental values in column 1. Furthermore, the 4th-order constants of the various isotopologs exhibit systematic variations as a function of the molecular weight of the isotopolog. On the other hand, the 6th-order constants display poor agreement between theory and experiment, and the systematic correlation with molecular weight of the isotopolog is not observed. The number of these 6th-order constants that could be included and well-determined in the fits also varies from one isotopolog to the next, depending on the data available. Thus, these higher order constants must be regarded as empirical with the present data. They are necessary to obtain predictive fits with standard errors near experimental accuracy (see Table III), but their values are probably not physically meaningful for comparison with the theoretical predictions.

STRUCTURE DETERMINATION

Initially, our goal was to improve upon and complete the published R_s structure.⁴ Kraitchman's equation (Eq. (3)) for single isotopic substitution⁶ yields the absolute value of the rectangular coordinates of the substituted atom (designated a_s) in the principal axis coordinate system of the unsubstituted (parent) species

$$|a_s| = \sqrt{\frac{I_{a_s} - I_a}{\mu} \left(1 + \frac{I_{b_s} - I_b}{I_b - I_a}\right)}, \quad \mu = \frac{M \times (M_s - M)}{M + (M_s - M)}. \quad (3)$$

This approach had already been utilized to determine both coordinates of the N atoms and C4 and C5, as well as the b coordinate of C3 and C6.⁴ Our improved rotational constants for the ground state and single substituted ¹⁵N and ¹³C forms did not appreciably modify the published values of the well-determined a and b coordinates. As mentioned above, this method does not allow for the determination of the a coordinate of the *ortho* carbon atoms, due to their very close proximity to the b principal axis. In the case of C3 and C6, the Kraitchman equation breaks down and the computed a coordinate is imaginary (the square-root of $-1.74 \times 10^{-3} \text{\AA}$). Our

moments of inertia for the singly deuterated species permit us to add the a and b coordinates of all the H atoms. Because H7 and H10 are also somewhat near the b principal axis, the a coordinates of those atoms are less accurate than the others, but they are at least meaningfully determined. The uncertainties in the distances, δa_s (Eq. (4)), were estimated from the absolute change in the inertial defect upon substitution and the reduced mass μ and the isotopic substitution distance calculated from Kraitchman's equation, a_s ,⁴⁰

$$\delta a_s = \frac{|\Delta_I - \Delta_0|}{4\mu|a_s|}. \quad (4)$$

To find the a -coordinate of C3 and improve upon the accuracy of our value for that of H7, we took advantage of the fact that the orientation of the principal axes change dramatically upon deuterium substitution and the availability of the moments for several doubly substituted species. Specifically, we used [4-²H] pyridazine as a second parent species in the Kraitchman analysis and found the coordinates of C3 and all H's from the corresponding double substitution (and ground state) moments. In this coordinate system, all atoms are far from principal axes, and all coordinates are well determined. The distances H8-C3 and H9-C3 obtained from this approach can be used in the original coordinate system to determine the a coordinate of C3. In this manner, we were able to find satisfactorily accurate values of all of the (R_s) rectangular coordinates of pyridazine. These are given in Table VI along with their estimated uncertainties. The latter are those derived from applying Eq. (4) to the current data and do not address the inherent limitations of the R_s method. In Table V, these are converted to bond angles and distances and compared to the results of the other methods we used (see below).

With the large number of isotopic forms of pyridazine we studied, it became possible to obtain R_0 and R_e structures from 28 independent moments of inertia (I_a and I_b) that considerably exceeded in number the nine structural parameters. An R_0 and two R_e structures were determined using xrefit (a module of CFOR²⁵), which is a least-square fitting approach that optimizes the molecular structural parameters to fit all available moments of inertia. The R_0 structure uses moments derived directly from unadjusted ground

TABLE IV. Experimental and computationally-corrected inertial defects for pyridazine isotopologs.

Isotopolog	Experimental Δ_i ($\mu\text{\AA}^2$)	Vibration-rotation corrected Δ_i ($\mu\text{\AA}^2$)	Vibration-rotation and electronic corrected Δ_i ($\mu\text{\AA}^2$)
$\text{C}_4\text{H}_4\text{N}_2$	0.0364	-0.0120	0.0008
[3- ^{13}C]- $\text{C}_4\text{H}_4\text{N}_2$	0.0370	-0.0119	0.0011
[4- ^{13}C]- $\text{C}_4\text{H}_4\text{N}_2$	0.0371	-0.0120	0.0012
[1- ^{15}N]- $\text{C}_4\text{H}_4\text{N}_2$	0.0369	-0.0121	0.0011
[3- ^2H]- $\text{C}_4\text{H}_4\text{N}_2$	0.0337	-0.0123	0.0013
[4- ^2H]- $\text{C}_4\text{H}_4\text{N}_2$	0.0341	-0.0123	0.0016
[3,4- ^2H]- $\text{C}_4\text{H}_4\text{N}_2$	0.0314	-0.0128	0.0019
[3,5- ^2H]- $\text{C}_4\text{H}_4\text{N}_2$	0.0314	-0.0129	0.0019
[3,6- ^2H]- $\text{C}_4\text{H}_4\text{N}_2$	0.0307	-0.0125	0.0023
[4,5- ^2H]- $\text{C}_4\text{H}_4\text{N}_2$	0.0318	-0.0121	0.0028
[3,4,5- ^2H]- $\text{C}_4\text{H}_4\text{N}_2$	0.0292	-0.0122	0.0035
[3,4,6- ^2H]- $\text{C}_4\text{H}_4\text{N}_2$	0.0288	-0.0128	0.0029
[3,4,5,6- ^2H]- $\text{C}_4\text{H}_4\text{N}_2$	0.0262	-0.0123	0.0044
[4- ^2H , 3- ^{13}C]- $\text{C}_4\text{H}_4\text{N}_2$	0.0350	-0.0119	0.0022

state rotational constants. The R_0 structure thus ignores the effects of vibrational motion and is inherently less accurate than the hypothetical equilibrium structure (R_e) which corresponds to the minimum energy structure on the potential energy surface. Determining an R_e structure solely on the basis of experimental data is not feasible, since it would require measurements of high-resolution rotational spectra of the vibrational satellites for each of the 24 normal modes of pyridazine. A mixed experimental/theoretical R_e structure, however, has been determined by correcting each of the experimental ground state rotational constants (A_0) with one half of the sum of the corresponding vibration-rotation interaction parameters (α_i) obtained from a VPT2 calculation at the CCSD(T)/ANO0 level of theory (Table III). The efficacy of this method for obtaining reliable α_i values is discussed in the following section that treats the excited vibrational levels. For a planar molecule, the computationally-corrected experimental rotational constants should have the effect of decreasing the inertial defect for all 14 isotopologs to an ideal value of zero. In the case of pyridazine, inclusion of the correction for vibration-rotation effects afforded inertial defects that still differed appreciably from zero (Table IV). This result prompted us to include an additional correction for electron mass to the moments of inertia. As previously noted in the case of SiC_3 ,⁴¹ inclusion of this electronic contribution led to a significant decrease in the magnitude of the inertial defect (Table IV). Following Flygare,⁴² the rotational g -tensor was evaluated at the CCSD(T) level of theory,⁴³ and the rotational constants then modified with the electronic contribution according to Eq. (5) (similar equations hold for the A and C constants),

$$\Delta B = \eta g^{bb} B, \quad (5)$$

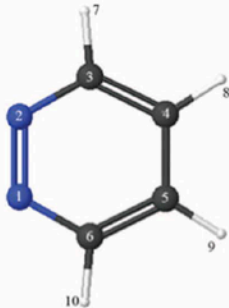
where η is the electron-proton mass ratio, g^{bb} is the (diagonal) element of the rotational g -tensor along the b inertial axis, and ΔB is the contribution to the rotational constant that clearly depends on the sign of g^{bb} .

A second R_e structure was therefore determined after correcting for both the vibration-rotation interaction and the electronic contribution (also calculated at CCSD(T)/ANO0 level) to the rotational constants (Table III). A comparison of

the corrected and uncorrected inertial defects is presented in Table IV. The inertial defects are reduced by a factor of roughly three by using the vibration-rotation corrections and by a further factor of three to ten when the electronic corrections are included.

A comparison of the structural parameters determined in the current analysis, those obtained in the previous works, and those obtained from our coupled-cluster calculations is presented in Tables V and VI. The R_e structure that includes vibration-rotation interaction and electronic correction is the most accurate of these, although the R_e structure without the electronic corrections is practically identical. A summary of the least-squares fitting output is provided in the supplementary material.⁴⁷ For the structure corrected for electron mass effects, the uncertainties from the least-squares fitting procedure for the distance parameters are all ≤ 0.0016 Å and all angle parameters are $\leq 0.06^\circ$ (Table V). The maximum value of the residual between the moment of inertia data and the moments calculated from the fitted R_e structure corresponds to about 0.2 MHz in the rotational constants. This is believed to be among the better determined structures for any molecule in this size range at this time. It can be seen in Table V that even though the structural parameters are nearly identical for the equilibrium structure without electron mass corrections, the statistical uncertainties from the least squares fit are consistently about three times larger than those in the corrected calculation (and those for the R_0 parameters are approximately another factor of three larger). The availability of the R_e structure provides an opportunity to calibrate the accuracy of the R_0 and R_s structures. The latter two methods have been applied to many large molecules in the past, and it can be seen in Table V that the agreement is fairly satisfactory for both of them, e.g., a few thousandths of an Angstrom in the bond distances. Furthermore, the agreement of our large basis set coupled-cluster bond distances and angles with the R_e structure is excellent. Because the discrepancies between R_s or R_0 structures and the R_e experimental results is quite comparable in magnitude to the discrepancies between the experimental and best theoretical R_e 's, the R_e structure provides a substantially better benchmark for the accuracy of current

TABLE V. Experimental and computational geometrical parameters for pyridazine.



Structural parameters	R_0^a	R_S	R_e α corrected ^a	R_e α and electron corrected ^a	CCSD(T)/ cc-pVTZ	CCSD(T)/ ANO0	CCSD(T)/ ANO1	CCSD(T)/ ANO2
R_{C4-C5}	1.3816 (131)	1.3756 (50)	1.3764 (48)	1.3761 (16)	1.383	1.391	1.382	1.380
R_{C4-H8}	1.0792 (29)	1.0829 (50)	1.0803 (11)	1.0802 (4)	1.082	1.089	1.082	1.082
R_{C3-C4}	1.4011 (94)	1.4012 (50)	1.3934 (35)	1.3938 (12)	1.400	1.408	1.399	1.397
R_{C3-H7}	1.0816 (21)	1.0832 (50)	1.0811 (8)	1.0810 (3)	1.083	1.090	1.083	1.083
R_{N2-C3}	1.3328 (97)	1.3336 (50)	1.3306 (36)	1.3302 (12)	1.337	1.3437	1.337	1.334
$A_{H8-C4-C5}$	122.34 (35)	122.66 (50)	122.36 (13)	122.37 (4)	122.4	122.7	122.4	122.4
$A_{C3-C4-C5}$	116.82 (24)	116.88 (50)	116.85 (9)	116.85 (3)	116.7	116.6	116.8	116.8
$A_{H7-C3-C4}$	121.28 (43)	120.87 (50)	121.36 (16)	121.35 (6)	121.2	120.9	121.3	121.3
$A_{N2-C3-C4}$	123.92 (31)	123.65 (50)	123.86 (11)	123.86 (4)	124.1	124.4	124.1	123.9

^aErrors given are the statistical uncertainties given by the least-squares fitting in xrefit. The actual uncertainties may be somewhat larger due to any remaining unaccounted for systematic errors.

theoretical calculations than do the R_S or R_0 structures, although all of the experimental structures are pleasingly consistent in this case.

ANALYSIS OF ROTATIONAL SPECTRA OF PYRIDAZINE IN EXCITED VIBRATIONAL LEVELS

Infrared and Raman spectral data for vibrationally excited pyridazine have been previously reported as gas-phase, liquid-phase, and solid-state spectra,⁴⁴⁻⁴⁶ but no rotational spectra are available. The two lowest-energy vibrationally excited species, whose spectra are easily discernible in Fig. 2(b), have anharmonic vibrational frequencies predicted to be 366.1 (ν_{13}) and 368.5 cm^{-1} (ν_{16}) by CCSD(T)/ANO1 cal-

culations. Both of these modes involve out-of-plane distortions of the aromatic ring and their observed transitions are summarized in Table VII along with the observed transitions for the next three higher energy vibrationally excited states of pyridazine. A complete list of the computed harmonic and anharmonic vibrational frequencies for pyridazine at several levels of theory, along with the calculated vibration-rotation interaction constants (α_i), can be found in Table S3 of the supplementary material.⁴⁷ As summarized in Table VIII, the two lowest energy excited states have values of C that are within 3.5 MHz of the ground state and 0.06 MHz of one another. Distinguishing between these two states' adjacent spectra on the basis of their very nearly equal relative intensities would be unreliable, but an unambiguous assignment is possible based upon their vibration-rotation interaction constants (see below). In addition to these two satellites, seven less populated vibrational states (with predicted energies up to 762 cm^{-1} at the CCSD(T)/ANO1 level) have been detected. The rotational constants of the next three fundamental states ν_{24} , ν_9 , and ν_{15} are also presented in

TABLE VI. Atom locations in principal axis coordinates.^a

Atom	R_S Ref. 4		R_S current work	
	a (\AA)	b (\AA)	a (\AA)	b (\AA)
N1	-1.1830	0.6650	-1.18298 (10)	-0.66511 (17)
N2	-1.1830	-0.6650	-1.18298 (10)	0.66511 (17)
C3	...	-1.3212	-0.022 (10)	1.32126 (12)
C4	1.2277	-0.6877	1.22782 (13)	0.6878 (2)
C5	1.2277	0.6877	1.22782 (13)	-0.6878 (2)
C6	...	1.3212	-0.022 (10)	-1.32126 (12)
H7	-0.097 (7)	2.4018 (3)
H8	2.1394 (3)	1.2722 (5)
H9	2.1394 (3)	-1.2722 (5)
H10	-0.097 (7)	-2.4018 (3)

^aThe molecule is planar so all coordinates along the c axis are zero. All distance values are reported in \AA . Values from Ref. 4 $R_{N(1)-N(2)} = 1.330 \text{\AA}$ and $R_{C(4)-C(5)} = 1.375 \text{\AA}$.

TABLE VII. Rotational transitions measured for vibrationally excited states of pyridazine.

Type	$C_4H_4N_2$	$C_4H_4N_2$	$C_4H_4N_2$	$C_4H_4N_2$	$C_4H_4N_2$
	ν_{13}	ν_{16}	ν_{24}	ν_9	ν_{15}
^a Q _{0,-1}	74	101	155	177	0
^a Q _{2,-1}	74	101	155	177	0
^a R _{0,1}	479	542	656	608	231
^a R _{2,-1}	0	2	13	61	29
Total	627	746	979	1023	260

TABLE VIII. Spectroscopic constants for vibrationally excited states of pyridazine (Watson's S-reduced Hamiltonian, Representation III^a).

Spectroscopic constants	C ₄ H ₄ N ₂ , ν_{13} ^a	C ₄ H ₄ N ₂ , ν_{16} ^a	C ₄ H ₄ N ₂ , ν_{24}	C ₄ H ₄ N ₂ , ν_9	C ₄ H ₄ N ₂ , ν_{15}
<i>A</i> (MHz)	6240.8668 (90)	6236.1283 (69)	6245.82924 (64)	6233.60637 (30)	6244.7534 (21)
<i>B</i> (MHz)	5956.2707 (80)	5961.5880 (63)	5956.67246 (56)	5963.89990 (27)	5962.2407 (15)
<i>C</i> (MHz)	3052.12909 (26)	3052.18018 (24)	3036.72028 (19)	3057.15234 (22)	3049.2651 (11)
<i>D_J</i> (kHz)	1.49329 (69)	1.46635 (73)	1.48266 (17)	1.45724 (12)	1.5048 (18)
<i>D_{JK}</i> (kHz)	-2.4697 (11)	-2.4318 (11)	-2.49473 (26)	-2.38563 (17)	-2.5012 (32)
<i>D_K</i> (kHz)	1.10318 (43)	1.09249 (38)	1.06194 (13)	1.13047 (12)	1.1237 (19)
<i>d₁</i> (kHz)	-0.1511 (60)	0.0479 (56)	-0.01674 (67)	-0.00786 (17)	-0.0309 (19)
<i>d₂</i> (kHz)	-0.090 (34)	0.0857 (40)	0.031014 (38)	0.022162 (28)	0.02400 (12)
<i>H_J</i> (Hz)	[0] ^b	0.000983 (65)	0.000534 (83)	0.000410 (19)	0.01304 (91)
<i>H_{JK}</i> (Hz)	[0] ^b	-0.00358 (22)	-0.00431 (16)	-0.000538 (26)	-0.0372 (25)
<i>H_{KJ}</i> (Hz)	-0.000464 (81)	0.00423 (31)	0.00655 (13)	-0.000245 (46)	0.0359 (29)
<i>H_K</i> (Hz)	0.000404 (73)	-0.00166 (15)	-0.003751 (54)	0.001297 (31)	-0.0115 (11)
<i>h₁</i> (Hz)	[0] ^b	[0] ^b	-0.00125 (41)	[0] ^b	0.0097 (13)
<i>h₂</i> (Hz)	[0] ^b	[0] ^b	[0] ^b	[0] ^b	[0] ^b
<i>h₃</i> (Hz)	[0] ^b	[0] ^b	0.000046 (33)	[0] ^b	0.000368 (83)
N lines	627	746	979	1023	260
Δ_1 ($\mu\text{\AA}^2$)	-0.245	-0.233	0.665	-0.503	0.046
κ	0.821	0.827	0.820	0.830	0.823
σ_{fit} (MHz)	0.0363	0.0352	0.0354	0.0403	0.0437

^aThese fits exclude many transitions that show Coriolis coupling between these closely lying vibrational states, ν_{13} and ν_{16} .

^bThese 6th-order distortion constants were fixed at zero.

Table VIII. The assignment and fitting of all of these five-lowest energy states are summarized in Tables VII and VIII. The assignment and fitting of the spectra of the other vibrational satellites detected is less complete (see below).

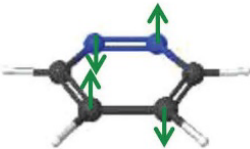

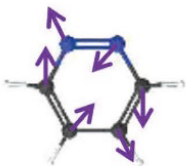
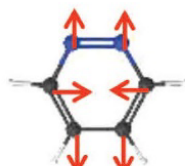


The theoretical and experimental values of the vibration-rotation interactions (α_i) of all states observed are presented in Table IX. We found B3LYP or MP2 calculations were entirely inadequate to predict the impact of vibrational excitation on the rotational constants of pyridazine, so we turned to coupled-cluster calculations. As expected, a higher level approach using CCSD(T)/cc-pVTZ, CCSD(T)/ANO0, or CCSD(T)/ANO1 calculations in conjunction with anharmonic force fields was considerably more helpful in enabling spectroscopic assignments. With these methods there is excellent agreement between the predicted and measured α values for each of the states we observed. The values predicted using the coupled-cluster method with any of the basis sets we tried were sufficient for prediction and assignment. The closest agreement between the experimental and theoretical values was at the CCSD(T)/ANO1 level, with typical discrepancies on the order of 200 kHz (Table IX). Once the spectroscopic constants for the ground state of pyridazine were known, this allowed us to easily find and assign the excited vibrational states by use of the theoretical α values and the ground state rotational and centrifugal distortion constants. Without such accurate predictions, the identification of lower intensity rotational bands associated with ν_9 , ν_{15} , and ν_{12} would have been more challenging. Because the pattern of the α values seen in the fundamental states was so different from one to the next, and because the predictions were so reliable, it was possible to assign the proper vibrational state to the observed rotational spectrum with a high degree of confidence (Table IX).

Unlike the previously investigated cases involving pyrimidine and pyridine,^{2,3} the lowest-energy vibrationally excited

states ν_{13} and ν_{16} of pyridazine are sufficiently close in energy that they are perturbed through a significant Coriolis-coupling interaction. The vibrational symmetries of the two states are A_2 and B_1 , which allows for a second order coupling. Fortunately, only rotational levels with quite low values of K_{oblate} (those furthest away from the obvious bandhead regions) are significantly perturbed. The rotational transitions and constants presented in Tables VII and VIII do not include any of these seriously perturbed transitions and the model used does not treat the Coriolis coupling. The obs-calc errors for the strongly perturbed transitions are tens or hundreds of MHz. Despite the lack of Coriolis-coupling treatment, the majority of the spectral lines of the ν_{13} and ν_{16} vibrational states of pyridazine are very well predicted and assigned unambiguously. The fits reported in Table VIII yield very satisfactory values of the unperturbed spectroscopic constants. Efforts to complete a satisfactory treatment of these two states including a full treatment of the Coriolis coupling are in progress.

Satellite ν_{24} represents an in-plane ring deformation motion. Unlike ν_{13} and ν_{16} , ν_{24} progresses to higher frequency from the bandheads in a manner similar to that of the ground state, with a large positive inertial defect of 0.665. Although all of the vibration-rotation interaction constants computed using CCSD(T)/ANO1 display good agreement with experimental values, the value of α_C has one of the largest discrepancies observed for any of the six fundamental states observed (almost 600 kHz), which still represents only a 5% error in the experimental value of -11.99 MHz. Satellite ν_9 is an in-plane ring deformation mode that has the greatest observed negative inertial defect ($\Delta_1 = -0.502$) among the single-quantum vibrational states, which results in the transitions progressing toward lower frequency from the bandhead in a manner similar to ν_{13} and ν_{16} . Fortunately, the bandhead origin is further separated from the ground state than ν_{13} and

TABLE IX. Experimental and theoretical vibration-rotation interactions and inertial defects for vibrationally excited states of pyridazine.^a

	α_A	α_B	α_C	Δ_i		α_A	α_B	α_C	Δ_i	
ν_{13} (364, A_2)						ν_{16} (369, B_1)				
Experimental	-2.0851	-4.8227	3.4144	-0.245		-6.8236	0.4946	3.4654	-0.233	
B3LYP/cc-pVTZ	3.92	3.20	1.63	0.044		4.61	1.16	1.32	0.041	
MP2/cc-pVTZ	4.31	3.62	1.84	0.044		4.68	1.95	1.55	0.041	
CCSD(T)/cc-pVTZ	-2.25	-4.53	3.38	-0.241		-6.92	0.54	3.37	-0.229	
CCSD(T)/ANO0	-2.39	-4.49	3.29	-0.237		-6.80	0.52	3.30	-0.224	
CCSD(T)/ANO1	-2.20	-4.63	3.36	-0.241		-6.94	0.60	3.39	-0.229	
ν_{24} (619, B_2)						ν_9 (668, A_1)				
Experimental	2.8774	-4.4209	-11.9945	0.665		-9.3455	2.8065	8.4376	-0.503	
B3LYP/cc-pVTZ	9.22	6.85	5.32	-0.036		7.57	-0.88	1.00	0.068	
MP2/cc-pVTZ	10.22	7.63	5.62	-0.028		6.72	1.33	2.12	0.027	
CCSD(T)/cc-pVTZ	3.12	-4.12	-10.99	0.618		-10.00	3.05	7.49	-0.456	
CCSD(T)/ANO0	2.84	-4.19	-11.15	0.622		-10.10	2.90	7.62	-0.467	
CCSD(T)/ANO1	3.03	-4.03	-11.40	0.641		-9.31	3.03	7.88	-0.469	
ν_{15} (746, B_1)						ν_{12} (755, A_2)				
Experimental	1.8015	1.1473	0.5504	0.046		-4.76 ^b	-4.07	0.91	-0.133	
B3LYP/cc-pVTZ	10.74	12.11	-1.0187	0.403		-10.42	1.52	2.60	-0.219	
MP2/cc-pVTZ	13.94	14.40	4.82	0.160		-10.82	-2.08	1.15	-0.196	
CCSD(T)/cc-pVTZ	2.58	1.49	0.60	0.058		-4.76	-4.00	0.87	-0.130	
CCSD(T)/ANO0	2.32	1.45	0.56	0.057		-4.69	-3.80	0.83	-0.123	
CCSD(T)/ANO1	1.89	1.10	0.57	0.046		-4.76	-4.02	0.87	-0.130	

^a α ($A_v - A_0$) values in MHz, Δ_i in $\mu\text{-\AA}^2$. Anharmonic vibrational frequencies in parenthesis in cm^{-1} are at the CCSD(T)/cc-pVTZ level. The vibration-rotation interaction constants (α_i) for all states, computed at various levels of theory, can be found in Table S3 of the supplementary material.⁴⁷

^b α_A was fixed in the partial least-squares fit of the ν_{12} spectrum.

ν_{16} , allowing many lines to be readily detectable. Satellite ν_{15} is the vibrational state that corresponds to the ring deformation caused by out-of-plane motion of the hydrogen atoms and has the smallest structural deviation from the ground vibrational state. The predicted changes in the rotational constants from the ground state to ν_{15} are quite small (1.9, 1.1, and 0.55 MHz at CCSD(T)/ANO1 for α_A , α_B , and α_C , respectively) resulting in a change in the inertial defect, Δ_i , of less than $0.01 \mu\text{-\AA}^2$. Unfortunately, the small values of the vibration-rotation interaction constants result in R-branch series origins

that are located between intense R-branch transitions in each ground state band. Nevertheless, a sufficient number of transitions can be measured and assigned at frequencies higher than the congested region of the ground state bands to enable a satisfactory determination of the rotational and distortion constants (Table VIII).

Satellite ν_{12} is the vibrational state of lowest intensity that we observed; this state has not yet been sufficiently well fit to enable an unambiguous prediction for unobserved transitions or unambiguous determination of the centrifugal distortion

constants. This is due more to the frequency at which transitions occur than to their low intensity. Most of the transitions appear in a region of the ground state bandhead that severely overlaps with states ν_{13} , ν_{16} , ν_{24} , ν_{15} , and the ground state R- and Q-branch transitions. There is excellent agreement between our tentative experimental and theoretical values of α_C and inertial defect, which allows us to identify, if not adequately fit, the species. (Although α_A was fixed in the fitting of ν_{12} , cancellation of error in α_A and α_B permits reliable evaluation of α_C and the inertial defect.) With intensities just greater than ν_6 , the overtones ($2\nu_{13}$ and $2\nu_{16}$) and combination ($\nu_{13} + \nu_{16}$) are easily seen in the spectrum in the same regions as ν_9 . Unfortunately, these transitions are highly susceptible to apparent shifts due to other underlying low-intensity transitions, are often obscured by larger transitions, and are themselves intermixed. While we have been able to identify the beginning of three series corresponding to these three states, we have not been able to completely assign them for all J 's or adequately fit them to determine their spectroscopic constants. Even though these states have very similar α_C values, meaning that their R-branch series are always strongly interwoven, the three satellites could be clearly distinguished from each other by their values of α_A and α_B .

All of the rotational and centrifugal distortion constants for the five lowest fundamental states of pyridazine are presented in Table VIII. The 4th-order distortion constants D_J , D_{JK} , D_K are very similar to each other and to the same constants for the ground state species: within a narrow range of 1.46–1.50 kHz for D_J , within a range of -2.50 to -2.39 kHz for D_{JK} , and a range of 1.06–1.13 kHz for D_K . This consistency was very helpful in predicting the line locations of the excited states. The rms residuals in all five fits are essentially equal to the measurement uncertainties.

ACKNOWLEDGMENTS

We gratefully acknowledge funding from the National Science Foundation for support of this project (CHE-1011959) and for support of shared Departmental computing resources (CHE-0840494). We thank Dr. Desiree M. Bates and Paul B. McGuire for their continued assistance and helpful discussions regarding the computing resources. Additionally, we thank Professor Edwin L. Sibert for his insight into the Coriolis coupling of the vibrational states. J.F.S. also thanks the National Science Foundation for support of the CFOUR program development.

¹V. M. Bierbaum, V. Le Page, and T. P. Snow, "PAHs and the chemistry of the ISM," *Eur. Astron. Soc. Publ. Ser.* **46**, 427–440 (2011).

²E. Ye, R. P. A. Bettens, F. C. De Lucia, D. T. Petkie, and S. Albert, "Millimeter and submillimeter wave rotational spectrum of pyridine in the ground and excited vibrational states," *J. Mol. Spectrosc.* **232**(1), 61–65 (2005).

³Z. Kisiel, L. Pszczółkowski, J. C. López, J. L. Alonso, A. Maris, and W. Caminati, "Investigation of the rotational spectrum of pyrimidine from 3 to 337 GHz: Molecular structure, nuclear quadrupole coupling, and vibrational satellites," *J. Mol. Spectrosc.* **195**(2), 332–339 (1999).

⁴W. Werner, H. Dreizler, and H. D. Rudolph, "Zum mikrowellenspektrum des pyridazins," *Z. Naturforsch., A: Phys. Sci.* **22**(4), 531–543 (1967).

⁵J. C. López, A. de Luis, S. Blanco, A. Lesari, and J. L. Alonso, "Investigation of the quadrupole coupling hyperfine structure due to two nuclei

by molecular beam Fourier transform microwave spectroscopy: Spectra of dichlorofluoromethane and pyridazine," *J. Mol. Struct.* **612**(2–3), 287–303 (2002).

⁶J. Kraitchman, "Determination of molecular structure from microwave spectroscopic data," *Am. J. Phys.* **21**(1), 17–24 (1953).

⁷F. C. De Lucia, "The submillimeter: A spectroscopist's view," *J. Mol. Spectrosc.* **261**(1), 1–17 (2010).

⁸J. R. Schmidt and W. F. Polik, WebMO Enterprise, v. 13.0, WebMO LLC, Holland, MI, 2013; www.webmo.net.

⁹J. Cernicharo, A. M. Heras, A. G. G. M. Tielens, J. R. Pardo, F. Herpin, M. Guélin, and L. B. F. M. Waters, "Infrared space observatory's discovery of C₄H₂, C₆H₂, and benzene in CRL 618," *Astrophys. J. Lett.* **546**(2), L123–L126 (2001).

¹⁰H. S. P. Müller, F. Schlöder, J. Stutzki, and G. Winnewisser, "The Cologne database for molecular spectroscopy, CDMS: A useful tool for astronomers and spectroscopists," *J. Mol. Struct.* **742**(1–3), 215–227 (2005).

¹¹H. S. P. Müller, S. Thorwirth, D. A. Roth, and G. Winnewisser, "The Cologne database for molecular spectroscopy," *CDMS. Astron. Astrophys.* **370**(3), L49–L52 (2001).

¹²S. L. W. Weaver, A. J. Remijan, R. J. McMahon, and B. J. McCall, "A search for ortho-benzyne (*o*-C₆H₄) in CRL 618," *Astrophys. J. Lett.* **671**(2), L153 (2007).

¹³M. N. Simon and M. Simon, "Search for interstellar acrylonitrile, pyrimidine, and pyridine," *Astrophys. J.* **184**, 757–762 (1973).

¹⁴S. B. Chamley, Y.-J. Kuan, H.-C. Huang, O. Botta, H. M. Butner, N. Cox, D. Despois, P. Ehrenfreund, Z. Kisiel, Y.-Y. Lee, A. J. Markwick, Z. Peeters, and S. D. Rodgers, "Astronomical searches for nitrogen heterocycles," *Adv. Space Res.* **36**(2), 137–145 (2005).

¹⁵M. Frenklach and E. D. Feigelson, "Formation of polycyclic aromatic hydrocarbons in circumstellar envelopes," *Astrophys. J.* **341**, 372–384 (1989).

¹⁶N. R. Hore and D. K. Russell, "Radical pathways in the thermal decomposition of pyridine and diazines: A laser pyrolysis and semi-empirical study," *J. Chem. Soc., Perkin Trans. 2* **1998**, 269–275.

¹⁷E. Kraka and D. Cremer, "Ortho-, meta-, and para-benzyne. A comparative CCSD(T) investigation," *Chem. Phys. Lett.* **216**(3–6), 333–340 (1993).

¹⁸R. C. Woods and T. A. Dixon, "A computer controlled microwave spectrometer system," *Rev. Sci. Instrum.* **45**(9), 1122–1126 (1974).

¹⁹R. H. Petrmichl, K. A. Peterson, and R. C. Woods, "The microwave spectrum of SiF⁺," *J. Chem. Phys.* **89**(9), 5454–5459 (1988).

²⁰LabVIEW 2010, 10.0 (32-bit), 2010.

²¹Z. Kisiel, L. Pszczółkowski, B. J. Drouin, C. S. Brauer, S. Yu, J. C. Pearson, I. R. Medvedev, S. Fortman, and C. Neese, "Broadband rotational spectroscopy of acrylonitrile: Vibrational energies from perturbations," *J. Mol. Spectrosc.* **280**(0), 134–144 (2012).

²²H.-Q. Do, R. M. K. Khan, and O. Daugulis, "A general method for copper-catalyzed arylation of arene C–H bonds," *J. Am. Chem. Soc.* **130**(45), 15185–15192 (2008).

²³A. R. Katritzky, B. E.-D. M. El-Gendy, B. Draghici, D. Fedoseyenko, A. Fadli, and E. Metais, "¹H, ¹³C, and ¹⁵N NMR spectra of some pyridazine derivatives," *Magn. Reson. Chem.* **48**(5), 397–402 (2010).

²⁴Z. Kisiel, PROSPE—Programs for ROTational SPectroscopy, see <http://info.ifpan.edu.pl/~kisiel/prospe.htm>.

²⁵J. F. Stanton, J. Gauss, M. E. Harding, P. G. Szalay with contributions from A. A. Auer, R. J. Barlett, U. Benedikt, C. Berger, D. E. Bernholdt, Y. J. Bomble, L. Cheng, O. Christiansen, M. Heckert, O. Heun, C. Huber, T.-C. Jagau, D. Jonsson, J. Jusélius, K. Klein, W. J. Lauderdale, D. A. Matthews, T. Metzroth, L. A. Müick, D. P. O'Neill, D. R. Price, E. Prochnow, C. Puzzarini, K. Ruud, F. Schiffmann, W. Schwalbach, S. Stopkiewicz, A. Tajti, J. Vázquez, F. Wang, J. D. Watts and the integral packages MOLECULE (J. Almlöf and P. R. Taylor), PROPS (P. R. Taylor), ABACUS (T. Helgaker, H. J. Aa. Jensen, P. Jørgensen, and J. Olsen), and ECP routines by A. V. Mitin and C. van Wüllen, see <http://www.cfour.de>.

²⁶A. D. Becke, "Density-functional thermochemistry. III. The role of exact exchange," *J. Chem. Phys.* **98**, 5648–5652 (1993).

²⁷C. Lee, W. Yang, and R. G. Parr, "Development of the Colle-Salvetti correlation-energy formula into a functional of the electron density," *Phys. Rev. B: Condens. Matter* **37**(2), 785–789 (1988).

²⁸W. J. Hehre, R. Ditchfield, and J. A. Pople, "Self-consistent molecular orbital methods. XII. Further extensions of Gaussian—Type basis sets for use in molecular orbital studies of organic molecules," *J. Chem. Phys.* **56**, 2257–2261 (1972).

²⁹T. H. Dunning, "Gaussian basis sets for use in correlated molecular calculations. I. The atoms boron through neon and hydrogen," *J. Chem. Phys.* **90**, 1007–1023 (1989).

- ³⁰M. Head-Gordon, J. A. Pople, and M. J. Frisch, "MP2 energy evaluation by direct methods," *Chem. Phys. Lett.* **153**(6), 503–506 (1988).
- ³¹M. J. Frisch, G. W. Trucks, H. B. Schlegel *et al.*, Gaussian 09, Revision B.1, Gaussian, Inc., Wallingford, CT, 2009.
- ³²M. H. Palmer, R. Wugt Larsen, and F. Hegelund, "Comparison of theoretical and experimental studies of infrared and microwave spectral data for 5- and 6-membered ring heterocycles: The rotation constants, centrifugal distortion and vibration rotation constants," *J. Mol. Spectrosc.* **252**(1), 60–71 (2008).
- ³³J. A. Pople, M. Head-Gordon, and K. Raghavachari, "Quadratic configuration interaction. A general technique for determining electron correlation energies," *J. Chem. Phys.* **87**(10), 5968–5975 (1987).
- ³⁴J. Almlof and P. R. Taylor, "General contraction of Gaussian basis sets. I. Atomic natural orbitals for first- and second-row atoms," *J. Chem. Phys.* **86**(7), 4070–4077 (1987).
- ³⁵G. E. Scuseria, "Analytic evaluation of energy gradients for the singles and doubles coupled-cluster method including perturbative triple excitations: Theory and applications to FOOF and Cr₂," *J. Chem. Phys.* **94**(1), 442–447 (1991).
- ³⁶T. J. Lee and A. P. Rendell, "Analytic gradients for coupled-cluster energies that include noniterative connected triple excitations: Application to cis- and trans-HONO," *J. Chem. Phys.* **94**(9), 6229–6236 (1991).
- ³⁷J. F. Stanton, C. L. Lopreore, and J. Gauss, "The equilibrium structure and fundamental vibrational frequencies of dioxirane," *J. Chem. Phys.* **108**(17), 7190–7196 (1998).
- ³⁸I. M. Mills, *Infrared Spectra. Vibration-Rotation Structure in Asymmetric- and Symmetric-Top Molecules* (Academic, 1972), pp. 115–140.
- ³⁹R. J. McMahon, M. C. McCarthy, C. A. Gottlieb, J. B. Dudek, J. F. Stanton, and P. Thaddeus, "The radio spectrum of the phenyl radical," *Astrophys. J. Lett.* **590**(1), L61 (2003).
- ⁴⁰W. Gordy and R. L. Cook, *Microwave Molecular Spectra*, 3rd ed. (Wiley, New York, 1984).
- ⁴¹J. F. Stanton, J. Gauss, and O. Christiansen, "Equilibrium geometries of cyclic SiC₃ isomers," *J. Chem. Phys.* **114**(7), 2993–2995 (2001).
- ⁴²W. H. Flygare, "Magnetic interactions in molecules and an analysis of molecular electronic charge distribution from magnetic parameters," *Chem. Rev.* **74**(6), 653–687 (1974).
- ⁴³J. Gauss, K. Ruud, and M. Kállay, "Gauge-origin independent calculation of magnetizabilities and rotational *g* tensors at the coupled-cluster level," *J. Chem. Phys.* **127**(7), 074101 (2007).
- ⁴⁴J. Vázquez, J. J. L. Gozález, F. Márquez, and J. E. Boggs, "Vibrational spectrum of pyridazine," *J. Raman Spectrosc.* **29**(6), 547–559 (1998).
- ⁴⁵Y. Ozono, Y. Nibu, H. Shimada, and R. Shimada, "Polarized Raman and infrared spectra of [¹H₄]- and [²H₄]-pyridazines," *Bull. Chem. Soc. Jpn.* **59**(10), 2997–3001 (1986).
- ⁴⁶H. D. Stidham and J. V. Tucci, "Vibrational spectra of pyridazine, pyridazine-d₄, pyridazine-3,6-d₂, and pyridazine-4,5-d₂," *Spectrochim. Acta, Part A* **23**(8), 2233–2242 (1967).
- ⁴⁷See supplementary material at <http://dx.doi.org/10.1063/1.4832899> for summaries of geometry optimizations, harmonic vibrational frequency, and anharmonic vibrational frequency calculations from Gaussian09 and CFOUR. Comparisons of isotopolog constants from Ref. 4 and our work and theoretical calculations. Theoretical predictions of the vibration-rotation interaction at various levels of theory. A full list of measured and fit lines for all species in the ASFIT output format.

Appendix B**Carbonyl Diazide, OC(N₃)₂: Synthesis, Purification, and IR Spectrum**

Alex M. Nolan
Brent K. Amberger
Brian J. Esselman
Venkatesan S. Thimmakonda
John F. Stanton
R. Claude Woods
Robert J. McMahon

Inorganic Chemistry, 2012, *51* (18), 9846-9851

Carbonyl Diazide, $\text{OC}(\text{N}_3)_2$: Synthesis, Purification, and IR Spectrum

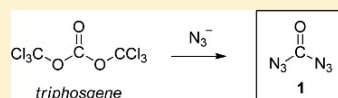
Alex M. Nolan,[†] Brent K. Amberger,[†] Brian J. Esselman,[†] Venkatesan S. Thimmakondur,[‡] John F. Stanton,^{*,‡} R. Claude Woods,^{*,†} and Robert J. McMahon^{*,†}

[†]Department of Chemistry, University of Wisconsin–Madison, 1101 University Avenue, Madison, Wisconsin 53706-1322, United States

[‡]Institute for Theoretical Chemistry, Department of Chemistry and Biochemistry, The University of Texas at Austin, Austin, Texas 78712, United States

Supporting Information

ABSTRACT: Carbonyl diazide (**1**), $\text{OC}(\text{N}_3)_2$, is prepared by reaction of triphosgene and tetra-*n*-butylammonium azide in a solution of diethyl ether or dimethyl ether. The advantage of this synthetic method, relative to other procedures, is that the use of triphosgene, $\text{OC}(\text{OCCl}_2)_2$, mitigates the need to use highly poisonous reagents such as phosgene, OCCl_2 , or chlorofluorocarbonyl, $\text{OC}(\text{Cl})\text{F}$. The identity and purity of $\text{OC}(\text{N}_3)_2$ are established by gas-phase IR spectroscopy, which reveals the presence of both *syn-syn* and *anti-syn* conformers. Computed anharmonic vibrational frequencies and infrared intensities of carbonyl diazide (**1**) display excellent agreement with experiment, and reveal the presence of strong Fermi resonances.



INTRODUCTION

Carbonyl diazide (**1**), $\text{OC}(\text{N}_3)_2$, is a highly explosive compound that has been the subject of recent studies concerning its synthesis, structure, and reactivity.¹ Among various interesting attributes, the compound is notable because it is a high energy structure composed of very stable diatomic species ($\text{CO} + 3\text{N}_2$), with a computed specific enthalpy of decomposition similar to industrial explosives TNT, RDX, and HMX.² Although known since the 1920s,^{3,4} the explosive nature of carbonyl diazide (**1**) discouraged isolation attempts, making the recent synthesis, purification, and characterization by Zeng et al. quite remarkable.¹

Recent interest in carbonyl diazide (**1**), CON_6 , stems from its ability to serve as a precursor to other high energy molecules on the CON_4 and CON_2 potential energy surfaces (Figure 1). Photolysis of $\text{OC}(\text{N}_3)_2$ (**1**) in an inert matrix results in loss of N_2 to generate CON_4 isomers: acyl nitrene $\text{N}_3-\text{C}(\text{O})\text{N}$ (**3**) and its Curtius rearrangement product N_3-NCO (**4**).⁵ Remarkably, flash vacuum pyrolysis of $\text{OC}(\text{N}_3)_2$ (**1**) at 400 °C yields diazirinone (**2**),^{6–8} the C_{2v} conjugate of molecular nitrogen and carbon monoxide. An intriguing species in terms of structure and bonding,^{9–11} diazirinone (**2**) has been the subject of a number of theoretical studies and has received recent attention because of its relevance to the chemistry of CO and N_2 under harsh reaction conditions. Kaiser and co-workers recently suggested that irradiation of N_2/CO ices generates diazirinone (**2**) under astronomically relevant conditions.¹² N_2CO isomers are also known to form under ionizing conditions in the gas phase,¹³ which presents the possibility that diazirinone (**2**) or other N_2CO isomers may be formed in interstellar or circumstellar space. Mechanistic details concerning the conversion of carbonyl diazide (**1**) to diazirinone (**2**) remain unclear at this time.

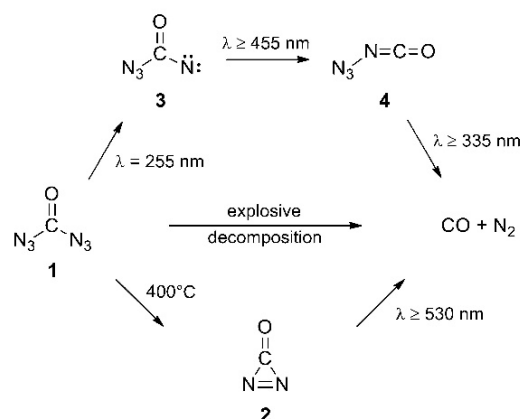


Figure 1. Experimentally observed decomposition pathways for carbonyl diazide, $\text{OC}(\text{N}_3)_2$.^{5–8}

After our earlier studies established that a previous report of the experimental observation of diazirinone (**2**) was incorrect,¹⁴ we turned our attention to the development of alternative methods for generating and detecting this species. We considered carbonyl diazide as a viable, if not especially attractive, precursor to diazirinone (**2**). Carbonyl diazide (**1**) was first synthesized in the 1920s via the diazotization of carbohydrazide (**5**)^{3,4} (Figure 2, eq 1) but was not studied in pure form due to its aforementioned explosive nature. In 2007, carbonyl diazide (**1**) was produced through the incidental hydrolysis of tetraazidomethane (**6**)¹⁵ in undried solvent (Figure 2, eq 2) and was identified by ¹³C and ¹⁵N NMR

Received: June 15, 2012

Published: August 28, 2012

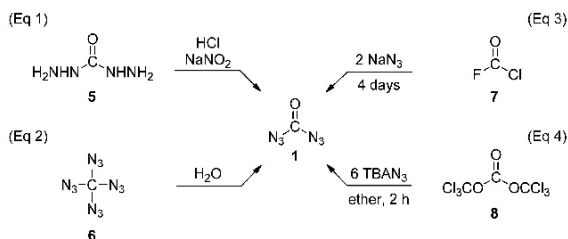


Figure 2. Synthetic routes to carbonyl diazide, $\text{OC}(\text{N}_3)_2$.

spectroscopy. In 2010, Zeng et al. reported a synthesis of carbonyl diazide from treatment of chlorofluorocarbonyl $\text{ClC}(\text{O})\text{F}$ (7) with sodium azide by nucleophilic substitution (Figure 2, eq 3).¹⁸ The product was isolated using trap-to-trap distillation and thoroughly characterized by IR spectroscopy (gas phase and argon matrix), Raman spectroscopy, and X-ray crystallography. Here we describe an alternative procedure for the synthesis of $\text{OC}(\text{N}_3)_2$ (1) using triphosgene (8) and tetra-*n*-butylammonium azide (Figure 2, eq 4), which avoids the use of chlorofluorocarbonyl $\text{ClC}(\text{O})\text{F}$ (7), a substance that is both highly poisonous and not readily available.

EXPERIMENTAL SECTION

Caution! Carbonyl diazide (1) is shock-sensitive and explosive. Proper safety precautions, which include the use of leather gloves, face shields, and blast shields, must be taken when handling this compound.^{1,16,17} Sodium azide (NaN_3) and its hydrolysis product, hydrazoic acid (HN_3) are toxic.¹⁷ Sodium azide, as well as metal azides that may be formed by reaction of sodium azide, represent explosion hazards.¹⁷

Many of the manipulations involved in the preparation and purification of carbonyl diazide (1) were performed using a stainless-steel vacuum manifold, which is described in greater detail in Supporting Information. The purity of carbonyl diazide (1) samples was examined by gas-phase IR spectroscopy, and percent yield was estimated from the pressure in a stainless-steel manifold of known volume. Unless noted otherwise, chemicals were acquired from commercial sources and were used without further purification.

Tetra-*n*-butylammonium Azide. (TBAN_3) was prepared using a literature procedure and recrystallized from toluene.¹⁸ On occasion, a residual toluene contaminant in TBAN_3 was carried through the subsequent synthetic procedures and could not be removed from the desired carbonyl diazide. In order to remove the toluene contaminant, a slurry of TBAN_3 (ca. 5 g) in 75 mL of diethyl ether was brought to reflux with stirring. The slurry was then cooled to room temperature; crystals were collected by filtration and washed with cold diethyl ether. Residual diethyl ether solvent was removed from TBAN_3 under high vacuum.

Carbonyl Diazide (1): Method A. Tetra-*n*-butylammonium azide (TBAN_3) (1.64 g, 5.77 mmol) was added to an oven-dried round-bottom flask, followed by anhydrous diethyl ether (10 mL) under positive nitrogen pressure. The volume of solvent was not sufficient to completely dissolve the ammonium salt. Triphosgene (194 mg, 0.655 mmol) was added, and the suspension was stirred for 2 h. The solution was then passed through a silica plug to remove the suspended ammonium salts, and diethyl ether (5 mL) was used to wash the silica. The organic layer was washed with saturated aqueous sodium chloride (10 mL) and dried over magnesium sulfate, and the drying agent removed by gravity filtration.

Although a dilute solution of $\text{OC}(\text{N}_3)_2$ in diethyl ether seems comparatively safe to handle in glass, a concentrated solution or the isolated material is not. In one instance, a neat sample of $\text{OC}(\text{N}_3)_2$ detonated upon insertion of a glass pipet; the round-bottom flask containing the sample was pulverized by the blast. Therefore, all manipulations following the removal of the magnesium sulfate drying agent were conducted in a 200-mL stainless-steel flask. The solution of

$\text{OC}(\text{N}_3)_2$ in diethyl ether in a stainless-steel flask was frozen at -196°C , and the vessel was evacuated. The sample was allowed to warm to room temperature, and all volatile materials were cryopumped to a second stainless-steel flask at -196°C to ensure that absolutely no nonvolatile or particulate matter contaminated the sample. The second flask was then held at -78°C , a temperature at which Et_2O is volatile but $\text{OC}(\text{N}_3)_2$ is not, and the ether was removed with a diffusion pump in conjunction with a liquid nitrogen trap. To remove all traces of ether from the flask, it was necessary to perform three or four freeze-pump-thaw cycles, wherein the sample flask was isolated from the vacuum, warmed to room temperature, and cooled back to -78°C before pumping was resumed. Carbonyl diazide synthesized and purified in this way typically afforded a yield of ca. 7.1 Torr-liter, (0.38 mmol, 19%).

Carbonyl Diazide (1): Method B. A modified version of the preparation allows the entire procedure to be carried out on the stainless-steel manifold. Use of dimethyl ether (bp -24°C), which is more volatile than diethyl ether (bp 35°C), improves the ease and efficiency of solvent removal from carbonyl diazide (1), although it also requires that the reaction be performed at low temperature or under pressure. Triphosgene (0.153 g, 0.516 mmol) and sodium azide (0.207 g, 3.184 mmol) were added to a 35-mL stainless-steel flask. The flask was attached to the stainless-steel manifold and evacuated, and gaseous dimethyl ether was condensed into the vessel at -196°C . In the 35-mL flask, 1400 Torr-liter of dimethyl ether was calculated to afford ~ 4 mL as liquid solvent. After stirring for 16 h, the solvent was distilled from the flask at -78°C . The flask was then allowed to warm to room temperature, and carbonyl diazide (1) was cryopumped to a clean stainless-steel flask at -196°C . Yields as high as 32% were observed; however, this procedure proved more fickle than the synthesis in diethyl ether.

Characterization. Following either synthetic procedure, a small portion of the sample was transferred to a stainless steel, gas-phase IR cell (ca. 1 Torr) using vacuum line techniques. The purity of the sample was assessed by comparison to spectral data described previously by Zeng et al.¹ A representative IR spectrum (Figure 3)

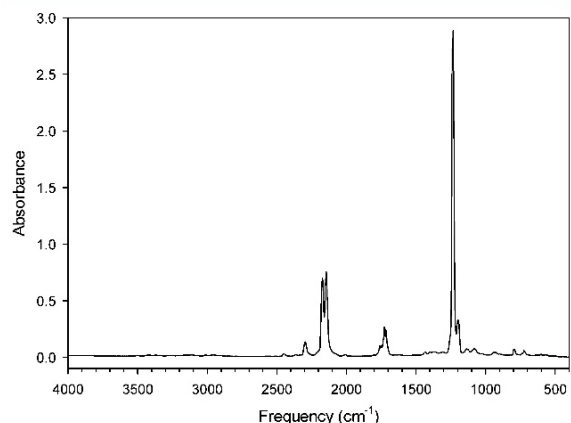


Figure 3. Infrared spectrum of gaseous carbonyl diazide, $\text{OC}(\text{N}_3)_2$ (1) (1 Torr, 298 K, spectral resolution of 2 cm^{-1}).

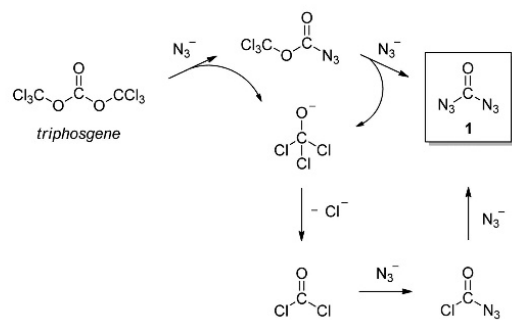
displays excellent agreement with literature data and is devoid of IR absorptions attributable to impurities (see discussion below). Carbonyl diazide can be stored at room temperature in a stainless steel flask for a few weeks with minor decomposition. Samples of $\text{OC}(\text{N}_3)_2$ must be handled gently, as physical shocks occasionally resulted in audible explosive decompositions within the steel flasks.

RESULTS AND DISCUSSION

Synthesis. A logical strategy for the preparation of carbonyl diazide (1) involves the use of phosgene or a “phosgene

equivalent". Given the serious hazards associated with the use of phosgene, triphosgene has supplanted phosgene as the electrophile of choice in reactions of this type.^{19,20} Triphosgene, $\text{OC}(\text{OCCl}_3)_2$, is a stable crystalline solid, which, in solution, serves as a surrogate for 3 equiv of phosgene. Although we have not engaged in a detailed mechanistic study of this reaction, the transformations depicted in Scheme 1 have

Scheme 1. Preparation of Carbonyl Diazide (1) Using Triphosgene



good precedent in the literature.²¹ Sequential nucleophilic attack of azide on the carbonyl carbon of triphosgene results in the formation of 1 equiv of $\text{OC}(\text{N}_3)_2$ (1) and the liberation of 2 equiv of trichloromethoxide ion. Trichloromethoxide ion rapidly eliminates chloride ion to generate phosgene. Phosgene generated *in situ* is more reactive than triphosgene, and subsequent reaction with azide yields additional $\text{OC}(\text{N}_3)_2$. In our initial studies, we used sodium azide as the source of azide ion and diethyl ether as solvent. Although these conditions were successful in generating carbonyl diazide (1), we reasoned that the very low solubility of sodium azide in diethyl ether was a factor in the slow conversion of starting material and low yield of product. We turned to tetra-*n*-butylammonium azide (TBAN_3) as a source of azide ion with greater solubility in organic solvents. Use of TBAN_3 enhanced the conversion of triphosgene to carbonyl diazide (1) while minimizing the risk of an explosive decomposition of solid sodium azide. Employing standard solution-phase reaction conditions also allowed the use of standard procedures to work up the reaction, including

an aqueous wash of the reaction mixture to ensure that any remaining starting materials are safely neutralized and removed. The final low-temperature, low-pressure distillation of solvent from the carbonyl diazide (1) product is performed in a stainless-steel vessel, which increases the quantity of pure $\text{OC}(\text{N}_3)_2$ that may be handled safely. A disadvantage of this procedure stems from the relative volatilities of carbonyl diazide (1) and diethyl ether. Removing all of the solvent, without losing an excessive amount of product, necessitates a series of freeze–pump–thaw cycles. This procedure can be safely performed with the stainless-steel apparatus, but it is tedious.

The alternate procedure involving triphosgene, sodium azide, and dimethyl ether offers a different set of advantages and disadvantages. The procedure is carried out entirely within a stainless-steel apparatus, which enhances the margin of safety although diminishes the ability to monitor the reaction in real time. The higher volatility of dimethyl ether facilitates solvent removal, but upon solvent removal, the neat product remains mixed with solid sodium azide. This procedure afforded both the greatest quantity and highest chemical yield of carbonyl diazide (1). That the procedure is fickle may reflect an instability of the mixture of neat carbonyl diazide and sodium azide, an observation noted independently by Zeng et al.²² Although we attempted the synthesis using tetra-*n*-butylammonium azide in dimethyl ether, we found the procedure to be complicated by experimental difficulties associated with transferring 2 g of the highly hygroscopic TBAN_3 to the 35-mL stainless-steel reaction vessel and ensuring that the viscous mass dissolved in dimethyl ether.

Without mitigating the dangers inherent in the preparation and handling of carbonyl diazide (1), our procedure addresses the complications associated with the literature procedure for the synthesis of this compound:¹ (i) the use of chlorofluorocarbonyl (7), which is highly poisonous and is not commercially available, (ii) the use of sodium azide under heterogeneous (gas/solid) reaction conditions, (iii) a reaction time of two hours vs four days, and (iv) the ability to quantitatively assess product yield.

Potential Energy Surface. Optimized geometries, energies, and infrared intensities were obtained using the CCSD method²³ with the cc-pVDZ²⁴ basis set as implemented in Gaussian 09.²⁵ The nature of stationary points was confirmed by calculation of the harmonic vibrational frequencies, which

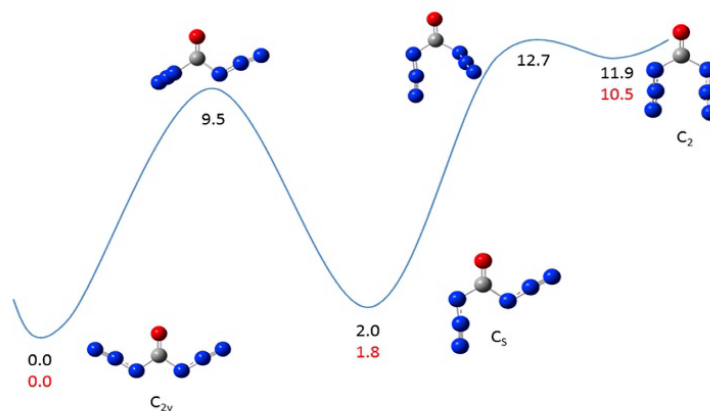


Figure 4. Potential energy surface of $\text{OC}(\text{N}_3)_2$. Relative energies (kcal/mol, including ZPVE) at CCSD/cc-pVDZ (upper, black) and CCSD(T)/cc-pVTZ (lower, red).

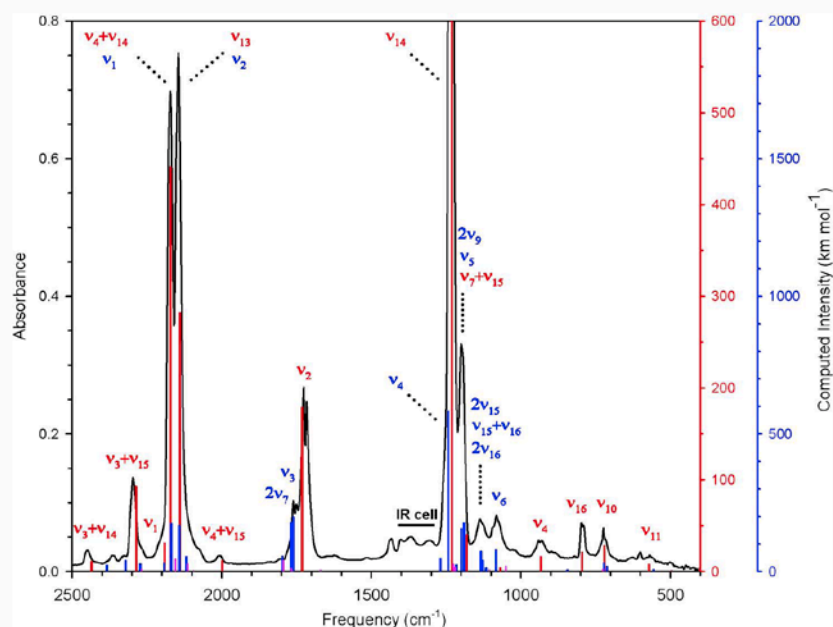


Figure 5. Infrared spectrum of gaseous carbonyl diazide, $\text{OC}(\text{N}_3)_2$ (1 Torr, 298 K) with computed vibrational frequencies and intensities of *syn-syn* (red) and *anti-syn* (blue) conformers superimposed as stick spectra. The y-axis scales for the computed infrared intensities have been adjusted to reflect a qualitative agreement with the experimental spectrum. Several weak absorptions arise from the IR cell.

also provided zero-point vibrational energy (ZPVE) corrections. The transition states were connected to their minima via IRC calculations. CCSD(T)/cc-pVTZ²⁶ optimized geometry and harmonic frequency calculations were performed using CFOUR²⁷ for each of the minima. Further details of the calculations can be found in Supporting Information.

The conformational isomers of carbonyl diazide (**1**) [*syn-syn* (C_{2v}), *anti-syn* (C_s), and *anti-anti* (C_2)] are depicted in Figure 4. In good agreement with recent literature data,^{1,2} the lowest energy conformer is *syn-syn*, with the *anti-syn* conformer lying 1.8 kcal/mol higher in energy at the CCSD(T)/cc-pVTZ level of theory. The *anti-anti* conformer does not adopt an idealized C_{2v} structure; it exhibits a slight distortion from planarity (C_2) and lies ca. 11 kcal/mol higher in energy than the *syn-syn* rotamer. The barriers to rotation of the N_3 groups are modest (Figure 4).

IR Spectrum. The gas-phase infrared spectrum of carbonyl diazide (**1**) has been described previously,¹ and we rely on the IR spectrum as the criterion of purity for our synthetic method. As such, it was of some concern to us that the computed harmonic vibrational frequencies and infrared intensities for *syn-syn* and *anti-syn* conformers of carbonyl diazide (**1**) do not account for all of the prominent features in the experimental spectrum, notably 2297, 2171, and 1200 cm^{-1} . The origin of these features is unclear. While it is possible that these absorptions may arise from carbonyl diazide (**1**) through the effects of anharmonicity (combinations, overtones, Fermi resonance), it is also possible that they may be attributable to unidentified impurities. We sought to explore this matter, in greater detail, through a more sophisticated theoretical treatment of the vibrational spectrum.

To help analyze the puzzling aspects of the infrared spectrum, we undertook high-level calculations that include the effects of anharmonicity on the vibrational frequencies and

infrared intensities. For each of the three conformational isomers of carbonyl diazide (**1**), geometries were optimized at CCSD(T)/ANO0 and CCSD(T)/ANO1 levels of theory using analytic gradients,^{28,29} and harmonic frequencies were obtained with analytic second derivatives.³⁰ The cubic and quartic force constants were then calculated by numerical differentiation of analytic second derivatives calculated at displaced points, following the approach of Stanton et al.³¹ Second-order vibrational perturbation theory (VPT2) was then used to compute the fundamental vibrational frequencies as well as the infrared intensities.^{32,33} Fermi resonances were analyzed using the approach of Matthews and Stanton.³⁴

In contrast to the harmonic analysis of the infrared spectrum, which cannot account for many of its most prominent features, the anharmonic analysis is in striking agreement with observation (Figure 5, Tables 1 and 2). The cluster of features seen from 2000 to 2300 cm^{-1} results from a strong and extensive Fermi resonance in the *syn-syn* conformer of $\text{OC}(\text{N}_3)_2$, whereby the combination levels $\nu_4 + \nu_{14}$, $\nu_4 + \nu_{15}$, and $\nu_3 + \nu_{15}$ borrow intensity from the very strong asymmetric $-\text{N}=\text{N}=\text{N}$ stretching mode, ν_{13} . Similarly, the intrinsically strong ν_{14} asymmetric C–N stretching mode mixes with the combination level $\nu_7 + \nu_{15}$. When these resonances are carefully treated within the context of VPT2, a confident assignment (rightmost column in Table 1) may be made for all of the principal features seen in the spectrum (as well as most of the minor features). It is rather remarkable that almost half of the vibrational levels with predicted infrared intensities above 10 km mol^{-1} (5 of 12) correspond to two-quantum overtone and combination levels, an observation that underscores the problems that are associated with relying on the harmonic treatment for the analysis of the spectrum.

The experimental infrared spectrum also reveals the presence of the *anti-syn* conformer of $\text{OC}(\text{N}_3)_2$ as a minor component

Table 1. Experimental and Computed Vibrational Frequencies and Infrared Intensities for the *syn-syn* Conformer of OC(N₃)₂^a

mode	sym	fc-CCSD(T)			exptl
		harmonic ANO0	harmonic ANO1	VPT2+F ANO1	
Fundamentals					
1	<i>a</i> ₁	2214 (54)	2228 (63)	2191 (31)	
2	<i>a</i> ₁	1782 (194)	1764 (194)	1731 (179)	<i>1721</i>
3	<i>a</i> ₁	1254 (4)	1266 (5)	1222 (4)	
4	<i>a</i> ₁	945 (19)	953 (20)	933 (16)	<i>941</i>
5	<i>a</i> ₁	553 (0)	553 (0)	544 (0)	
6	<i>a</i> ₁	407 (2)	408 (2)	403 (1)	
7	<i>a</i> ₁	122 (0)	122 (0)	114 (0)	
8	<i>a</i> ₂	569 (0)	570 (0)	557 (0)	
9	<i>a</i> ₂	152 (0)	155 (0)	151 (0)	
10	<i>b</i> ₁	733 (29)	730 (25)	720 (28)	<i>723</i>
11	<i>b</i> ₁	580 (9)	581 (7)	571 (8)	<i>569</i>
12	<i>b</i> ₁	75 (1)	76 (1)	72 (1)	
13	<i>b</i> ₂	2198 (858)	2212 (875)	2140 (282)	<i>2145</i>
14	<i>b</i> ₂	1266 (1755)	1277 (1735)	1230 (1633)	<i>1235</i>
15	<i>b</i> ₂	1095 (17)	1107 (13)	1069 (4)	
16	<i>b</i> ₂	807 (23)	808 (26)	795 (21)	<i>794</i>
17	<i>b</i> ₂	500 (2)	503 (3)	496 (1)	
18	<i>b</i> ₂	206 (1)	206 (1)	204 (1)	
Two-Quantum Levels					
3 + 14	<i>b</i> ₂			2435 (11)	<i>2450</i>
3 + 15	<i>b</i> ₂			2286 (93)	<i>2295</i>
4 + 14	<i>b</i> ₂			2171 (441)	<i>2172</i>
4 + 15	<i>b</i> ₂			1998 (12)	<i>2005</i>
7 + 15	<i>b</i> ₂			1181 (40)	<i>1200</i>

^aComputed harmonic and Fermi-resonance corrected (VPT2+F) frequencies (cm⁻¹), along with intensities given in parentheses (km mol⁻¹). Two-quantum (overtone and combination) levels with intensity greater than 10 km mol⁻¹ also included. Computed frequencies are not scaled. Assigned experimental levels in italics.

of the gaseous mixture. The anharmonic analysis suggests that the observed C=O stretching frequency at 1756 cm⁻¹ is composed of contributions from both the fundamental, ν_3 , and an overtone, $2\nu_7$ vibration (Table 2). The most intense vibration of the *anti-syn* conformer (ν_4 , 1257 cm⁻¹) appears as a shoulder on the high-energy side of the C–N stretching vibration of the *syn-syn* conformer (ν_{14} , 1235 cm⁻¹). Fundamental, combination, and overtone bands of the *anti-syn* conformer contribute to absorptions observed at 1200, 1138, and 1082 cm⁻¹. We also computed the anharmonic infrared spectrum of the *anti-anti* conformer (see Supporting Information section), but this conformer does not contribute to the observed spectrum.

SUMMARY

Carbonyl diazide, OC(N₃)₂ (**1**), serves as a precursor to several unusual, high-energy molecules; a safe and reliable preparation for this substance represents an important objective. Our synthesis provides advantages over previous methods in terms of ready availability of starting materials, scalability of the procedure, and, most importantly, safety. The infrared spectrum of OC(N₃)₂ serves as the criterion of purity for most synthetic procedures, which forced us to analyze this spectrum in considerable detail. The spectrum is not well-described by computed harmonic vibrational frequencies and

Table 2. Experimental and Computed Vibrational Frequencies and Infrared Intensities for the *anti-syn* Conformer of OC(N₃)₂^a

mode	sym	fc-CCSD(T)			exptl
		harmonic ANO0	harmonic ANO1	VPT2+F ANO1	
Fundamentals					
1	<i>a'</i>	2212 (295)	2226 (308)	2169 (174)	<i>2172</i>
2	<i>a'</i>	2192 (528)	2206 (552)	2142 (167)	<i>2145</i>
3	<i>a'</i>	1813 (475)	1801 (482)	1760 (198)	<i>1756</i>
4	<i>a'</i>	1279 (766)	1290 (736)	1243 (583)	<i>1257</i>
5	<i>a'</i>	1226 (354)	1237 (374)	1190 (177)	<i>1200</i>
6	<i>a'</i>	1114 (148)	1125 (147)	1083 (80)	<i>1082</i>
7	<i>a'</i>	894 (7)	901 (7)	884 (6)	
8	<i>a'</i>	727 (34)	730 (33)	722 (30)	
9	<i>a'</i>	611 (2)	613 (2)	600 (2)	
10	<i>a'</i>	495 (1)	497 (1)	491 (1)	
11	<i>a'</i>	433 (1)	436 (1)	430 (1)	
12	<i>a'</i>	200 (2)	200 (2)	199 (2)	
13	<i>a'</i>	127 (0)	126 (0)	127 (0)	
14	<i>a''</i>	720 (27)	718 (24)	712 (18)	
15	<i>a''</i>	576 (2)	576 (1)	567 (2)	
16	<i>a''</i>	566 (11)	568 (10)	556 (7)	
17	<i>a''</i>	135 (0)	138 (0)	134 (0)	
18	<i>a''</i>	91 (0)	94 (0)	95 (0)	
Two-Quantum Levels					
2(5)	<i>a'</i>			2384 (23)	
4 + 6	<i>a'</i>			2321 (40)	
5 + 6	<i>a'</i>			2272 (28)	
2(6)	<i>a'</i>			2192 (31)	
4 + 7	<i>a'</i>			2118 (54)	
6 + 8	<i>a'</i>			1797 (55)	
2(7)	<i>a'</i>			1768 (178)	<i>1756</i>
14 + 16	<i>a'</i>			1269 (47)	
8 + 10	<i>a'</i>			1215 (24)	
2(9)	<i>a'</i>			1199 (156)	<i>1200</i>
2(15)	<i>a'</i>			1133 (73)	<i>1138</i>
15 + 16	<i>a'</i>			1127 (40)	<i>1138</i>
2(16)	<i>a'</i>			1116 (13)	<i>1138</i>

^aComputed harmonic and Fermi-resonance corrected (VPT2+F) frequencies (cm⁻¹), along with intensities given in parentheses (km mol⁻¹). Two-quantum (overtone and combination) levels with intensity greater than 10 km mol⁻¹ also included. Computed frequencies are not scaled. Assigned experimental levels in italics.

intensities. After including the effects of anharmonicity, the computed vibrational frequencies and infrared intensities of carbonyl diazide (**1**) display excellent agreement with experiment, and reveal the presence of strong Fermi resonances.

ASSOCIATED CONTENT

Supporting Information

Description of stainless-steel vacuum manifold used for synthesis and purification. Gas-phase IR spectra of OC(N₃)₂ obtained using various preparations. Details of computational results at CCSD/cc-pVDZ and CCSD(T)/cc-pVTZ levels of theory, including computed energies, zero-point vibrational corrections, and Cartesian coordinates. Harmonic (CCSD(T)/ANO0, CCSD(T)/ANO1) and Fermi-resonance corrected (VPT2+F) frequencies and infrared intensities for the *anti-anti* conformer of OC(N₃)₂. This material is available free of charge via the Internet at <http://pubs.acs.org>.

AUTHOR INFORMATION

Corresponding Author

*E-mail: jfstanton@mail.utexas.edu (J.F.S.), rcwoods@wisc.edu (R.C.W.), mcMahon@chem.wisc.edu (R.J.M.).

Notes

The authors declare no competing financial interest.

ACKNOWLEDGMENTS

We gratefully acknowledge the National Science Foundation (CHE-1011959, R.J.M.) and the Robert A. Welch Foundation (Grant F-1283, J.F.S.) for support of this project. We also thank NSF for support of shared computing facilities at Wisconsin (CHE-0840494).

REFERENCES

- Zeng, X.; Gerken, M.; Beckers, H.; Willner, H. *Inorg. Chem.* **2010**, *49*, 9694–9699.
- Ball, D. W. *Comput. Theor. Chem.* **2011**, *965*, 176–179.
- Kesting, W. *Ber. Dtsch. Chem. Ges.* **1924**, *57B*, 1321–1324.
- Curtius, T.; Bertho, A. *Ber. Dtsch. Chem. Ges.* **1926**, *59B*, 565–589.
- Zeng, X.; Beckers, H.; Willner, H. *Angew. Chem., Int. Ed.* **2011**, *123*, 502–505.
- (a) Zeng, X.; Beckers, H.; Willner, H.; Stanton, J. F. *Angew. Chem., Int. Ed.* **2011**, *50*, 1720–1723. (b) Shaffer, C. J.; Schröder, D. *Angew. Chem., Int. Ed.* **2011**, *50*, 2677–2678.
- Perrin, A.; Zeng, X.; Beckers, H.; Willner, H. *J. Mol. Spectrosc.* **2011**, *269*, 30–35.
- Zeng, X.; Beckers, H.; Willner, H.; Stanton, J. F. *Eur. J. Inorg. Chem.* **2012**, 3403–3409.
- Korkin, A. A.; von Ragué Schleyer, P.; Boyd, R. J. *Chem. Phys. Lett.* **1994**, *227*, 312–320.
- Korkin, A. A.; Balkova, A.; Bartlett, R. J.; Boyd, R. J.; Schleyer, P. v. R. *J. Phys. Chem.* **1996**, *100*, 5702–5714.
- Skandke, A.; Liebman, J. F. *J. Org. Chem.* **1999**, *64*, 6361–6365.
- Kim, Y. S.; Zhang, F.; Kaiser, R. I. *Phys. Chem. Chem. Phys.* **2011**, *13*, 15766–15773.
- de Petris, G.; Cacace, F.; Cipollini, R.; Cartoni, A.; Rosi, M.; Troiani, A. *Angew. Chem., Int. Ed.* **2005**, *44*, 462–465.
- Shaffer, C. J.; Esselman, B. J.; McMahon, R. J.; Stanton, J. F.; Woods, R. C. *J. Org. Chem.* **2010**, *75*, 1815–1821.
- Banert, K.; Joo, Y.-H.; Rüfner, T.; Walfort, B.; Lang, H. *Angew. Chem., Int. Ed.* **2007**, *46*, 1168–1171.
- Organic Azides: Syntheses and Applications*; Bräse, S., Banert, K., Eds.; John Wiley and Sons, Ltd.: Chichester, U.K., 2010.
- Prudent Practices in the Laboratory, Updated Version*; National Research Council: Washington, DC, 2011.
- Brandstrom, A.; Lamm, B.; Palmertz, I. *Acta Chem. Scand., Ser. B* **1974**, *28*, 699–701.
- Cotarca, L.; Delogu, P.; Nardelli, A.; Šunjić, V. *Synthesis* **1996**, 553–576.
- Cotarca, L. *Org. Process Res. Dev.* **1999**, *3*, 377.
- Pasquato, L.; Modena, G.; Cotarca, L.; Delogu, P.; Mantovani, S. *J. Org. Chem.* **2000**, *65*, 8224–8228.
- Zeng, X. Personal communication.
- Purvis, G. D., III; Bartlett, R. J. *J. Chem. Phys.* **1982**, *76*, 1910–1918.
- Dunning, T. H., Jr. *J. Chem. Phys.* **1989**, *90*, 1007–1023.
- Frisch, M. J.; Trucks, G. W.; Schlegel, H. B.; Scuseria, G. E.; Robb, M. A.; Cheeseman, J. R.; Scalmani, G.; Barone, V.; Mennucci, B.; Petersson, G. A.; Nakatsuji, H.; Caricato, M.; Li, X.; Hratchian, H. P.; Izmaylov, A. F.; Bloino, J.; Zheng, G.; Sonnenberg, J. L.; Hada, M.; Ehara, M.; Toyota, K.; Fukuda, R.; Hasegawa, J.; Ishida, M.; Nakajima, T.; Honda, Y.; Kitao, O.; Nakai, H.; Vreven, T.; Montgomery, J. J. A.; Peralta, J. E.; Ogliaro, F.; Bearpark, M.; Heyd, J. J.; Brothers, E.; Kudin, K. N.; Staroverov, V. N.; Kobayashi, R.; Normand, J.; Raghavachari, K.; Rendell, A.; Burant, J. C.; Iyengar, S. S.; Tomasi, J.; Cossi, M.; Rega, N.; Millam, N. J.; Klene, M.; Knox, J. E.; Cross, J. B.; Bakken, V.; Adamo, C.; Jaramillo, J.; Gomperts, R.; Stratmann, R. E.; Yazyev, O.; Austin, A. J.; Cammi, R.; Pomelli, C.; Ochterski, J. W.; Martin, R. L.; Morokuma, K.; Zakrzewski, V. G.; Voth, G. A.; Salvador, P.; Dannenberg, J. J.; Dapprich, S.; Daniels, A. D.; Farkas, Ö.; Foresman, J. B.; Ortiz, J. V.; Cioslowski, J.; Fox, D. J. *Gaussian 09, Revision B.1*; Gaussian, Inc.: Pittsburgh, PA, 2009.
- Pople, J. A.; Head-Gordon, M.; Raghavachari, K. *J. Chem. Phys.* **1987**, *87*, 5968–5975.
- Stanton, J. F.; Gauss, J.; Harding, M. E.; Szalay, P. G. *CFOUR, Coupled-Cluster Techniques for Computational Chemistry*; with contributions from Auer, A. A.; Bartlett, R. J.; Benedikt, U.; Berger, C.; Bernholdt, D. E.; Bomble, Y. J.; Cheng, L.; Christiansen, O.; Heckert, M.; Heun, O.; Huber, C.; Jagau, T.-C.; Jonsson, D.; Jusélius, J.; Klein, K.; Lauderdale, W. J.; Matthews, D. A.; Metzroth, T.; O'Neill, D. P.; Price, D. R.; Prochnow, E.; Ruud, K.; Schifmann, F.; Schwalbach, W.; Stopkiewicz, S.; Tajti, A.; Vázquez, J.; Wang, F.; Watts, J. D.; the integral packages MOLECULE (Almlöf, J.; Taylor, P. R.), PROPS (Taylor, P. R.), and ABACUS (Helgaker, T.; Jensen, H. J. Aa; Jørgensen, P.; Olsen, J.); and ECP routines by Mitin, A. V.; van Wüllen, C.; www.cfour.de.
- Scuseria, G. E. *J. Chem. Phys.* **1991**, *94*, 442–447.
- Lee, T. J.; Rendell, A. P. *J. Chem. Phys.* **1991**, *94*, 6229–6236.
- Gauss, J.; Stanton, J. F. *Chem. Phys. Lett.* **1997**, *276*, 70–77.
- Stanton, J. F.; Lopreore, C. L.; Gauss, J. *J. Chem. Phys.* **1998**, *108*, 7190–7196.
- Mills, I. M. In *Molecular Spectroscopy: Modern Research*; Rao, K. N., Mathews, C. W., Eds.; Academic Press: New York, 1972; Vol. 1, pp 115–140.
- Vázquez, J.; Stanton, J. F. *Mol. Phys.* **2007**, *105*, 101–109.
- Matthews, D. A.; Stanton, J. F. *Mol. Phys.* **2009**, *107*, 213–222.

Appendix C

Millimeter-wave spectroscopy of carbonyl diazide, $\text{OC}(\text{N}_3)_2$

Brent K. Amberger
Brian J. Esselman
R. Claude Woods
Robert J. McMahon

Journal of Molecular Spectroscopy, 2014, 295, 15-20



Contents lists available at ScienceDirect

Journal of Molecular Spectroscopy

journal homepage: www.elsevier.com/locate/jmsMillimeter-wave spectroscopy of carbonyl diazide, $\text{OC}(\text{N}_3)_2$ 

Brent K. Amberger, Brian J. Esselman, R. Claude Woods, Robert J. McMahon*

Department of Chemistry, University of Wisconsin-Madison, 1101 University Avenue, Madison, WI 53706, United States

ARTICLE INFO

Article history:

Received 30 September 2013

Available online 8 November 2013

Keywords:

Carbonyl diazide

Millimeter-wave

Rotational spectroscopy

Conformational isomers

Vibration-rotation interaction

Centrifugal distortion

ABSTRACT

Millimeter-wave absorption spectra for carbonyl diazide ($\text{OC}(\text{N}_3)_2$) are reported in the frequency range of 243–360 GHz, at both 293 K and 213 K. Transitions for two of the three possible conformations, one with both of the azide groups *syn* to the carbonyl group, or with one *syn* and the other *anti*, were observed in the spectra. Theoretical calculations at the CCSD(T)/ANO1 level do an excellent job of predicting the ground state rotational constants and 4th order centrifugal distortion terms for both conformers. Relative line intensities, along with theoretically predicted dipole moments, were used to estimate the energy difference of the two observed forms, yielding a result in good agreement with the *ab initio* potential energy surface. The spectra of the ν_{12} , ν_7 , ν_9 and $2\nu_{12}$ excited vibrational states for the more abundant *syn-syn* conformer have been assigned, and a great many transitions for each of them have been fit using partial 6th and 8th order centrifugal distortion Hamiltonians. Anharmonic vibration-rotation interaction constants from the CCSD(T)/ANO1 calculations are in excellent agreement with the experimentally determined constants in the case of ν_7 and ν_9 , but not for ν_{12} .

© 2013 Elsevier Inc. All rights reserved.

1. Introduction

Carbonyl diazide ($\text{OC}(\text{N}_3)_2$) is a high energy compound which has been known in the literature for more than 100 years [1–5]. Recently, carbonyl diazide has been the subject of multiple theoretical, synthetic, and spectroscopic studies [6–9]. This recent attention stems from the work of Zeng et al., which showed that carbonyl diazide can be decomposed to several interesting species on the CON_4 and CON_2 potential energy surfaces [10,11]. As shown in Fig. 1, gas phase pyrolysis of carbonyl diazide (1) has been shown to yield diazirinone (2), while irradiation of (1) in an inert gas matrix yields both the acylnitrene (3) and its Curtius rearrangement product, isocyanate (4).

To date, carbonyl diazide appears to be the only practical precursor for generating the CON_2 isomer diazirinone, a molecule of recent interest [11–14]. Diazirinone can be considered a covalent dimer of the ubiquitous interstellar species N_2 and CO and is structurally analogous to the known space molecule cyclopropenone [15] (a covalent dimer of CO and acetylene). Thus, diazirinone may itself be of astrochemical interest. As will become evident, carbonyl diazide has a very dense and fairly strong rotational spectrum. We have been able to assign the most prominent features of the carbonyl diazide millimeter-wave spectrum, including ground vibrational spectra of the two lowest lying theoretically predicted forms and the four lowest energy vibrational satellite spectra of the *syn-syn* form. Together, these account for most of the strong

features in the spectrum. Transitions for the ground state and first excited state (ν_{12}) of the *syn-syn* form have been fit to near experimental error with a rigid rotor/centrifugal distortion model. The spectra observed in states ν_7 , ν_9 , and $2\nu_{12}$ present additional challenges, because they appear to show some effects of mutual Coriolis perturbations. Nevertheless, the rigid rotor/centrifugal distortion models we have used, *i.e.*, ones not accounting for the perturbations, are adequate to assign a great majority of the observable transitions and to fit them with only small systematic errors in the highest J cases. The fit for the *anti-syn* form is successful in reproducing the many observed lines, but the variety of transition types and the accessible quantum number range is smaller than that of the *syn-syn* form, because of its less intense spectrum.

2. Experimental details

WARNING. Carbonyl diazide is highly explosive, and very slight physical shocks can cause it to detonate. Use blast shields, full personal safety equipment, strong metal containers, and extreme caution when working with this substance. To minimize risk of injury, only work with very small quantities [16,17].

Our $\text{OC}(\text{N}_3)_2$ samples were prepared via the reaction of triphosgene and tetrabutyl ammonium azide as previously described [8], or in a modified synthesis in which triphosgene and sodium azide were allowed to react in a very small volume of polyethylene glycol (MW 400). Polyethylene glycol was chosen as a nonvolatile solvent, from which we could vacuum distill our product after the

* Corresponding author.

E-mail address: mcmahon@chem.wisc.edu (R.J. McMahon).

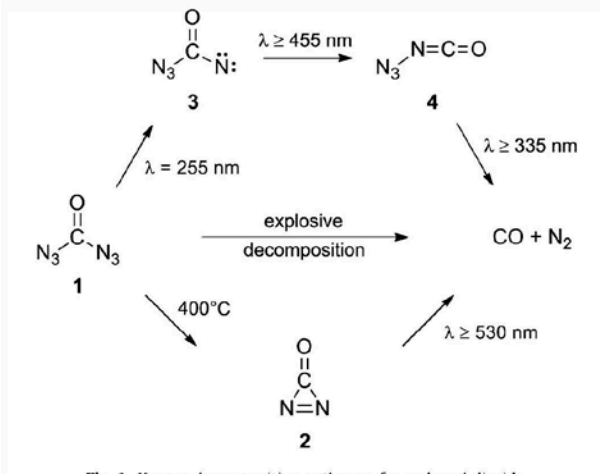


Fig. 1. Known decomposition pathways for carbonyl diazide.

reaction. Polyethylene glycol also acts as a catalyst by sequestering the Na^+ ions of NaN_3 , much like a crown ether, giving higher soluble concentrations of the nucleophilic anion [18]. In a typical reaction, 240 mg (0.82 mmol) triphosgene and 490 mg (7.6 mmol) NaN_3 were placed in a specially constructed brass reaction vessel (inner diameter 1 cm). The reaction vessel was placed in a stainless steel vacuum flask (shown in Supplementary materials). A volume of 0.3 mL polyethylene glycol was dripped onto the crystalline reagents, and the vacuum flask was quickly attached to a vacuum manifold, evacuated to less than 100 mTorr, and then sealed. After being sealed for ~ 16 h, any condensable gasses which had been generated were transferred to a second stainless steel flask held at liquid nitrogen temperature. In a final purification step, this second flask was cooled to dry ice-acetone temperature and placed under high vacuum for 5 min to remove any impurities more volatile than carbonyl diazide. The resulting product was analyzed for purity by gas phase IR spectroscopy, and the yield was estimated by measuring the pressure of the sample in a large gas manifold of known volume. A typical yield was 7.0 Torr liters of gas (0.38 mmol, 15%) and thus comparable to our previous method using ether as a solvent [8]. A benefit of this new method of synthesis is that the carbonyl diazide is generated and handled entirely in stainless steel vessels until it is introduced into the spectrometer, enhancing the safety of the procedure. Additionally, purification is straightforward, which is convenient and lessens the chance of losing the sample to an accidental explosive decomposition. The development of the expedited synthesis was motivated by the need to produce multiple samples for spectroscopic study. Samples much larger than the size just mentioned were not safe to handle, and because of the degradation of the sample in the spectrometer over a period of a few hours, samples of this size were only adequate for 1 or 2 days of experiments.

The spectrometer used is a millimeter-wave absorption instrument with a 3 m path length [19]. The cell is made of Pyrex pipe, and sheathed with coolant coils plumbed to an ultra-low temperature chiller for temperature control. The millimeter-wave radiation is generated by an $18\times$ multiplication (Virginia Diodes amplification multiplication chain) of the tone-burst modulated output from a 0–20 GHz frequency synthesizer (Agilent N5183A). Radiation passes into and out of the cell by way of Teflon lenses. At the far end of the cell, the signal is detected by a zero-bias diode detector (Virginia Diodes), the output of which is passed through a lock-in amplifier (Stanford Research Systems SR850 DSP) and back to a PC running a custom data acquisition program built in LabView 2010 [20]. The nominal range of operation for our detector

and amplifier multiplier chain is between 270 and 360 GHz, but strong lines at lower frequency (by as much as 30 GHz) can often be observed. The spectrometer cell was filled to a typical pressure of 6 mTorr and sealed, and data was collected for 2–3 h, yielding roughly 15 GHz of spectrum. The chamber was then evacuated and re-filled with fresh sample for the next segment. The final broadband spectra were the average of two scans, each with 10 data points per MHz. The complete spectra between 259 and 360 GHz were taken at both 213 K and 293 K, with select regions being observed at lower frequencies than 259 GHz. While 10 points per MHz yielded precise measurements, particularly dense or interesting regions of the spectra were taken at higher resolutions of up to 100 points per MHz. Spectra were analyzed and least-squares fits were performed using Kisiel's AABS, ASROT and ASFIT programs [21].

Calculated structures were optimized at CCSD(T)/ANO1 and CCSD(T)/cc-pVTZ levels of theory. Molecular geometries were optimized in CFOUR [22] using analytic gradients [23,24] with the frozen core approximation, GEO_CONV = 7, SCF_CONV = 10, and CC_CONV = 9. To determine the vibration–rotation interaction constants, the cubic and quartic force constants were calculated by numerical differentiation of the analytic second derivatives at displaced points following the approach of Stanton et al. [25,26]. Rotational constants, centrifugal distortion constants, and vibration–rotation interaction constants were calculated with CFOUR using the structure and force field results. Summaries of the outputs of each of the theoretical calculations and our analysis can be found in the Supplementary materials.

3. Theoretical energy separation and dipole moment components

The potential energy surface for carbonyl diazide is shown in Fig. 2. The lowest energy conformation has both azide groups *syn* to the carbonyl. An *anti-syn* conformer is predicted to be 1.8 kcal/mol higher energy (CCSD(T)/cc-pVTZ) [8,9], which results in it being an approximate factor of 10 times less abundant than the more stable conformer. The Boltzmann factor is about 1/20, but there is a weight factor of 2 because either azide group can be in the *anti* position. Facilitating our detection, this higher energy *anti-syn* conformer has a stronger calculated *b* component of the dipole moment, $\mu_b = 2.06$ D, than does the *syn-syn* conformer, $\mu_b = 0.68$ D. This predicted dipole moment ratio favors the signal intensity of the *anti-syn* conformer by about a factor of nine. There is a small factor in favor of the *syn-syn* form because of its somewhat smaller rotational partition function. Thus, the signal intensity is observed to be stronger for the more abundant species, but by a much smaller factor than would be expected from the energy difference alone. The *anti-syn* conformer also is predicted to have a much smaller μ_a dipole component (0.29 D), but the *a*-type transitions were too weak to be observable, even when we could accurately predict their frequencies.

4. Spectral data and analysis

The observed spectra were dense with detectable absorptions throughout our frequency range. The most intense absorptions in our observed spectra were due to the impurities HN_3 , HNCO , and CO , that resulted from unintended products of the synthesis or decomposition products of carbonyl diazide. These three light molecules have intrinsically intense transitions relative to carbonyl diazide because of their much smaller number of populated states, so even small concentrations produce very strong absorptions. Spectra were collected at both 293 K and 213 K. Due to the large number of low-lying vibrational states, including many combina-

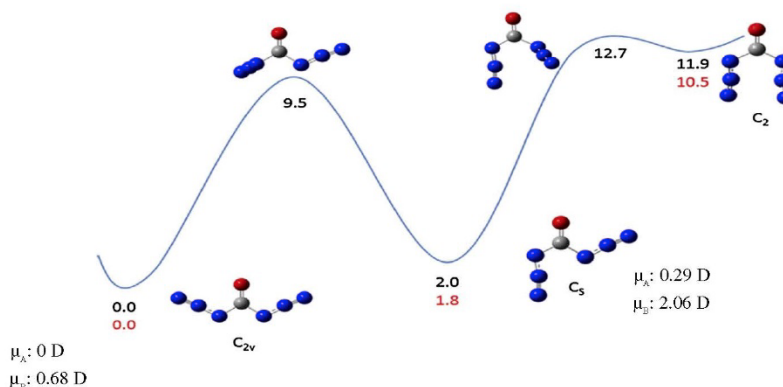


Fig. 2. Potential energy surface for carbonyl diazide. Relative energies (kcal/mol, including ZPVE) at CCSD/cc-pVDZ (upper, black) and CCSD(T)/cc-pVTZ (lower, red). The lowest energy *syn-syn* conformer and the next highest *anti-syn* conformer are observed in this work. (For interpretation of the references to color in this figure legend, the reader is referred to the web version of this article.)

tions and overtones, the high temperature spectrum is considerably more congested with excited state lines than the low temperature spectrum. Less than 3% of the *syn-syn* molecules are in the ground vibrational state at room temperature. This fraction increases to 8% at 213 K. The lowest lying vibrational satellites are also more intense at 213 K than at 293 K. As temperatures are reduced below 213 K, carbonyl diazide begins to condense. Due to these considerations, 213 K was used for our final measurements for the ground and excited vibrational states of the *syn-syn* conformer. The spectrum at 293 K, however, was used for assigning the spectrum of the higher-energy *anti-syn* conformer.

For the ground vibrational state of the *syn-syn* conformer, a very near prolate asymmetric top, the most apparent spectral features are the Q-branch series with fixed values of $K_{prolate}$, which have series origins occurring at roughly $(2K_{prolate} + 1)(A - (B + C)/2)$.

As seen in Fig. 3, the band origins are highly spectrally congested, and generally, the first few dozen lines of the series could not be sufficiently resolved to be independently measured. In the $K_{prolate}$ 17–18 series shown in Fig. 3, the region between 341 058 and 341 081 MHz contains $J = 19 - J = 54$, and most of these lines were excluded from the least-squares fitting. Like the other similar series, the lowest J lines increase in frequency as J increases, then turn towards lower frequency with further increase, forming a readily visible band head feature at the turn-around. Emerging from the congested band head regions are series of easily measured lines which gradually spread out as the lines progress to lower frequencies and higher J values. Initial least-squares fitting the Q-branch series, which gives the differences $A - B$ and $B - C$, along with the low inertial defect planarity condition, provided a basis for readily assigning the R-branch transitions.

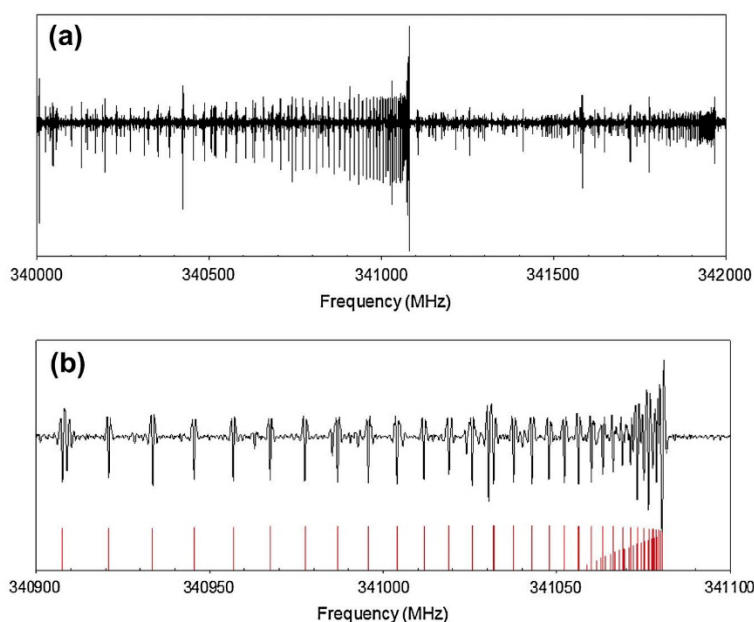


Fig. 3. (a) A 2 GHz region of the spectrum for carbonyl diazide at 213 K. The band starting at 241 080 MHz is the $K_{prolate}$ 17–18 Q-branch for the ground state of the *syn-syn* conformer. At 341 960 MHz, the $K_{prolate}$ 18–19 Q-branch series for $2\nu_{12}$ can be seen. (b) An expansion ($10\times$) of the central portion of this spectral region clearly shows the start of the ground-state Q-branch series. The stick spectrum more clearly shows the congestion in the band head region where the series reverses direction.

The R-branch transitions exist as series of transitions with the same $K_{prolate}$ values and increasing J values with an approximate separation of $B+C$ between successive lines. For the *syn-syn* conformer in its ground vibrational state, a total of 1105 b-type transitions were observed, consisting of 628 Q-branch transitions from 6 different $K_{prolate}$ series and 477 R-branch transitions from 8 different $K_{prolate}$ series. As seen in Table 1, all of these transitions were fit to experimental accuracy ($\sigma = 0.038$ MHz) with an S-reduced, representation I^r , centrifugal distortion Hamiltonian with all five 4th order constants and the four diagonal 6th order constants. The very small observed inertial defect confirms that this molecule is planar. The complete fitting output files of this and the other cases given below, including all measured frequencies, residuals, correlation matrices, etc., are available in the Supplemental materials. Also given in Table 1 are the results of our coupled-cluster calculation (ANO1 basis set) for the rotational constants and 4th order centrifugal distortion constants of this conformer. It can be seen that these theoretical predictions are in excellent agreement with the experimental results.

With an excellent fit for the ground vibrational state of the *syn-syn* conformer in hand, along with the theoretical predictions of vibration-rotation corrections, it was possible to assign the transitions for several excited vibrational states of the *syn-syn* conformer. These excited vibrational states have distinctive Q-branch series with band heads quite similar to those already described for the ground state. The $K_{prolate}$ 18–19 Q-branch series band head for the $2\nu_{12}$ state is readily apparent at 341 960 MHz in Fig. 3(a). Also, in a fashion similar to the ground state, the R-branch series for the excited vibrational states span a wide region of the spectrum, with analogous separations of approximately $B+C$. Many transitions for states ν_{12} , ν_7 , ν_9 and $2\nu_{12}$ were identified, measured, and least-squares fit. As shown in Fig. 4, ν_{12} is a B1 symmetric out-of-plane twisting motion of the azide groups. Vibrational mode ν_7 is an A1 symmetric in-plane bending of the azide substituents. Vibrational mode ν_9 is an A2 asymmetric out-of-plane twisting movement of the azide substituents. As an overtone vibrational mode, $2\nu_{12}$ has A1 symmetry.

Unlike the ground state case, the incorporation of some 8th order centrifugal distortion terms in the Hamiltonian was necessary in order to acquire a satisfactory least-squares fit of these vibrational satellites. The need for these higher order terms likely goes hand-in-hand with the large inertial defects accompanying these vibrational modes (see below), both attributable to the low frequency, large amplitude, nature of these bending motions of the two azide groups. Vibrational states ν_7 , ν_9 , and $2\nu_{12}$ all show clear

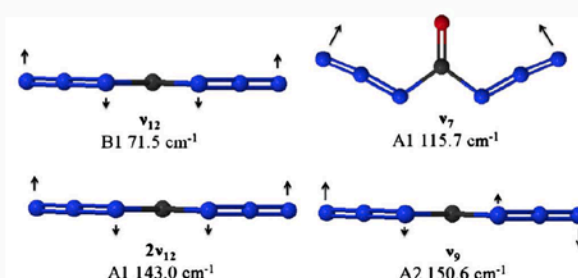


Fig. 4. Motions for the observed excited vibrational states for the *syn-syn* conformation of carbonyl diazide. Excitation energies are calculated at the CCSD(T)/ANO1 level of theory.

signs of what is presumed to be Coriolis perturbation in two of their Q-branch series. For ν_7 and $2\nu_{12}$ the series $K_{prolate}$ 16–17 and $K_{prolate}$ 17–18 fit poorly into rigid rotor models, as do the series for $K_{prolate}$ 13–14 and 14–15 for ν_9 . The obvious implication is that the perturbed energy levels are the $K_{prolate} = 17$ states for ν_7 and $2\nu_{12}$ and the $K_{prolate} = 14$ states for ν_9 . The detailed assignment and fitting of these strongly perturbed transitions is incomplete but in progress. All of these transitions have been omitted from the data sets used for the rotational/centrifugal distortion fits. The results of the fits for these three vibrational states are summarized in Table 2. In the case of the lowest-energy vibrational state (ν_{12}), however, it was possible to include all the measured transitions in the fit summarized in Table 2. As can be seen in Table 2, a fit to within near experimental error accuracy is obtained for a quite large data set for the ν_{12} excited vibrational state (after inclusion of some 8th order centrifugal distortion constants). In the ν_7 state spectrum we were able to assign 56 R-branch transitions where the asymmetry splitting was resolved, but when these were included in the fit the high- J , Q-branch lines show some systematic residuals and the standard deviation of the residuals σ is greater than the experimental error level (Table 2). If only the un-split R-branch lines and the non- $K_{prolate} = 17$ Q-branch lines are included, σ drops by a factor of two. In the cases of ν_9 and $2\nu_{12}$ we were not able to assign the weak split R-branch lines, because of the dense background spectrum, but if they could be measured and included in the fits, a similar increase in σ might be expected. Different combinations of centrifugal distortion constants were required to achieve the fits reported in Table 2, and only the D_J constant seems to be relatively invariant to vibrational state. In Table 3

Table 1

Experimental and calculated constants for the two lowest energy conformations of carbonyl diazide. Calculations are at the CCSD(T)/ANO1 level of theory, and all constants are presented in the S-reduced I^r representation.

	<i>syn-syn</i>		<i>anti-syn</i>	
	Experimental	CCSD(T)/ANO1	Experimental	CCSD(T)/ANO1
A (MHz)	10807.32121(80)	10758.5	4860.3329(15)	4844.2
B (MHz)	1101.93922(32)	1100.0	1448.9307(80)	1446.9
C (MHz)	999.95107(39)	997.9	1115.7777(50)	1114.1
D_J (kHz)	0.076261(36)	0.0748	0.19588(32)	0.191
D_{JK} (kHz)	-1.19632(16)	-1.17	-1.2477(18)	-1.18
D_K (kHz)	19.7585(40)	18.89	11.9279(28)	11.47
d_1 (kHz)	-0.010738(34)	-0.0108	-0.0670(23)	-0.0659
d_2 (kHz)	-0.000602(18)	-0.00057	-0.0090(30)	-0.00529
H_J (Hz)	0.0000469(31)			
H_{JK} (Hz)	-0.002860(17)			
H_{KJ} (Hz)	0.03728(43)		-0.01055(44)	
H_K (Hz)	-0.1393(71)		0.06943(82)	
σ (MHz)	0.038		0.044	
Δ_I (amu Å ²)	0.01415	0.0322	0.1640	0.0103
N lines	1105		786	

Table 2

Experimental constants for the four lowest-energy vibrational satellites of the *syn-syn* conformer of carbonyl diazide. All constants are presented in the S-reduced I^r representation.

	ν_{12}	ν_7	ν_9	$2\nu_{12}$
E (cm ⁻¹) ^a	71.5	115.7	150.6	143.0
A (MHz)	10515.8293(18)	11083.483(11)	10687.5090(26)	10245.6949(37)
B (MHz)	1102.30411(87)	1102.4041(57)	1102.3112(30)	1102.5814(33)
C (MHz)	1001.5272(11)	1000.3624(70)	1000.5791(35)	1003.1971(33)
D_j (kHz)	0.077850(65)	0.07634(39)	0.07586(20)	0.07675(33)
D_{jk} (kHz)	-0.90795(64)	-1.2761(66)	-1.2848(21)	-0.5615(24)
D_k (kHz)	-42.116(12)	82.166(97)	9.075(13)	-87.948(27)
d_1 (kHz)	-0.01219(14)	0.0176(20)	-0.0449(19)	0.0
d_2 (kHz)	0.00305(35)	0.0296(56)	0.137(10)	0.0
H_j (Hz)	0.0000479(62)	0.000520(31)	0.000680(46)	-0.000368(81)
H_{jk} (Hz)	-0.002216(37)	-0.00531(87)	-0.01184(93)	0.00096(14)
H_{jq} (Hz)	0.1716(21)	0.418(32)	-0.0236(97)	0.5292(77)
H_k (Hz)	-24.515(41)	21.82(40)	-1.792(22)	-36.641(89)
h_1 (Hz)	0.0000336 (67)	-0.00655(19)	-0.00270(19)	-0.000692(31)
h_2 (Hz)	0.0	0.01387(77)	0.0	0.0
h_3 (Hz)	-0.000123(18)	-0.030482(36)	0.0	0.00340(35)
L_j (mHz)	0.0	0.0	0.0	0.0000233(67)
L_{jk} (mHz)	0.0	0.0	-0.001418(62)	-0.0000134(88)
L_{jk} (mHz)	0.0	-0.0118(15)	0.0226(16)	0.0
L_{jq} (mHz)	-0.0673 (25)	-0.794(55)	0.224(16)	-0.4258(84)
L_k (mHz)	7.967 (48)	-4.67(61)	0.0	11.06(10)
σ (MHz)	0.040	0.109	0.046	0.056
Δ_I (amu Å ²)	-1.9256	1.1649	-0.6725	-3.9174
N lines	1119	834	672	768

^a CCSD(T)/ANO1.

Table 3

Comparison of calculated and experimental vibration-rotation corrections for carbonyl diazide.

		α_A (MHz)	α_B (MHz)	α_C (MHz)	Δ_I (amu Å ²)
ν_{12}	Experimental	-291.492	0.36489	1.57613	-1.9256
	CCSD(T)/ANO1	-263.41	-2.15	-0.36	-1.86
ν_7	Experimental	276.162	0.4648	0.4113	1.1649
	CCSD(T)/ANO1	270.95	0.67	0.16	1.35
ν_9	Experimental	-119.812	0.37198	0.62803	-0.6725
	CCSD(T)/ANO1	-115.54	0.29	0.70	-0.72
$2\nu_{12}$	Experimental	561.626	0.64218	3.24603	-3.9174
	CCSD(T)/ANO1	-526.82	-4.3	-0.72	-3.8147
	$2 \times$ (Experimental ν_{12})	582.984	0.72978	3.15226	-3.9369

the vibration-rotation interaction constants and inertial defects for all four states from the experimental rotational constants and the coupled cluster calculations are compared. For ν_7 and ν_9 the agreement is reasonable, but the α_A and α_B values are in quite poor agreement in the case of ν_{12} . The α values and inertial defects for $2\nu_{12}$ are, however, very close to two times the values of the same constants in the fundamental state ν_{12} (see Table 3), which was very helpful in assigning the spectra of the overtone. The very large negative inertial defects observed for the out-of-plane modes and the large positive defects for the in-plane mode are very well predicted by the theoretical calculations and are consistent with expectation for these low frequency bending vibrations [27].

Identifying five vibrational states for the *syn-syn* conformer explained many of the stronger lines in our spectrum, making it feasible to search for transitions from the *anti-syn* conformer. Predictions for the *b*-type transitions showed widely spaced R-branch series spanning the length of our spectral range. It proved possible to find and assign these lines. The Q-branch series predicted in our spectral region all had $K_{prolate}$ values greater than 38, and they (and the non-degenerate R-branch transitions) were not intense enough for us to distinguish them from the great many unassigned lines (presumably of higher vibrationally excited states). The spectroscopic constants from the fit of the *anti-syn* conformer are given in Table 1, along with the predictions of the

same constants from coupled-cluster theory. As for the other conformer, the agreement of the rotational constants and 4th order centrifugal distortion constants is excellent (somewhat less so for d_2), and the mean square of the residuals is near the experimental error limit (Table 1). In spite of this low value of σ , the determination of the rotational constants is not as accurate as in the fit of the *syn-syn* form. The lack of transitions where the asymmetry splitting is resolved and of Q-branch transitions in the data set is the origin of this problem, and the somewhat large unphysical inertial defect in Table 1 is symptomatic of it. The inertial defect from the coupled-cluster calculation, however, is typical of what would be expected for a planar molecule.

With the spectra of both conformers well fit, it was possible to estimate their relative energies based on peak intensities. We used a particularly clean segment of our 293 K spectrum between 310 and 330 GHz. To compensate for the gradual decrease in intensity during the course of a sample fill, intensities were compared in a matched pair fashion. Each well-measured *syn-syn* line was fit to a Gaussian line shape and compared with the nearest well-measured *anti-syn* line at higher frequency and at lower frequency. The integrated intensity for each line was normalized with its computed integrated intensity (corrected for the factor of two in favor of the *anti-syn* discussed previously), and the ratio of the pair of normalized intensities was taken as the Boltzmann factor. In total,

118 of these pairs were used, a few outliers with ratios more than 3 standard deviations away from the mean having been dropped from the set. These 118 pairs gave an average Boltzmann factor of 0.0515 , yielding an energy difference of 2.4 ± 0.6 kcal/mol, which is consistent with the *ab initio* values presented in Fig. 2.

Acknowledgments

We gratefully acknowledge funding from the National Science Foundation for support of this project (CHE-1011959) and for support of shared Departmental computing resources (CHE-0840494). We thank Dr. Desiree M. Bates and Paul B. McGuire for their continued assistance and helpful discussions regarding the computing resources.

Appendix A. Supplementary material

Supplementary data for this article are available on ScienceDirect (www.sciencedirect.com) and as part of the Ohio State University Molecular Spectroscopy Archives (http://library.osu.edu/sites/msa/jmsa_hp.htm). Supplementary data associated with this article can be found, in the online version, at <http://dx.doi.org/10.1016/j.jms.2013.11.001>.

References

- [1] W. Kesting, Ber. Dtsch. Chem. Ges. B 57B (1924) 1321–1324.
- [2] T. Curtius, A. Bertho, Ber. Dtsch. Chem. Ges. B 59B (1926) 565–589.
- [3] L.E. Chapman, R.F. Robbins, Chem. Ind. (Lond.) (1966) 1266–1267.
- [4] K. Banert, Y.-H. Joo, T. Rüffer, B. Walfort, H. Lang, Angew. Chem. Int. Ed. 46 (2007) 1168–1171.
- [5] T. Curtius, K. Heidenreich, J. Prakt. Chem. 52 (1895) 454–489.
- [6] X. Zeng, M. Gerken, H. Beckers, H. Willner, Inorg. Chem. 49 (2010) 9694–9699.
- [7] D.W. Ball, Comput. Theor. Chem. 965 (2011) 176–179.
- [8] A.M. Nolan, B.K. Amberger, B.J. Esselman, V.S. Thimmakondū, J.F. Stanton, R.C. Woods, R.J. McMahon, Inorg. Chem. 51 (2012) 9846–9851.
- [9] B. Napolion, J.D. Watts, M.-J. Huang, F.M. McFarland, E.E. McClendon, W.L. Walters, Q.L. Williams, Chem. Phys. Lett. 559 (2013) 18–25.
- [10] X. Zeng, H. Beckers, H. Willner, Angew. Chem. Int. Ed. 50 (2011) 482–485.
- [11] X. Zeng, H. Beckers, H. Willner, J.F. Stanton, Angew. Chem. Int. Ed. 50 (2011) 1720–1723.
- [12] Y.S. Kim, F. Zhang, R.I. Kaiser, Phys. Chem. Chem. Phys. 13 (2011) 15766–15773.
- [13] A. Perrin, X. Zeng, H. Beckers, H. Willner, J. Mol. Spectrosc. 269 (2011) 30–35.
- [14] X. Zeng, H. Beckers, H. Willner, J.F. Stanton, Eur. J. Inorg. Chem. (2012) 3403–3409.
- [15] J.M. Hollis, A.J. Remijan, P.R. Jewell, F.J. Lovas, Astrophys. J. 642 (2006) 933.
- [16] S. Bräse, K. Banert, Organic Azides: Syntheses and Applications, John Wiley & Sons Ltd., Chichester, 2010.
- [17] Prudent Practices in the Laboratory, Updated Version, National Academy Press, Washington, DC, 2011.
- [18] J. Chen, S.K. Spear, J.G. Huddleston, R.D. Rogers, Green Chem. 7 (2005) 64–82.
- [19] B.J. Esselman, Ph.D. Dissertation, University of Wisconsin-Madison, Madison, Wisconsin, 2012.
- [20] LabVIEW 2010, 10.0 (32-bit) ed., National Instruments, Austin, TX, 2010.
- [21] Z. Kisiel, PROSPE – Programs for ROTational SPEctroscopy, Warsaw. <http://info.ifpan.edu.pl/~kisiel/prospe.htm>.
- [22] J.F. Stanton, J. Gauss, M.E. Harding, P.G. Szalay, with contributions from A.A. Auer, R.J. Bartlett, U. Benedikt, C. Berger, D.E. Bernholdt, Y.J. Bomble, L. Cheng, O. Christiansen, M. Heckert, O. Heun, C. Huber, T.-C. Jagau, D. Jonsson, J. Jusélius, K. Klein, W.J. Lauderdale, D.A. Matthews, T. Metzroth, L.A. Mück, D.P. O'Neill, D.R. Price, E. Prochnow, C. Puzzarini, K. Ruud, F. Schiffmann, W. Schwalbach, S. Stopkowitz, A. Tajti, J. Vázquez, F. Wang, J.D. Watts and the integral packages MOLECULE (J. Almlöf and P.R. Taylor), PROPS (P.R. Taylor), ABACUS (T. Helgaker, H.J. Aa. Jensen, P. Jørgensen, and J. Olsen), and ECP routines by A. V. Mitin, C. van Wüllen. For the current version, see <http://www.cfour.de>.
- [23] G.E. Scuseria, J. Chem. Phys. 94 (1991) 442–447.
- [24] T.J. Lee, A.P. Rendell, J. Chem. Phys. 94 (1991) 6229–6236.
- [25] J.F. Stanton, C.L. Lopreore, J. Gauss, J. Chem. Phys. 108 (1998) 7190–7196.
- [26] I.M. Mills, in: K.N. Rao, C.W. Mathews (Eds.), Molecular Spectroscopy: Modern Research, Academic, New York, 1972, pp. 115–140.
- [27] J.K.G. Watson, J. Chem. Phys. 98 (1993) 5302–5309.

Appendix D**Precise Equilibrium Structure Determination of Hydrazoic Acid (HN₃) by Millimeter-wave Spectroscopy**

Brent K. Amberger
Brian J. Esselman
John F. Stanton
R. Claude Woods
Robert J. McMahon

The Journal of Chemical Physics, 2015, *143*, (pages not yet assigned)

Precise equilibrium structure determination of hydrazoic acid (HN₃) by millimeter-wave spectroscopy

Brent K. Amberger,¹ Brian J. Esselman,¹ John F. Stanton,² R. Claude Woods,¹ and Robert J. McMahon¹

¹Department of Chemistry, University of Wisconsin–Madison, Madison, Wisconsin 53706, USA

²Institute for Theoretical Chemistry, Department of Chemistry, The University of Texas–Austin, Austin, Texas 78712, USA

(Received 9 July 2015; accepted 17 August 2015; published online XX XX XXXX)

The millimeter-wave spectrum of hydrazoic acid (HN₃) was analyzed in the frequency region of 235–450 GHz. Transitions from a total of 14 isotopologues were observed and fit using the A-reduced or S-reduced Hamiltonian. Coupled-cluster calculations were performed to obtain a theoretical geometry, as well as rotation-vibration interaction corrections. These calculated vibration-rotation correction terms were applied to the experimental rotational constants to obtain mixed theoretical/experimental equilibrium rotational constants (A_e , B_e , and C_e). These equilibrium rotational constants were then used to obtain an equilibrium (R_e) structure using a least-squares fitting routine. The R_e structural parameters are consistent with a previously published R_s structure, largely falling within the uncertainty limits of that R_s structure. The present R_e geometric parameters of HN₃ are determined with exceptionally high accuracy, as a consequence of the large number of isotopologues measured experimentally and the sophisticated theoretical treatment (coupled-cluster single double triple (CCSD(T))/ANO2) of the vibration-rotation interactions. The R_e structure exhibits remarkable agreement with the CCSD(T)/cc-pCVSZ predicted structure, validating both the accuracy of the *ab initio* method and the claimed uncertainties of the theoretical/experimental structure determination. © 2015 AIP Publishing LLC. [<http://dx.doi.org/10.1063/1.4929792>]

INTRODUCTION

Hydrazoic acid (HN₃) has been of fundamental interest since the earliest days of spectroscopy. In 1890, hydrazoic acid was reported by Curtius; he noted the molecule to be both highly toxic and extremely explosive.¹ At the time, the nitrogen atoms of HN₃ were thought to be arranged in a three-membered ring. In 1935, Herzberg used the overall shape of the partially resolved near-infrared overtone bands to conclude that the nitrogen backbone was linear, with the hydrogen atom bound either to the central nitrogen atom or to one of the terminal nitrogen atoms.² The H–N–N–N connectivity was firmly established by IR spectroscopy in 1940.³ The authors determined a bent H–N–N angle of 110.9° and assumed a 180° N–N–N angle. An electron diffraction study in 1942⁴ found nitrogen-nitrogen bond distances in agreement with those in the IR study. Amble and Dailey synthesized all four singly isotopically labeled HN₃ isotopomers, found the corresponding values of ($B + C$) by microwave spectroscopy, and published the first substitution structure in 1950.⁵ Winnewisser and co-workers obtained microwave and millimeter-wave spectra for H¹⁴N₃, D¹⁴N₃, H¹⁵NNN, and HNN¹⁵N and obtained a substitution structure.^{6–8} Their work provided good values for many of the geometric parameters, but ambiguity remained in the position of the central nitrogen atom because the HN¹⁵NN isotopomer was not observed. Winnewisser used the center of mass condition to estimate the position of the central nitrogen and published an R_s structure with an N–N–N angle of 171.3°.⁹ High-level calculations have consistently supported this bent

structure.^{10–12} In the 1980s and 1990s, the rovibrational spectra for HN₃ and DN₃ were thoroughly studied by high resolution FTIR,^{13–25} but the structure was not significantly refined. Evers *et al.* obtained the crystal structure of hydrazoic acid in 2011.²⁶ Fundamental interest in the molecular geometry of HN₃ continues with Toyota *et al.* discussing the likely origins of the N–N–N angle as recently as 2013.¹²

Precise structural knowledge of hydrazoic acid is valuable in further understanding the family of tetratomic, 16 valence electron molecules, which includes HNCO, its isomers, and their heavier-element analogues. In this family, molecular geometries range from linear through quasilinear to manifestly non-linear.^{27–29} In comparative studies probing the origins of these geometries, the relative electronegativity of atoms in the backbone is an important variable. Hydrazoic acid is unique in this family in that all non-hydrogen atoms are identical. For this reason, HN₃ serves as a useful reference for untangling the subtle contributions, which give rise to varying geometries in this family.

In the present work, we observed transitions for numerous isotopologues of hydrazoic acid. Samples enriched with ¹⁵N at the first or third nitrogen atom were prepared for both HN₃ and DN₃. Transitions for additional isotopologues containing a ¹⁵N atom at natural abundance were also measured. In all, we present spectroscopic fits with well-determined rotational constants for 14 (of 16 possible) isotopologues of hydrazoic acid involving H/D and ¹⁴N/¹⁵N. The isotopologues absent from our dataset are the triply ¹⁵N substituted H¹⁵N₃ and D¹⁵N₃. Six of the studied isotopologues contain a ¹⁵N label on the central

nitrogen, which eliminates most ambiguity about its location within the molecule. We used these data for a highly redundant determination of the molecule's equilibrium structure.

A coupled-cluster single double triple (CCSD(T))/ANO2 optimized geometry was obtained and used in subsequent harmonic and anharmonic frequency calculations to estimate the quartic centrifugal distortion constants for each isotopologue and estimate the vibration-rotation interaction parameters for each isotopologue. An additional magnetic property calculation was performed to estimate the electron mass contributions to rotational constants. The vibration-rotation interaction constants (α_i) were used for the equilibrium structure determination and provided some guidance in the location of the vibrationally excited state spectra of hydrazoic acid and deuterated hydrazoic acid.

We observed pure-rotational transitions for seven vibrationally excited states (four fundamentals, two overtones, and one combination) of both hydrazoic acid and deuterated hydrazoic acid (all ^{14}N) — the most energetic of these being at $\sim 1267\text{ cm}^{-1}$ (1197 cm^{-1} for DN_3).^{23,24} A complex web of perturbations exists between these states, to the point where none of them can be completely analyzed using a single-state fit. The ground vibrational state is largely isolated from these perturbations, exhibiting only a centrifugal distortion interaction with the lowest energy excited vibrational state (537 cm^{-1} for HN_3 and 496 cm^{-1} for DN_3).^{18,19} In the current analysis, we used only ground-state transitions that are unperturbed or only slightly perturbed; this allows the use of single-state fits. We excluded significantly perturbed lines even where they are well understood (for H^{14}N_3 and D^{14}N_3) for better continuity with our fits for isotopologues where analysis of these perturbations would be completely impractical. A detailed analysis of the higher vibrational and rotational states of HN_3 and DN_3 will be published separately.

EXPERIMENTAL METHODS

Hydrazoic acid was prepared by adding sodium azide (NaN_3) to water which had been acidified with phosphorus pentoxide (P_2O_5). A typical batch used 15 ml water, 0.5 g P_2O_5 , and 0.1 g NaN_3 . *Reagent amounts were kept small to minimize the hazards of working with these potentially explosive materials.* The reagents were combined in a vacuum line connected directly to the microwave spectrometer, and for 1 minute after combination, all escaping condensable vapors were trapped and stored in a thick-walled glass trap at $-78\text{ }^\circ\text{C}$. Under these conditions, water in the trap remained condensed, while hydrazoic acid had a conveniently large apparent vapor pressure of $\sim 300\text{ mTorr}$ and could be introduced into the spectrometer chamber as desired. After the process was optimized, our millimeter-wave spectra appeared to be very pure. No yields were calculated, but a sample of this scale proved sufficient for several days of data collection. Samples of DN_3 were prepared analogously using D_2O . In our setup, the syntheses of DN_3 contained large amounts of HN_3 as an impurity. Rigorously rinsing the reaction flasks with D_2O , using fresh reagents, and attempting to saturate the manifold and the spectrometer chamber with D_2O vapors prior to reaction still resulted in a mixture of DN_3 and HN_3 . Fortunately, this mixture proved adequate for

assigning the spectra of HN_3 , DN_3 , and the six isotopologues containing a single ^{15}N atom occurring at natural abundance. To enrich the ^{15}N content, isotopically labeled sodium azide (Na^{15}NNN), purchased from Cambridge Isotope Laboratories, was used in place of Na^{14}N_3 . This gave access to milligrams or tens of milligrams of H^{15}NNN , HNN^{15}N , D^{15}NNN , and DNN^{15}N . Due to the presence of naturally occurring ^{15}N , we were also able to observe all six doubly ^{15}N labeled isotopologues.

The millimeter-wave spectrometer used has been described previously.^{30,31} It has a nominal range of 270–360 GHz, but strong lines can be observed at frequencies as low as 230 GHz. Using a spurious $30\times$ harmonic in the $18\times$ amplification multiplication chain, we can occasionally observe lines significantly above 360 GHz. Additionally, for some of our experiments, we were able to utilize a higher range frequency synthesizer (Agilent MXG Analog Signal Generator N5183B) which gave continuous usable spectra up to $\sim 370\text{ GHz}$. The chamber was filled with roughly 10 mTorr of sample, and refreshed every 1–2 h. Spectra were collected at room temperature. For each sample, we measured a 100 GHz broadband spectrum, followed by targeted searches for very weak transitions and for transitions lying outside of our nominal operational range. Spectral viewing and analysis were done with Kisiel's AABS³² package and Pickett's SPFIT/SPCAT.³³ Kisiel's PIFORM³² was used to format the SPFIT output files and give proper standard errors for spectroscopic parameters. These least-squares fitting output files are deposited in the supplementary material.³⁴

COMPUTATIONAL METHODS

All geometry optimizations and frequency calculations were carried out in CFOUR 2.00.³⁵ CCSD(T)/ANO2³⁶ optimized geometries were obtained using analytic gradients^{37,38} with the frozen core approximation. To determine the vibration-rotation interaction constants (α_i 's), the cubic force constants were calculated by numerical differentiation of the analytic second derivatives at displaced points following the approach of Stanton *et al.*^{39,40} The VPT2 anharmonic frequency output allowed for a convenient calculation of the quartic distortion constants and the vibration-rotation interaction for each of the isotopologues. A very high level calculation of the equilibrium geometry was also completed at the all-electron CCSD(T) level with the cc-pCV5Z basis set. Output summary files of each of the theoretical calculations and our analysis can be found in the supplementary material.³⁴

Analysis of rotational spectra

The dipole in HN_3 is roughly parallel to the H–N bond, and thus not along any of the principal axes, resulting in strong *a*-type and *b*-type transitions ($\mu_a = 0.837\text{ D}$ and $\mu_b = 1.48\text{ D}$).^{7,41} The predominant features in all of the spectra for hydrazoic acid are *a*-type R-branches which follow a typical pattern for near-linear molecules shown in Fig. 1.

For a series with a given $J + 1 \leftarrow J$, transitions progress towards lower frequency with increasing K_{prolate} value. The $K_{\text{prolate}} = 1$ lines are widely split by several gigahertz, the

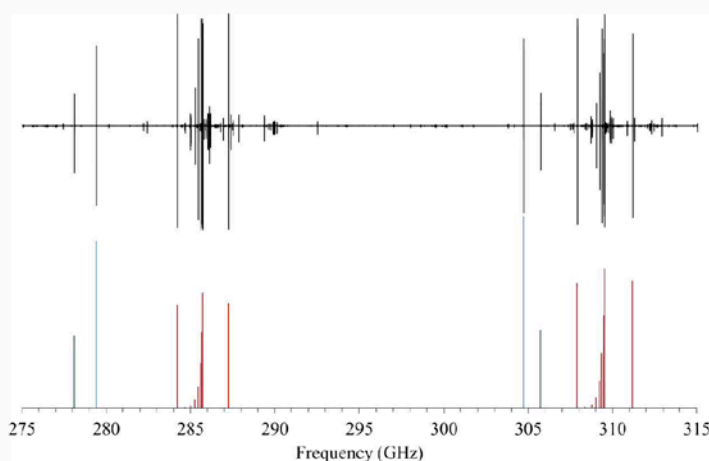


FIG. 1. Experimental (upper) and predicted (lower) spectrum of HN_3 from 275 GHz to 315 GHz. Red lines represent the a -type R-branches with $J_{\text{upper}} = 12$ and 13. The blue transitions belong to the b -type $K_{\text{prolate}} = 1(-) \leftarrow 0$ P-branch with J_{upper} values of 10 and 11 which progress to lower frequency. The green series is a continuation of the P-branch re-entering the spectrum with J values 34 and 35.

$K_{\text{prolate}} = 2$ lines are split by tens or hundreds of megahertz, and the $K_{\text{prolate}} = 3$ lines are typically split by less than a megahertz. Transitions for $K_{\text{prolate}} = 4$ and higher appear degenerate on our instrument. For DN_3 , the pattern in a -type R-branch transitions is roughly the same as for HN_3 , but there is more of a “turn around” in the series, with the $K_{\text{prolate}} = 0$ line generally appearing at lower frequencies than the $K_{\text{prolate}} = 2$ and $K_{\text{prolate}} = 3$ lines.

For b -type transitions, HN_3 has a series of P-branch $K_{\text{prolate}} = 1 \leftarrow 0$ transitions which run through our spectrometer range from high to low frequency ($J_{\text{upper}} = 9$ -13). Outside of our frequency range, the $K_{\text{prolate}} = 0$ states surpass the nearby $K_{\text{prolate}} = 1$ states in energy, and thus the series re-enters our spectra as R-branch $K_{\text{prolate}} = 0 \leftarrow 1$ transitions which progress to high frequency ($J_{\text{upper}} = 33$ -36). There is also a series of P-branch $K_{\text{prolate}} = 2 \leftarrow 1$ transitions ($J_{\text{upper}} = 52$ -55). Finding these transitions proved critical in determining A and D_K (or A and Δ_K) independently of one another.

HN_3 and DN_3 have somewhat dissimilar b -type spectra in our frequency range. This is the result of the hydrogen atom being the only mass appreciably off the a -axis, resulting in a substantial difference in the A constant between the two isotopologues (611 GHz for HN_3 and 345 GHz for DN_3). Hence, we observed more b -type transitions in the frequency range of our spectrometer for DN_3 than for HN_3 . Most notably, a b -type Q-branch occurs (starting at 334 GHz) in our spectral range for DN_3 , while the same branch is too high in frequency (predicted to start at 599 GHz) for us to observe for HN_3 .

We fit our spectral data using both the A-reduced and the S-reduced Hamiltonians in the Γ^1 representation for each isotopologue. The choice of A- or S-reduction did not affect the quality of the fits; the spectroscopic constants obtained by S-reduction, when converted into the A-reduction,⁴² were nearly identical to those obtained in our fit using the A-reduced Hamiltonian. As further proof of the quality of the A-reduction or S-reduction least squares fits, the rotational constants ($B_0^{(A)}$ or $B_0^{(S)}$) were converted into nearly identical determinable constants (B_0'') using the experimentally determined quartic distortion constants (see below). These two analyses of the constants can be found in the supplementary material.³⁴

For higher values of K_{prolate} , the energy levels are perturbed by a centrifugal distortion interaction with the first

vibrationally excited state.^{18,19} For HN_3 , we found evidence of slight perturbation in the $K_{\text{prolate}} = 4$ transitions, with the perturbation becoming progressively larger at higher K_{prolate} values. Empirically, we found that including L_{KKJ} in our fits compensates for much of the perturbation and allows us to include a -type transitions up to $K_{\text{prolate}} = 5$ in single-state fits for HN_3 with satisfactory values of σ , although the values of L_{KKJ} are unphysically large. For DN_3 , we were able to include transitions up to $K_{\text{prolate}} = 7$.

Transitions with $K_{\text{prolate}} = 1 \leftarrow 2$ are required in order to independently determine A and D_K . More of these transitions occur in our frequency region for DN_3 than for HN_3 , and they have greater intensity in DN_3 . We were unable to positively identify any $K_{\text{prolate}} = 1 \leftarrow 2$ transitions in the four HN_3 isotopologues requiring a ^{15}N atom at natural abundance. In our fits for HN^{15}NN , $\text{H}^{15}\text{N}^{15}\text{NN}$, $\text{H}^{15}\text{NN}^{15}\text{N}$, and $\text{HN}^{15}\text{N}^{15}\text{N}$, we fixed D_K to reasonable values estimated based on ratios between the experimentally determined values of D_K for the other ten isotopologues.

Our spectroscopic constants from the fits for HN_3 and DN_3 are presented in Tables I and II, alongside our CCSD(T)/ANO2 and CCSD(T)/cc-pCV5Z values for the rotational constants and quartic centrifugal distortion terms. In these tables, our data are presented in the A-reduction for easier comparison to previously reported values. Previously reported values for the rotational constants, determined by either microwave/millimeter-wave spectroscopy^{7,8} or far-IR spectroscopy,^{16,17} are presented side-by-side with our values. Because independent determination of A and Δ_K is not possible without adequate diversity of observed b -type transitions, the value of $A - \Delta_K$ is also presented in these tables. The apparent discrepancy between our A value for HN_3 in Table I and A from Ref. 7 is largely the result of a fixed value for Δ_K as the values of $A - \Delta_K$ match well. Discrepancies in the higher order distortion terms are likely due in part to different subsets of these terms being used. Our choice of higher order distortion terms was based on which ones were beneficial to the fit and were determined to a value greater than their standard error for all isotopologues. With these caveats in mind, the general agreement is very good between the current work and the previous works. The rotational constants determined at the CCSD(T)/cc-pCVZ level were notably closer to our experimentally determined constants than were

TABLE I. Rotational constants for HN_3 from *ab initio* calculations, experimental spectroscopic data, and the previous literature.

H^{14}N_3	CCSD(T)/ANO2 ^a	CCSD(T)/cc-pCV5Z ^a	This work Millimeter-wave	Bendtsen and Nicolaisen Far-IR ¹⁶	Bendtsen and Winnewisser Microwave/millimeter ⁷
A_0 (MHz)	605 073	610 794	611 034.132(29)	611 026.8(21)	610 996.2(60)
B_0 (MHz)	11 989	12 054	12 034.983 8(62)	12 034.78(27)	12 034.146 5(50)
C_0 (MHz)	11 736	11 800	11 780.671 3(66)	11 780.49(27)	11 781.451 2(50)
Δ_J (kHz)	4.754		4.917 4(10)	5.01(15)	4.673(35)
Δ_{JK} (kHz)	765.8		797.98(15)	789.1(27)	791.185 8(11)
Δ_K (kHz)	217 900		267 559(27)	268 464(180)	[230 000] ⁴³
δ_J (kHz)	0.078 06		0.091 18(22)	0.080 9(90)	0.088 8(27)
δ_K (kHz)	313.8		403.9(31)	104.9(90)	[0]
Φ_J (Hz)			[0]	0.006(45)	0.088(36)
Φ_{JK} (Hz)			1.19(10)	4.49(12)	40.6(8.6)
Φ_{KJ} (Hz)			255(14)	-1 199(60)	-0.001 210(35)
Φ_K (Hz)			[0]	383 734(6000)	[0]
L_{KKJ} (mHz)			-40 010(400)	[0]	[0]
Δ_i ($\text{u } \text{\AA}^2$)	0.075 2	0.074 3	0.079 415 223	0.079 354 396	0.073 599 658
$A - \Delta_K$ (MHz)	604 855		610 766.6	610 758.3	610 764.2

^aThe B_e values from the CCSD(T)/ANO2 and CCSD(T)/cc-pCV5Z calculations have been converted to B_0 values from the CCSD(T)/ANO2 vibration rotation corrections provided by the anharmonic frequency calculation.

the CCSD(T)/ANO2 values. The 4th order centrifugal distortion constants determined by the CCSD(T)/ANO2 calculation were in good enough agreement with experimental values to be helpful in our assignments.

The ^{15}N -containing isotopologues exhibit spectra very similar to those for H^{14}N_3 and D^{14}N_3 . Transitions for the four synthetically ^{15}N -enriched species (H^{15}NNN , HNN^{15}N , D^{15}NNN , and DNN^{15}N) were observed at comparable intensity to their parent molecules. Eight isotopologues were observed for molecules containing one ^{15}N atom at natural abundance. Transitions for these species were intense enough to observe $K_{prolate} = 0$ through $K_{prolate} = 5$ and most of the b -type features. Because of the proximity of the center nitrogen atom to the center of mass, transitions for the six observed isotopologues with a label on the central nitrogen atom appeared as satellites to the corresponding transitions of their parent isotopologue. These isotopic satellites were particularly

close to their parent transitions for the a -type R-branches. This proximity often led to the rapid assignment of transitions using Loomis-Wood type plots^{32,45} centered on transitions of the parent isotopologues. In the case of $\text{HN}^{15}\text{N}^{15}\text{N}$, however, transitions were sometimes too close to the significantly stronger transitions of HNN^{15}N to be observed or measured. As a result, our set of measured transitions for $\text{HN}^{15}\text{N}^{15}\text{N}$ is the least complete, missing half of the a -type $K_{prolate} = 1$ transitions and all $K_{prolate} = 4$ and $K_{prolate} = 5$ transitions. With fewer observed transitions of $\text{HN}^{15}\text{N}^{15}\text{N}$, we chose to fix the value of L_{KKJ} in its least-squares fitting, and the values of H_{JK} and H_{KJ} do not closely match the values determined for the other HN_3 isotopologues. The rest of the fit parameters for $\text{HN}^{15}\text{N}^{15}\text{N}$ match nicely with expected values. Most importantly, the determinable constants (B'') and inertial defects for $\text{HN}^{15}\text{N}^{15}\text{N}$ with and without corrections for vibration-rotation interactions and electron mass were consistent with the other 13 isotopologues

TABLE II. Rotational constants for DN_3 from *ab initio* calculations, experimental spectroscopic data, and the previous literature.

D^{14}N_3	CCSD(T)/ANO2 ^a	CCSD(T)/cc-pCV5Z ^a	This work Millimeter-wave	Bendtsen and Nicolaisen Far IR ¹⁷	Bendtsen and Winnewisser Microwave/millimeter ⁸
A_0 (MHz)	340 873	344 046	344 746.613(17)	344 724.8(15)	344 746.589(64)
B_0 (MHz)	11 314	11 370	11 350.940 41(96)	11 351.55(24)	11 350.983(16)
C_0 (MHz)	10 927	10 984	10 964.825 71(45)	10 965.45(24)	10 964.755(15)
Δ_J (kHz)	4.135		4.314 94(72)	4.89(21)	4.281(16)
Δ_{JK} (kHz)	466.7		446.084(42)	435.9(21)	444.51(44)
Δ_K (kHz)	56 910		91 942.9(42)	91 227(30)	92 242(33)
δ_J (kHz)	0.1511		0.172 965(33)	0.171(15)	0.186 4(41)
δ_K (kHz)	263.9		338.82(28)	318(12)	365.1(77)
Φ_J (Hz)			[0]	0.060(60)	[0]
Φ_{JK} (Hz)			1.248(19)	2.7(1.2)	-3.4(1.1)
Φ_{KJ} (Hz)			-213.7(26)	-606(18)	-0.000 308(21)
Φ_K (Hz)			[0]	86 040(300)	[0.059] ⁴⁴
L_{KKJ} (mHz)			-3516.(42)	[0]	[0]
Δ_i ($\text{u } \text{\AA}^2$)	0.098 0	0.096 9	0.101 9	0.101 6	0.102 4
$A - \Delta_K$ (MHz)	340 816		344 654.7	344 633.6	344 654.3

^aThe B_e values of the rotational constants from the CCSD(T)/ANO2 and CCSD(T)/cc-pCV5Z calculations have been converted to B_0 values using the CCSD(T)/ANO2 vibration-rotation interactions from the anharmonic frequency calculation.

TABLE III. Spectroscopic parameters for isotopologues of HN₃ in the S-reduced Hamiltonian F representation.

	HN ₃	H ¹⁵ NNN	HN ¹⁵ NN	HNN ¹⁵ N	H ¹⁵ N ¹⁵ NN	H ¹⁵ NN ¹⁵ N	HN ¹⁵ N ¹⁵ N
A ₀ (MHz)	611 034.135(29)	605 576.892(35)	610 032.993(90)	610 977.569(30)	604 507.434(46)	605 510.183(32)	609 961.086(60)
B ₀ (MHz)	12 034.175 91(56)	11 667.543 36(74)	12 033.343 8(25)	11 641.775 20(65)	11 665.579 9(14)	11 282.358 89(93)	11 641.880 7(22)
C ₀ (MHz)	11 781.478 99(83)	11 427.856 1(10)	11 780.294 1(24)	11 405.079 97(91)	11 425.569 3(19)	11 058.038 4(12)	11 404.819 0(32)
D _J (kHz)	4.8749(11)	4.622 8(13)	4.872 8(27)	4.537 2(12)	4.620 8(38)	4.305 7(22)	4.539 3(51)
D _{JK} (kHz)	798.23(15)	769.00(17)	796.07(20)	752.43(15)	765.97(29)	724.80(20)	751.93(68)
D _K (kHz)	267 561(27)	263 929(34)	[265 241]	268 092(27)	[266 172]	[263 987]	[261 923]
d ₁ (kHz)	-0.091 20(22)	-0.083 97(26)	-0.087 4(35)	-0.082 47(23)	-0.084 05(79)	-0.074 73(49)	-0.076 8(20)
d ₂ (kHz)	-0.021 27(16)	-0.018 93(18)	-0.023 51(99)	-0.018 93(17)	-0.023 2(11)	-0.018 29(85)	-0.023 8(15)
H _{JK} (Hz)	0.88(10)	0.64(11)	0.77(31)	0.73(11)	0.73(40)	0.75(27)	5.5(14)
H _{KJ} (Hz)	256(14)	348(16)	320(18)	226(14)	363(25)	349(16)	106(37)
L _{KKJ} (mHz)	-40 010(399)	-35 790(439)	-43 930(501)	-39 040(388)	-38 040(662)	-35 580(462)	[-380 40]
Δ _i (u Å ²)	0.073 655	0.073 944	0.073 708	0.0737 62	0.074 028 3	0.074 040	0.073 790
N _{lines}	78	84	49	88	42	56	32
σ _{fit} (MHz)	0.032 213	0.040 708	0.029 478	0.036 615	0.036 002	0.030 417	0.043 468

(see Table V). The fits for the HN₃ isotopologues are presented in Table III. The fits for the DN₃ isotopologues are presented in Table IV.

STRUCTURE DETERMINATION

The structure of HN₃ was computed from the experimental rotational constants using several different methods. First, the rotational constants were corrected from the A- or S-reduced Hamiltonian constants ($B_0^{(A)}$ or $B_0^{(S)}$) to remove the impact of centrifugal distortion and obtain the determinable constants (B_0'') using Eqs. (1)–(6) below.⁴² The determinable constants for each isotopologue are presented in the supplementary material.³⁴ The average of the B_0'' values obtained from A-reduced or S-reduced Hamiltonian constants was used in any structural determinations,

$$A'' = A^{(A)} + 2\Delta_J, \quad (1)$$

$$B'' = B^{(A)} + 2\Delta_J + \Delta_{JK} - 2\delta_J - 2\delta_K, \quad (2)$$

$$C'' = C^{(A)} + 2\Delta_J + \Delta_{JK} + 2\delta_J + 2\delta_K, \quad (3)$$

$$A'' = A^{(S)} + 2D_J + 6d_2, \quad (4)$$

$$B'' = B^{(S)} + 2D_J + D_{JK} + 2d_1 + 4d_2, \quad (5)$$

$$C'' = C^{(S)} + 2D_J + D_{JK} + 2d_1 + 4d_2. \quad (6)$$

The use of Kraitchman's equation (Eq. (7)) for single isotopic substitution⁴⁶ yields the absolute value of the Cartesian coordinates of the substituted atom (designated $|a_s|$) in the principal axis coordinate system of the reference isotopologue of HN₃. An R_s structure, determined from the application of Kraitchman's equation, is presented in Table V using the average determinable constants for all 14 observed isotopologues. With our data, the analysis could be performed using eight separate coordinate systems (HN₃, DN₃, and their six singly ¹⁵N substituted isotopologues). Of these coordinate systems, HNN¹⁵N was problematic because the center nitrogen was too close to the center of mass, resulting in an undetermined value of $|b|$ for the center nitrogen. The other seven coordinate systems worked effectively, and the geometric parameters for the R_s structure reported below are the average of the parameters from the seven calculations. The reported error is the standard deviation of the mean for those seven calculations,

$$|a_s| = \sqrt{\frac{I_{a_s} - I_a}{\mu} \left(1 + \frac{I_{b_s} - I_b}{I_b - I_a} \right)} \quad (7)$$

$$\mu = \frac{M * (M_s - M)}{M + (M_s - M)},$$

TABLE IV. Spectroscopic parameters for isotopologues of DN₃ in the S-reduced Hamiltonian F representation.

	DN ₃	D ¹⁵ NNN	DN ¹⁵ NN	DNN ¹⁵ N	D ¹⁵ N ¹⁵ NN	D ¹⁵ NN ¹⁵ N	DN ¹⁵ N ¹⁵ N
A ₀ (MHz)	344 746.613(17)	340 247.304(14)	344 618.810(52)	344 727.736(17)	340 093.976(29)	340 233.190(15)	344 602.430(35)
B ₀ (MHz)	11 350.262 67(51)	11 045.066 25(59)	11 347.891 1(15)	10 979.465 01(61)	11 041.403 9(13)	10 679.690 72(70)	10 978.495 5(13)
C ₀ (MHz)	10 965.503 24(49)	10 675.916 53(51)	10 963.175 8(18)	10 618.979 71(57)	10 672.362 5(16)	10 334.128 62(86)	10 617.974 0(18)
D _J (kHz)	4.217 46(66)	4.002 10(73)	4.215 7(35)	3.929 48(78)	4.000 0(30)	3.721 7(15)	3.930 2(34)
D _{JK} (kHz)	446.669(42)	446.986(49)	446.52(14)	420.523(40)	445.93(15)	420.302(78)	420.19(18)
D _K (kHz)	91 942.1(42)	87 571.1(34)	91 145(26)	92 014.3(40)	86 908(16)	87 592.9(89)	91 358(20)
d ₁ (kHz)	-0.172 982(32)	-0.155 562(53)	-0.175 4(13)	-0.155 442(45)	-0.157 35(73)	-0.140 28(36)	-0.155 95(94)
d ₂ (kHz)	-0.048 796(41)	-0.045 163(53)	-0.049 1(11)	-0.043 371(57)	-0.044 75(40)	-0.039 63(19)	-0.043 62(51)
H _{JK} (Hz)	0.890(19)	0.975(39)	0.80(18)	0.692(21)	0.59(20)	0.61(10)	0.65(30)
H _{KJ} (Hz)	-212.6(26)	-156.7(28)	-172.7(67)	-221.6(30)	-167.3(83)	-201.2(44)	-231.1(99)
L _{KKJ} (mHz)	-3 516(42)	-3411(47)	-4 873(94)	-3379(51)	-3 709(162)	-258 0(88)	-359 8(214)
Δ _i (u Å ²)	0.096 383 8	0.096 816 4	0.096 3191	0.096 551 0	0.096 734 03	0.096 989 8	0.096 460 9
N _{lines}	136	143	60	135	46	61	41
σ _{fit} (MHz)	0.052 628	0.052 537 0	0.049 499 7	0.057 067 9	0.038 468	0.025 424	0.042 606

TABLE V. Inertial defects for the isotopologues of HN_3 from various determinations of the moments of inertia.

Isotopologue	Experimental $B_0'' \Delta_i$ ($\text{u } \text{\AA}^2$) ^a	B_e from vibration-rotation corrected $B'' \Delta_i$ ($\text{u } \text{\AA}^2$) ^a	B_e from vibration-rotation and electronic corrected $B'' \Delta_i$ ($\text{u } \text{\AA}^2$)
HNNN	0.0735	0.003 53	0.003 60
H ¹⁵ NNN	0.0738	0.003 55	0.003 63
HN ¹⁵ NN	0.0736	0.003 50	0.003 57
HNN ¹⁵ N	0.0736	0.003 53	0.003 62
H ¹⁵ N ¹⁵ NN	0.0739	0.003 54	0.003 62
H ¹⁵ NN ¹⁵ N	0.0739	0.003 54	0.003 63
HN ¹⁵ N ¹⁵ N	0.0737	0.003 48	0.003 56
DNNN	0.0963	0.003 42	0.003 43
D ¹⁵ NNN	0.0967	0.003 45	0.003 45
DN ¹⁵ NN	0.0962	0.003 45	0.003 46
DNN ¹⁵ N	0.0964	0.003 43	0.003 44
D ¹⁵ N ¹⁵ NN	0.0966	0.003 46	0.003 47
D ¹⁵ NN ¹⁵ N	0.0969	0.003 46	0.003 47
DN ¹⁵ N ¹⁵ N	0.0963	0.003 43	0.003 45

^aReported values are the average of determinable constants calculated from the $B^{(S)}$ and the $B^{(A)}$ values.

Several R_0 and R_e structures were determined using xrefit (a module of CFOUR), which is a least-squares fitting program that optimizes the molecular structural parameters to fit all available moment of inertia data. The R_0 structure uses moments of inertia derived directly from the observable constants (B_0''). This optimized structure still does not include the contributions of vibration-rotation interactions or the electron mass on the observed rotational constants.

A purely experimental value for R_e is possible only if rotational constants are found for each vibrational fundamental for each isotopologue and there are no perturbations between the states. Without experimentally determined vibration-rotation interactions (α_i) for each vibrational mode, we determined a mixed experimental/theoretical equilibrium structure (R_e). The determinable rotational constants for each isotopologue were adjusted for the effects of vibration by correcting each of the rotational constants with one half of the sum of the corresponding vibration-rotation interaction parameters (α_i) obtained from a VPT2 calculation at the CCSD(T)/ANO2 level of theory. This basic approach has been used recently with great success for a variety of molecules, with various levels of theory for the vibration-rotation corrections.^{30,47–51} For a planar molecule like HN_3 , the vibration-rotation corrections to the rotational constants should adjust the inertial defects of all isotopologues to an ideal value of zero. As shown in Table V, the inertial defects are much closer to zero for our vibration-rotation corrected constants, while the correction for electron mass does not further reduce the inertial defects. In the previous studies, the electronic mass was shown to be important for the equilibrium structure determination of molecules which

contain conjugated π systems.^{30,52} Our R_s , R_0 , and R_e structures are presented in Table VI below along with the computed structures and the best previously published R_s structure.⁹ The R_e structural parameters in Table VI are in very good agreement with the CCSD(T)/cc-pCV5Z results and have unusually small uncertainty limits. Fig. 3 shows more clearly the relationship between the experimental, CCSD(T)/cc-pCV5Z, and CCSD(T)/ANO2 structural parameters. The small error bars in the experimental structural parameters make it possible to discern a dramatic improvement in the accuracy of the CCSD(T)/cc-pCV5Z *ab initio* results in comparison to the CCSD(T)/ANO2 values.

DISCUSSION

Although the potential of rotational spectroscopy to be the most accurate method for determining molecular structures has been recognized since its beginnings, the degree to which this accuracy has actually been achieved in published ‘microwave structures’ has varied widely.⁵³ The measurement accuracy for spectral lines has always been very high, but the determination of bond distances and angles with great accuracy has usually been limited by two distinct issues: the lack of sufficient isotopic data and/or the sophistication of the data analysis. Isotopic substitution at all atomic positions is critical — multiple substitutions leading to more accurate structures. Of comparable importance is the treatment (or lack thereof) of vibration-rotation interaction effects and, to a lesser extent, the centrifugal distortion and the non-spherical distributions of electron mass. In the present work, we have endeavored to

TABLE VI. Geometric parameters for HN_3 determined by various methods.

	R_s Winnewisser ⁹	$R_s B_0''$	$R_0 B_0''$	$R_e B_e, \alpha_i$ corrected from B_0''	$R_e B_e, \alpha_i$ and electron corrected from B_0''	R_e CCSD(T)/cc-pCV5Z	R_e CCSD(T)/ANO2
$R_{\text{H-N1}}$ (\AA)	1.0150(150)	1.014 88(23)	1.0222(41)	1.015 79(16)	1.015 77(16)	1.015 59	1.017 22
$R_{\text{N1-N2}}$ (\AA)	1.2430(50)	1.229 3(14)	1.2453(89)	1.241 75(36)	1.241 74(37)	1.241 53	1.244 70
$R_{\text{N2-N3}}$ (\AA)	1.1340(20)	1.146 3(14)	1.1346(91)	1.130 68(37)	1.130 66(38)	1.130 56	1.132 71
$\angle_{\text{H-N1-N2}}$ ($^\circ$)	108.80(400)	108.995(32)	108.58(39)	109.137(17)	109.133(17)	109.211	108.710
$\angle_{\text{N1-N2-N3}}$ ($^\circ$)	171.30(500)	171.90(22)	170.91(115)	171.505(50)	171.503(51)	171.626	171.656

address all of these issues as completely as possible. Hydrazoic acid is a favorable case in that the simplicity of its synthesis and the sensitivity of current millimeter-wave spectrometers make practical the study of a great many isotopologues. On the other hand, it poses substantial challenges with respect to the interaction of vibration and rotation and moreover exhibits large values of the centrifugal distortion constants. The rotational level spacings are much more comparable with vibrational spacings than is the case for most molecules. Therefore, the vibration-rotation interactions are unusually strong and complex. Although there are high resolution spectral data for all six of the fundamental states of HN_3 and DN_3 ,^{11,13–25} using those data to extract the true α_i constants has proven intractable because of strong perturbations. Furthermore, finding experimental α_i 's for the rare isotopologues is not a realistic objective with current experimental methods. Hydrazoic acid thus provides an excellent test case for the method of combining experimental ground state rotational constants with *ab initio* sum of α_i constants to obtain a mixed equilibrium structure.^{30,47–51}

Careful examination of the least-squares fits of the equilibrium moments of inertia to the structure (I_a^e , I_b^e , and I_c^e) reveals several things. The pattern of residuals among I_a^e , I_b^e , and I_c^e (denoted δI_a^e , δI_b^e , and δI_c^e) is nearly the same for all 14 isotopologues. In our R_e structure fit shown in Fig. 2, the average of the residuals, δI_a^e , δI_b^e , and δI_c^e , over the 14 cases is, respectively, 0.001 18(3), 0.001 17(11), and -0.001 18(10) u \AA^2 . The very small standard deviations (in parentheses) confirm the precision of the experimental ground state rotational constants and the precision of *ab initio* calculations of the isotopic variation for the sum of α_i 's at the level of theory employed. Most of these (albeit small) residuals are due to the remaining non-zero inertial defects found in Table V. Indeed, $\delta I_a^e + \delta I_b^e - \delta I_c^e$ exactly match the remaining inertial defects of the theoretical/experimental I_e values input to the least-

squares structure fit (shown in Table V). The optimized R_e output structure by definition has an inertial defect of precisely zero.

The magnitude of the estimated statistical uncertainties given by xrefit for the five structural parameters can largely be attributed to this small but systematic deviation of the theoretical/experimental R_e inertial defects from zero. The supplementary material contains xrefit outputs where only I_a^e and I_b^e data, or only I_a^e and I_c^e data, or only I_b^e and I_c^e data were used.³⁴ This approach serves to shunt the systematic error related to nonzero A_i into the third set of I_e 's, while still giving the fit more than ample degrees of freedom. The average of the parameters determined by these three two-moment fits is precisely the same as the parameters from the original three-moment fit. The parameter variation between the three two-moment fits is quite comparable to the reported statistical uncertainties produced by xrefit for the three-moment fit. The statistical error of the parameters determined by the two-moment fits is decreased by roughly a factor of ten compared to the original three-moment fit. The remaining statistical error in the two-moment fits should be the portion of error attributable to random variations in the moments of inertia rather than the systematic error caused by the non-zero inertial defects.

From the above discussion, it is clear that obtaining starting B_e 's with inertial defects even closer to the ideal value of zero would further improve the accuracy of the structural determination. The origin of these residual non-zero inertial defects is a matter of some speculation at this point. It is clear that electron mass effects are not an issue, because including them has little effect on the inertial defects (Table V). We have also observed that the use of a higher level of theory in the VPT2 calculation of the α_i 's does not solve the problem. Our suspicion is that the source of the trouble is our lack of inclusion of the next higher order terms in the vibration-rotation

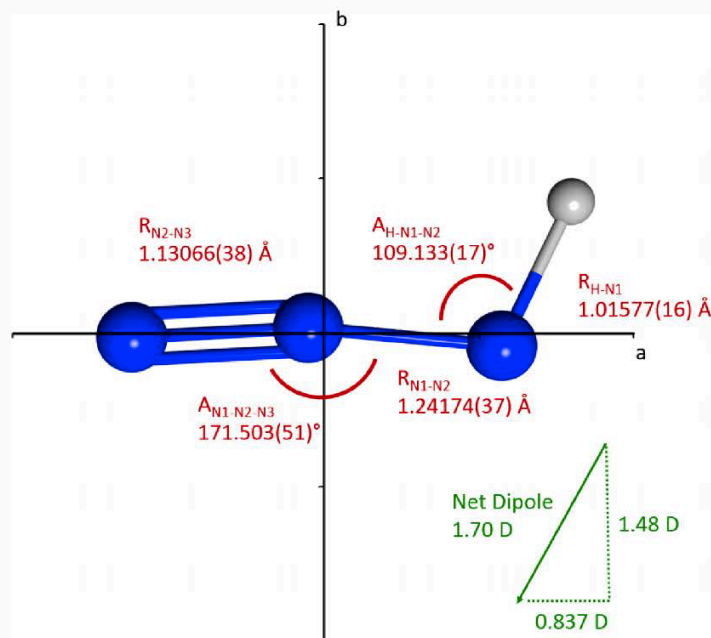


FIG. 2. R_e Structure of HN_3 . Dipole moments are from the previous Stark measurements.^{7,41}

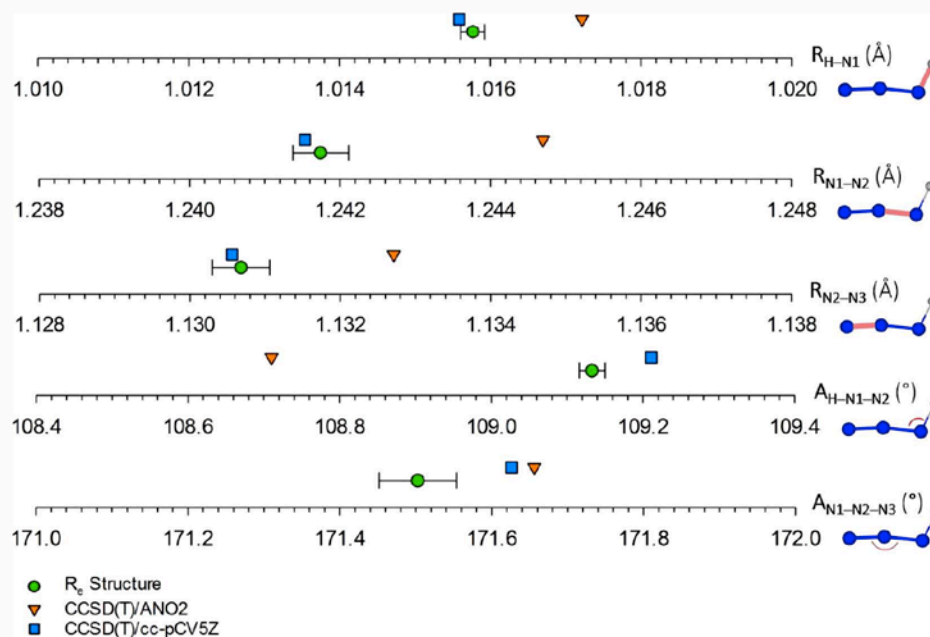


FIG. 3. Graphical representation of the equilibrium parameters of hydrazoic acid obtained experimentally and from the CCSD(T)/ANO2 and CCSD(T)/cc-pCV5Z calculations.

expansion (those quadratic in the vibrational quantum numbers, i.e., the γ_i corrections). Future theoretical calculations, not currently implemented, will be required to test this hypothesis.

For achieving the level of accuracy sought here, careful consideration of the fairly large centrifugal distortion effects is also required. The xrefit routine of CFOUR can accept experimental A-reduction constants ($A_0^{(A)}$, $B_0^{(A)}$, $C_0^{(A)}$), S-reduction constants ($A_0^{(S)}$, $B_0^{(S)}$, $C_0^{(S)}$), or determinable constants (A_0'' , B_0'' , C_0''), and make internal conversions to equilibrium values (I_A^e , I_B^e , I_C^e) based upon supplied vibration-rotation interaction and electron mass corrections. We found that our equilibrium moments (I_e 's) derived from S-reduced moments ($I_0^{(S)}$'s) were in excellent agreement with our values calculated from the determinable moments (I_0'' 's). The agreement with the equilibrium moments deriving from our A-reduction moments ($I^{(A)}$'s) was still good but not to the same extent. For example, our I_e moments for H^{14}N_3 calculated from I_0'' , $I_0^{(S)}$, and $I_0^{(A)}$ moments yielded inertial defects of 0.003 53, 0.003 54, and 0.004 81 $\mu\text{Å}^2$, respectively. Notably, the inertial defects for the I'' , $I^{(S)}$, and $I^{(A)}$ moments for H^{14}N_3 before vibration-rotation correction are 0.0735, 0.0737, and 0.079 42 $\mu\text{Å}^2$, respectively (full table available in the supplementary material).³⁴ The source of this discrepancy is not entirely understood, although there would be an *a priori* expectation that the S-reduction might work better than the A-reduction for a molecule so close to being a prolate symmetric top. We have used the determinable moments (I_0'' 's) as the experimental moments in determining the R_e structure shown in Figs. 2 and 3.

The above issues notwithstanding, the accuracy reported in Table VI is quite high for our R_e structures. The largest bond distance uncertainty is 0.000 38 Å and the largest bond angle

uncertainty is 0.05°. Using the determinable moments (I_0'' 's) derived from the S-reduction moments alone has no substantial impact on the determined structure and did not result in a reduction of the structural uncertainties. The largest resulting change to a bond distance and a bond angle is $-0.000\,03$ Å and -0.004° , respectively, well within the error of the parameter values presented in Figs. 2 and 3. At this level of accuracy, the experimental structure becomes a significantly better benchmark for the quality of the *ab initio* predictions of molecular structure than has typically been the case. Although both of the theoretical methods reported here obtain excellent agreement with experiment by usually applied standards, the ANO2 frozen core structure does exhibit significant deviations from experiment in comparison to the claimed experimental uncertainty. On the other hand, the higher level all-electron quintuple zeta basis set coupled cluster calculation produces bond distances that fall within the experimental error bars and bond angles that are only slightly outside them—almost an order of magnitude better agreement. This improvement is clearly visible in Figure 3. The rather spectacular agreement between mixed experimental/theoretical structure with the very high-quality *ab initio* result is particularly gratifying, in that it serves to confirm both the reasonableness of our reported experimental error limits and also the power of the best modern theoretical methods to produce great accuracy in the prediction of molecular structure of small molecules.

ACKNOWLEDGMENTS

We gratefully acknowledge funding from the National Science Foundation for support of this Project (Nos. CHE-1362264 and CHE-1011959) and for support of shared Departmental computing resources (No. CHE-0840494). We thank

Dr. Mark Wendt for access to the Agilent MXG Analog Signal Generator N5183B. J.F.S. thanks the U.S. National Science Foundation (No. CHE-1361031).

- ¹T. Curtius, *Ber. Dtsch. Chem. Ges.* **23**, 3023–3033 (1890).
- ²G. Herzberg, F. Patat, H. Verleger, and Z. Elektrochem, *Angew. Phys. Chem.* **41**, 522–524 (1935).
- ³E. H. Eyster, *J. Chem. Phys.* **8**, 135–142 (1940).
- ⁴V. Schomaker and R. Spurr, *J. Am. Chem. Soc.* **64**, 1184–1187 (1942).
- ⁵E. Amble and B. P. Dailey, *J. Chem. Phys.* **18**, 1422 (1950).
- ⁶M. Winnewisser and R. L. Cook, *J. Chem. Phys.* **41**, 999–1004 (1964).
- ⁷J. Bendtsen and M. Winnewisser, *Chem. Phys. Lett.* **33**, 141–145 (1975).
- ⁸J. Bendtsen and M. Winnewisser, *Chem. Phys.* **40**, 359–365 (1979).
- ⁹B. P. Winnewisser, *J. Mol. Spectrosc.* **82**, 220–223 (1980).
- ¹⁰J. Lievin, J. Breulet, and G. Verhaegen, *Theor. Chim. Acta* **52**, 75–88 (1979).
- ¹¹J. Bendtsen, *J. Raman Spectrosc.* **9**, 162–165 (1980).
- ¹²A. Toyota, T. Muramatsu, and S. Koseki, *RSC Adv.* **3**, 10775–10785 (2013).
- ¹³K. Yamada and M. Takami, *J. Mol. Spectrosc.* **84**, 431–446 (1980).
- ¹⁴J. Bendtsen, *J. Raman Spectrosc.* **15**, 113–119 (1984).
- ¹⁵J. Bendtsen, F. Hegelund, and F. M. Nicolaisen, *J. Mol. Spectrosc.* **118**, 121–131 (1986).
- ¹⁶J. Bendtsen and F. M. Nicolaisen, *J. Mol. Spectrosc.* **119**, 456–466 (1986).
- ¹⁷J. Bendtsen and F. M. Nicolaisen, *J. Mol. Spectrosc.* **125**, 14–23 (1987).
- ¹⁸F. Hegelund and J. Bendtsen, *J. Mol. Spectrosc.* **124**, 306–316 (1987).
- ¹⁹J. Bendtsen, F. Hegelund, and F. M. Nicolaisen, *J. Mol. Spectrosc.* **128**, 309–320 (1988).
- ²⁰A. S. C. Cheung and A. J. Merer, *J. Mol. Spectrosc.* **127**, 509–526 (1988).
- ²¹J. Bendtsen and F. M. Nicolaisen, *J. Mol. Spectrosc.* **133**, 193–200 (1989).
- ²²J. Bendtsen and F. M. Nicolaisen, *J. Mol. Spectrosc.* **145**, 123–129 (1991).
- ²³J. Bendtsen and F. M. Nicolaisen, *J. Mol. Spectrosc.* **152**, 101–108 (1992).
- ²⁴C. S. Hansen, J. Bendtsen, and F. M. Nicolaisen, *J. Mol. Spectrosc.* **175**, 239–245 (1996).
- ²⁵J. Bendtsen and G. Guelachvili, *J. Mol. Spectrosc.* **165**, 159–167 (1994).
- ²⁶J. Evers, M. Göbel, B. Krumm, F. Martin, S. Medvedyev, G. Oehlinger, F. X. Steemann, I. Troyan, T. M. Klapötke, and M. I. Eremets, *J. Am. Chem. Soc.* **133**, 12100–12105 (2011).
- ²⁷B. M. Gimarc and D. A. Woodcock, *J. Mol. Struct.: THEOCHEM* **85**, 37–43 (1981).
- ²⁸J. H. Teles, G. Maier, B. Andes Hess, L. J. Schaad, M. Winnewisser, and B. P. Winnewisser, *Chem. Ber.* **122**, 753–766 (1989).
- ²⁹M. Mladenović, M. Elhiyani, and M. Lewerenz, *J. Chem. Phys.* **130**, 154109 (2009).
- ³⁰B. J. Esselman, B. K. Amberger, J. D. Shutter, M. A. Daane, J. F. Stanton, R. C. Woods, and R. J. McMahon, *J. Chem. Phys.* **139**, 224304 (2013).
- ³¹B. K. Amberger, B. J. Esselman, R. C. Woods, and R. J. McMahon, *J. Mol. Spectrosc.* **295**, 15–20 (2014).
- ³²Z. Kisiel, PROSPE—Programs for ROTational SPEctroscopy, 2012, <http://info.ifpan.edu.pl/~kisiel/prospe.htm>.
- ³³H. M. Pickett, *J. Mol. Spectrosc.* **148**, 371–377 (1991).
- ³⁴See supplementary material at <http://dx.doi.org/10.1063/1.4929792> for summaries of computed geometries, harmonic vibrational frequencies, anharmonic vibrational frequencies, and vibration-rotation interaction constants computed using CF4OUR. Measured and fit rotational transitions for all species in the ASFIT output format, determinable constants, inertial defects, and full details concerning structure determinations.
- ³⁵J. F. Stanton, J. Gauss, M. E. Harding, P. G. Szalay, and R. J. Bartlett with contributions from A. A. Auer, U. Benedikt, C. Berger, D. E. Bernholdt, Y. J. Bomble, L. Cheng, O. Christiansen, M. Heckert, O. Heun, C. Huber, T.-C. Jagau, D. Jonsson, J. Jusélius, K. Klein, W. J. Lauderdale, D. A. Matthews, T. Metzroth, L. A. Mück, D. P. O’Neill, D. R. Price, E. Prochnow, C. Puzzarini, K. Ruud, F. Schiffmann, W. Schwalbach, S. Stopkiewicz, A. Tajti, J. Vázquez, F. Wang, J. D. Watts, and the integral packages MOLECULE (J. Almlöf and P. R. Taylor), PROPS (P. R. Taylor), ABACUS (T. Helgaker, H. J. Aa. Jensen, P. Jørgensen, and J. Olsen), and ECP routines by A. V. Mitin and C. van Wüllen, CF4OUR, Coupled-Cluster Techniques for Computational Chemistry, ■, <http://www.cf4our.de>.
- ³⁶J. A. Pople, M. Head-Gordon, and K. Raghavachari, *J. Chem. Phys.* **87**, 5968–5975 (1987).
- ³⁷G. E. Scuseria, *J. Chem. Phys.* **94**, 442–447 (1991).
- ³⁸T. J. Lee and A. P. Rendell, *J. Chem. Phys.* **94**, 6229–6236 (1991).
- ³⁹I. M. Mills, in *Molecular Spectroscopy: Modern Research*, edited by K. N. Rao and C. W. Mathews (Academic Press, New York, 1972), Vol. 1, pp. 115–140.
- ⁴⁰J. F. Stanton, C. L. Lopreore, and J. Gauss, *J. Chem. Phys.* **108**, 7190–7196 (1998).
- ⁴¹K. J. White and R. L. Cook, *J. Chem. Phys.* **46**, 143–151 (1967).
- ⁴²W. Gordy and R. Cook, *Microwave Molecular Spectra*, 3rd ed. (Wiley Interscience, New York, 1984).
- ⁴³B. Krakow, R. C. Lord, and G. O. Neely, *J. Mol. Spectrosc.* **27**, 148–176 (1968).
- ⁴⁴J. Bendtsen, *J. Raman Spectrosc.* **6**, 306–313 (1977).
- ⁴⁵F. W. Loomis and R. W. Wood, *Phys. Rev.* **32**, 223–236 (1928).
- ⁴⁶J. Kraitichman, *Am. J. Phys.* **21**, 17–24 (1953).
- ⁴⁷C. Puzzarini and V. Barone, *Phys. Chem. Chem. Phys.* **13**, 7189–7197 (2011).
- ⁴⁸M. C. McCarthy, L. Cheng, K. N. Crabtree, O. Martinez, T. L. Nguyen, C. C. Womack, and J. F. Stanton, *J. Phys. Chem. Lett.* **4**, 4133–4139 (2013).
- ⁴⁹C. C. Womack, K. N. Crabtree, L. McCaslin, O. Martinez, R. W. Field, J. F. Stanton, and M. C. McCarthy, *Angew. Chem., Int. Ed.* **53**, 4089–4092 (2014).
- ⁵⁰N. M. Kidwell, V. Vaquero-Vara, T. K. Ormond, G. T. Buckingham, D. Zhang, D. N. Mehta-Hurt, L. McCaslin, M. R. Nimlos, J. W. Daily, B. C. Dian, J. F. Stanton, G. B. Ellison, and T. S. Zwier, *J. Phys. Chem. Lett.* **5**, 2201–2207 (2014).
- ⁵¹O. Martinez, K. N. Crabtree, C. A. Gottlieb, J. F. Stanton, and M. C. McCarthy, *Angew. Chem., Int. Ed.* **54**, 1808–1811 (2015).
- ⁵²J. F. Stanton, J. Gauss, and O. Christiansen, *J. Chem. Phys.* **114**, 2993–2995 (2001).
- ⁵³P. Groner, in *Vibrational Spectra and Structure*, edited by R. D. James (Elsevier, 1999), Vol. 24, pp. 165–252.